Molecular Design Implications of Esterified Therapeutic Peptides and Their Delivery Vehicles

---

A

Dissertation

Presented to

the faculty of the School of Engineering and Applied Science

University of Virginia

---

in partial fulfillment

of the requirements for the degree

Doctor of Philosophy

by

Mark Stephen Bannon

December 2024

APPROVAL SHEET

This

Dissertation

is submitted in partial fulfillment of the requirements
for the degree of

Doctor of Philosophy

Author: Mark Stephen Bannon

This Dissertation has been read and approved by the examing committee:

Advisor: Rachel Letteri

Advisor:

Committee Member: Geoff Geise

Committee Member: Rachel Letteri

Committee Member: Guarav Giri

Committee Member: Kyle Lampe

Committee Member: Nick Tsihlis

Committee Member:

Accepted for the School of Engineering and Applied Science:

Jennifer L. West, School of Engineering and Applied Science

December 2024

Acknowledgments

While I'm incredibly proud of the work that I put into this thesis, it would not be possible without any of the people below. Thank you to everyone.

First and foremost, I'd like to dedicate this thesis to my advisor, mentor, and friend Rachel Letteri. I still remember the day that I learned I was going to be joining your lab, because I immediately went outside and called my family to tell them the great news. You are the reason I've enjoyed graduate school so much, the reason I was able to write this thesis, and you are 100% the reason that I want to be a professor. Thanks for taking the chance and letting a "toolbox" like me join your lab, and thank you for having the confidence in me that I sometimes didn't have in myself.

To all of the members of the Letteri Lab – Mara, Vince, Israt, Kelly, Jerwin, Darren, Hadley, Mobina, Emma, James, Justin, Justin, Chris, Taylor, JP, Josh, Elli, Esme, Jack, Clare. Liza, Janine, and Anthony - thank you so much for supporting me, helping me work through various issues in the lab, and for making every day at work a good one, even when it wasn't. To Taylor, Jack, and Esme, thank you for all of your hard work, it was truly a pleasure to do research with you.

Zixian, thanks for being there whenever anything was going wrong, whenever I needed help with something, and, most importantly, if I wanted to laugh. Vince, you were the first person I met from UVA, and I'm so happy you ended up being one of my closest friends – you're one of the most cool, calm, collected, and loyal people I know. Mara, I don't know if anyone else helped mold me as a researcher as much as you - thanks for being an amazing role model and friend. Aditi, I've never worked with anyone as dedicated, thoughtful, and empathetic as you – I feel confident that I'm leaving our work in extremely capable hands, and thanks for being my first student.

To all of my collaborators – Rob, Spencer, Jane, Gino, Prince, Mara, Ankit, Jeff, Dilza, and Nick - thank you for making research exciting and involving me in your amazing work. To Rob, Spencer, and Jane - besides all of the fun dinners and Rob's amazing one liners, it's been truly inspiring to get to see the potential of the work we do. I've always appreciated you all taking the time out of your schedules to answer questions or entertain thoughts I had on the project, because it truly made me a better researcher. Gino, Prince, and Ankit – thanks for teaching me about MOFs, and for making every Wednesday afternoon for 3 years intellectually stimulating and fun. Jeff, thanks for taking the time to turn in my quick pop-ins with questions about 2D NMR into hour long conversations to help me really understand – you made NMR fun and easy, which is a very hard thing to do.

To my committee members, Drs. Geoff Geise, Gaurav Giri, Kyle Lampe, and Nick Tshilis, thank you for your support towards the completion of my Ph.D. Geoff, thanks for being an awesome neighbor, mentor, and advisor to Sean.

To the friends I've met in Charlotteville – Anu, Anna, Prince, Greg, Ivan, Anna, Charlie, Cayla, Sammy, Kadie, Vince, Colby, Aditi, Mara, Jamie, Natalie, Zach, Kelly, Rhea, Sanha, Grayson, Karl, and Sarah - I couldn't have ever imagined that I would have found the community and friendship down here that I did. Thank you for being amazing people, accepting me for who I am, and making graduate school so fun. To Chuck, thanks for the great times watching lacrosse, coaching lacrosse, and teaching me that it's okay to speak my mind.

To Dave King, Kyle Seago, Sean O'Rourke, and the whole Albemarle High School Boys Lacrosse team, thank you for giving me the chance to be involved in the sport that I love. Go Patriots!

To my family - Sean, Val, Penny, Mom, Dad, Grandma and Bob – thank you for being the loving, supporting, and amazing people you are. I can always count on you, and none of this would have been possible without you. Sean, thanks for always being my teammate – whether it's in lacrosse, the band, or research – there's nobody else I'd rather be next to. Val, I couldn't imagine Sean with anyone else, and am so happy to get to call you sister. Dad, thank you for teaching me that it's okay to have fun every once in a while, and Mom, thank you for teaching me to always dance when I get the chance. Grandma, thanks for passing down your ability to see the best in people. To my Grandpa, Bob, I miss you a lot, but thank you for teaching me to always go to college whenever we played the game of Life – it paid off.

To Jess, these past 5 years have been the hardest time in my life; not because of the Ph.D., but because I had to be away from you. You're my best friend, you're always in my corner, and I love you more than I love peptides (which is a lot, if you can't tell from this thesis). I can't wait to spend the rest of my life with you.

When I first joined the lab, I hung this quote up on my desk in my office. It's the first thing I saw every day for the past 5 years, and the last thing I saw before I went home.

"It's supposed to be hard. If it wasn't hard, everyone would do it. The hard is what makes it great." – A League of Their Own

Abstract

As naturally potent molecules with low off-site toxicity, peptides have massive therapeutic potential, highlighted by successful drugs like insulin; however, their low cell membrane permeability and short *in vivo* half-lives prevent their clinical translation. In this thesis, we tailor both therapeutic peptides and relevant carrier systems towards overcoming these drawbacks and realizing the therapeutic potential of peptides. Historically, efforts to overcome these two drawbacks involve increasing the hydrophobicity and net cationic charge of therapeutic peptides through chemical modifications to peptide sequence, which can increase cell membrane permeability and/or enable encapsulation into relevant carriers. Yet, these modifications are often permanent, which comes at the expense of structurally-related activity or release from carriers. To reversibly modify the hydrophobicity and net cationic charge of therapeutic peptides to enable access to intracellular targets or encapsulation and release into relevant carriers, we have developed esterification of therapeutic peptides, where hydrophilic, anionic carboxylic acids are replaced with hydrophobic, but hydrolytically cleavable, ester groups. Hydrolysis of the esters enables restoration of the unesterified form of the therapeutic so as to return any structurally-related activity, a reaction that can be accelerated in the presence of endogenous esterases. In **Chapter 2**, we show that the number and position of esters installed onto the therapeutic peptide α carboxyl terminus 11 (αCT11, RPRPDDLEI) affect peptide hydrophobicity and hydrolytic stability of the ester caps, with the C-terminal ester being the most influential in modifying αCT11 properties. *In vitro* proof-of-concept experiments showed esterifying αCT11 to increase cell migration into a scratch, indicative

of increased wound healing activity. In **Chapter 3**, we leverage the reversible increase in net cationic charge afforded by esterification to reversibly encapsulate αCT11 into polyelectrolyte complexes (PECs) through electrostatic interactions with anionic poly(methacrylic acid) (PMAA). We then study αCT11 ester hydrolysis in the presence and absence of PMAA, showing it to not only proceed slower in the presence of PMAA, but also correspond to a decrease in turbidity in mixtures of PMAA and esterified αCT11, suggesting hydrolysis to cause PEC dissociation and peptide release. In **Chapter 4**, we design polymer-metal organic framework (MOF) composite gels, materials that combine the high sorptive capacity of MOFs into a processable polymer hydrogel template, as potential carriers for the anti-inflammatory peptide angiotensin 1-7 (Ang 1-7). Through investigating how polymer chemistry influences MOF formation and how MOF formation in turn influences gelation, we find that interactions between weakly metal-binding polymer functional groups (i.e., hydroxyls) and MOF metal nodes as well as polymer entrapment within MOF crystals simultaneously enables the formation of crystalline, self-supporting composite gels. Further, polymer-MOF composite hydrogels were capable of sorbing Ang 1-7 and showed sustained release of a small molecule dye relative to the individual polymer and MOF constituents. Altogether, this dissertation serves to influence the future design of both therapeutic peptides and their carriers, and in particular showcases the potential of therapeutic peptide esterification to reversibly tailor the properties of therapeutic peptides and expand their clinical implementation.

TABLE OF CONTENTS

TABLE OF FIGURES

retained in the bloodstream, as the biocompatible carrier cannot pass through the glomerular membrane. c) Degradation of therapeutic peptides by proteases (red), enzymes capable of cleaving peptide structures at the peptide bond (amide between individual amino acids). Biocompatible carriers block proteases from accessing encapsulated therapeutic peptides. d) Tuning interactions between the drug and the biocompatible carriers can tune the release of the drug. 4

Figure 1.4. Molecular structure of the therapeutic peptide α carboxyl terminus 11 (αCT11, RPRPDDLEI). The structure is reflective of the charge state at physiological pH (7.4), with positively and negatively charged groups are shown in blue and red, respectively. 8

Figure 1.5. Therapeutic peptide esterification. Carboxylic acids on peptides can be reversible esterified to modify hydrophobicity (orange) and cationic net charge (blue). Installed esters can then be hydrolyzed to return any negatively charged (red) carboxylic acids and restore the original, hydrophilic (light blue) peptide structure. 10

Figure 2.1. Identifying the numbers and positions of methyl esters installed onto αCT11 through Fischer esterification. a) RP-HPLC of αCT11 (peak is blue), αCT11 with 2 methyl esters (peak is yellow), 4 different conformations of αCT11 with 3 esterified esters in either the D5, D6, E8, and/or I9 residues (αCT11-3OMe(D5,D6,E8, or I9), peaks are orange), and fully esterified αCT11, with 4 methyl esters (αCT11-4OMe, peaks are red). Retention time, and thus hydrophobic character, increased with the number of esters installed onto αCT11. The mobile phase consisted of water and acetonitrile (ACN), each with 0.1% trifluoroacetic acid, and each sample eluted between 23 and 26% ACN. Retention times were normalized to those of the αCT11 and αCT11-4OMe samples. ^{1}H NMR (800 MHz, DMSO-d6) spectra of b) αCT11 (blue), c-f) each of the 4 αCT11-3OMe samples (orange), and g) αCT11-4OMe (red) methyl ester proton singlets (3.56 – 3.63 ppm) show which amino acids are esterified in which formulations. Integrals for each peak in are plotted in gray on the spectra. Selective heteronuclear multiple bond correlation (selHMBC) of h) αCT11-3OMe(D5/D6/E8) (orange) and i) αCT11-4OMe (red) shows the most abundant -3OMe peak (-3OMe(A)) has esters installed on the D5, D6, and E8 positions, but not the C-terminal I9. 24

Figure 2.2. Recovery of unesterified αCT11 from esterified formulations in aqueous conditions. αCT11-3OMe(D5,D6,E8) (orange) and -4OMe (red) were incubated in 1X PBS (pH 7.4, squares) or 100 mM carbonate buffer (pH 10, triangles) and the amount of unmodified αCT11 present over ~1 week was quantified using RP-HPLC. Basic conditions were required to fully hydrolyze installed esters, where αCT11-3OMe(D5,D6,E8) and -4OMe were fully reverted to unesterified αCT11 after 3 d and 5 d in carbonate buffer (pH 10), respectively (denoted on the plot with an 'x'). Full recovery of unesterified αCT11 was not achieved in 1X PBS. 28

Figure 2.3. Relative abundance of intermediates observed during hydrolysis of esterified αCT11 formulations in 37 °C 1X PBS. LC-MS of a) αCT11-3OMe(D5,D6,E8) and b) -

via inversion tests, and grazing incidence X-ray diffraction (GIXD) patterns comparing the crystal structures of the MOFs formed in each composite gel to the simulated patterns for the corresponding MOFs. (d) Image showing that the PVA-UiO-66 composite gel thin film is free-standing. (e) Powder X-ray diffraction (PXRD) of the PVA-UiO-66 composite gel thin film. (f) Image showing that the PVA-UiO-66 composite gel thin film exhibits conformality. For the PVA-UiO-66 composite gel thin film, the PVA wt% is 2.5. Image of NU-901 crystal structure is reprinted (adapted) with permission from *Chem. Mater.* 2020, *32* (24), 10556–10565.[31] Copyright 2020 American Chemical Society. Image of UiO-67 crystal structure is reprinted (adapted) with permission from *Chem. Mater.* 2017, *27* (7), 3111-3117.[56] Copyright 2017 American Chemical Society. Image of MOF-525 crystal structure is reprinted (adapted) with permission from *Inorg. Chem.* 2012, *51* (12), 6443–6445.[33] Copyright 2012 American Chemical Society. GIXD data and images of the composite gels were collected by Prince Verma. GIXD data and images of the composite gel film were collected by Ankit Dhakal. 99

hydrogels (red, squares), PVA-Zr-oxo hydrogels (blue, circles), and MOF-525 powder (purple, triangles) all display burst release behavior, releasing 90% of their cargo within less than 24 h. Error bars represent the standard deviation between three separately synthesized samples, with * in (a) and (b) indicating an equal variances two sample t-test giving $p < 0.05$.

CHAPTER 1:
INTRODUCTION

1.1 Therapeutic peptides: Beneficial therapeutics with some drawbacks

1.1.1 Therapeutic peptides: an overview

Beginning in 1922 with the use of insulin, therapeutic peptides, molecules composed of between 2-100 amino acids (**Figure 1.1**), have been rapidly growing in the drug discovery space due to their potency, selectivity for specific targets, versatility, and low off-site toxicity.[1–3] Insulin set the stage for the discovery and approval of over 80 other peptide therapeutics, including glucagon-like peptide-1 (GLP-1) receptor agonists to treat diabetes (e.g, dulaglutide and semaglutdide), as well as the neuropeptide hormones oxytocin and vasopressin.[1,2,4] Despite their inherent benefits, therapeutic peptides only account for ~5% of the 1.2 trillion global pharmaceutical market as of 2019.[2] While this class of drugs has shown promise, clinical implementation of peptides is limited by their low cell membrane permeability and short circulatory half-lives.[5]
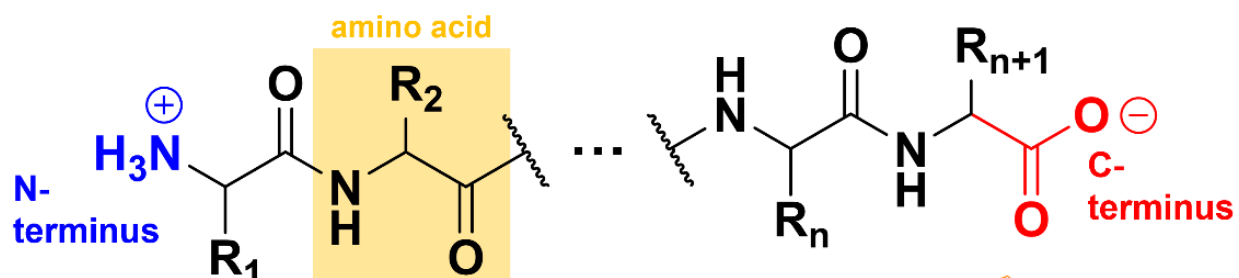
Figure 1.1. Chemical structure of a generic peptide. Shows the N-terminus (left end, blue), C-terminus (right end, red), and an individual amino acid (yellow). Examples of common functional side groups (R) naturally found in therapeutic peptides are listed below the general structure.

1.1.2 Therapeutic peptides have low cell membrane permeability

The main function of the cell membrane is to separate the interior organelles and cytoplasm of the cells from extracellular space, which also makes it responsible for regulating what enters the cell.[6] Eukaryotic cell membranes are composed of amphiphilic phospholipids, lipid molecules with a polar headgroup and hydrocarbon tails, packed into

form a bilayer, with cholesterols and transmembrane proteins dispersed between them (**Figure 1.2**). From a transport perspective, diffusion across cell membranes can be described through the homogeneous solubility diffusion model (known as Overton's rule), which deconvolutes them into a 3-phase membrane composed of a hydrophobic hydrocarbon layer flanked by intracellular and extracellular polar phospholipid headgroups, the former of which often contains a high concentration of negatively charged phosphatidylserine (Figure 1.2).[7–10] To this end, cell membrane permeability is specifically dependent on the ability of the therapeutic to partition into the hydrophobic hydrocarbon layer and electrostatically interact with the anionic intracellular leaflet, and, therefore, the size, charge, and hydrophobicity of the solute.[7,9,11–19]
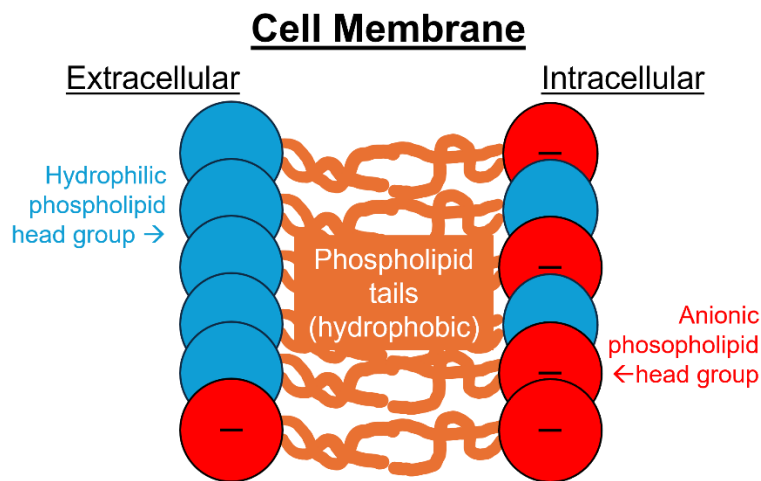
Cell Membrane

Figure 1.2. Eukaryotic cell membranes, which are composed of a hydrophobic phospholipid tail region (orange) flanked by intracellular and extracellular phospholipid headgroup leaflets (blue), the former of which have a relatively higher concentration of anionic charge (red).

Historically, therapeutic peptides are well known for having low cell membrane permeabilities, limiting their clinical implementation.[2,3,5,20] Illustrating this point, less than 10% of therapeutic peptides in active clinical development had intracellular targets (as of 2018).[3] Given the structure of cell membranes, intracellular delivery particularly remains a challenge for therapeutic peptides with low net charge. Therefore, to realize the clinical

implementation of this beneficial class of therapeutics, we need to develop methods to increase the hydrophobicity and net charge of therapeutic peptides and, subsequently, their eukaryotic cell membrane permeabilities.

1.1.3 Therapeutic peptides have low in vivo half-lives

A common metric used to evaluate therapeutics is *in vivo* half-life, which defines the time taken for the concentration of a therapeutic to decrease by 50% inside of the body. The half-life of a therapeutic is dependent on many different factors; however, it is primarily controlled by the rate of clearance, or removal from the body.[5,20,21] The human body has many different mechanisms to clear a drug, including renal clearance and proteolytic degradation. Renal clearance, where molecules are removed from the bloodstream through the kidneys and into the urine, can rapidly remove small molecules (generally under 5 kDa) from the bloodstream, preventing them from reaching their intended target and having therapeutic activity.[20] Additionally, proteases, natural enzymes present in the bloodstream, can recognize and rapidly degrade therapeutic peptides at their peptide bond (amide between individual amino acids), effectively removing therapeutic peptides from circulation prior to them reaching their intended site of action.[21] Both of these processes contribute to the low *in vivo* half-lives of therapeutic peptides. For example, the anti-tumor, cardioprotective, and anti-inflammatory peptide angiotensin 1-7 (Ang 1-7, 899 Da) has a half-life of 30 minutes in blood plasma[22,23] and somostatin (1640 Da), a peptide used to treat gastrointestinal tumors, has a half-life of only 2-3 minutes in blood plasma.[24] To realize the potential of therapeutic peptides, we need to overcome their low *in vivo* stability.

A common method to extend the *in vivo* half-lives of small molecule or protein therapeutics is to encapsulate them within a biocompatible carrier (**Figure 1.3a**), which

can affect *in vivo* half-life through multiple mechanisms. First, encapsulating therapeutics into carriers increases their effective molecular weight in the bloodstream, which can prevent renal clearance (**Figure 1.3b**). Encapsulation also shields therapeutics from proteolytic enzymes, preventing their premature degradation prior to reaching their intended site of action (**Figure 1.3c**). Finally, as opposed to bolus injections of an unencapsulated therapeutic, which cause short-burst pharmacokinetic profiles, different therapeutic carriers offer tunable and often extended release profiles, which can subsequently control and/or prolong *in vivo* half-life (**Figure 1.3d**).[25–27] Therapeutic encapsulation into and subsequent release from carriers are dependent upon interactions between the two, which are often hydrophobic or electrostatic in nature. Therefore, tuning the hydrophobicity and/or charge of therapeutic peptides can facilitate their encapsulation into and subsequent release from various carriers, such as lipid vesicles,[28–36] polyelectrolyte complexes,[37–41] or hydrogels,[42–47] to name a few.
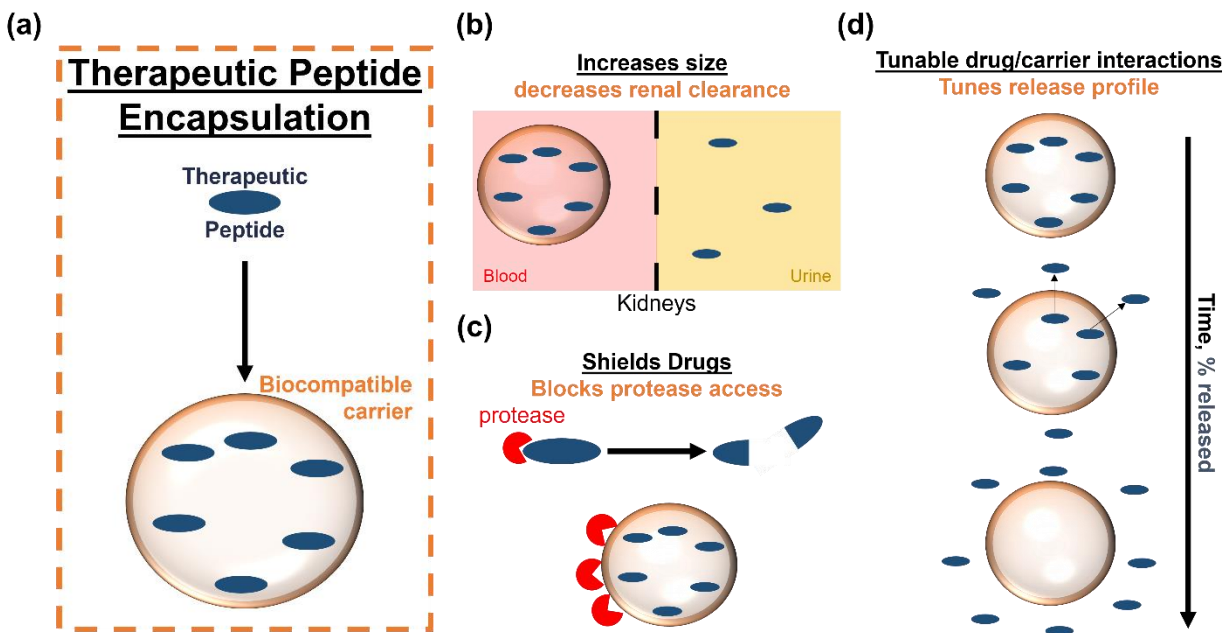
Figure 1.3. a) Therapeutic peptide encapsulation, where therapeutic peptides (navy) are stored in the interior of a biocompatible carrier (orange). **b)** Renal clearance of unencapsulated peptide from the blood

to the urine in the kidneys. Encapsulated drug is retained in the bloodstream, as the biocompatible carrier cannot pass through the glomerular membrane. **c)** Degradation of therapeutic peptides by proteases (red), enzymes capable of cleaving peptide structures at the peptide bond (amide between individual amino acids). Biocompatible carriers block proteases from accessing encapsulated therapeutic peptides. **d)** Tuning interactions between the drug and the biocompatible carriers can tune the release of the drug.

1.1.4 Overcoming therapeutic peptide drawbacks through control over hydrophobicity and net charge

The clinical implementation of therapeutic peptides is limited due to their low cell membrane permeabilities and short *in vivo* half-lives. While these two drawbacks are independent issues, both can be addressed by increasing peptide hydrophobicity and net charge. Therefore, we require strategies to modify the properties of therapeutic peptides and enable their intracellular delivery and/or encapsulation into viable delivery systems.

1.2 Strategies to permanently modify therapeutic peptide hydrophobicity and net charge

1.2.1 Supercharging

Supercharging, where charged amino acids are replaced with oppositely charged substitutes, is a common method to alter the net charge of therapeutics. Supercharging has been extensively used to modify the net charge of proteins to enable their complexation with polymers.[48–51] For example, Obermeyer *et al.* used succinic anhydride to convert cationic lysine amines on proteins to anionic carboxylic acids, making the proteins more negatively charged to enable complexation with cationic polymers. However, supercharging can also be used to increase the cationic charge of amino acid-based therapeutics and, subsequently, their cell membrane permeabilities. Notably, cationic supercharged green fluorescent protein (GFP) was able to effectively bypass cell membranes and enter the cytosol.[49]

1.2.2 Appending peptide tags

Adding a peptide sequence with desired charges and/or hydrophobicity, or a "tag", to a therapeutically active sequence is another common method to modify the net charge

5

and/or hydrophobicity of small molecule, peptide, or protein therapeutics. For example, adding different numbers of repeats of an anionic peptide sequence (DEEEDD) to GFP enabled complex coacervation with different cationic polyelectrolytes.[52] Further, a glutamic acid enabled encapsulation of GFP into arginine-functionalized nanoparticles, which led to higher intracellular delivery than cationic supercharged GFP variants.[53]

While D or E-based peptide tags can make otherwise incompatible peptides/proteins amenable to encapsulation with polymers, cell-penetrating peptides (CPPs), amino acid sequences which are well-known to permeate cell membranes, can be used to directly increase the cell membrane permeability.[54,55] CPPs, such as the Trans-Activator of Transcription (TAT)[56] or antennapedia,[57] often contain an excess of positive charge, usually from protonated lysine and/or arginine residues,[18,58] and hydrophobic amino acids (e.g., arginine, tryptophan, phenylalanine),[59] which are conducive to electrostatic interactions with anionic phospholipid headgroups (both intracellular and extracellular),[60] and partitioning into the hydrocarbon region, respectively (Figure 1.3). CPPs are widely used to facilitate the intracellular delivery of therapeutics, including small molecules, therapeutic proteins, and therapeutic peptides.[61–65]

1.2.3 Permanent modifications to sequence can prevent release from carriers or detract from therapeutic activity

While supercharging and appending peptide tags to therapeutics can enable both encapsulation and cell membrane permeability of therapeutics, they involve permanent changes to molecular structure that could affect therapeutic performance. For example, permanent changes to hydrophobicity or net charge could permanently increase the binding strength between the therapeutic and delivery vehicle, which could in turn prevent adequate release from vehicles. Further, permanent changes to the molecular structure

6

of a therapeutic could affect structurally-related therapeutic activity. Relative to supercharging, appending peptide tags is attractive because it does not involve direct modifications to the therapeutically active sequence. For example, supercharging 11 lysine residues on GFP to imbue a charge of -24 resulted in a 60% decrease in fluorescence, but appending 3 DEED tags (16 amino acids) to imbue a matching charge of -24 only caused a 10% decrease in fluorescence.[52] CPPs have also been shown to detract from the activity of the therapeutic in question, as they can affect how the therapeutic is presented to its intracellular target and possibly affect binding, as seen with the therapeutic peptide α carboxyl terminus 11 (αCT11, RPRPDDLEI).

1.2.4 α carboxyl terminus 11: A wound healing, cardioprotective peptide

αCT11 is a relatively hydrophilic, mixed charge peptide (56% hydrophilic groups, 3 positive charges, 4 negative charges) (**Figure 1.4**). αCT11 has applications in dermal wound healing and cardioprotection, and its activity relies on its interactions with the intracellular H2 domain of the transmembrane protein ZO-1 and/or the cytoplasmic PDZ-2 domain of the scaffolding protein ZO-1;[66–68] however, it's low hydrophobicity and anionic net charge prevent its cell internalization and subsequent interaction with these target proteins.
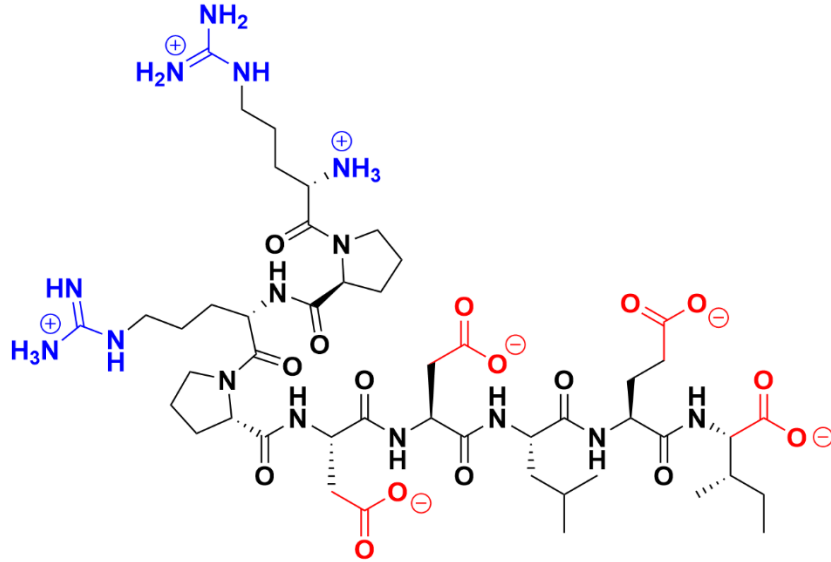
Figure 1.4. Molecular structure of the therapeutic peptide α carboxyl terminus 11 (αCT11, RPRPDDLEI). The structure is reflective of the charge state at physiological pH (7.4), with positively and negatively charged groups are shown in blue and red, respectively.

To enable its intracellular delivery, prior work appended αCT11 to the CPP antennapedia (RQPKIWFPNRRKPWKK) at the N-terminus (termed αCT1) enabled improvement in scar healing in a recent phase II clinical trial.[66,69] However, a separate study showed that αCT11 alone restored 20% more left ventricular function in *ex vivo* ischemic cardiomyocytes than αCT1, suggesting that attaching the 16 amino acid CPP sequence decreased αCT11 wound healing activity.[67] Further illustrating this point, the cardioprotective activity of αCT11 was found to be directly tied to its structure, where replacing the D5, D6, and E8 amino acids with alanine led to decreased interactions with Cx43 H2 and ZO-1 PDZ-2, and subsequent reduced activity in *ex vivo* ischemic mouse hearts. While it is likely that ischemic cardiomyocytes directly internalize αCT11 through open Cx43 hemichannels, antennapedia was required to enable αCT11-dependent dermal wound healing, yet was found to decrease the overall activity of αCT11.

1.2.5 *Reversible modifications to hydrophobicity and net charge of therapeutic peptides are necessary to increase cell membrane permeability and enable encapsulation without sacrificing activity*

While the decrease in activity from appending peptide tags is relatively small, even small decreases in activity could require increased therapeutic amounts and/or repeat treatments, which would lead to increased production costs and/or increased costs for patients. Further, as therapeutic encapsulation into carriers is facilitated by interactions between the two, permanent increases in therapeutic hydrophobicity and net charge could prevent release and, subsequently, prevent the therapeutic from interacting with its target at the proposed site of action. As any permanent changes to peptide sequence can detract from either activity or release from carriers, yet modifications to peptide hydrophobicity and net charge remain necessary to overcome their low cell membrane permeabilities and short *in vivo* half-lives, we require reversible strategies that are capable of modifying peptide properties to ultimately deliver the native, active sequence.

1.3 Esterification: A reversible strategy to tailor therapeutic peptides for delivery

Esterification is a simple and widely used reaction where hydrophilic, anionic carboxylic acids (COOHs) are converted to esters (R-(C=O)OR) to simultaneously increase the hydrophobicity and net charge of therapeutics (**Figure 1.5**). What sets esterification apart from methods listed in Section 1.2 is its reversibility, where installed esters can be reverted to carboxylic acids through hydrolysis to return the active structure of the therapeutic, a process that can be catalyzed *in vivo* by intracellular enzymes called esterases.[70–74] Historically, esterification has been used to increase the cell membrane permeability of small molecule, peptide, and protein therapeutics.[75–79] For example, Mix *et al.* showed intracellular delivery of an esterified GFP variant, where the native GFP was not able to cross the cell membrane.[76] Further, while supercharged GFP was able to

pass the cell membrane, it was not distributed throughout the cells like esterified GFP, instead appearing to localize in the endosomes. Esterification has also been shown to increase the cell membrane permeability of the peptide thyrotropin-releasing hormone, as shown by immobilized artificial membrane chromatography.[78]
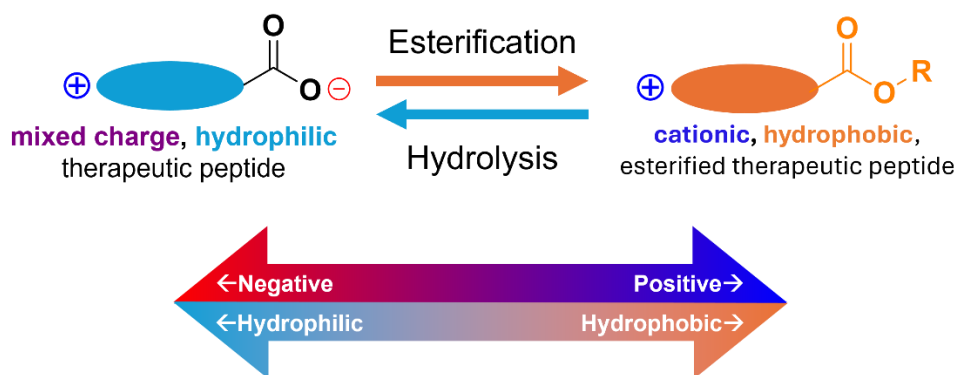
Figure 1.5. Therapeutic peptide esterification. Carboxylic acids on peptides can be reversible esterified to modify hydrophobicity (orange) and cationic net charge (blue). Installed esters can then be hydrolyzed to return any negatively charged (red) carboxylic acids and restore the original, hydrophilic (light blue) peptide structure.

As esterification has been used to increase the cell membrane permeability of therapeutics, it has also been used to enable encapsulation of hydrophilic therapeutics into lipid vesicles such as liposomes[80] and exosomes,[81–83] which also contain lipid bilayer membranes. Notably, Roffler & coworkers used esterification as a strategy to encapsulate therapeutics into liposomes, inside of which the esters could be hydrolyzed to trap the drugs within the liposomes until they reach their intended target.[80] As esterification increases the hydrophobicity and net charge of therapeutics, it is also a potential strategy to enable encapsulation into PECs or even hydrogels. As ester hydrolysis can then return the hydrophilicity or negative charge (at physiological pH) of carboxylic acids, esterification provides an opportunity to not only enable encapsulation but also to dissociate hydrophobic or electrostatic interactions controlling encapsulation, enabling hydrolytically-tunable release. Through its reversible control over the hydrophobicity and

net charge of therapeutics, esterification holds immense potential as a strategy to increase cell membrane permeability and enable encapsulation of therapeutic peptides without sacrificing ultimate therapeutic activity upon delivery.

1.4 Summary of Dissertation

In this dissertation, we investigate the molecular design of therapeutic peptides and their carrier systems. First, we establish multi-site esterification as a strategy to selectively and reversibly increase the hydrophobicity and net charge of the therapeutic peptide αCT11 (Figures 1.4-1.5). Through reversible modification of therapeutic peptide hydrophobicity and net charge, we use esterification as a method to increase its cell membrane permeability and reversible encapsulation polyelectrolyte complexes. Finally, we study the design of polymer-metal organic framework (MOF) composite gels for encapsulation of therapeutic peptides. This dissertation serves to influence the future design of both therapeutic peptides and their relevant drug carriers, specifically showcasing the potential of therapeutic peptide esterification to reversibly tailor the properties of therapeutic peptides and expand their clinical implementation.

1.4.1 Multi-site Fischer esterification: A tunable, reversible strategy to modify the hydrophobicity and net charge of a therapeutic peptide

Chapter 2 focuses on establishing multi-site Fischer esterification of the therapeutic peptide αCT11. As most esterified therapeutics to date contain either a single esterification site or multiple esters randomly incorporated on multiple sites, we were interested in determining how the number and position of esters installed onto peptides affect their properties. Specifically, we examine the role of both the number and position of esters installed onto peptides on their hydrophobicity, reversion to the unesterified formulation, and wound healing activity. We show that both the number and position of

installed esters indeed affect peptide hydrophobicity and reversion, with the C-terminal ester being the most influential in modifying peptide properties. *In vitro* proof-of-concept experiments showed esterifying αCT11 to increase cell migration into a scratch, indicative of increased wound healing activity. Through reversible control over hydrophobicity and charge, we show that peptide esterification these studies provide molecular design insight into the viability of multi-site esterification for therapeutic peptides.

1.4.2 Esterification of therapeutic peptides to enable reversible encapsulation in polyelectrolyte complexes (PECs)

In Chapter 3, we leverage the net charge increase afforded by esterification to reversibly encapsulate therapeutic peptides within PECs. Specifically, we study the effect of fully esterifying αCT11 on its complexation with anionic poly(methacrylic acid) (PMAA). and subsequent formation of supramolecular structures. We then study the differences in hydrolysis in the presence and absence of PMAA while attempting to correlate ester hydrolysis with the turbidity of peptide and polymer mixtures. We indeed show that fully esterifying αCT11 enables complexation with PMAA, and that this complexation is electrostatically driven. While the presence of PMAA only resulted in minor changes in αCT11 ester hydrolysis, we show that ester hydrolysis corresponds with a decrease in turbidity, suggesting it to cause PEC dissociation and peptide release. Esterification provides a compelling strategy to enable reversible encapsulation into PECs, one that could be quite useful in increasing the *in vivo* half-life of therapeutic peptides.

1.4.3 Expanding the design space of polymer-metal organic framework (MOF) gels by understanding polymer-MOF interactions

Chapter 4 will discuss our work developing polymer-MOF composite gels, a novel class of materials that combine the high sorptive capacity of MOFs and processable

template of polymer hydrogels to create a highly beneficial system for sorptive applications. To leverage the full potential of this material, we investigate how polymer chemistry influences MOF formation and vice versa, finding that both interactions between polymer functional groups and MOF metal nodes and polymer entrapment within forming MOF crystals synergistically enable the formation of crystalline, self-supporting composite gels. Further, only polymers toting low densities of carboxylic acids or weak metal-binding hydroxyl groups permit simultaneous MOF and gel formation. We then go on to study the sorptive capacity and release profiles of polymer-MOF composites, finding them to outperform their individual polymer and MOF constitutes for sorbing a small molecule dye while enabling also enabling sustained release profiles (~7 d). Polymer-MOF composite gels were also capable of sorbing the therapeutic peptide angiotensin 1-7 (Ang 1-7). Through studying the effects of both polymer and MOF molecular details on the formation of these composite gels, we hope to expand the design space for these beneficial carriers and develop them as carriers for therapeutics, such as peptides.

1.5 Bibliography

(1) Wang, L.; Wang, N.; Zhang, W.; Cheng, X.; Yan, Z.; Shao, G.; Wang, X.; Wang, R.; Fu, C. Therapeutic Peptides: Current Applications and Future Directions. *Signal Transduct Target Ther* **2022**, *7* (48). https://doi.org/10.1038/s41392-022-00904-4.

(2) Muttenthaler, M.; King, G. F.; Adams, D. J.; Alewood, P. F. Trends in Peptide Drug Discovery. *Nat Rev Drug Discov* **2021**, *20* (4), 309–325. https://doi.org/10.1038/s41573-020-00135-8.

(3) Lau, J. L.; Dunn, M. K. Therapeutic Peptides: Historical Perspectives, Current Development Trends, and Future Directions. *Bioorg Med Chem* **2018**, *26* (10), 2700–2707. https://doi.org/10.1016/j.bmc.2017.06.052.

(4) Meyer-Lindenberg, A.; Domes, G.; Kirsch, P.; Heinrichs, M. Oxytocin and Vasopressin in the Human Brain: Social Neuropeptides for Translational

Medicine. *Nat Rev Neurosci* **2011**, *12* (9), 524–538.
https://doi.org/10.1038/nrn3044.

(5)   Di, L. Strategic Approaches to Optimizing Peptide ADME Properties. *AAPS Journal* **2015**, *17* (1), 134–143. https://doi.org/10.1208/s12248-014-9687-3.

(6)   Alberts, B.; Johnson, A.; Lewis, J.; Raff, M.; Roberts, K.; Waller, P. Membrane Structure. In *Molecular Biology of the Cell*; Garland Science: New York, NY, 2002; pp 617–651.

(7)   Al-Awqati, Q. One Hundred Years of Membrane Permeability: Does Overton Still Rule? *Nat Cell Biol* **1999**, *1* (8), E201–E202. https://doi.org/10.1038/70230.

(8)   Overton, E. Ueber Die Allgemeinen Osmotischen Egenschaften Der Zelle, Ihre Vermutlichen Ursachen Und Ihr Bedeutung Fur Die Phsyiologie. *Vjschr. Naturfosch Ges Zurich* **1899**, 44–88.

(9)   Yang, N. J.; Hinner, M. J. Getting across the Cell Membrane: An Overview for Small Molecules, Peptides, and Proteins. *Methods in molecular biology (Clifton, N.J.).* NIH Public Access 2015, pp 29–53. https://doi.org/10.1007/978-1-4939-2272-7_3.

(10)   Leventis, P. A.; Grinstein, S. The Distribution and Function of Phosphatidylserine in Cellular Membranes. *Annu Rev Biophys* **2010**, *39* (1), 407–427. https://doi.org/10.1146/annurev.biophys.093008.131234.

(11)   Parisio, G.; Stocchero, M.; Ferrarini, A. Passive Membrane Permeability: Beyond the Standard Solubility-Diffusion Model. *J Chem Theory Comput* **2013**, *9* (12), 5236–5246. https://doi.org/10.1021/ct400690t.

(12)   Hannesschlaeger, C.; Horner, A.; Pohl, P. Intrinsic Membrane Permeability to Small Molecules. **2019**. https://doi.org/10.1021/acs.chemrev.8b00560.

(13)   Nagle, J. F.; Mathai, J. C.; Zeidel, M. L.; Tristram-Nagle, S. Theory of Passive Permeability through Lipid Bilayers. *Journal of General Physiology* **2008**, *131* (1), 77–85. https://doi.org/10.1085/jgp.200709849.

(14)   Zocher, F.; Van Der Spoel, D.; Pohl, P.; Hub, J. S. Local Partition Coefficients Govern Solute Permeability of Cholesterol-Containing Membranes. *Biophys J* **2013**, *105* (12), 2760–2770. https://doi.org/10.1016/j.bpj.2013.11.003.

(15)   Chakrabarti, A. C. Permeability of Membranes to Amino Acids and Modified Amino Acids: Mechanisms Involved in Translocation. *Amino Acids* **1994**, *6* (3), 213–229. https://doi.org/10.1007/BF00813743.

(16)   Marrink, S. J.; Berendsen, H. J. C. Simulation of Water Transport through a Lipid Membrane. *Journal of Physical Chemistry* **1994**, *98* (15), 4155–4168. https://doi.org/10.1021/j100066a040.

(17)   Conradi, R. A.; Hilgers, A. R.; Ho, N. F.; Burton, P. S. The Influence of Peptide
        Structure on Transport across Caco-2 Cells. II. Peptide Bond Modification Which
        Results in Improved Permeability. *Pharm Res* **1992**, *9* (3), 435–439.
        https://doi.org/10.1023/a:1015867608405.

(18)   Cardenas, A. E.; Shrestha, R.; Webb, L. J.; Elber, R. Membrane Permeation of a
        Peptide: It Is Better to Be Positive. *J Phys Chem B* **2015**, *119* (21), 6412–6420.
        https://doi.org/10.1021/acs.jpcb.5b02122.

(19)   Marrink, S. J.; Berendsen, H. J. C. Permeation Process of Small Molecules
        across Lipid Membranes Studied by Molecular Dynamics Simulations. *J Phys
        Chem* **1996**, *100* (41), 16729–16738.

(20)   Werle, M.; Bernkop-Schnürch, A. Strategies to Improve Plasma Half Life Time of
        Peptide and Protein Drugs. *Amino Acids* **2006**, *30* (4), 351–367.
        https://doi.org/10.1007/S00726-005-0289-3.

(21)   Boöttger, R.; Hoffmann, R.; Knappe, D. Differential Stability of Therapeutic
        Peptides with Different Proteolytic Cleavage Sites in Blood, Plasma and Serum.
        PLoS One **2017**, *12* (6). https://doi.org/10.1371/journal.pone.0178943.

(22)   Petty, W. J.; Miller, A. A.; McCoy, T. P.; Gallagher, P. E.; Tallant, E. A.; Torti, F.
        M. Phase I and Pharmacokinetic Study of Angiotensin-(1-7), an Endogenous
        Antiangiogenic Hormone. *Clinical Cancer Research* **2009**, *15* (23), 7398–7404.
        https://doi.org/10.1158/1078-0432.CCR-09-1957.

(23)   Jiang, F.; Yang, J.; Zhang, Y.; Dong, M.; Wang, S.; Zhang, Q.; Liu, F. F.; Zhang,
        K.; Zhang, C. Angiotensin-Converting Enzyme 2 and Angiotensin 1-7: Novel
        Therapeutic Targets. *Nature Reviews Cardiology*. Nature Publishing Group April
        29, 2014, pp 413–426. https://doi.org/10.1038/nrcardio.2014.59.

(24)   Bauer, W.; Briner, U.; Doepfner, W.; Haller, R.; Huguenin, R.; Marbach, P.;
        Petcher, T. J.; Pless, J. SMS 201–995: A Very Potent and Selective Octapeptide
        Analogue of Somatostatin with Prolonged Action. *Life Sci* **1982**, *31* (11), 1133–
        1140. https://doi.org/10.1016/0024-3205(82)90087-X.

(25)   Mitchell, M. J.; Billingsley, M. M.; Haley, R. M.; Wechsler, M. E.; Peppas, N. A.;
        Langer, R. Engineering Precision Nanoparticles for Drug Delivery. *Nat Rev Drug
        Discov* **2021**, *20* (2), 101–124. https://doi.org/10.1038/S41573-020-0090-8.

(26)   Prossnitz, A. N.; Pun, S. H. Modulating Boronic Ester Stability in Block Copolymer
        Micelles via the Neighbor Effect of Copolymerized Tertiary Amines for Controlled
        Release of Polyphenolic Drugs. **2022**.
        https://doi.org/10.1021/acsmacrolett.1c00751.

(27)   Jana, P.; Shyam, M.; Singh, S.; Jayaprakash, V.; Dev, A. Biodegradable
        Polymers in Drug Delivery and Oral Vaccination. *European Polymer Journal*.
        Elsevier Ltd January 5, 2021. https://doi.org/10.1016/j.eurpolymj.2020.110155.

(28) Rezaei, N.; Mehrnejad, F.; Vaezi, Z.; Sedghi, M.; Asghari, S. M.; Naderi-Manesh, H. Encapsulation of an Endostatin Peptide in Liposomes: Stability, Release, and Cytotoxicity Study. *Colloids Surf B Biointerfaces* **2020**, *185*, 110552. https://doi.org/10.1016/j.colsurfb.2019.110552.

(29) Roux, E.; Passirani, C.; Scheffold, S.; Benoit, J. P.; Leroux, J. C. Serum-Stable and Long-Circulating, PEGylated, PH-Sensitive Liposomes. *Journal of Controlled Release* **2004**, *94* (2–3), 447–451. https://doi.org/10.1016/J.JCONREL.2003.10.024.

(30) Mallick, S.; Choi, J. S. Liposomes: Versatile and Biocompatible Nanovesicles for Efficient Biomolecules Delivery. *J Nanosci Nanotechnol* **2014**, *14* (1), 755–765. https://doi.org/10.1166/jnn.2014.9080.

(31) Agrawal, A. K.; Aqil, F.; Jeyabalan, J.; Spencer, W. A.; Beck, J.; Gachuki, B. W.; Alhakeem, S. S.; Oben, K.; Munagala, R.; Bondada, S.; Gupta, R. C. Milk-Derived Exosomes for Oral Delivery of Paclitaxel. *Nanomedicine* **2017**, *13* (5), 1627–1636. https://doi.org/10.1016/j.nano.2017.03.001.

(32) Munagala, R.; Aqil, F.; Jeyabalan, J.; Gupta, R. C. Bovine Milk-Derived Exosomes for Drug Delivery. *Cancer Lett* **2016**, *371* (1), 48–61. https://doi.org/10.1016/j.canlet.2015.10.020.

(33) Zhuang, M.; Du, D.; Pu, L.; Song, H.; Deng, M.; Long, Q.; Yin, X.; Wang, Y.; Rao, L. SPION-Decorated Exosome Delivered BAY55-9837 Targeting the Pancreas through Magnetism to Improve the Blood GLC Response. *Small* **2019**, *15* (52), 1903135. https://doi.org/10.1002/SMLL.201903135.

(34) Jella, K.; Nasti, T.; Li, Z.; Malla, S.; Buchwald, Z.; Khan, M. Exosomes, Their Biogenesis and Role in Inter-Cellular Communication, Tumor Microenvironment and Cancer Immunotherapy. *Vaccines (Basel)* **2018**, *6* (4), 69. https://doi.org/10.3390/vaccines6040069.

(35) Li, X. Engineered Exosomes for the Targeted Delivery of a Novel Therapeutic Cargo to Enhance Sorafenib- Mediated Ferroptosis in Hepatocellular Carcinoma . *Theranostics* **2021**, *11* (7), 3183–3195.

(36) Jasiewicz, N.; Drabenstott, C.; Nguyen, J. Harnessing the Full Potential of Extracellular Vesicles as Drug Carriers. *Curr Opin Colloid Interface Sci* **2021**, *51*, 101412. https://doi.org/10.1016/j.cocis.2020.101412.

(37) Zheng, P.; Liu, Y.; Chen, J.; Xu, W.; Li, G.; Ding, J. Targeted PH-Responsive Polyion Complex Micelle for Controlled Intracellular Drug Delivery. *Chinese Chemical Letters* **2020**, *31* (5), 1178–1182. https://doi.org/10.1016/J.CCLET.2019.12.001.

(38) Kembaren, R.; Fokkink, R.; Westphal, A. H.; Kamperman, M.; Kleijn, J. M.; Borst, J. W. Balancing Enzyme Encapsulation Efficiency and Stability in Complex

Coacervate Core Micelles. *Langmuir* **2020**, *36* (29), 8494–8502. https://doi.org/10.1021/acs.langmuir.0c01073.

(39)   Li, K.; Chen, F.; Wang, Y.; Stenzel, M. H.; Chapman, R. Polyion Complex Micelles for Protein Delivery Benefit from Flexible Hydrophobic Spacers in the Binding Group. *Macromol Rapid Commun* **2020**, *41* (18), 2000208. https://doi.org/10.1002/MARC.202000208.

(40)   Li, X.; Lu, C.; Xia, W.; Quan, G.; Huang, Y.; Bai, X.; Yu, F.; Xu, Q.; Qin, W.; Liu, D.; Pan, X. Poly(L-Glutamic Acid)-Based Brush Copolymers: Fabrication, Self-Assembly, and Evaluation as Efficient Nanocarriers for Cationic Protein Drug Delivery. *AAPS PharmSciTech* **2020**, *21* (78). https://doi.org/10.1208/s12249-020-1624-4.

(41)   Pack, D. W.; Hoffman, A. S.; Pun, S.; Stayton, P. S. Design and Development of Polymers for Gene Delivery. *Nat Rev Drug Discov* **2005**, *4* (7), 581–593. https://doi.org/10.1038/nrd1775.

(42)   Aminabhavi, T. M.; Nadagouda, M. N.; More, U. A.; Joshi, S. D.; Kulkarni, V. H.; Noolvi, M. N.; Kulkarni, P. V. Controlled Release of Therapeutics Using Interpenetrating Polymeric Networks. *Expert Opin Drug Deliv* **2015**, *12* (4), 669–688. https://doi.org/10.1517/17425247.2014.974871.

(43)   Ruel-Gariépy, E.; Leclair, G.; Hildgen, P.; Gupta, A.; Leroux, J. C. Thermosensitive Chitosan-Based Hydrogel Containing Liposomes for the Delivery of Hydrophilic Molecules. *Journal of Controlled Release* **2002**, *82* (2–3), 373–383. https://doi.org/10.1016/S0168-3659(02)00146-3.

(44)   Bernhard, S.; Tibbitt, M. W. Supramolecular Engineering of Hydrogels for Drug Delivery. *Adv Drug Deliv Rev* **2021**, *171*, 240–256. https://doi.org/10.1016/J.ADDR.2021.02.002.

(45)   Quick, D. J.; Anseth, K. S. DNA Delivery from Photocrosslinked PEG Hydrogels: Encapsulation Efficiency, Release Profiles, and DNA Quality. *Journal of Controlled Release* **2004**, *96* (2), 341–351. https://doi.org/10.1016/J.JCONREL.2004.01.021.

(46)   Peppas, N. A.; Bures, P.; Leobandung, W.; Ichikawa, H. Hydrogels in Pharmaceutical Formulations. *European Journal of Pharmaceutics and Biopharmaceutics* **2000**, *50* (1), 27–46. https://doi.org/10.1016/S0939-6411(00)00090-4.

(47)   Li, J.; Mooney, D. J. Designing Hydrogels for Controlled Drug Delivery. *Nat Rev Mater* **2016**, *1* (12), 1–18. https://doi.org/10.1038/natrevmats.2016.71.

(48)   Obermeyer, A. C.; Mills, C. E.; Dong, X.-H.; Flores, R. J.; Olsen, B. D. Complex Coacervation of Supercharged Proteins with Polyelectrolytes †. *Soft Matter* **2016**, *12*, 3570. https://doi.org/10.1039/c6sm00002a.

(49) Thompson, D. B.; Villaseñor, R.; Dorr, B. M.; Zerial, M.; Liu, D. R. Cellular Uptake Mechanisms and Endosomal Trafficking of Supercharged Proteins. *Chem Biol* **2012**, *19* (7), 831–843. https://doi.org/10.1016/j.chembiol.2012.06.014.

(50) Cummings, C. S.; Obermeyer, A. C. Phase Separation Behavior of Supercharged Proteins and Polyelectrolytes. *Biochemistry* **2018**, *57* (3), 314–323. https://doi.org/10.1021/acs.biochem.7b00990.

(51) Zervoudis, N. A.; Obermeyer, A. C. The Effects of Protein Charge Patterning on Complex Coacervation. *Soft Matter* **2021**, *17* (27), 6637–6645. https://doi.org/10.1039/D1SM00543J.

(52) Kapelner, R. A.; Obermeyer, A. C. Ionic Polypeptide Tags for Protein Phase Separation. *Chem Sci* **2019**, *10* (9), 2700–2707. https://doi.org/10.1039/C8SC04253E.

(53) Mout, R.; Rotello, V. A General Method for Intracellular Protein Delivery through 'E-Tag' Protein Engineering and Arginine Functionalized Gold Nanoparticles. *Bio Protoc* **2017**, *7* (24). https://doi.org/10.21769/bioprotoc.2661.

(54) Copolovici, D. M.; Langel, K.; Eriste, E.; Langel, Ü. Cell-Penetrating Peptides: Design, Synthesis, and Applications. *ACS Nano* **2014**, *8* (3), 1972–1994. https://doi.org/10.1021/nn4057269.

(55) Sato, A. K.; Viswanathan, M.; Kent, R. B.; Wood, C. R. Therapeutic Peptides: Technological Advances Driving Peptides into Development. *Curr Opin Biotechnol* **2006**, *17* (6), 638–642. https://doi.org/10.1016/j.copbio.2006.10.002.

(56) Frankel, A. D.; Pabo, C. O. Cellular Uptake of the Tat Protein from Human Immunodeficiency Virus. *Cell* **1988**, *55* (6), 1189–1193. https://doi.org/10.1016/0092-8674(88)90263-2.

(57) Derossi, D.; Joliot, A. H.; Chassaing, G.; Prochiantz, A. The Third Helix of the Antennapedia Homeodomain Translocates through Biological Membranes. *Journal of Biological Chemistry* **1994**, *269* (14), 10444–10450. https://doi.org/10.1016/s0021-9258(17)34080-2.

(58) Gräslund, A.; Madani, F.; Lindberg, S.; Langel, Ü.; Futaki, S. Mechanisms of Cellular Uptake of Cell-Penetrating Peptides. *Journal of Biophysics* **2011**, *2011*, 414729. https://doi.org/10.1155/2011/414729.

(59) Kalafatovic, D.; Giralt, E. Cell-Penetrating Peptides: Design Strategies beyond Primary Structure and Amphipathicity. *Molecules* **2017**, *22* (11). https://doi.org/10.3390/molecules22111929.

(60) Povilaitis, S. C.; Webb, L. J. Leaflet-Dependent Effect of Anionic Lipids on Membrane Insertion by Cationic Cell-Penetrating Peptides. *J Phys Chem Lett* **2023**, *14* (25), 5841–5849. https://doi.org/10.1021/acs.jpclett.3c00725.

(61) Fawell, S.; Seery, J.; Daikh, Y.; Moore, C.; Chen, L. L.; Pepinsky, B.; Barsoum, J. Tat-Mediated Delivery of Heterologous Proteins into Cells. *Proceedings of the National Academy of Sciences* **1994**, *91* (2), 664–668.

(62) Wang, K. K.; Villalobo, A.; Roufogalis, B. D.; Schwarze, S. R.; Ho, A.; Vocero-Akbani, A.; Dowdy, S. F. In Vivo Protein Transduction: Delivery of a Biologically Active Protein into the Mouse. *Proc. Natl. Acad. Sci. U.S.A* **1995**, *18*, 247.

(63) Stewart, K. M.; Horton, K. L.; Kelley, S. O. Cell-Penetrating Peptides as Delivery Vehicles for Biology and Medicine. *Org Biomol Chem* **2008**, *6* (13), 2242–2255. https://doi.org/10.1039/b719950c.

(64) Tünnemann, G.; Martin, R. M.; Haupt, S.; Patsch, C.; Edenhofer, F.; Cardoso, M. C. Cargo-dependent Mode of Uptake and Bioavailability of TAT-containing Proteins and Peptides in Living Cells. *The FASEB Journal* **2006**, *20* (11), 1775–1784. https://doi.org/10.1096/fj.05-5523com.

(65) Lindgren, M.; Rosenthal-Aizman, K.; Saar, K.; Eiríksdóttir, E.; Jiang, Y.; Sassian, M.; Östlund, P.; Hällbrink, M.; Langel, Ü. Overcoming Methotrexate Resistance in Breast Cancer Tumour Cells by the Use of a New Cell-Penetrating Peptide. *Biochem Pharmacol* **2006**, *71* (4), 416–425. https://doi.org/10.1016/j.bcp.2005.10.048.

(66) Montgomery, J.; Richardson, W. J.; Marsh, S.; Rhett, J. M.; Bustos, F.; Degen, K.; Ghatnekar, G. S.; Grek, C. L.; Jourdan, L. J.; Holmes, J. W.; Gourdie, R. G. The Connexin 43 Carboxyl Terminal Mimetic Peptide ACT1 Prompts Differentiation of a Collagen Scar Matrix in Humans Resembling Unwounded Skin. *FASEB Journal* **2021**, *35* (8). https://doi.org/10.1096/fj.202001881R.

(67) Jiang, J.; Hoagland, D.; Palatinus, J. A.; He, H.; Iyyathurai, J.; Jourdan, L. J.; Bultynck, G.; Wang, Z.; Zhang, Z.; Schey, K.; Poelzing, S.; McGowan, F. X.; Gourdie, R. G. Interaction of α Carboxyl Terminus 1 Peptide With the Connexin 43 Carboxyl Terminus Preserves Left Ventricular Function After Ischemia-Reperfusion Injury. *J Am Heart Assoc* **2019**, *8* (16). https://doi.org/10.1161/JAHA.119.012385.

(68) Rhett, J. M.; Jourdan, J.; Gourdie, R. G. Connexin 43 Connexon to Gap Junction Transition Is Regulated by Zonula Occludens-1. *Mol Biol Cell* **2011**, *22* (9), 1516–1528. https://doi.org/10.1091/mbc.E10-06-0548.

(69) Grek, C. L.; Montgomery, J.; Sharma, M.; Ravi, A.; Rajkumar, J. S.; Moyer, K. E.; Gourdie, R. G.; Ghatnekar, G. S. A Multicenter Randomized Controlled Trial Evaluating a Cx43-Mimetic Peptide in Cutaneous Scarring HHS Public Access. *J Invest Dermatol* **2017**, *137* (3), 620–630. https://doi.org/10.1016/j.jid.

(70) Lockridge, O.; Quinn, D. M. 4.14 - Esterases. In *Comprehensive Toxicology (Second Edition)*; McQueen, C. A., Ed.; Elsevier: Oxford, 2010; pp 243–273. https://doi.org/https://doi.org/10.1016/B978-0-08-046884-6.00414-0.

(71) Dong, H.; Pang, L.; Cong, H.; Shen, Y.; Yu, B. Application and Design of Esterase-Responsive Nanoparticles for Cancer Therapy. *Drug Deliv* **2019**, *26* (1), 416–432. https://doi.org/10.1080/10717544.2019.1588424.

(72) Lavis, L. D. Ester Bonds in Prodrugs. *ACS Chem Biol* **2008**, *3* (4), 203–206. https://doi.org/10.1021/cb800065s.

(73) Liederer, B. M.; Borchardt, R. T. Enzymes Involved in the Bioconversion of Ester-Based Prodrugs. *J Pharm Sci* **2006**, *95* (6), 1177–1195. https://doi.org/10.1002/JPS.20542.

(74) Afrimzon, E.; Deutsch, A.; Shafran, Y.; Zurgil, N.; Sandbank, J.; Pappo, I.; Deutsch, M. Intracellular Esterase Activity in Living Cells May Distinguish between Metastatic and Tumor-Free Lymph Nodes. *Clin Exp Metastasis* **2008**, *25* (3), 213–224. https://doi.org/10.1007/S10585-007-9135-1/TABLES/6.

(75) Huttunen, K. M.; Raunio, H.; Rautio, J. Prodrugs-from Serendipity to Rational Design. *Pharmacol Rev* **2011**, *63* (3), 750–771. https://doi.org/10.1124/pr.110.003459.

(76) Mix, K. A.; Lomax, J. E.; Raines, R. T. Cytosolic Delivery of Proteins by Bioreversible Esterification. *J Am Chem Soc* **2017**, *139* (41), 14396–14398. https://doi.org/10.1021/jacs.7b06597.

(77) Beaumont, K.; Webster, R.; Gardner, I.; Dack, K. Design of Ester Prodrugs to Enhance Oral Absorption of Poorly Permeable Compounds: Challenges to the Discovery Scientist. *Curr Drug Metab* **2005**, *4* (6), 461–485. https://doi.org/10.2174/1389200033489253.

(78) Prokai-Tatrai, K.; Nguyen, V.; Zharikova, A. D.; Braddy, A. C.; Stevens, S. M.; Prokai, L. Prodrugs to Enhance Central Nervous System Effects of the TRH-like Peptide PGlu-Glu-Pro-NH2. *Bioorg Med Chem Lett* **2003**, *13* (6), 1011–1014. https://doi.org/10.1016/S0960-894X(03)00081-7.

(79) Jun, J. V.; Petri, Y. D.; Erickson, L. W.; Raines, R. T. Modular Diazo Compound for the Bioreversible Late-Stage Modification of Proteins. *J Am Chem Soc* **2023**, *145* (12), 6615–6621. https://doi.org/10.1021/jacs.2c11325.

(80) Burnouf, P. A.; Leu, Y. L.; Su, Y. C.; Wu, K.; Lin, W. C.; Roffler, S. R. Reversible Glycosidic Switch for Secure Delivery of Molecular Nanocargos. *Nat Commun* **2018**, *9* (1), 1–13. https://doi.org/10.1038/s41467-018-04225-5.

(81)   Weston, S. A.; Parish, C. R. New Fluorescent Dyes for Lymphocyte Migration Studies: Analysis by Flow Cytometry and Fluorescence Microscopy. *J Immunol Methods* **1990**, *133* (1), 87–97. https://doi.org/10.1016/0022-1759(90)90322-M.

(82)   Bratosin, D.; Mitrofan, L.; Palii, C.; Estaquier, J.; Montreuil, J. Novel Fluorescence Assay Using Calcein-AM for the Determination of Human Erythrocyte Viability and Aging. *Cytometry Part A* **2005**, *66A* (1), 78–84. https://doi.org/10.1002/CYTO.A.20152.

(83)   Gray, W. D.; Mitchell, A. J.; Searles, C. D. An Accurate, Precise Method for General Labeling of Extracellular Vesicles. *MethodsX* **2015**, *2*, 360–367. https://doi.org/10.1016/j.mex.2015.08.002.

CHAPTER 2:
MULTI-SITE FISCHER ESTERIFICATION: A TUNABLE, REVERSIBLE STRATEGY
TO TAILOR A THERAPEUTIC PEPTIDE FOR DELIVERY

This chapter has been adapted from: Bannon, M.S., Ellena, J.F., Gourishankar, A.S., Marsh, S.R., Sherman, N.E., Silva, D.T., Jourdan, J., Gourdie, R.G., Letteri, R.A., Multi-site esterification: A tunable, reversible strategy to tailor a therapeutic peptide for delivery. *Mol. Syst. Des. Eng.* In Review.

2.1 Introduction

In this chapter, we use multi-site esterification to increase the cell membrane permeability of the therapeutic peptide α carboxyl terminus 11 (αCT11). αCT11 is a relatively hydrophilic, mixed charge peptide (56% hydrophilic groups, 3 positive charges, 4 negative charges).[1–4] αCT11 has applications in dermal wound healing and cardioprotection, and its activity relies on its interactions with the intracellular H2 domain of the transmembrane protein ZO-1 and/or the cytoplasmic PDZ-2 domain of the scaffolding protein ZO-1; however, it's low hydrophobicity and anionic net charge prevent its cell internalization and subsequent interaction with these target proteins.

To temporarily modify the molecular structure of αCT11 while retaining activity, we can esterify the anionic, hydrophilic carboxylic acids (COOHs) to simultaneously increase the hydrophobicity and reduce the net charge of therapeutics (**Scheme 2.1**).[5–8] After installation, esters can be hydrolyzed to restore the active, unesterified form of αCT11, a reaction that can be accelerated in the presence of endogenous esterases.[9–12] While esterification has been widely used as a strategy to increase the cell membrane permeability of small molecules,[13–15] proteins,[16] and even peptide[17] therapeutics, most esterified therapeutics contain either a single esterification site or multiple esters randomly incorporated on multiple sites.

As αCT11 has 4 possible esterification sites at the D5, D6, E8, and C-terminal I9 residues, there are 15 possible esterified formulations that can be synthesized, each likely having different properties. Therefore, understanding how the number and position of installed esters affects hydrophobicity and hydrolysis/reversion into the therapeutically active form is critical to leveraging esterification as a reversible strategy to realize the therapeutic potential of peptides. In this work, we install methyl esters onto αCT11 and assess how the number and position of installed esters affect the hydrophobicity and hydrolysis of the esterified peptide formulations. Then, we test the viability of multi-site esterification with *in vitro* experiments designed to gauge peptide activity by promoting cell migration into a scratch.

2.2 Results and discussion

2.2.1 Esterification of αCT11

To install methyl esters onto αCT11, we stirred the peptide in excess MeOH containing 5% (v/v) HCl. After 24 h, RP-HPLC revealed a mixture of peaks, each eluting later than unmodified αCT11, consistent with the expected increase in hydrophobicity upon esterification (**Figure 2.1a**, **Figure A.1-A.2, Table A.2**). The product mixture was quite reproducible, as 3 reactions set up using independently prepared solutions led to nearly identical RP-HPLC chromatograms (Figure A.1). With 4 esterification sites on αCT11(D5, D6, E8, I9), there are 15 possible esterified products; therefore, we next sought to separate the product mixture and for the isolatable products, identify the number and position of the installed methyl esters. Then, to determine the effects of methyl ester number and position on peptide hydrophobicity, we could compare the RP-HPLC retention times of each isolated product to gauge their relative hydrophobicity. For a more precise comparison of retention times for samples run in different batches of RP-HPLC

mobile phase, we normalized each sample to an αCT11 and a fully esterified αCT11

sample set to normalized retention times $\tau = 0$ and 1, respectively.

Figure 2.1. Identifying the numbers and positions of methyl esters installed onto αCT11 through Fischer esterification. **a)** RP-HPLC of αCT11 (peak is blue), αCT11 with 2 methyl esters (peak is yellow), 4 different conformations of αCT11 with 3 esterified esters in either the D5, D6, E8, and/or I9 residues (αCT11-3OMe(D5,D6,E8, or I9), peaks are orange), and fully esterified αCT11, with 4 methyl esters (αCT11-4OMe, peaks are red). Retention time, and thus hydrophobic character, increased with the number of esters installed onto αCT11. The mobile phase consisted of water and acetonitrile (ACN), each with 0.1% trifluoroacetic acid, and each sample eluted between 23 and 26% ACN. Retention times were normalized to those of the αCT11 and αCT11-4OMe samples. ^{1}H NMR (800 MHz, DMSO-d6) spectra of **b)** αCT11 (blue), **c-f)** each of the 4 αCT11-3OMe samples (orange), and **g)** αCT11-4OMe (red) methyl ester proton singlets (3.56 – 3.63 ppm) show which amino acids are esterified in which formulations. Integrals for each peak in are plotted in gray on the spectra. Selective heteronuclear multiple bond correlation (selHMBC) of **h)** αCT11-3OMe(D5/D6/E8) (orange) and **i)** αCT11-4OMe (red) shows the most abundant -3OMe peak (-3OMe(A)) has esters installed on the D5, D6, and E8 positions, but not the C-terminal I9.

We used preparative scale RP-HPLC to separate the product mixture, first focusing our attention on the most abundant (74% peak area) and latest eluting peak ($\tau = 1$) (Figure 1a, Table S2). Matrix-assisted laser desorption/ionization-time of flight (MALDI-TOF) mass spectrometry (MS) revealed this product to have a molecular weight of 1166.3 g/mol, coinciding to αCT11 with all 4 sites esterified (αCT11-4OMe) (**Figure A.3**, **Table A.3**). That the fully esterified peptide is the most abundant product is consistent with the 400x molar excess of MeOH used in the reaction relative to αCT11 COOHs. The next most abundant peak (19% peak area) eluted at $\tau = 0.35$ and had a molecular weight of 1151.6 g/mol, corresponding to αCT11 with 3 methyl esters (αCT11-3OMe(A)) (Figure 2.1a, **A.4**, Tables A.2-A.3). Though the 3 peaks eluting at $\tau = 0.69$, $\tau = 0.70$, and $\tau = 0.75$ accounted for only 4% of the total peak area, we were able to isolate them and determine that each of them also had 3 methyl esters (αCT11-3OMe(B-D)) (Figures 1.1a, **A.5-A.7**, Tables A.2-A.3). Finally, we collected the product that eluted at $\tau = 0.22$ and accounted for just 1% of the peak area, identifying it as αCT11 with 2 methyl esters (αCT11-2OMe) (Figure 2.1a, **A.8**, Tables A.2-A.3). As the αCT11-2OMe and -3OMe products eluted before αCT11-4OMe, it is evident that hydrophobic character increases with the number of installed methyl esters. Yet, the 3 methyl ester products had a large range of retention times, spanning $\tau = 0.35 - 0.74$, pointing to the substantial effect of ester position on αCT11 hydrophobicity.

To determine the positions of esters installed onto αCT11 in each isolated product, we used NMR spectroscopy. The ^{1}H NMR spectrum of αCT11-4OMe (**Figure 2.1g**, **A.9-A.11**, **Table A.4**) showed 4 distinct singlets at ~3.6 ppm, each integrating to 3 protons, that were not present in the spectrum of unesterified αCT11 **(Figure 2.1b, A.12)**. Ascribing

these singlets to the methyl ester protons, we next used 2D NMR spectroscopy to assign these singlets to the D5, D6, E8, and I9 esterification sites. To do so, we first assigned the relevant carbonyl carbon resonances (i.e., the D5 and D6 γ carbons, the E8 δ carbon, and the C-terminal I9 carbonyl carbon) using a combination of 2D techniques, described in detail in Section A2 of Appendix A (**Figures A.9-A.24**, Table A.4). Since the methyl ester protons are 3 bonds from these carbonyl carbons, we used H-C selective heteronuclear multiple bond correlation (selHMBC) spectroscopy, which shows correlations between protons and carbons separated by 2-4 bonds, to assign each methyl ester to a residue. We observed 4 clear correlations between the D5 and D6 γ carbons, the E8 δ carbon, and the C-terminal I9 carbonyl carbon and the 4 methyl esters (**Figure 2.1i**). These correlations allowed us to assign the most downfield methyl ester singlet (3.61 ppm) as that on the C-terminal I9, followed by the D5 (3.59 ppm), E8 (3.58 ppm), and D6 (3.57 ppm) methyl ester singlets.

Similar analysis of the most abundant αCT11-3OMe(A) product (τ = 0.35), showed esters installed on the D5, D6, and E8 positions (αCT11-3OMe(D5,D6,E8)) (**Figures 2.1c, 2.1h**, A.12, **A.25-A.28**). Since the chemical shift order of the methyl ester proton singlets was conserved in both the αCT11-3OMe(D5,D6,E8) and -4OMe ^{1}H NMR spectra, we assumed that this order persisted across all esterified αCT11 formulations. With this assumption, we then used ^{1}H NMR spectroscopy to identify the ester positions in the remaining -3OMe products. αCT11-3OMe(B) (τ = 0.65) had methyl esters on the D5, D6, and C-terminal I9 positions (αCT11-3OMe(D5,D6,I9)), -3OMe(C) (τ = 0.69) had esters on the D6, E8, and C-terminal I9 positions (αCT11-3OMe(D6,E8,I9)), and -3OMe(D) (τ =

0.74) had esters on the D5, E8, and C-terminal I9 positions (αCT11-3OMe(D5,E8,I9)) (**Figure 2.1d-f,** A.12).

Having determined the positions of methyl esters installed onto the 4 αCT11-3OMe products, we compared their normalized RP-HPLC retention times to establish relationships between hydrophobicity and installed ester position (Figure 1a). We note that the different pKas of the D5, D6, E8, and C-terminal I9 COOHs will result in different protonation states in physiological conditions, which will affect their relative hydrophobicities. However, as RP-HPLC comparisons were made in acidic conditions (0.1% TFA), peptides should be fully protonated, allowing us to determine the relative increases in hydrophobicity upon ester installation at constant protonation state. αCT11-3OMe(D5,D6,E8), the most abundant of the -3OMe products, lacked an ester on the C-terminal I9 site and eluted earliest (τ = 0.35). In contrast, the remaining 3 methyl ester products, all with the C-terminal I9 position esterified, eluted later than αCT11-3OMe(D5,D6,E8) and close together, with αCT11-3OMe(D5,D6,I9) at τ = 0.65, -3OMe(D6,E8,I9) at τ = 0.69, and -3OMe(D5,E8,I9) at τ = 0.74. Together, these data suggest that esterifying the C-terminal I9 position imparts the largest increase in hydrophobic character.

2.2.2 *Hydrolysis of esterified αCT11 formulations*

After identifying the number and positions of methyl esters installed onto the various αCT11 products, we sought to determine the lability of the installed esters and subsequent recovery of the therapeutically active unesterified form of αCT11. We incubated the most abundant products αCT11-3OMe(D5,D6,E8) and -4OMe in 1X PBS (pH 7.4) at 37 °C and monitored ester hydrolysis as a function of time using RP-HPLC. Using these chromatograms, we then determined the recovery of unesterified αCT11 (%)

as the integration of the αCT11 peak relative to the total integration between 5 and 15 min (Table A.1, Equation 2.2). After 3 d, we only observed 6 +/- 2% recovery of unesterified αCT11 from αCT11-3OMe(D5,D6,E8), and no unesterified αCT11 was recovered from -4OMe (**Figure 2.2, Figures A.29-A.31, Tables A.5-A.6**). After 7 d, we observed 10.5 +/- 2.3% recovery of unesterified αCT11 from αCT11-3OMe(D5,D6,E8), but only 1.1 +/- 0.3% recovery from -4OMe was observed after 8 d.
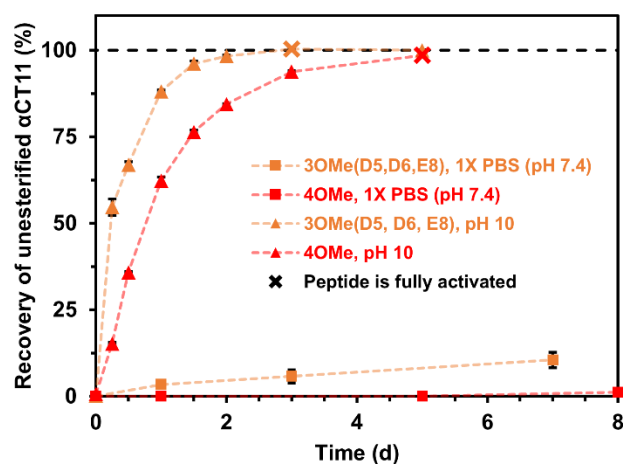
Figure 2.2. Recovery of unesterified αCT11 from esterified formulations in aqueous conditions. αCT11-3OMe(D5,D6,E8) (orange) and -4OMe (red) were incubated in 1X PBS (pH 7.4, squares) or 100 mM carbonate buffer (pH 10, triangles) and the amount of unmodified αCT11 present over ~1 week was quantified using RP-HPLC. Basic conditions were required to fully hydrolyze installed esters, where αCT11-3OMe(D5,D6,E8) and -4OMe were fully reverted to unesterified αCT11 after 3 d and 5 d in carbonate buffer (pH 10), respectively (denoted on the plot with an 'x'). Full recovery of unesterified αCT11 was not achieved in 1X PBS.

As 37 °C 1X PBS was insufficient to fully hydrolyze esterified αCT11 formulations, we attempted to catalyze ester hydrolysis with porcine liver esterase (PLE), which is often used to mimic native esterases.[23,24] At high concentrations of PLE (10:1 and 100:1 PLE enzyme units:peptide μmol), we observed a loss of αCT11-related signal in both RP-HPLC and MALDI-TOF MS (**Figures A.32-A.37, Tables A.7-A.9**). Given that RP-HPLC and MALDI-TOF confirmed that unmodified αCT11 was stable for 7 d in 1X PBS (Figure A.31, Table A.5), we suspected that PLE was non-selectively catalyzing methyl ester and

backbone amide hydrolysis, consistent with prior findings.[25] Decreasing the PLE concentration to 1:1 PLE enzyme units:peptide µmol minimized loss of αCT11 signal but did not provide ester hydrolysis beyond that achieved in 1X PBS. Therefore, in our hands, PLE did not offer a viable route to selectively cleave these esters. A full discussion of the PLE hydrolysis experiments can be found in Section A3 of Appendix A (Figures A.32-A.37, Tables A.7-A.9).

   To compare the time required to fully hydrolyze αCT11-3OMe(D5,D6,E8) and -4OMe, we used basic aqueous conditions (i.e., 100 mM carbonate buffer, pH 10) to accelerate ester hydrolysis. After confirming that αCT11 backbone amides were stable in 37 °C pH 10 carbonate buffer for 5 d, we monitored hydrolysis of the esterified products under these conditions (**Figure A.38**). After only 6 h, we observed 54.7 +/- 2.4% and 15.2 +/- 0.4% recovery of unesterified αCT11 from αCT11-3OMe(D5,D6,E8) and -4OMe, respectively (Figure 2, Table S6, **Figures A.39-A.40**). We observed complete recovery of unesterified αCT11 from αCT11-3OMe(D5,D6,E8) and -4OMe after 3 d and 5 d, respectively, with liquid chromatography-mass spectrometry (LC-MS) showing both formulations to contain > 95% αCT11 at this time (**Figure A.41-A.42, Tables A.10-A.11**).

2.2.3 *Intermediates identified during esterified αCT11 hydrolysis*

   As early as 2 h after incubation, RP-HPLC chromatograms revealed the presence of several peaks eluting between the starting esterified product and unesterified αCT11 peaks in both physiological and basic conditions (Figure A.29-A.30). MALDI-TOF MS showed both αCT11-3OMe(D5,D6,E8) and -4OMe samples to contain αCT11 with 1 – 3 esters after only 2 h (**Figures A.43-A.44**). Further, we observed corresponding esterified products minus either 1 or 2 H_2O molecules, suggesting intramolecular amide or imide formation. As a prior report involving peptides with side-chain esters and primary N-

terminal amines showed that the primary amine was only involved in intramolecular ester cleavage when the ester was on the same N-terminal amino acid, we suspect that it is unlikely that the αCT11 N-terminal amine reacts with installed esters, and that this water loss is the result of intramolecular imide formation.[26]

To identify the relative abundances of the different αCT11 hydrolysis intermediates, we used LC-MS. Specifically, we incubated αCT11-3OMe(D5,D6,E8) and -4OMe in 37 °C 1X PBS for 7 d. For each timepoint, we obtained a total ion chromatogram, which included all ions collected over the same m/z range (525 – 590 m/z region containing the most abundant +2 ions for all potential αCT11 species) inclusive of all expected hydrolysis intermediates identified by MALDI-TOF MS. We then collected selective ion chromatograms (SICs) specific to each intermediate and calculated the abundance (%) of each intermediate by dividing the integrated SIC signal by that of the total ion chromatogram (**Figures A.45-A.58, Tables A.12-A.13**). Since after only 2 h, LC-MS revealed both the αCT11-3OMe(D5,D6,E8) and -4OMe samples to contain just 6% and 4% of these starting products, respectively, it appears that 1 or more of the esters hydrolyze rapidly after exposure to aqueous solution (**Figure 2.3a-b**, Table A.12-A13). At this 2 h timepoint, the αCT11-3OMe(D5,D6,E8) formulation contained 40% αCT11 with 1 methyl ester missing 1 H_2O molecule (i.e., -1OMe – 1 H_2O), as well as 31% -1OMe – 2 H_2O and 14% -2OMe (Figure 3a, Table S12). The αCT11-4OMe formulation hydrolyzed into -3OMe (16% abundance), 3OMe – 1 H_2O (4% abundance), -2OMe (9% abundance), -2OMe – 1 H_2O (47% abundance), and -2OMe – 2 H_2O (19% abundance) (Figure 2.3b, Table A.13). In all, more than 50% of each formulation contained imides after 2 h of hydrolysis, and these intermediates had higher LC-MS retention times than those with the

same number of esters without imides, suggesting that these intramolecular reactions increase peptide hydrophobicity more than ester installation alone (Table A.12-A.13). However, intermediates containing imides were transient, as less than 25% imide containing products remained after 6 h, less than 5% remained after 24 h, and less than 2% remained after 7 d in both esterified formulations. The transient nature of this water loss further supports that these intermediates are not intramolecular amides, but imides that are known to hydrolyze.[27]
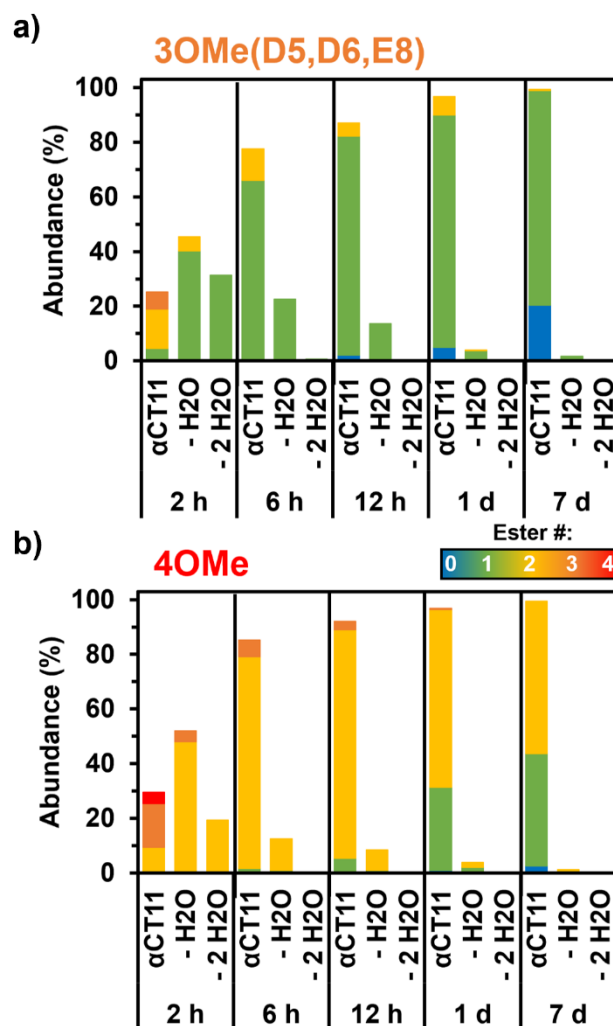
Figure 2.3. Relative abundance of intermediates observed during hydrolysis of esterified αCT11 formulations in 37 °C 1X PBS. LC-MS of **a)** αCT11-3OMe(D5,D6,E8) and **b)** -4OMe samples showed the

presence of multiple esterified intermediates, including those containing intramolecular imides (- H_2O, - 2 H_2O), during hydrolysis.

After 7 d, the αCT11-3OMe(D5,D6,E8) sample consisted of 79% -1OMe and 20% unmodified αCT11. αCT11-4OMe consisted of 56% -2OMe, 41% -1OMe, and 3% unmodified αCT11. As the αCT11-3OMe(D5,D6,E8) sample contained only a -1OMe intermediate after 7 d, yet the -4OMe sample contained both -1OMe and -2OMe intermediates, it stood to reason that an extra ester position was remaining on the -4OMe sample relative to -3OMe(D5,D6,E8). As αCT11-4OMe contained a C-terminal I9 methyl ester, which imbued the esterified formulations with the most hydrophobicity, we suspected it to be responsible for the increased hydrolytic stability of the -4OMe intermediates. Thus, to gauge the hydrolytic stability of different ester positions, we sought to isolate the persistent αCT11-1OMe intermediates from each and determine which positions were esterified in them.

2.2.4 *Hydrolytic stability of different ester positions on esterified αCT11 formulations*

To determine the position of the most stable esters on αCT11-3OMe(D5,D6,E8) and -4OMe, we isolated the persistent αCT11-1OMe hydrolysis intermediates observed immediately prior to complete recovery of unesterified αCT11 in 37 °C 100 mM carbonate buffer (pH 10) (**Figure 2.4a-b**, Figures A.39-A.40). For these experiments, we used accelerated hydrolysis conditions to more rapidly obtain sufficient amounts of these persistent intermediates for ^{1}H and ^{13}C NMR spectroscopy, allowing αCT11-3OMe(D5,D6,E8) and -4OMe to hydrolyze for 6 and 24 h, respectively. After using preparative scale RP-HPLC to isolate the persistent hydrolysis intermediates and remove buffer salts, we used selHMBC to identify that the persistent hydrolysis intermediate of αCT11-3OMe(D5,D6,E8) (relative retention time (RRT) = 0.20) was αCT11 containing a

single ester in the E8 position (-1OMe(E8)) (**Figure 2.4c**, **Figure A.59**). In the αCT11-4OMe formulation, the persistent hydrolysis intermediate (RRT = 0.62) was αCT11 containing a single ester in the I9 position (-1OMe(I9)) (**Figure 2.4d**, **Figure A.60)**. As αCT11-3OMe(D5,D6,E8), which did not have an esterified C-terminal I9 position, was fully hydrolyzed faster than αCT11-4OMe (Figure 2.3), we concluded that the ester installed in the C-terminal I9 position was more hydrolytically stable than the methyl ester installed in the E8 position. Additionally, the rapid appearance of the persistent intermediates in both samples under both physiological and basic conditions indicated that the D5 and D6 methyl esters hydrolyze quickly (Figures A.29-A.30, A.39-A.40). Further, as the imide products are most abundant in samples collected at the earliest hydrolysis timepoints, it is likely that they involve the D5 and D6 methyl esters, suggesting that the transient intermediates we observe are aspartimides (Figure 2.3, Tables A.12-A.13). That the aspartic acid (D5, D6) esters seem to hydrolyze fastest, followed by those on glutamic acid (E8) and finally C-terminal I9 also raises questions about the role of esterification site type vs. position in hydrolytic stability, which we plan to pursue in future studies.
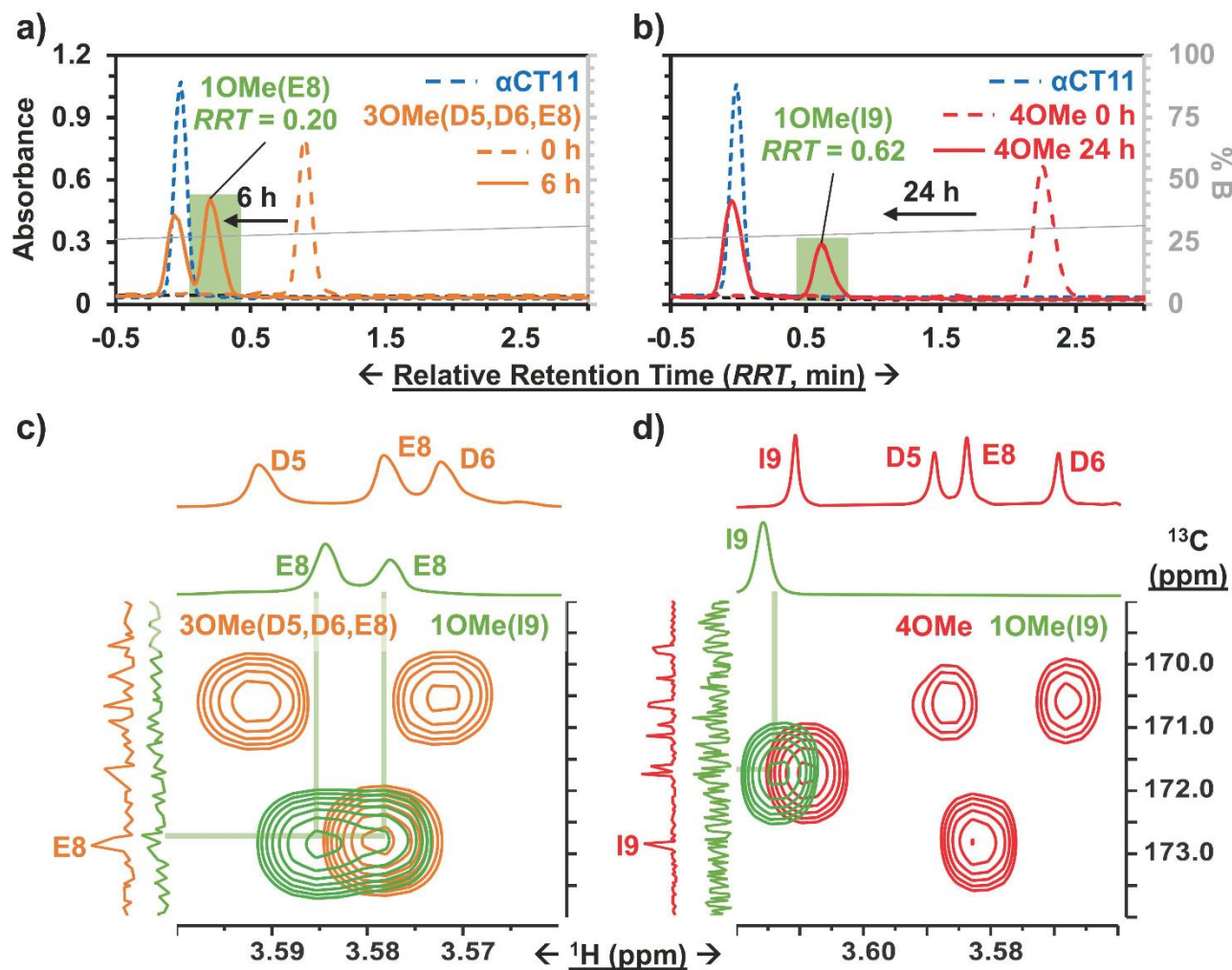
Figure 2.4. Hydrolytic stability of persistent hydrolysis intermediates of esterified αCT11. RP-HPLC chromatograms of **a)** αCT11-3OMe(D5,D6,E8) (orange) and **b)** αCT11-4OMe (red) in 37 °C 100 mM carbonate buffer (pH 10), showing each formulation after 6 and 24 h of hydrolysis, respectively. Persistent hydrolysis intermediates are highlighted in green, and αCT11 controls are in blue. Mobile phase composition (% B, gray) is plotted against relative retention time in each RP-HPLC chromatogram. 2D selHMBC of **c)** αCT11-3OMe(D5,D6,E8) (orange) and **d)** αCT11-4OMe (red) and their persistent hydrolysis intermediates (green) were used to show -3OMe(D5,D6,E8) hydrolyzes into -1OMe(E8) (green, left) and -4OMe hydrolyzes into -1OMe(I9) (green, right).

2.2.5 Activity of esterified αCT11

Despite not observing full recovery of unesterified αCT11 from αCT11-3OMe(D5,D6,E8) or -4OMe in aqueous buffer at physiologically relevant conditions, we were interested to gauge the activity of the esterified αCT11 formulations *in vitro*. In prior work,[2] we probed αCT11 wound healing activity by tracking cell migration into a scratch.

In these experiments, we cultured human dermal fibroblasts (huDFs), with migratory behavior known to organize scar tissue,[28–32] scratched them, and assessed their migration upon the addition of αCT1, which is αCT11 attached to the cell penetrating peptide antennapedia (RQPKIWFPNRRKPWKK)[33]. We found that αCT1 afforded higher cell migration into a scratch than the vehicle control, which was attributed to intracellular Cx43/ZO-1 binding-mediated wound healing. Therefore, we anticipated that installing methyl esters onto αCT11 would provide an alternative, reversible strategy towards realizing its intracellular localization. Thus, we performed *in vitro* cell culture scratch wound assays on huDFs (ATCC, PCS-201-012) treated with αCT11, αCT11-3OMe(D5,D6,E8), or -4OMe.

Prior to their use in the scratch wound assays, each αCT11 peptide was dialyzed against 30% acetic acid to replace trifluoroacetate (TFA) counterions, known to skew physiological experiments,[34,35] with acetate counterions. MALDI-TOF MS revealed that some hydrolysis occurred during the counterion exchange process, as the counterion switched αCT11-3OMe(D5,D6,E8) sample contained peaks commensurate with -3OMe, -2OMe, and -2OMe – 1 H_2O (**Figure A.59**). Similarly, the counterion switched αCT11-4OMe sample contained -4OMe, 3OMe, -3OMe – 1 H_2O, -2OMe – 1 H_2O, -2OMe – 2 H_2O, and -1OMe (**Figure A.60**). Despite some hydrolysis of the samples and the presence of intramolecular imide products, it was clear that both counterion-switched αCT11-3OMe(D5,D6,E8) and -4OMe still contained esters. Presumably, esters on the D5 and D6 aspartic acids hydrolyzed and some aspartimide formation occurred. Thus, we proceeded with these experiments to compare cell migration into the scratch resulting

after addition of the esterified peptide formulations containing or lacking a C-terminal I9 methyl ester.

In the scratch assays, huDFs were cultured on polypropylene culture dishes for 24 h, after which the peptides or vehicle control were added, the cultures were scratched with a 200 μL pipette tip, and 10 images were taken at different positions along the scratch immediately and 6 h after scratching. We measured a "migration index" for the cells in each image, which was calculated by dividing the difference in the area of the scratch after 6 h by the initial area. We then divided each migration index by the average of those for cells treated with the vehicle control (DMSO in HEPES buffer) to calculate a "relative migration index" (**Equation 2.3**) for each image. This was repeated 2 more times for a total of n = 3 scratched cell cultures, and we then calculated an overall average relative migration index for cells treated with each formulation. For cultures treated with αCT11-3OMe(D5,D6,E8) and -4OMe, we observed significantly higher relative migration indexes (-4OMe = 6.2 +/- 2.1; -3OMe(D5,D6,E8) = 4.8 +/- 1.5, with $p < 0.05$ for both formulations) than unmodified αCT11 (1.4 +/- 0.4), which had a statistically similar relative migration index to the vehicle alone (1.0, $p = 0.11$) (**Figure 2.5**, **Table A.14-A.15**). Interestingly, despite the relative differences in hydrophobicity and hydrolytic stability observed between αCT11-3OMe(D5,D6,E8) and -4OMe, cultures treated with the 2 formulations did not have statistically significant relative migration indices ($p = 0.19$). Regardless, the higher relative migration indices observed in the cell cultures treated with esterified αCT11 suggest that esters offer benefit by facilitating cell internalization and/or increasing activity.
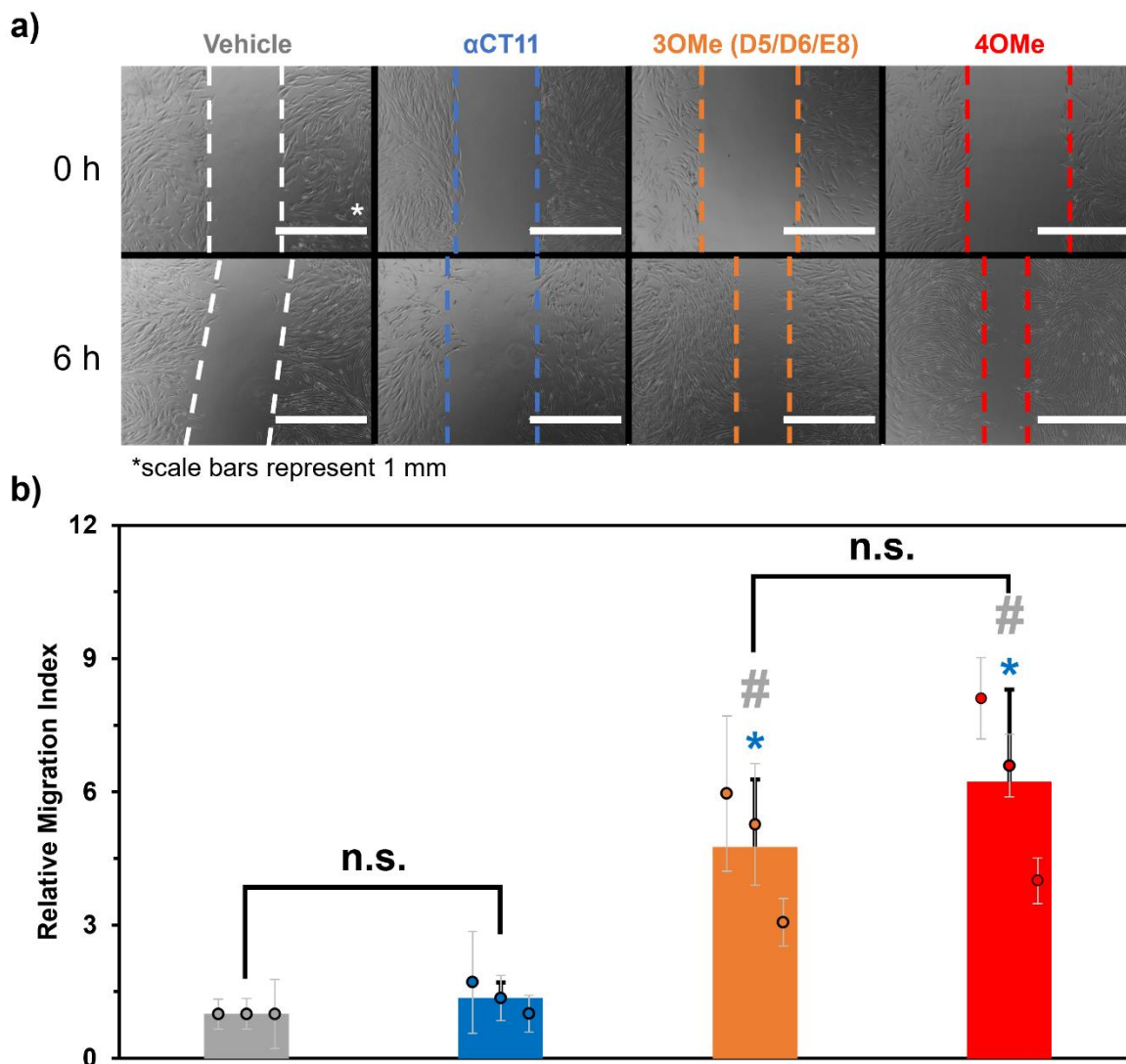
Figure 2.5. Multi-site esterification of αCT11 increases cell migration into a scratch. **a)** Representative images of the initial scratch wounds (top) and the same wounds after 6 h (bottom) of cell culture. Prior to the scratch, samples were treated with either the vehicle control (DMSO in HEPES, pH 7.4, gray), unmodified αCT11 (blue), αCT11-3OMe(D5,D6,E8) (orange), or αCT11-4OMe (red). Dashed lines are added to guide the eye along the edges of the scratch. **b)** Relative migration indexes of scratched cells when exposed to the vehicle (gray), αCT11 (blue), -3OMe(D5,D6,E8) (orange), and -4OMe (red). Scratch assays were performed with a human adult dermal fibroblast line (ATCC, PCS-201-012). Plotted circular markers represent the average between n = 10 individual images of a single scratch, and their respected standard deviations are noted by the gray error bars. Plotted bars represent the average relative migration index across n = 3 different cell cultures, and the bolded black error bars represent the standard deviation of those averages. Statistics were determined from the average relative migration indexes of the n = 3 cell cultures using a one-tailed paired two-sample t-test assuming unequal variances, where # (gray) and * (blue) denote statistical significance relative to the vehicle and αCT11, respectively ($p < 0.05$) and "n.s." represents no statistical significance ($p > 0.05$).

2.3 Conclusions

Through these studies, we showed that varying the number of methyl esters installed onto the therapeutic peptide αCT11 is an effective way to reversibly modify the hydrophobicity and number of anionic COOHs; however, controlling the position of esters on the peptide is just as important. 2D NMR spectroscopy revealed which residues were esterified, a key development in establishing structure property relationships for esterified αCT11 formulations. Of the 4 sites on αCT11, the C-terminal I9 was the most influential in modifying αCT11 properties, as methyl esters on the C-terminal I9 imparted the highest increase in hydrophobicity and were the most hydrolytically stable. Additionally, observed intramolecular imides seemed to offer a further increase in hydrophobicity relative to products with just esters, suggesting imides as an alternative method to reversible affect therapeutic peptide properties.; however, further experiments will be required to confirm imidization as a viable strategy, as aspartimide formation has been shown to lead to esterified peptide racemization.[57] Considering that the D5/D6, E8, and C-terminal I9 methyl esters each affected αCT11 hydrophobicity and hydrolytic stability differently, these experiments raise important future questions about the relative roles of ester position (i.e., 5, 6, 8, C-terminus) vs. amino acid type (i.e., D, E, I) on modifying therapeutic peptide properties. As αCT11 therapeutic activity is thought to rely on its interaction with the H2 domain of the transmembrane protein Cx43 and/or the PDZ2 domain of the scaffolding protein ZO-1,[4] we were encouraged by the increased migration observed in *in vitro* scratch wound assays treated with esterified αCT11 relative to those treated with unmodified αCT11. These results show that esterification provides a clear benefit to αCT11-mediated wound healing and raises exciting future questions about whether installed esters serve mainly to increase cell internalization of therapeutic

peptides and/or to provide inherently higher activity themselves. Through reversible control over hydrophobicity and charge, multi-site esterification offers a compelling strategy to modify the hydrophobicity and net charge of hydrophilic peptides with multiple COOHs and tailor them for delivery, an imperative step towards transitioning intracellularly targeting therapeutic peptides into the clinic.

2.4 Future Directions

2.4.1 Elucidating the mechanism of esterified αCT11 activity

This study showed esterified αCT11 to be beneficial to treat wounded cells *in vitro*; however, we are still not yet sure the exact mechanism by which esterified αCT11 promotes increased wound healing relative to the unesterified formulation. While it is possible that installing esters onto αCT11 increased its overall activity through increasing cell membrane permeability, intracellular ester cleavage, and then binding of unesterified αCT11 to either Cx43 and/or ZO-1, it is also possible that esterified αCT11 yields wound healing through alternative mechanisms than those already established for αCT11. Therefore, future work will focus on directly testing the cell membrane permeability of αCT11 with different numbers of ester groups in different positions within the sequence, and determining if esterified αCT11 binds to Cx43 and/or ZO-1. To study cell membrane permeability, suggested future directions include developing methods to synthetically attach biotin to αCT11, which can be used to detect molecules *in celluo* through specific binding to streptavidin. Finally, similar to prior work by Gourdie & coworkers,[4] we plan to compare the ability of esterified αCT11 to bind Cx43 and ZO-1 relative to unesterified αCT11 to determine if esterification indeed increases activity. Taken together, these proposed experiments should assist in elucidating the mechanism by which esterified

αCT11 shows improved *in vitro* wound healing through the scratch assays presented in **Figure 2.5**.

2.4.2 *Installed ester position vs. amino acid type*

Our investigation into the effect of ester position on αCT11 hydrophobicity and hydrolytic stability raised an important distinction between how the relative roles of the amino acid position within the sequence type affect the hydrophobicity and hydrolytic stability of an installed ester. As esterifying the C-terminal I9 methyl ester induced the most significant observed changes to αCT11 properties, we could envision two phenomena at play. First, we hypothesized that amino acid type (i.e., D, E, C-terminal I) determined how installed esters controlled hydrophobicity and hydrolytic stability. Here, we hypothesized that because isoleucine (I) is more hydrophobic than either the aspartic acid (D) or glutamic acid (E) residues within the αCT11 sequence, esterifying the isoleucine residue would yield the highest increase in hydrophobicity and hydrolytic stability. To gauge this, we have synthesized a library of esterified αCT11-based peptides with either glycine (αCT11-G), alanine (αCT11-A), or isoleucine (αCT11) C-termini and fully esterified them (**Figure 2.6, Figures A.61-A.64, Tables A.16-A.19**). As fully esterifying each of the αCT11 variants led to a 4.8 – 4.9 min increase in retention time, this suggests that esterifying αCT11 has the same exact effects on hydrophobicity regardless of the C-terminal amino acid type. However, we also plan to run hydrolysis experiments and determine the most hydrolytically stable amino acid, similar to our studies in **Figures 2.3-2.4.**
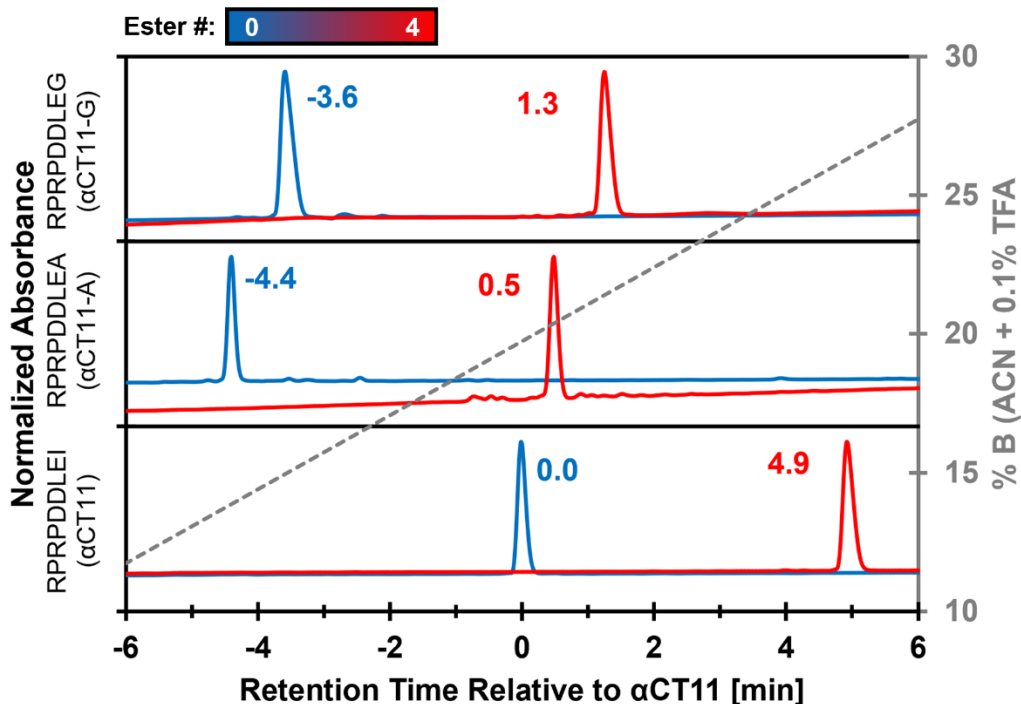
Figure 2.6. RP-HPLC of αCT11 with either C-terminal isoleucine (αCT11, bottom), alanine (αCT11-A, middle), or glycine (αCT11-G, top). Retention times of each peaks are plotted relative to αCT11, which was set to a retention time of 0 min. Absorbance was normalized to the highest peak between -6 and 6 min. Both unesterified αCT11 variants (blue) and fully esterified αCT11 variants (red) are plotted with relative retention times reported on the plots next to the peaks. % composition of B (ACN + 0.1% TFA) in the mobile phase gradient (gray) is also plotted.

Alternative to amino acid type determining hydrophobicity, we reasoned that the position in the sequence where the ester is installed controls hydrophobicity. In this scenario, we envisioned esterifying the C-terminus of the peptide would enable greater changes in conformation, where hydrophobic interactions could form between the hydrophobic N-terminal arginine residues and the C-terminal I9 to cause a cyclic ring-like structure. As peptide cyclization is often associated with an increase in hydrophobicity,[36,37] this would cause much larger variations in hydrophobicity than esterifying the aspartic acid or glutamic acid residues in the middle of the sequence. In the future, we aim to synthesize and esterify RPRPEELEE-NH$_2$ to determine the effect of amino acid position within the sequence (i.e., 5, 6, 8, C-terminus) on ester hydrophobicity

41

and hydrolytic stability when amino acid type is held constant. To do so, we hope simultaneously develop a site-selective esterification method to install only one ester onto different positions within αCT11, which we will discuss in **Section 2.5.4**. Additionally, esterification and subsequent hydrolysis of the RPRPEELEE-NH$_2$ peptide would also tell us if the imide formation observed during αCT11 hydrolysis is indeed a product of aspartic acid (D) hydrolysis alone. These proposed studies will build upon the design rules for multi-site esterification of therapeutic peptides established in this chapter, further enabling its implementation into the toolbox of researchers aiming to tailor therapeutic peptides for *in vivo* delivery.

2.4.3 Alternatives to Fischer esterification: Amide esterification

While not shown in Figure 2.6, we had also studied the effect of esterifying an αCT11 variant with a C-terminal glutamine (Q), which contains an amide on its side chain, instead of an isoleucine (αCT11-Q) (**Figures 2.6a**, **A.65**, **Table A.20)**. Upon Fischer esterification and purification of this αCT11-Q variant, we observed the production of a peak that corresponded to αCT11 with 5 installed methyl ester groups (Figures 2.6a, **A.66**, **Table A.21**). Interestingly, this suggests that the conditions used for Fischer esterification facilitated the replacement of the glutamine side chain amide with a methyl ester. While this was not intended, this result implied that primary amides within the αCT11 sequences could be esterified using the same conditions as Fischer esterification, opening new synthetic possibilities for esterifying peptides.
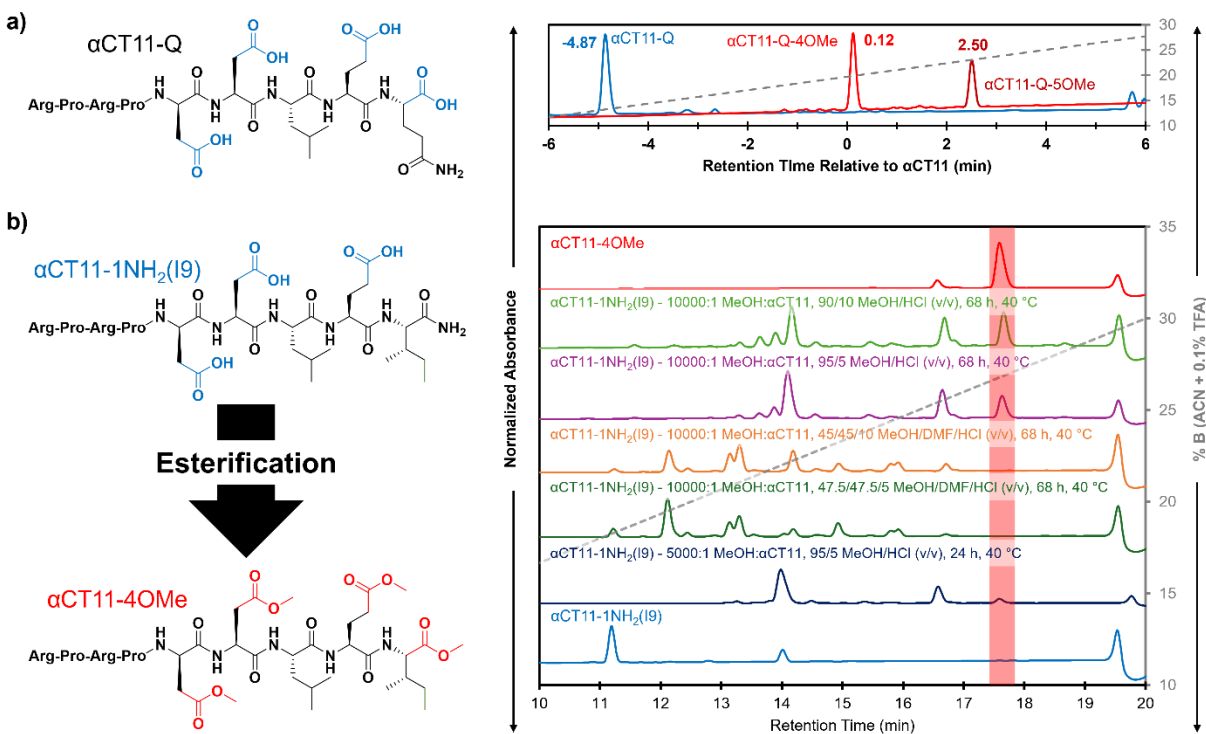
Figure 2.7. Esterification of amides within the αCT11 sequence. **a)** Rp-HPLC chromatograms showing esterification of αCT11-Q (RPRPDDLEQ), which results in 2 major products: αCT11-Q with 4 methyl esters (αCT11-Q-4OMe, red) and with 5 methyl esters (αCT11-Q-5OMe, dark red). Esterification was performed at 5000:1 MeOH:αCT11 with 5% HCl (v/v) at 40 °C for 24 h. Molecular weight was determined by MALDI-TOF MS. **b)** RP-HPLC chromatograms depicting esterification of αCT11 with an amidated C-terminus (αCT11-1NH$_2$(I9), blue). Esterification was performed using various conditions, which are listed on each chromatogram. Samples are shown relative to αCT11 alone (blue, bottom), and αCT11-4OMe to determine the amount of fully esterified peptide in each reaction mixture%B in the mobile phase gradient (gray) is superimposed on each chromatogram according to the x-axis.

Naturally, peptide sequences contain an N-terminal amine and a C-terminal carboxylic acid (Figure 1.1). Synthetically, this requires the use of 2-chlorotrityl chloride resin, which is connected to growing peptide chains by a heat-labile ester bond. While efficient, this synthesis is relatively time intensive, as the ester bond prevents the use of microwave-assisted methods; therefore, synthesizing peptides with a C-terminal carboxylic acid, such as αCT11, prior to esterification requires an hour per amino acid attachment, and is usually on the order of days. Alternatively, Rink amide resin is attached to the growing peptide chain by an amide bond, which is stable at 90 °C and, thus, requires only a few minutes per amino acid attachment, and on the order of hours for

synthesis; however, as this resin synthesizes peptides with a C-terminal amide instead of a C-terminal carboxylic acid, we had originally opted to use 2-chlorotrityl chloride resin to enable the Fischer esterification of naturally occurring therapeutic peptides with C-terminal carboxylic acids. Upon the realization that primary amides could be esterified under the same conditions as Fischer esterification of carboxylic acids on αCT11, future directions will include the direct esterification of amides to leverage the high-throughput ability of microwave-assisted solid phase peptide synthesis methods.

To assess if αCT11 synthesized using rink amide resin to yield a C-terminal amide (αCT11-1NH$_2$(I9)) could be converted to αCT11-4OMe, we reacted αCT11-1NH$_2$(I9) using similar conditions to those presented in **Chapter 3** (5000:1 MeOH:αCT11, 5% HCl, 40 °C, 24 h), which were found to increase the yield of fully esterified αCT11-4OMe to > 95% (Figures 2.7b, **A.67-A.68, Tables A.22-A.23**). However, we were unable to detect fully esterified αCT11-4OMe from the reaction products by RP-HPLC or MALDI-TOF MS, instead only observing the addition of 3 methyl esters to the original amidated αCT11 variant (αCT11-1NH$_2$/3OMe). Therefore, we increased the ratio of MeOH to αCT11 to 10000:1 (mol/mol) and allowed the reaction to proceed for 68 h. We also tested the effect of doubling the concentration of acid catalyst in the reaction (5% to 10% HCl) and the effect of using DMF as a 50:50 (v/v) cosolvent with MeOH to improve solubility of the peptides in solution (Figures 2.7b, **A.69-A.72, Tables A.24-A.27**). After measuring the samples on RP-HPLC, we only saw the appearance of αCT11-4OMe peaks (confirmed by MALDI-TOF MS) in the samples without the DMF cosolvent. Interestingly, doubling the HCl content did appear to slightly increase the overall conversion of αCT11-4OMe by a small amount. These preliminary results show that we can decrease synthesis timescales

through N-terminal amides without sacrificing the ability to fully esterify αCT11, an exciting result that could lead to higher-throughput synthesis that require an order of magnitude less hours to complete; however, more experiments need to be done to find conditions where the yield of fully esterified αCT11-1NH$_2$(I9) from Fischer esterification conditions approach those from αCT11 reported in **Chapter 3** (> 95%) to actually make use of this strategy. Interestingly, these results also show that glutamine side chain amides were more susceptible to esterification than the αCT11 C-terminus, which raises similar questions involving the role of amino acid position and type in amide esterification to those proposed in Section 2.5.1.

2.4.4 *Alternatives to Fischer esterification: Allyl ester installation*

Fischer esterification is a relatively cost-effective reaction, only requiring excess methanol and a catalytic amount of HCl, offering yields of above 70-80%, and provides the ability to simultaneously esterify multiple carboxylic acid sites on a single therapeutic peptide; however, it lacks the ability for site-selective placement of esters onto specific residues. While purification of Fischer esterified peptide mixtures with preparative RP-HPLC can provide isolated fractions of one esterified variant, this process is time-consuming and substantially decreases the overall peptide yield. Peptides containing D or E residues are commonly synthesized using tert-butyl ester protecting groups, which are acid-labile and easily removed through the trifluoroacetic acid-mediated deprotection step used to remove the synthesized peptide from the resin scaffold, a process that yields carboxylic acid groups that need to be converted to esters by Fischer esterification post-synthesis. Alternatively, allyl esters, which are stable in acid and will remain on the peptide through deprotection, can be used as protecting groups for D and E residues during peptide synthesis (**Figure 2.8a**). Despite being stable in acid, allyl esters are still labile to

base- or esterase- catalyzed hydrolytic activation,[38] and are thus still viable options for esterification of therapeutic peptides. Thus, one future direction will be to use allyl ester protecting groups to directly place different numbers of esters onto specific positions in the αCT11 sequence, allowing more control over the ester installation process than Fischer esterification.
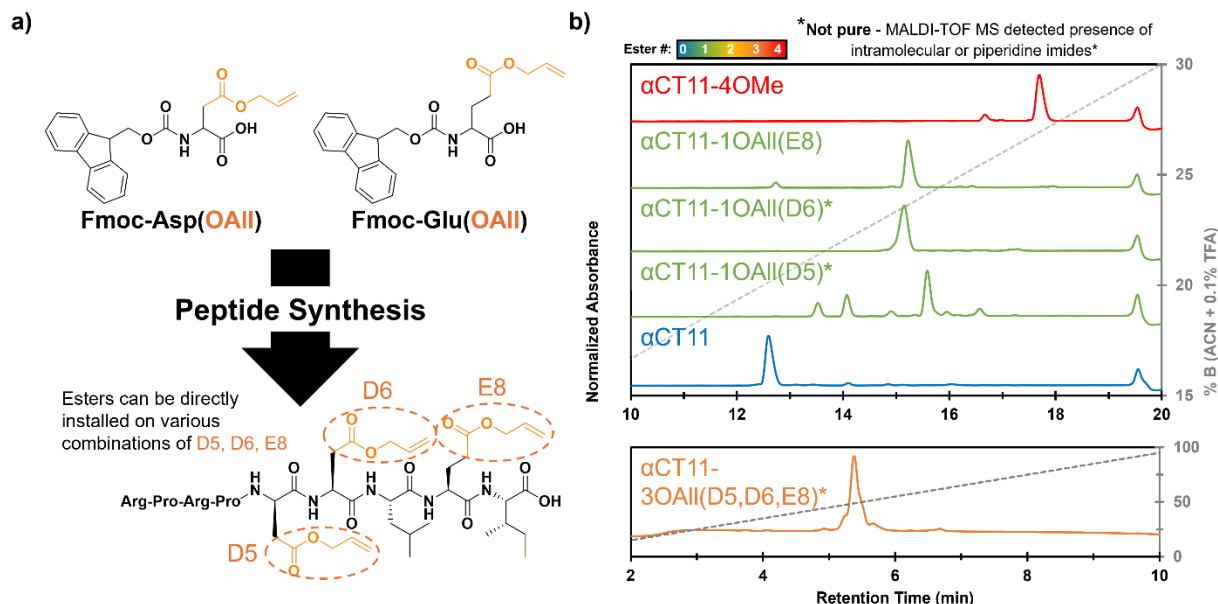
Figure 2.8. Allyl ester installation onto αCT11. A) Schematic depicting aspartic and glutamic acid residues with allyl ester protecting groups, with solid phase peptide synthesis directly yielding esterified αCT11. **b)** RP-HPLC chromatogram of αCT11-1OAll(E8), αCT11-1OAll(D6), αCT11-1OAll(D5) (all in green), as well as αCT11-3OAll(D5,D6,E8) (orange). Chromatograms are shown in reference to αCT11 (blue) and αCT11-4OMe (red) as a reference for hydrophobicity. %B in the mobile phase (gray) is superimposed onto the chromatograms. A * in the chromatogram label denotes that the sample contained the presence of intramolecular or piperidine aspartimides, and that the plotted peaks are not necessarily representative of the purified peptide as suggested in the label.

To selectively place allyl esters on specific amino acids on αCT11, we synthesized the peptide with allyl esters on the D5, D6, or E8 sites, as well as with allyl esters on all 3 sites (**Figure 2.8b**). While we were able to synthesize αCT11 with an allyl ester installed on the E8 (αCT11-1OAll(E8)) residue, MALDI-TOF MS revealed the presence of imides, either by the loss of H_2O or the addition of piperidine, which can form an imide with carboxylic-acid toting amino acids during peptide synthesis, in all samples containing

either a D5 or D6 allyl ester (**Figures A.73-A.76, Tables A.27-A.31**). As imides were not present in αCT11-1OAll(E8), we attributed these imides to be aspartimides, agreeing with our results presented in **Section 2.3.3**. Interestingly, while we could detect imides in the αCT11-1OAll(D6) sample, the RP-HPLC was relatively pure, with only one major product appearing in the RP-HPLC. This suggests that the D5 ester was primarily involved in aspartimide formation. While the use of allyl esters provide significant potential for site-selective esterification of therapeutic peptides, like αCT11, syntheses involving aspartic acids need to be optimized to prevent the formation of aspartimides for this potential to be realized.

2.5 Materials and Methods

2.5.1 Materials

Fluorenylmethoxycarbonyl(Fmoc)-protected amino acids and 2-chlorotrityl chloride resin (0.6 mmol/g) were purchased from Advanced ChemTech (Louisville, Kentucky). Diisopropyl carbodiimide (DIC, 99.8%), N,N'-dimethylformamide (DMF, 99%), Oxyma Pure (99%), piperidine (99%), N,N-Diisopropylethylamine (DIPEA, 99%), trifluoroacetic acid (TFA, 99%), triisopropyl silane (TIPS, 98%), 2,2'-(ethylenedioxy)diethanethiol (DODT, 95%), diethyl ether (99%), methanol (MeOH, 99.8%), acetonitrile (ACN, HPLC-grade, 99.9%), hydrochloric acid (HCl, 37% in H2O), deuterated dimethyl sulfoxide (DMSO-d6, 99.5%), sodium bicarbonate (99.7%), sodium carbonate (99.5%), phosphate buffered saline tablets (PBS, 1 tablet/200mL for 1X concentration, pH 7.2-7.6), SpectraPor6 dialysis membranes (0.5 – 1 kDa), esterase from porcine liver (PLE, E3019, 19 units/mg solid), and Amicon ultra centrifugal filters (3 kDa MWCO) were purchased from Sigma Aldrich. Glacial acetic acid (99.7 -100.5%) and potassium iodide (KI) were purchased from VWR. All chemicals were used as received.

All water was purified by in-house reverse osmosis (RO). Ultrapure water refers to water purified by a Thermo Scientific Barnstead Smart2Pure water purification system (18.2 mΩxcm).

2.5.2 αCT11 synthesis

αCT11 was prepared using Fmoc-solid phase peptide synthesis with a CEM Liberty Blue automated microwave-assisted peptide synthesizer. To prepare the peptide with a COOH C-terminus, 2-chlorotrityl chloride resin (0.6 mmol/g) was used, and the entire synthesis was conducted at 25 ºC to prevent premature cleavage of the ester bond connecting the peptide to the resin, which was observed above 50 ºC. DIC (1 M in DMF) and Oxyma Pure (1 M in DMF) were used to mediate amino acid coupling, except for the first amino acid, which was coupled to the resin using KI (0.125 M in DMF) and DIPEA (1 M in DMF). Piperidine (20% v/v in DMF) was used to deprotect Fmoc groups preceding amino acid additions. After synthesis, the peptide was cleaved from the resin using a deprotection cocktail composed of TFA, water, TIPS and DODT (92.5/2.5/2.5/2.5 v/v) for 3 h at room temperature under constant stirring. Following deprotection, the peptide solution was separated from the resin by filtration, and the peptide was isolated by precipitation into diethyl ether and centrifugation (5 min, 2420 xg, 4 °C). The supernatant was decanted and the peptide was washed again with diethyl ether and isolated by centrifugation under the same conditions. The peptide pellet was dried under vacuum for 1 h, dissolved in 5% ACN in H_2O (both with 0.1% TFA) and frozen in liquid N_2 immediately prior to lyophilization for 48 h to produce a fluffy cake that was easy to manipulate. 60-70% yield was achieved for each synthesis.

2.5.3 Fischer Esterification of αCT11 with MeOH

For each esterification, between 20 – 150 mg of αCT11 was mixed at a 1600:1 molar ratio of MeOH:αCT11 (400:1 MeOH:COOH) containing 5% HCl (v/v). The solution was stirred for 24 h, after which it was precipitated into diethyl ether and the peptide was isolated by centrifugation (5 min, 2420 xg, 4 °C). The supernatant was decanted, and the peptide was washed with diethyl ether, isolated by centrifugation under the same conditions, and dried under vacuum for 1 h. The peptide was dissolved in 5% ACN in H2O (both with 0.1% TFA) and frozen with liquid N_2 immediately prior to lyophilization for 48 h to produce a fluffy cake that was easy to manipulate. 50 – 70% yield was achieved for each esterification, assuming all 4 COOHs were esterified and peptides all contained trifluoroacetic acid counterions.

Scheme 2.1. Fischer esterification of αCT11 (RPRPDDLEI)
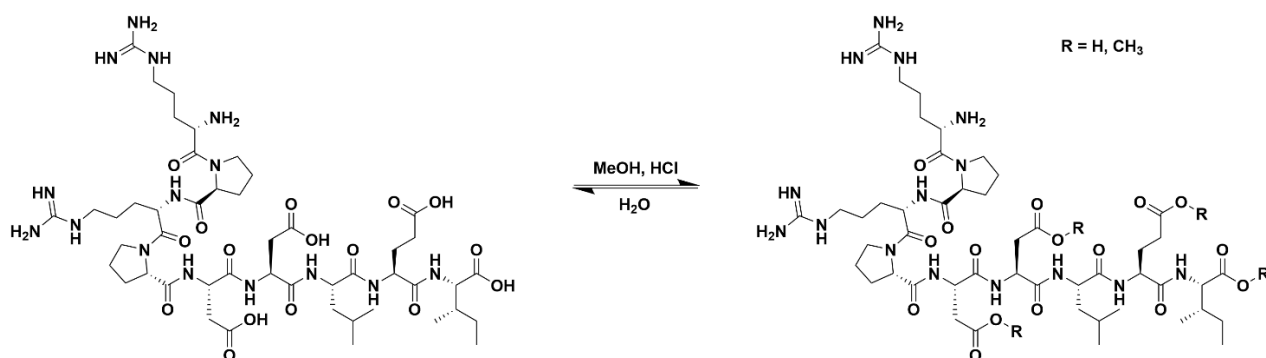
2.5.4 Analytical reverse-phase high-performance liquid chromatography (RP-HPLC)

Analytical RP-HPLC was performed at 35 °C with a flow rate of 1 mL/min on a Waters e2695 Alliance Separations Module, equipped with a XBridge® C18 chromatographic separation column (4.6 mm x 50 mm, 3.5 µm beads) and a photodiode array detector (Waters 2489 UV/Visible). The mobile phase consisted of ultrapurified water containing 0.1% TFA (A) and ACN containing 0.1% TFA (B), where TFA was included to maintain pH. For a discussion of mobile phase gradient composition, see

Table A.1. UV absorbance was monitored at 214 nm. For all chromatograms shown in **Figure 2.1**, the retention time of each sample was normalized to the maximum absorbances of the unesterified αCT11 and fully esterified αCT11-4OMe peaks, which were set to normalized retention times (τ) of 0 and 1, respectively. Absorbance was also normalized to the minimum and maximum absorbances of each chromatogram, between $\tau = 0$ and $\tau = 1$. For the hydrolysis experiments, the retention time of each sample was reported relative to an αCT11 sample, which was set to a retention time of 0, and absorbance was not normalized. Peak area (%) for a given αCT11-related peak ($\alpha CT11_i$) was calculated as the integration of the chromatogram within the respective bounds of that peak ($t_{i,start}$ and $t_{i,end}$) relative to the sum of all integrals in the elution phase (between 5 and 15 min, Table S1) of the chromatogram (**Equation 2.1**). Since the solvent blanks (5% ACN in H_2O (both with 0.1% TFA), 1X PBS, or 100 mM carbonate buffer, when applicable) did not produce any features in the elution phase, we neglected solvent influence in the peak area calculations.

Equation 2.1) $\text{Peak Area}_i\ (\%) = \dfrac{\int_{t_{i,\ start}}^{t_{i,\ end}} \alpha CT11_i}{\sum_i \left(\int_{t_{i,\ start}}^{t_{i,start}} \alpha CT11_i \right)}$

2.5.5 Preparative RP-HPLC

To purify crude αCT11 variants and collect the isolated products, preparative RP-HPLC was performed at 25.52 mL/min at room temperature on a Waters Empower system, equipped with a XBridge® Prep C18 optimum bed density chromatographic separation column (30 mm x 150 mm, 5 μm beads) and a photodiode array detector (Waters 2489 UV/Visible). UV absorbance was monitored at 214 nm. The mobile phase consisted of ultrapurified water containing 0.1% TFA (A) and ACN containing 0.1% TFA (B), where TFA was included to maintain pH. Mobile phase gradients can be found in

Table S1. For each purification, the eluent was collected at desired times and re-analyzed on analytical RP-HPLC using analogously scaled gradients to ensure purity, which was determined as the peak area fraction (Equation 1) in the relevant retention time range (between $\tau = 0$ and $\tau = 1$). Like fractions were then combined and lyophilized to obtain solid, purified peptide. Between 30 – 80 mg of peptide were routinely injected, with 20 – 60% recovery achieved for each injection.

2.5.6 *Matrix-assisted laser desorption/ionization-time of flight (MALDI-TOF) mass spectrometry (MS)*

Molecular weights of each purified peptide sample were measured using a Shimadzu MALDI-8030 mass spectrometer with a 200 Hz solid-state laser (355 nm). The instrument was calibrated with a standard MALDI calibration kit (TOFMix and CHCA matrix, Shimadzu), for which samples were dissolved at 670 femtomoles/µL in 70% v/v ACN with 0.1% TFA. All samples were dissolved in 5% ACN in ultrapure H_2O, each with 0.1% TFA (except for the acetate counterion-switched samples, which were dissolved in 5% ACN in ultrapure H_2O without any TFA), at approximately 1 mg/mL and co-crystallized in a 1:1 ratio (v/v) with a α-cyano-4-hydroxycinnamic acid (CHCA) matrix solution (5 mg/mL in 70% v/v ACN with 0.1% TFA). Peaks with less than 2% intensity or those that could be attributed to a CHCA blank were not reported.

2.5.7 *Nuclear Magnetic Resonance (NMR) Spectroscopy*

A Bruker Avance III 800 MHz spectrometer equipped with a 25 K cryoprobe was used to obtain NMR spectra. αCT11 formulations were dissolved in DMSO-d6 at 5 mg/mL when possible (i.e., αCT11, αCT11-3OMe(D5/D6/E8), αCT11-4OMe); however, as we were unable to obtain more than 1 mg of the minor αCT11-3OMe products (-3OMe(D5/D6/I9, D6/E8/I9, D5/E8/I9)), they were dissolved at less than 1 mg/mL in

DMSO-d6. Chemical shifts were referenced to the DMSO-d6 residual peaks at 2.5 ppm or 39.5 ppm for ^{1}H and ^{13}C spectra, respectively. All integrals were referenced to the R1/R3 Hδ peak (3.11 ppm), which was set to 2 protons. 1D ^{1}H and ^{13}C, 2D H-H clean in-phase correlation spectroscopy (CLIPCOSY),[18] H-H total correlation spectroscopy (TOCSY),[19] H-H nuclear Overhauser spectroscopy (NOESY),[20] H-C heteronuclear multiple bond correlation (HMBC),[21] and selective H-C HMBC (selHMBC)[22] spectra were obtained by using standard Bruker pulse programs. The TOCSY and NOESY mixing times were 100 ms and 250 ms, respectively. The center of the ^{13}C dimension of the selective HMBC was set to 170.4 ppm and the ^{13}C sweep width was 7.2 ppm; the selective ^{13}C pulse had a Q3_surbop.1 shape and a 1470 Hz bandwidth. 50% nonuniform sampling was used for all 2D spectra except selHMBC, for which uniform sampling was used. Spectra were processed and analyzed by using Mestrenova 14 and Topspin 3.

2.5.8 Hydrolysis experiments

Stock solutions of αCT11, αCT11-3OMe(D5/D6/E8), and αCT11-4OMe in 5% ACN in ultrapure H2O (0.1% TFA) were prepared at 1 mg/mL using >10 mg peptide, for accuracy, and aliquots (0.6 mL) of each solution were lyophilized to minimize hydrolysis during storage at -20 °C. Each lyophilized sample was incubated in 2 mL of either 1X phosphate buffered saline (PBS, pH 7.4) or carbonate buffer (100mM, pH 10), creating a final concentration of 0.1 mM for each sample. 1X PBS was prepared by dissolving a PBS tablet into 200 mL of distilled H_2O. Carbonate buffer (100 mM) was prepared by combining 775 mg (9.23 mmol) of sodium bicarbonate and 1142 mg (10.77 mmol) of sodium carbonate in distilled H2O (200 mL). Carbonate and PBS buffer concentrations were selected to exceed those of the protonatable/deprotonatable groups on the peptide samples (0.6 mM for αCT11, 0.4 mM for αCT11-3OMe(D5/D6/E8), and 0.3 mM for

αCT11-4OMe) to provide adequate buffering. The pH of each buffer was measured using a Mettler Toledo Benchtop pH meter and was adjusted using 100 mM solutions of NaOH and HCl until the desired pH was achieved within a tenth of a unit. Solutions were stirred continuously at 37°C and hydrolysis was monitored using RP-HPLC and MALDI-TOF MS. The percent of unesterified αCT11 recovered from hydrolysis was determined by integrating the chromatogram within the respective bounds ($t_{i,start}$ and $t_{i,end}$) of the unmodified αCT11 peak (αCT11) at each timepoint relative to the sum of αCT11 and all esterified αCT11 (αCT11-OMe$_i$) peak integrals visible in the relevant retention time range (the unmodified and most hydrophobic peaks αCT11) of the RP-HPLC run (**Equation 2.2**). As the buffered solvent alone produced no significant peaks within the elution phase (Table S1) in their respective chromatograms, they were not considered in the recovery of unesterified αCT11 (%) calculations. Hydrolysis experiments for all αCT11-xOMe samples were repeated in triplicate.

Equation 2.2) Recovery of unesterified αCT11 (%)= $\dfrac{\int_{t_{\alpha CT11,start}}^{t_{\alpha CT11,end}} \alpha CT11}{\int_{t_{\alpha CT11,start}}^{t_{\alpha CT11,end}} \alpha CT11 + \sum_i \left(\int_{t_{i,\,start}}^{t_{i,\,end}} \alpha CT11\text{-}OMe_i \right)}$

2.5.9 Porcine Liver Esterase (PLE) Hydrolysis Experiments

Lyophilized peptide samples were prepared as described for the hydrolysis experiments. A PLE (19 units/mg) stock solution (1 mg/mL) was prepared in 1X PBS (pH 7.4) and was diluted to create 3 separate solutions: 0.526 mg/mL (20 units/mL), 0.053 mg/mL (2 units/mL), and 0.005 mg/mL (0.2 units/mL). 2 mL of each solution was added to αCT11, αCT11-3OMe(D5,D6,E8), and αCT11-4OMe aliquots (final peptide concentration of 0.1 mM) to vary the PLE concentration between 1:1, 10:1, and 100:1 enzyme units:μmol peptide. Solutions were stirred continuously at 37 °C for 24 h and the peptide was isolated through centrifugal filtration (3 kDa membranes, 5 min, 2420 xg, 4

°C) prior to analysis. Isolated peptide samples were then filtered through a 0.45 µm filter and hydrolysis was monitored by RP-HPLC and MALDI-TOF MS.

2.5.10 Liquid Chromatography-Mass Spectrometry (LC-MS)

LC-MS measurements were performed with a Thermo nanoEASY-LC 1200 coupled to a Thermo Orbitrap Exploris 480 mass spectrometer with an Easy Spray ion source. Hydrolysis of αCT11, αCT11-3OMe(D5,D6,E8) and -4OMe was halted by of TFA (0.1% v/v), which lowered the pH to under 2.0, for less than 24 h prior to analysis. Samples (50 µL) were desalted using C-18 tips (Protocol: dx.doi.org/10.17504/protocols.io.36wgqjzmyvk5/v1), suspended with 50 µL of 0.1% formic acid (FA) and diluted 10x for LC-MS injection. Samples were injected into the mass spectrometer through an analytical PepMAP RSLC C-18 Easy Spray column (Thermo Scientific – 3 µm particle size, 100 Å pore size, 150 mm column length, 75 µm internal diameter) with a pre-column Acclaim PepMap 100 C-18 (Thermo Scientific – 3 µm particle size, 100 Å pore size, 20 mm column length, 75 µm internal diameter). The mobile phase consisted of water with 0.1% FA (v/v) (A) and 20/80 water/ACN with 0.1% FA (v/v) (B). Peptides were eluted from the column using an a ACN gradient in 0.1% FA (5 – 60 % B in 20 min, 60 – 95 %B in 4 min, and hold at 95% B for 6 min). The mass spectrometer was operated in positive, data-dependent mode, in which one full MS scan as acquired in the m/z range of 375-1500 (l µscan, resolution = 120 K, RF Lens 40%, AGC = 300%, Max Inject = 60 ms) followed by MS/MS acquisition using higher energy collisional dissociation (HCD) of the 10 most intense ions (1 µscan, repeat count = 3, exclusion duration = 20 s, intensity threshold = 1E+06, 10 ppm tolerance, resolution = 30 K, AGC = 100%, NCE = 30) from the MS scan using window width of 2.0 m/z. For each timepoint, a total ion chromatogram (m/z = 525.0 – 590.0 for +2 ions related to any αCT11 products)

and a selective ion chromatogram (monoisotopic +2 m/z, 10 ppm window) for each αCT11 species was measured, and the area of the selective ion chromatograms were corrected to account for different isotopes of each product by multiplying by a correction factor of 1.9 (Figures S41-S42, S45-S58). Abundance (%) of different αCT11 species was calculated by integrating the area under the curve for each selective ion chromatogram, applying the correction factor, and dividing it by the area of the total ion chromatogram.

2.5.11 Trifluoroacetic acid counterion switch

To replace TFA counterions with acetate counterions, we dissolved >10 mg of αCT11, αCT11-3OMe(D5/D6/E8), or αCT11-4OMe into distilled H_2O (5 – 10 mL). We then placed the solution into a 0.5 – 1 kDa dialysis membrane. We first dialyzed each peptide sample against 30% acetic acid in distilled H2O for 4 h to replace the counterions, followed by 3 additional dialysis solution changes (greater than 4 h each) against 0.1% acetic acid in distilled H_2O to lower the overall concentration of acetic acid in the solution prior to lyophilization. After lyophilization, counterion-switched samples were weighed and dissolved in 5% ACN in ultrapurified H_2O (1 mg/mL) and 1 mL aliquots were prepared and lyophilized, yielding 1 mg lyophilized samples of each αCT11 formulation.

2.5.12 Cell-cultured scratch wound assays

Scratch wound assays were repeated as described in a prior publication.[2] Cells used in this experiment were human dermal fibroblasts (huDF; ATCC, PCS-201-012). Medium used for huDF was Dulbecco's Modified Eagle Medium – High Glucose (DMEM HG, 4.5 g/L Glucose) with 2% Normal Calf Serum (NCS; Thermo Fisher/Gibco, 16010-159, Lot 2490415) and 4% Fetal Bovine Serum (FBS; Thermo Fisher/Gibco, 26140-079). Cells were expanded and stored in liquid N_2 until plating on polypropylene culture dishes in culture medium (20 mL media per expansion). Cells were expanded to confluency, then

passaged into 12-well plates and allowed to adhere and grow prior to removing serum from media to eliminate proliferation. Lyophilized counterion-switched peptide samples (αCT11, αCT11-3OMe(D5,D6,E8), αCT11-4OMe) were solubilized in the vehicle control (DMSO in HEPES buffer) at 100 mM (100X). 10 μL of the 100X solution was then added to 1 mL of DMEM HG to dilute the concentration to ~ 100 μM (1X). When serum was removed, either the 1X peptide solutions or the vehicle control were administered to the cells. The scratch wound assay was performed 24 h after the treatment, using a 200 μL sterile pipette tip to scratch the surface of the well, then cells were rinsed 1X in Dulbecco's phosphate buffered saline (dPBS) and provided fresh culture (1 mL per well) medium post-treatment. Cells were then imaged along the length of each scratch, and images were analyzed to determine initial scratch areas. After 6 h, cultures were rinsed in 1X Dulbecco's PBS (dPBS), fixed in 2% paraformaldehyde, then rinsed 4 times in dPBS and stained in 1:20000 (v/v) Hoechst prior to imaging on a Leica SP8 laser scanning confocal microscope. The initial area ($Area_{x,0h}$) and final area after 6 h ($Area_{x,6h}$) and initial scratch areas were determined for a sample (x) using automated ImageJ Area Analysis software, then a "migration index" was calculated by dividing the difference between the initial area and the final area of the scratch by the initial area, with a smaller number indicating greater movement towards a final area of 0. Each migration index was reported relative to the average of that of the vehicle (v), creating a relative migration index (**Equation 2.3**). The calculated relative migration indexes from 10 images different of 3 different cell cultures for each tested formulation were then averaged. Standard error was calculated for each formulation by dividing the standard deviation of the average by the square root of the 3, as there were 3 separate experiments; however, these values were all less than

0.05, and were therefore unable to be displayed on the plot. Each formulation was statistically compared using a one-tailed paired 2 sample t-test assuming unequal variances.

Equation 2.3) Relative Migration Index = $\dfrac{\dfrac{Area_{x,\,0h} - Area_{x,6h}}{Area_{x,0h}}}{\dfrac{Area_{v,\,0h} - Area_{v,6h}}{Area_{v,0h}}}$

2.6 Acknowledgments

2.7 References

(1)   Grek, C. L.; Montgomery, J.; Sharma, M.; Ravi, A.; Rajkumar, J. S.; Moyer, K. E.; Gourdie, R. G.; Ghatnekar, G. S. A Multicenter Randomized Controlled Trial Evaluating a Cx43-Mimetic Peptide in Cutaneous Scarring HHS Public Access. *J Invest Dermatol* **2017**, *137* (3), 620–630. https://doi.org/10.1016/j.jid.

(2)   Montgomery, J.; Richardson, W. J.; Marsh, S.; Rhett, J. M.; Bustos, F.; Degen, K.; Ghatnekar, G. S.; Grek, C. L.; Jourdan, L. J.; Holmes, J. W.; Gourdie, R. G. The Connexin 43 Carboxyl Terminal Mimetic Peptide ACT1 Prompts Differentiation of a Collagen Scar Matrix in Humans Resembling Unwounded Skin. *FASEB Journal* **2021**, *35* (8). https://doi.org/10.1096/fj.202001881R.

(3)   Rhett, J. M.; Jourdan, J.; Gourdie, R. G. Connexin 43 Connexon to Gap Junction Transition Is Regulated by Zonula Occludens-1. *Mol Biol Cell* **2011**, *22* (9), 1516–1528. https://doi.org/10.1091/mbc.E10-06-0548.

(4)   Jiang, J.; Hoagland, D.; Palatinus, J. A.; He, H.; Iyyathurai, J.; Jourdan, L. J.; Bultynck, G.; Wang, Z.; Zhang, Z.; Schey, K.; Poelzing, S.; McGowan, F. X.; Gourdie, R. G. Interaction of α Carboxyl Terminus 1 Peptide With the Connexin 43 Carboxyl Terminus Preserves Left Ventricular Function After Ischemia-Reperfusion Injury. *J Am Heart Assoc* **2019**, *8* (16). https://doi.org/10.1161/JAHA.119.012385.

(5)   Huttunen, K. M.; Raunio, H.; Rautio, J. Prodrugs-from Serendipity to Rational Design. *Pharmacol Rev* **2011**, *63* (3), 750–771. https://doi.org/10.1124/pr.110.003459.

(6)   Lavis, L. D. Ester Bonds in Prodrugs. *ACS Chem Biol* **2008**, *3* (4), 203–206. https://doi.org/10.1021/cb800065s.

(7)   Chan, O. H.; Stewart, B. H. Physicochemical and Drug-Delivery Considerations for Oral Drug Bioavailability. *Drug Discov Today* **1996**, *1* (11), 461–473. https://doi.org/10.1016/1359-6446(96)10039-8.

(8)   Beaumont, K.; Webster, R.; Gardner, I.; Dack, K. Design of Ester Prodrugs to Enhance Oral Absorption of Poorly Permeable Compounds: Challenges to the Discovery Scientist. *Curr Drug Metab* **2005**, *4* (6), 461–485. https://doi.org/10.2174/1389200033489253.

(9)   Liederer, B. M.; Borchardt, R. T. Enzymes Involved in the Bioconversion of Ester-Based Prodrugs. *J Pharm Sci* **2006**, *95* (6), 1177–1195. https://doi.org/10.1002/JPS.20542.

(10)   Afrimzon, E.; Deutsch, A.; Shafran, Y.; Zurgil, N.; Sandbank, J.; Pappo, I.; Deutsch, M. Intracellular Esterase Activity in Living Cells May Distinguish between Metastatic and Tumor-Free Lymph Nodes. *Clin Exp Metastasis* **2008**, *25* (3), 213–224. https://doi.org/10.1007/S10585-007-9135-1/TABLES/6.

(11)   Lockridge, O.; Quinn, D. M. 4.14 - Esterases. In *Comprehensive Toxicology (Second Edition)*; McQueen, C. A., Ed.; Elsevier: Oxford, 2010; pp 243–273. https://doi.org/https://doi.org/10.1016/B978-0-08-046884-6.00414-0.

(12)   Larsen, E. M.; Johnson, R. J. Microbial Esterases and Ester Prodrugs: An Unlikely Marriage for Combatting Antibiotic Resistance. *Drug Dev Res* **2019**, *80* (1), 33. https://doi.org/10.1002/DDR.21468.

(13)   Bratosin, D.; Mitrofan, L.; Palii, C.; Estaquier, J.; Montreuil, J. Novel Fluorescence Assay Using Calcein-AM for the Determination of Human Erythrocyte Viability and Aging. *Cytometry Part A* **2005**, *66A* (1), 78–84. https://doi.org/10.1002/CYTO.A.20152.

(14)   Burnouf, P. A.; Leu, Y. L.; Su, Y. C.; Wu, K.; Lin, W. C.; Roffler, S. R. Reversible Glycosidic Switch for Secure Delivery of Molecular Nanocargos. *Nat Commun* **2018**, *9* (1), 1–13. https://doi.org/10.1038/s41467-018-04225-5.

(15)   Gray, W. D.; Mitchell, A. J.; Searles, C. D. An Accurate, Precise Method for General Labeling of Extracellular Vesicles. *MethodsX* **2015**, *2*, 360–367. https://doi.org/10.1016/j.mex.2015.08.002.

(16)   Mix, K. A.; Lomax, J. E.; Raines, R. T. Cytosolic Delivery of Proteins by Bioreversible Esterification. *J Am Chem Soc* **2017**, *139* (41), 14396–14398. https://doi.org/10.1021/jacs.7b06597.

(17)   Prokai-Tatrai, K.; Nguyen, V.; Zharikova, A. D.; Braddy, A. C.; Stevens, S. M.; Prokai, L. Prodrugs to Enhance Central Nervous System Effects of the TRH-like Peptide PGlu-

Glu-Pro-NH2. *Bioorg Med Chem Lett* **2003**, *13* (6), 1011–1014.
https://doi.org/10.1016/S0960-894X(03)00081-7.

(18)   Koos, M. R. M.; Kummerlöwe, G.; Kaltschnee, L.; Thiele, C. M.; Luy, B. CLIP-COSY: A
       Clean In-Phase Experiment for the Rapid Acquisition of COSY-Type Correlations.
       Angew Chem Int Ed Engl **2016**, *55* (27), 7655–7659.
       https://doi.org/10.1002/anie.201510938.

(19)   Hwang, T. L.; Shaka, A. J. Water Suppression That Works. Excitation Sculpting Using
       Arbitrary Wave-Forms and Pulsed-Field Gradients. *J Magn Reson A* **1995**, *112* (2),
       275–279. https://doi.org/https://doi.org/10.1006/jmra.1995.1047.

(20)   Wagner, R.; Berger, S. Gradient-Selected NOESY-A Fourfold Reduction of the
       Measurement Time for the Noesy Experiment. *J Magn Reson A* **1996**, *123* (1), 119–
       121. https://doi.org/10.1006/jmra.1996.0222.

(21)   Willker, W.; Leibfritz, D.; Kerssebaum, R.; Bermel, W. Gradient Selection in Inverse
       Heteronuclear Correlation Spectroscopy. *Magnetic Resonance in Chemistry* **1993**, *31*
       (3), 287–292. https://doi.org/https://doi.org/10.1002/mrc.1260310315.

(22)   Claridge, T. D. W.; Pérez-Victoria, I. Enhanced 13C Resolution in Semi-Selective
       HMBC: A Band-Selective{,} Constant-Time HMBC for Complex Organic Structure
       Elucidation by NMR. *Org. Biomol. Chem.* **2003**, *1* (21), 3632–3634.
       https://doi.org/10.1039/B307122G.

(23)   Jun, J. V.; Petri, Y. D.; Erickson, L. W.; Raines, R. T. Modular Diazo Compound for the
       Bioreversible Late-Stage Modification of Proteins. *J Am Chem Soc* **2023**, *145* (12),
       6615–6621. https://doi.org/10.1021/jacs.2c11325.

(24)   Tian, L.; Yang, Y.; Wysocki, L. M.; Arnold, A. C.; Hu, A.; Ravichandran, B.; Sternson, S.
       M.; Looger, L. L.; Lavis, L. D. Selective Esterase-Ester Pair for Targeting Small
       Molecules with Cellular Specificity. *Proc Natl Acad Sci U S A* **2012**, *109* (13), 4756–
       4761. https://doi.org/10.1073/PNAS.1111943109/-/DCSUPPLEMENTAL.

(25)   Zhou, Q.; Xiao, Q.; Zhang, Y.; Wang, X.; Xiao, Y.; Shi, D. Pig Liver Esterases PLE1 and
       PLE6: Heterologous Expression, Hydrolysis of Common Antibiotics and
       Pharmacological Consequences. *Sci Rep* **2019**, *9* (1), 1–12.
       https://doi.org/10.1038/s41598-019-51580-4.

(26)   Zhu, Y.; Shmidov, Y.; Harris, E. A.; Theus, M. H.; Bitton, R.; Matson, J. B. Activating
       Hidden Signals by Mimicking Cryptic Sites in a Synthetic Extracellular Matrix. *Nat
       Commun* **2023**, *14* (1). https://doi.org/10.1038/s41467-023-39349-w.

(27)   Neumann, K.; Farnung, J.; Baldauf, S.; Bode, J. W. Prevention of Aspartimide
       Formation during Peptide Synthesis Using Cyanosulfurylides as Carboxylic Acid-
       Protecting Groups. *Nat Commun* **2020**, *11* (1). https://doi.org/10.1038/s41467-020-
       14755-6.

(28) Richardson, W. J.; Kegerreis, B.; Thomopoulos, S.; Holmes, J. W. Potential Strain-Dependent Mechanisms Defining Matrix Alignment in Healing Tendons. *Biomech Model Mechanobiol* **2018**, *17* (6), 1569–1580. https://doi.org/10.1007/s10237-018-1044-5.

(29) Xue, M.; Jackson, C. J. Extracellular Matrix Reorganization During Wound Healing and Its Impact on Abnormal Scarring. *Adv Wound Care (New Rochelle)* **2015**, *4* (3), 119–136. https://doi.org/10.1089/wound.2013.0485.

(30) Rouillard, A. D.; Holmes, J. W. Mechanical Regulation of Fibroblast Migration and Collagen Remodelling in Healing Myocardial Infarcts. *Journal of Physiology* **2012**, *590* (18), 4585–4602. https://doi.org/10.1113/jphysiol.2012.229484.

(31) McDougall, S.; Dallon, J.; Sherratt, J.; Maini, P. Fibroblast Migration and Collagen Deposition during Dermal Wound Healing: Mathematical Modelling and Clinical Implications. In *Philosophical Transactions of the Royal Society A: Mathematical, Physical and Engineering Sciences*; Royal Society, 2006; Vol. 364, pp 1385–1405. https://doi.org/10.1098/rsta.2006.1773.

(32) Karppinen, S. M.; Heljasvaara, R.; Gullberg, D.; Tasanen, K.; Pihlajaniemi, T. Toward Understanding Scarless Skin Wound Healing and Pathological Scarring. *F1000Research*. F1000 Research Ltd 2019. https://doi.org/10.12688/f1000research.18293.1.

(33) Derossi, D.; Joliot, A. H.; Chassaing, G.; Prochiantz, A. The Third Helix of the Antennapedia Homeodomain Translocates through Biological Membranes. *Journal of Biological Chemistry* **1994**, *269* (14), 10444–10450. https://doi.org/10.1016/s0021-9258(17)34080-2.

(34) Cornish, J.; Callon, K. E.; Lin, C. Q. X.; Xiao, C. L.; Mulvey, T. B.; Cooper, G. J. S.; Reid, I. R. Trifluoroacetate, a Contaminant in Purified Proteins, Inhibits Proliferation of Osteoblasts and Chondrocytes. *Am J Physiol Endocrinol Metab* **1999**, *277* (5 40-5), 779–783. https://doi.org/10.1152/ajpendo.1999.277.5.e779.

(35) Tipps, M. E.; Iyer, S. V.; John Mihic, S. Trifluoroacetate Is an Allosteric Modulator with Selective Actions at the Glycine Receptor. *Neuropharmacology* **2012**, *63* (3), 368–373. https://doi.org/10.1016/j.neuropharm.2012.04.011.

(36) Dougherty, P. G.; Sahni, A.; Pei, D. Understanding Cell Penetration of Cyclic Peptides. *Chem Rev* **2019**, *119* (17), 10241–10287. https://doi.org/10.1021/acs.chemrev.9b00008.

(37) Rand, A. C.; Leung, S. S. F.; Eng, H.; Rotter, C. J.; Sharma, R.; Kalgutkar, A. S.; Zhang, Y.; Varma, M. V.; Farley, K. A.; Khunte, B.; Limberakis, C.; Price, D. A.; Liras, S.; Mathiowetz, A. M.; Jacobson, M. P.; Lokey, R. S. Optimizing PK Properties of Cyclic Peptides: The Effect of Side Chain Substitutions on Permeability and Clearance. *Medchemcomm* **2012**, *3* (10), 1282–1289. https://doi.org/10.1039/c2md20203d.

(38) Fotakopoulou, I.; Barbayianni, E.; Constantinou-Kokotou, V.; Bornscheuer, U. T.; Kokotos, G. Enzymatic Removal of Carboxyl Protecting Groups. III. Fast Removal of Allyl and Chloroethyl Esters by Bacillus Subtilis Esterase (BS2). *Journal of Organic Chemistry* **2007**, *72* (3), 782–786. https://doi.org/10.1021/JO061871F/SUPPL_FILE/JO061871FSI20061122_092406.PDF.

CHAPTER 3:
ESTERIFICATION TO ENABLE REVERSIBLE ENCAPSULATION OF THERAPEUTIC PEPTIDES INTO POLYECTROLYTE COMPLEXES

3.1 Introduction

Therapeutic peptides combine the advantages offered by small molecules and biologics, making them a unique class of therapeutics. However, their susceptibility to proteolytic degradation and renal filtration leads to rapid clearance, resulting in short *in vivo* half-lives and hampering their clinical implementation.[1–4] For example, the wound healing and cardioprotective peptide α carboxyl terminus 11 (αCT11, RPRPDDLEI)[5,6] has a *in vivo* half-life of only 10 minutes in rat blood plasma.[7] To realize the therapeutic potential of peptides, we must develop methods to protect them from proteolysis and renal filtration to extend their *in vivo* half-lives.

One method to increase the *in-vivo* half-lives of therapeutics is to encapsulate them into polyelectrolyte complexes (PECs), complexes formed by non-covalent interactions between two oppositely charged electrolyte chains in aqueous solution.[8–10] While most commonly used to encapsulate anionic DNA or RNA for gene delivery,[11–14] multiple studies have developed polyelectrolyte complexes to encapsulate proteins[15–19] or antimicrobial peptides,[20–22] a specific class of therapeutic peptides used to treat bacterial infections. As antimicrobial peptides commonly contain a high net cationic charge to interact and disrupt anionic membranes,[23] they are particularly amenable to encapsulation in PECs; however, this is specific to antimicrobial peptides, as general therapeutic peptides can contain multiple anionic and cationic charges. For example, the therapeutic peptide α carboxyl terminus 11 (αCT11, RPRPDDLEI) contains 3 cationic charges (N-terminus, R1, R3) and 4 anionic COOHs (D5, D6, E8, C-terminus) at

physiological pH, which could cause charge repulsion with either anionic or cationic charged polymers and prevent its encapsulation into PECs. As prior studies have established that assembly between mixed charge proteins and charged polymers only occur above a protein net charge ratio threshold,[17,19,24] which varies from protein to protein, methods to modify the net charge of therapeutic peptides, such as αCT11, could enable their encapsulation into PECs.

There exist a few different methods to modify the net charge of amino-acid based therapeutics (i.e., peptides and proteins) to enable PEC formation. For example, Obermeyer *et al.* "supercharged" therapeutic proteins, where succinic anhydride was reacted with the cationic amines of lysines in the protein sequence, converting their charge to from positive to negative.[17] Alternatively, adding highly anionic peptide tags to GFP increased its negative charge to enable complexation with cationic polymers.[19] While both of these strategies are effective towards modifying the net charge of therapeutic peptides above the necessary charge ratio threshold to complex with an oppositely charged polymer, they both induced permanent changes in amino acid structure, which could induce undesired loss of biological function. For example, supercharging GFP caused a loss of protein fluorescence.[19] Additionally, the increased binding strength caused by modifications to therapeutic charge could hamper release. Therefore, we require methods to temporarily modify the net charge of therapeutic peptides to enable reversible PEC formation without sacrificing therapeutic activity or subsequent release.

To temporarily increase the net cationic charge of therapeutic peptides, we can esterify them, converting anionic carboxylic acids to ester groups and enabling PEC formation between now-cationic esterified peptides and anionic polymers. Further, ester

hydrolysis would not only return the native, active sequence, but also reveal anionic carboxylic acids and enable the release of the therapeutic in question through charge repulsion between the peptide and polymer. In this study, we esterify the therapeutic peptide αCT11 to reversibly increase its cationic charge and enable PEC formation with poly(methacrylic acid) (pMAA), an anionic polymer. Specifically, we track PEC formation and stability in aqueous solution over time. Additionally, we determine the effect of buffer concentration and solution pH on PEC formation. Finally, we correlate observed ester hydrolysis with PEC solution turbidity while simultaneously assessing how the presence of anionic polymers affects the hydrolysis of esters installed onto αCT11.

3.2 Results & Discussion

3.2.1 *Esterifying αCT11 enables complexation with anionic PMAA*

We first sought to determine if replacing the 4 anionic carboxylic acids on the wound healing peptide αCT11 with neutral ester groups would enable interactions with anionic poly(methacrylic acid) (PMAA) polymer (2.3 kDa, 23 repeat units, **Figure B.1**) to form PECs. αCT11-4OMe was prepared as described in Chapter 2, incubating αCT11 in excess methanol (5000:1 mol MeOH: mol αCT11) containing 5% v/v HCl for 24 h, followed by isolation using preparative scale RP-HPLC (**Scheme 3.1**). We note that we increased the MeOH:αCT11 ratio from 1600:1 to 5000:1 and increased the temperature from room temperature to 40 °C to increase our yield of αCT11-4OMe from 77% (Figure 2.1, Table A.2) to >95% (Figure B.2) after 24 h.

To determine the effect of esterification on PEC formation, we mixed PMAA with either esterified αCT11-4OMe (PMAA/4OMe) or unesterified αCT11 (**Figure B.3, Table B.2**) (PMAA/αCT11) in aqueous solution and used turbidimetry to assess the presence of supramolecular structures large enough to scatter light. As we were also interested in the

stability of any formed supramolecular structures over time, we performed these measurements over 22 h. We opted to combine PMAA with peptide at a 1:1 charge ratio (negative PMAA charges:positive αCT11 charges) to ensure every charge on either the peptide on the polymer was matched with an opposite charge on the other material with which to complex. We performed these studies in phosphate buffer (pH 7.4), where the αCT11 N-terminus and R1/R2 guanidinium groups should be protonated and the PMAA COOHs should be deprotonated to allow for electrostatic interactions to occur. To find a suitable concentration to conduct our experiments, we measured the turbidimetry of mixtures containing 0.25, 0.50, 1.00, and 1.50 mg PMAA/mL and the corresponding amount of either esterified or unesterified αCT11 over 22 h. For each concentration of PMAA, we varied buffer concentration to ensure 2x the amount of buffer necessary to control pH based on the concentration of charged groups on the polymer and peptide. For all concentrations tested, we were encouraged to see that PMAA/4OMe had increased turbidity relative PMAA/αCT11; however, the turbidity curves of PMAA/4OMe mixtures at 1.50 and 1.00 mg PMAA/mL (**Figure B.4a-b**) were also dynamic, featuring decreases and increases in turbidity at various times that were not as pronounced at the lower concentrations (0.50 and 0.25 mg PMAA/mL, **Figure B.4c-d**). Therefore, to gauge the statistical significance of the difference between the turbidity vs. time data collected for PMAA/4OMe and PMAA/αCT11, we repeated the experiments at 1 mg PMAA/mL solution in triplicate, a concentration at which we were able to conserve peptide without sacrificing resolution in turbidity.

After repeating our 1 mg PMAA/mL experiments in triplicate with independently prepared solutions over 22 h, we observed that PMAA/4OMe turbidity was significantly

higher than PMAA/αCT11 turbidity over the first 19 h in solution using a one-tailed t-test assuming unequal variances. As control solutions of αCT11-4OMe, unesterified αCT11, and PMAA alone all produced negligible turbidity relative to PMAA/4OMe, this suggested that esterifying αCT11 was indeed necessary to induce the formation of supramolecular structures, and that αCT11-4OMe was indeed being encapsulated within PMAA-based PECs (**Figure 3.1**). While there were slight differences between PMAA/αCT11, αCT11-4OMe, and PMAA, they were all less than 0.02 absorbance units, which we considered to be within error of the instrument, and, thus, we did not make conclusions from these differences. Interestingly, there was a relatively high amount of variation between the 3 separate PMAA/4OMe mixtures, with their maximum absorbances ranging from 0.08 to 0.17. This variation was reasonable, as minor changes in either PMAA or αCT11-4OMe concentration, solution pH, buffer concentration, etc. could lead to differences in complexation and subsequent turbidity. Yet, despite this variation, the dynamic features observed in the PMAA/4OMe turbidity curves were quite reproducible, as the 3 replicate mixtures tested all reached a maximum turbidity between 4.5 and 6 h, followed by a gradual decrease until the final measured timepoint (Figure 3.1).

We were particularly interested in the observed decrease in turbidity observed over the latter 16 h, which suggested that the size and/or number of complexes in solution was decreasing and, specifically, that the complexes were dissociating. To this end, there was no statistically significant difference in PMAA/4OMe and PMAA/αCT11 turbidity after 19 h in aqueous solution, which supported the idea that PMAA/4OMe supramolecular structures were indeed dissociating. While the decrease in turbidity from 6 to 22 h is indicative of what we would expect upon dissociation, we would expect the turbidity of

PMAA/4OMe and PMAA/αCT11 to overlap upon full dissociation of the PMAA/4OMe complexes. Yet, the individual PMAA/4OMe mixtures had differences of 0.02, 0.08, and 0.09 absorbance units relative to PMAA/αCT11 at 20 h after mixing (Figure 3.1). Therefore, as the gradual decrease in turbidimetry over the latter 16 h of the experiment is indicative of dissociation, it is more likely that we are not capturing the full timescale of PEC dissociation in 22 h, and this result was more reflective of the relatively high variance of PMAA/4OMe mixtures.
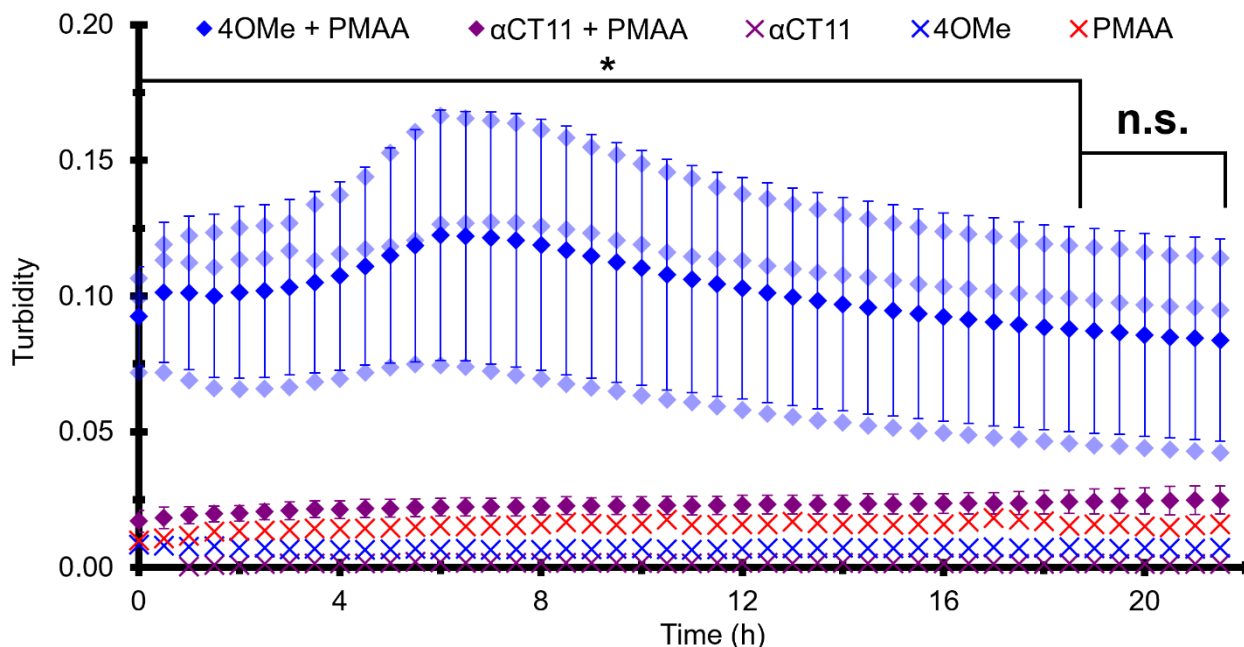
Figure 3.1. Effect of αCT11 esterification on PEC formation over time. **a)** Turbidity of mixtures of αCT11-4OMe (blue, diamonds) and αCT11 (purple, diamonds) with PMAA over ~21 h (n = 3). For mixtures of αCT11-4OMe and PMAA, the 3 individual turbidimetry plots are also shown under the plotted averages (transparent blue diamonds). Control solutions of only αCT11 (purple, x), αCT11-4OMe (blue, x), and PMAA (red, x) are also shown. Error bars represent the standard deviation between 3 separately synthesized samples, with * indicating a one-tailed two sample t-test assuming unequal variances giving p < 0.05 and while "n.s." representing no statistical significance. Turbidity data were collected by Aditi S. Gourishankar.

3.2.2 *Complexation between PMAA and αCT11-4OMe is electrostatically driven*

After determining that esterifying αCT11 enabled the formation of light scattering supramolecular structures with PMAA, we sought to determine the driving force behind complexation. While observing an increase in turbidity upon replacing the anionic carboxylic ester groups suggested that complexation was driven by noncovalent electrostatic interactions between positive charges on αCT11-4OMe and negative charges on PMAA, it was also possible that the increased hydrophobicity of αCT11-4OMe relative to αCT11 was enabling non-covalent hydrophobic interactions to drive complexation. Since increasing salt concentration screens electrostatics interactions, we expected that increasing salt complexation would prevent any electrostatic interactions to form between anionic PMAA carboxylic acids and cationic αCT11 N-termini/R1 or R2 guanidiniums, and, if complexation was indeed electrostatically driven, result in decreased solution turbidity.[25,26] Therefore, we sought to vary the concentration of buffer salt within our PMAA/4OMe mixtures.

To test if PMAA/4OMe complexation was electrostatically driven, we doubled the phosphate buffer concentration from 38 mM to 77 mM. Upon doing so, we immediately observed a loss in turbidity relative to mixtures in the 38 mM buffer (**Figure 3.2**). While there was still a slight difference in PMAA/4OMe and PMAA/αCT11 turbidity in 52 mM buffer, they were much less pronounced than those seen in 38 mM buffer. Additionally, the PMAA/4OMe turbidity curves were no longer dynamic, staying relatively constant around 0.04 absorbance units over the 22 h tested. Taken together, these results suggested that doubling the buffer concentration prevented interactions between αCT11-4OMe and PMAA, and esterifying αCT11 indeed facilitated electrostatically-driven PEC formation with PMAA in 38 mM buffer.
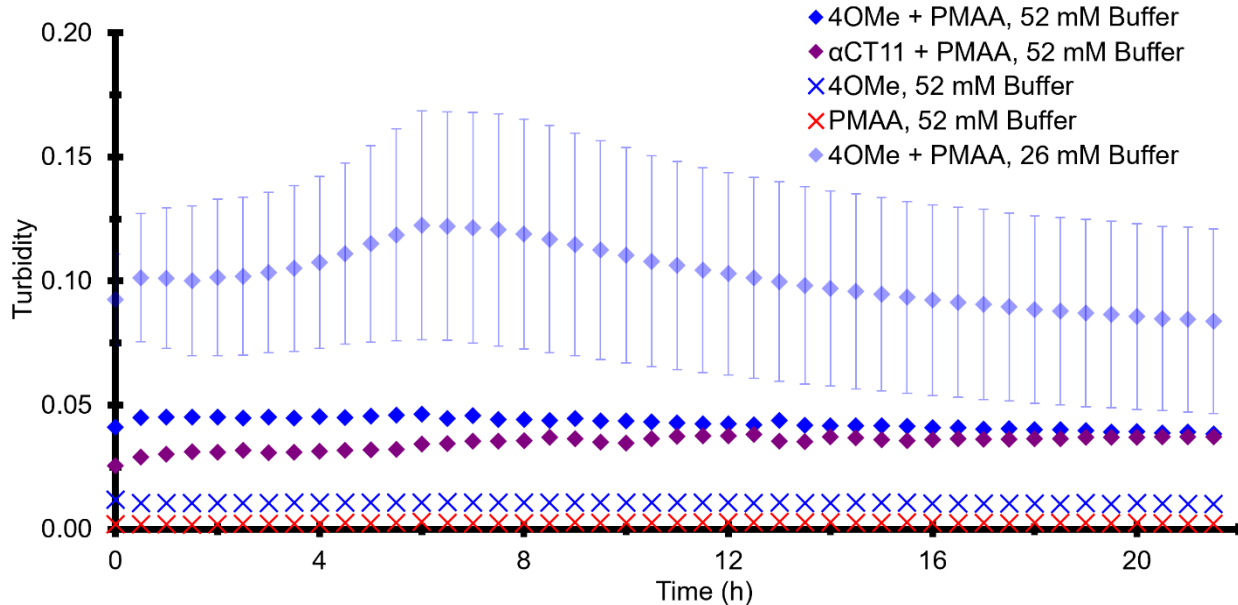
Figure 3.2. Increasing buffer concentration prevents electrostatic interactions between esterified αCT11-4OMe and PMAA. **a)** A mixture of αCT11-4OMe and PMAA in 52 mM phosphate buffer (blue, diamonds) is significantly less turbid than the same mixture in 38 mM phosphate buffer (pH 7.4), suggesting that the formation of supramolecular structures was prevented by increased salt concentration and, therefore, interactions between PMAA and αCT11-4OMe are electrostatic in nature. Turbidity of solutions of only αCT11-4OMe (blue, x), and PMAA (red, x) are also shown at the same buffer concentration. Turbidity data were collected by Aditi S. Gourishankar.

3.2.3 Controlling the pH of PEC solutions without sacrificing complexation

After determining that PMAA/αCT11-4OMe PEC formation was driven by electrostatic interactions, we sought to more closely control the pH of the solution. As the solution pH controls the protonation state of the negatively charged PMAA carboxylic acids and positively charged αCT11 R1/R2/N-terminus we required solution pH to be constant for each formulation (i.e., PMAA/αCT11-4OMe, PMAA/αCT11, αCT11-4OMe) over the entire 22 h tested. Further, the rate of αCT11-4OMe ester hydrolysis is highly dependent on solution pH, leading us to require a constant pH to determine the effect of PMAA on ester hydrolysis. Therefore, we measured the pH of PMAA/4OMe, PMAA/αCT11, and αCT11-4OMe solutions over time.

We first measured the pH of each solution prepared in 38 mM phosphate buffer, as presented in Figure 3.1. We found that while 38 mM phosphate buffer was able to control the pH within an individual formulation over time, it was not able to keep the pH constant between groups, as the pHs of PMAA/4OMe, PMAA/αCT11, and αCT11-4OMe were held at 6.9, 6.5, and between 7.1-7.3 over the 22 h measured (**Figure 3.3a**). While the αCT11-4OMe solution, which did not have any negatively charged groups initially, matched the buffer pH, the dissolution of solutes with negatively charged carboxylic acids (i.e., PMAA, unesterified αCT11) decreased the solution pH. The range of pHs observed in all the tested samples still fell above the pKa of the PMAA carboxylic acids (~4.8) and below the pKa of the αCT11 R1/R2 guandiniums (~13.8) and/or N-termini (~10.2) (**Figure 3.3d**), the different pHs could have a slight effect on the protonation states between groups, meaning that the actual charge of each solute in solution would not be held constant.
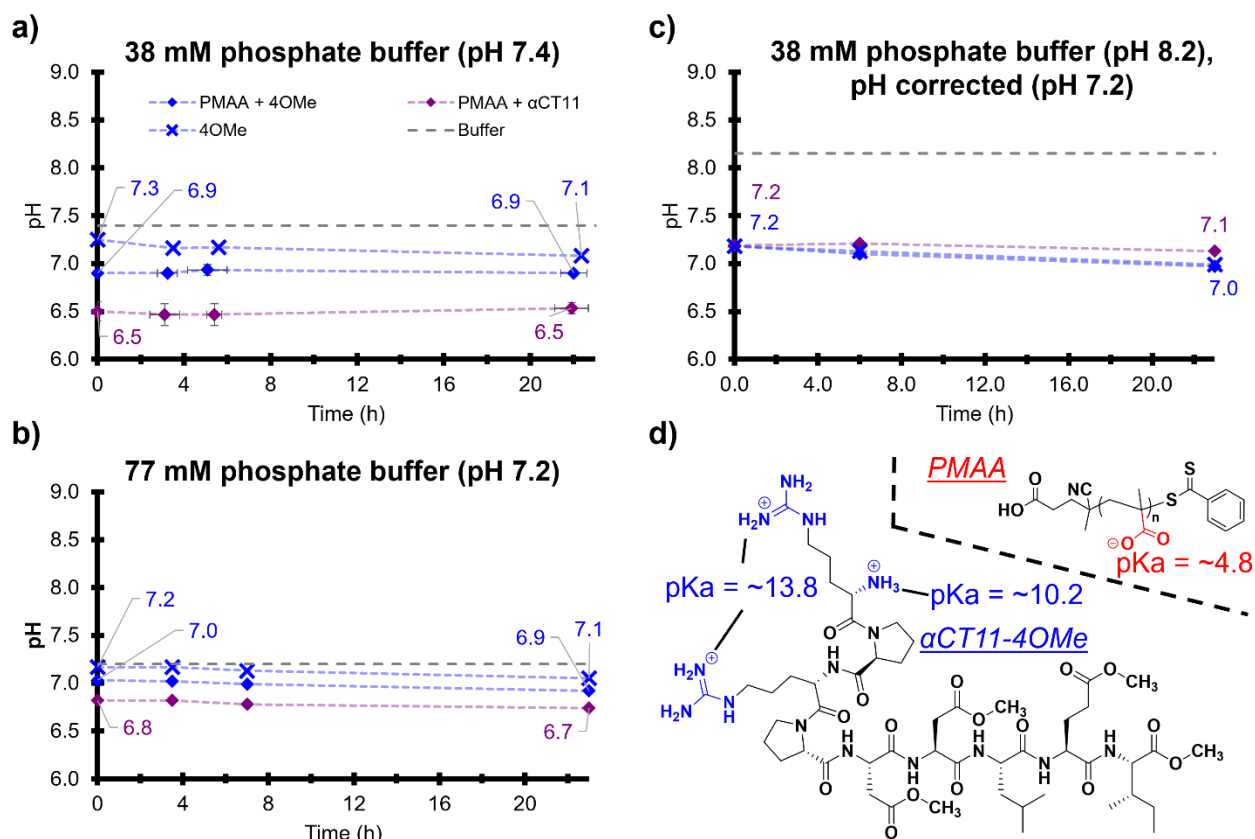
Figure 3.3. Controlling the pH of PEC solutions. pH of solutions containing PMAA and αCT11-4OMe mixtures (blue, diamonds), PMAA and αCT11 mixtures (purple, diamonds), and αCT11-4OMe alone (blue, xs) in **a)** 38 mM phosphate buffer (pH 7.4), **b)** 77 mM phosphate buffer (pH 7.2), and **c)** 38 mM phosphate buffer (pH 8.2), corrected to pH 7.2 immediately after adding peptide. While both 38 and 77 mM phosphate buffer was able to control pH over time, only pH correction was able to hold all different samples at the same pH over 22 h. Error bars in (a) represent the standard deviation between 3 independently prepared samples. **d)** Structures of αCT11-4OMe and PMAA, with estimated pKas of the protonatable groups shown. pKas were determined using Chemdraw. pH data were collected by Aditi S. Gourishankar.

As 38 mM buffer was not able to hold pH constant between the different formulations, we decided to double the phosphate buffer concentration from 38 to 77 mM. We note that while we were not able to detect PEC formation by turbidimetry at this higher buffer concentration (Figure 3.2), we still sought to determine if the 38 mM buffer was not concentrated enough to do so, or if we just needed to adjust pH immediately after dissolution. Like the 38 mM phosphate buffer, 77 mM phosphate buffer controlled pH within an individual formulation over time, as the pHs of each individual solution fell within 0.1 of the initial pH over the 22 h tested (**Figure 3.3b**). While the increased buffer

concentration was able to narrow the ranges of pH seen between the different groups, where the PMAA/4OMe, PMAA/αCT11, and αCT11-4OMe solutions had pHs of 7.1 – 7.2, 6.9 – 7.0, and 6.7 – 6.8, respectively, it was still not able to keep the pH constant between groups. As we could not detect PEC formation or control the pH of different solutions in 77 mM buffer, we decided to instead reattempt to control pH in 38 mM buffer, in which we could detect PEC formation using turbidimetry.

As we saw a significant drop in solution pH only upon the addition of solutes with negatively charged carboxylic acids (i.e., PMAA, unesterified αCT11) in 38 mM pH buffer, yet this buffer concentration was sufficient to control the pH of the solutions/mixtures over time, we sought to raise the pH of the 38 mM buffer to counteract this initial pH drop and maintain a physiological pH (pH 7.0 – 7.4) in the PMAA/4OMe sample without adding more salt, which was shown to prevent PEC formation. Then, we could use small amounts of acid and base to further correct the pH of the PMAA/αCT11, αCT11-4OMe, αCT11, and PMAA controls, whose turbidity was not dependent on salt concentration, to match the pH of the PMAA/4OMe solution. By preparing the phosphate buffer at pH 8.2 and using this method, the PMAA/4OMe, PMAA/αCT11 and αCT11-4OMe solutions were all held between pH 7.2 and 7.0 for 22 h, and allowed us to observe the expected increase in turbidity of mixtures of PMAA and αCT11-4OMe relative to those with unesterified αCT11, as well as the dynamic features of the PMAA/αCT11-4OMe turbidity curves discussed in 3.1.1 (**Figure 3.4a**). Further, the decrease in turbidity over the latter timepoints resulted in PMAA/4OMe and PMAA/αCT11 samples almost overlapping after 22 h, only differing by 0.1 absorbance units, which suggested even more dissociation of

PECs. As we were now able to hold pH constant, we next sought to study αCT11-4OMe ester hydrolysis in the presence of PMAA.

3.2.4 Hydrolytic conversion of αCT11 esters to carboxylic acids decreases turbidity of PEC solutions

As methyl esters installed onto αCT11-4OMe can be hydrolytically reverted to anionic carboxylic acids and cause charge repulsion-facilitated PMAA/4OMe PEC dissociation, we hypothesized that the observed decrease in PMAA/4OMe turbidity after 6 h was due to this phenomenon. To correlate ester hydrolysis with observed trends in turbidity, we used RP-HPLC to measure ester hydrolysis at the same timescale that we were measuring turbidimetry (**Figure 3.4b**). Specifically, we tracked the % αCT11-4OMe (Equation 3.1) present in RP-HPLC chromatograms of PMAA/4OMe mixtures prepared in pH-corrected 38 mM phosphate buffer at different timepoints over the 22 h measured (**Figure 3.4c**), and then compared it to the turbidity of the PMAA/4OMe solutions at that same timepoint. After only 1.5 h, we saw a 12% and 26% decrease in % αCT11-4OMe and turbidity in the PMAA/4OMe solution, respectively, initially suggesting ester hydrolysis and turbidity to be directly related. However, despite observing an additional 24% decrease in % αCT11-4OMe in the PMAA/4OMe solution between 1.5 and 5 h after mixing, we instead observed a 26% increase in turbidity. While these early trends caused changes in turbidity to seem unrelated to ester hydrolysis, we then observed a simultaneous 41% and 79% decrease in % αCT11-4OMe and turbidity in the PMAA/4OMe solution, respectively, between 5 and 22 h. While we could not develop any direct trends between PMAA/4OMe turbidity and % αCT11-4OMe from these data, we hypothesized that there was still a relationship between turbidity and ester hydrolysis that we were not capturing through only monitoring the % αCT11-4OMe over time.
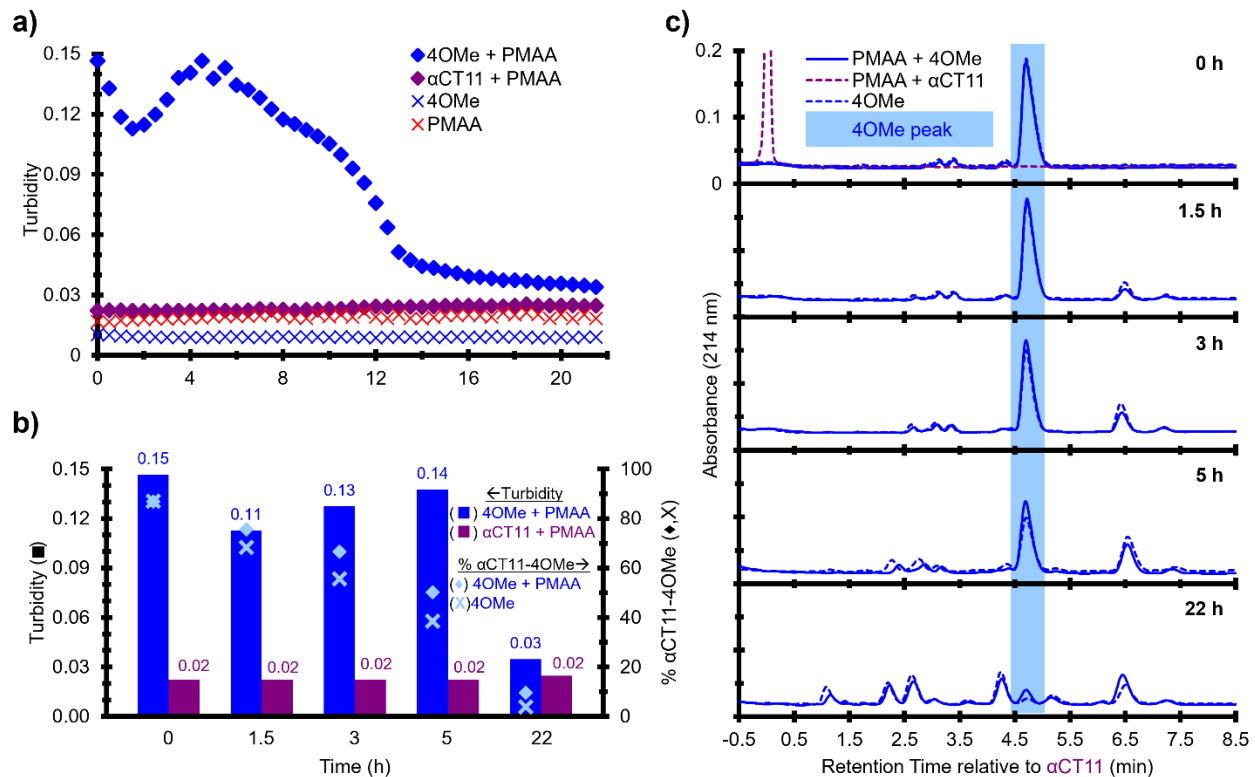
Figure 3.4. Hydrolysis of αCT11-4OMe drives decreases in turbidity of mixtures with PMAA. **a)** Turbidity of αCT11-4OMe and PMAA mixtures (blue, diamonds), αCT11 and PMAA mixtures (purple, diamonds), αCT11-4OMe alone (blue, xs), and PMAA alone (red, xs) in 38 mM phosphate buffer (pH 8.2), where all samples were corrected to pH 7.2 immediately after addition of the peptide. **b)** Turbidity (bars) and αCT11-4OMe peak area % (light blue diamonds, xs) of various timepoints depicted in (a) and (c), respectively. Turbidity of PMAA and αCT11-4OMe (blue bars) mixture is higher than those of PMAA and αCT11 (purple bars) until 22 h. αCT11-4OMe peak area decreases over time in the presence and absence of PMAA but decreases slightly faster in the absence of PMAA. **c)** RP-HPLC chromatograms depicting αCT11 peptide in the mixture of PMAA and αCT11-4OMe (blue, solid line) mixture of PMAA and unesterified α (purple, dashed line), and αCt11-4OMe solutions alone (blue, dashed line) shown in (a). Retention time was adjusted relative to that of αCT11 alone at each timepoint. The αCT11-4OMe peak over various timepoints is highlighted (light blue). Turbidity and hydrolysis data was collected by Aditi S. Gourishankar.

As the correlation between PMAA and αCT11-4OMe mixture turbidity and ester hydrolysis was unclear from only looking at αCT11-4OMe peak area % over time, we instead sought to analyze the esterified αCT11 species produced by hydrolysis (**Figure 3.4c**). As we had previously used LC-MS to perform a detailed analysis of αCT11-4OMe ester hydrolysis in 1X PBS (pH 7.4) (Figure 2.4), we compared these data to the chromatograms depicting αCT11-4OMe ester hydrolysis in PMAA/4OMe mixtures. While ~35x higher αCT11-4OMe concentrations (i.e., lower water:peptide ratios) in the

PMAA/4OMe solutions relative to those tested in Figure 2.4 caused a significantly slower hydrolysis rate, we still assumed that ester hydrolysis would persist in a similar fashion, with different hydrolysis products appearing in the same order, and continued our comparison.

We first chose to focus on the first 5 h of mixing, where we observed a temporary decrease in turbidity followed by an increase. Our prior experiments established that αCT11-4OMe ester hydrolysis and reversion to carboxylic acids was sometimes preceded by the temporary formation of intramolecular imides (likely involving the aspartic acids D5 and D6), which had higher retention times than esterified products. To this end, despite the 37% decrease in % αCT11-4OMe observed in the PMAA/4OMe solutions 5 h after mixing, we only observed the production of one new peak (retention time relative to αCT11 = 6.5) that we reasoned to be contain one or more imides due to its higher retention time than αCT11-4OMe (retention time relative to αCT11 = 4.7). As we did not observe the production of any other peaks with lower retention times than αCT11-4OMe over the first 5 h, we presumed that little to no carboxylic acids were being produced in this timescale, and the decreases and increases observed over the first 5 h was likely an effect of varying PEC rate of formation and size over this initial timescale, and not charge repulsion-facilitated PEC dissociation.

After establishing that little-to-no esters were hydrolyzed to carboxylic acids over the first 5 h, we turned our comparison to the latter 17 h, where we observed a permanent decrease in PMAA/4OMe turbidity. After 22 h, 57% of the total peak area corresponded to peaks with a lower retention time than αCT11-4OMe, suggesting that, at this point, the majority of the esterified peptide now contained negatively charged carboxylic acids

capable of dissociating PECs (Figure 3.4c). As the 79% decrease in PMAA/4OMe turbidity occurred over the same timescale, the appearance of products with lower retention times than αCT11-4OMe, which likely had anionic carboxylic acids, seemed to cause to a decrease in turbidity, and suggests the dissociation of PMAA/αCT11-4OMe PECs.

As we were also interested in the ability of PEC formation to shield αCT11 from external stimuli, we compared the % αCT11-4OMe in each chromatogram over time in the presence and absence of PMAA. At each measured timepoint after 0 h, PMAA/4OMe mixtures had a slightly higher % αCT11-4OMe than the solutions of αCT11-4OMe alone (Figure 3.4c). While these results will have to be repeated to determine the robustness of these slight differences, these data suggests that PMAA may slow the rate of ester hydrolysis from αCT11-4OMe. This result is particularly exciting, as it suggests that encapsulation of αCT11-4OMe into PMAA-based PECs limits the ability of external molecules to access the peptide, and, therefore, that PECs could provide protection from proteolytic degradation *in vivo*.

3.3 Conclusions

The studies disclosed within this chapter demonstrate esterification as a viable strategy to make mixed charge therapeutic peptides amenable to reversible interactions with anionic polymers to form PECs. PEC formation not only serves as a method to encapsulate peptides, but the dynamic turbidity profiles of mixtures of PMAA and αCT11-4OMe suggest the PECs formed to be reversible, providing an opportunity to release the peptide. Further, as PEC formation was shown to be electrostatically-driven, we look forward to varying the ratio of positively charged αCT11-4OMe to negatively charged PMAA to vary important variable such as binding strength, PEC size and shape, and

release. As the reversion of αCT11-4OMe esters to carboxylic acids led to a gradual, permanent decrease in PMAA/4OMe turbidity, we expect that controlling the hydrolysis of esters installed onto αCT11 could tune the release of peptides from PECs. As we showed in Chapter 2, both the number and, more importantly, the position of esters installed onto αCT11 significantly affects hydrolysis, and should serve as important parameters to control hydrolytically-dependent αCT11 release from PECs. Excitingly, the presence of PMAA slowed the hydrolysis rate of αCT11-4OMe, suggesting that external water molecules were not able to access αCT11-4OMe esters as easily upon formation of PECs. As the motivation of this work was rooted in increasing the *in vivo* half-life of therapeutic peptides, this result bodes well towards PECs being able to protect αCT11 from proteases capable of degrading therapeutic peptides. In the future, we are excited to not only characterize the encapsulation efficiency of these PECs, but also characterize their shape and size over time through microscopic methods. Additionally, we plan to leverage the increase in peptide hydrophobicity through esterification to study hydrophobically-facilitated encapsulation with different polymers, or a combination of hydrophobically- and electrostatically-facilitated complexation with block copolymers. Esterification provides a compelling strategy to reversibly modify the net charge of therapeutic peptides to enable temporary encapsulation into PECs, facilitating the ability to increase the *in vivo* half-life of peptides without sacrificing their ability to release from the carrier and reach their desired site of action.

3.4 Future Directions

This chapter provided a proof of concept towards leveraging peptide esterification to enable reversible encapsulation into PECs, a process that we aim to continue characterizing. First, we aim to support our turbidity results using imaging, specifically

using either optical or transmission electron microscopy to physically track the formation and dissociation of PMAA/4OMe PECs as well as their shape and size over time. Further, we aim to determine the encapsulation efficiency of PECs for esterified αCT11. To do so, we plan to use RP-HPLC monitor the concentration of either esterified or unesterified αCT11 in the supernatant of mixtures of PMAA and esterified αCT11 to complete a material balance on the system and determine how much peptide is incorporated into the supramolecular structures we detected using turbidimetry. Finally, we plan to gauge the ability of PECs to protect encapsulated peptide from proteases by incubating esterified αCT11 with Proteinase K in the presence and absence of PMAA. Through these further experiments, we aim to strengthen some of the conclusions presented in this chapter and showcase esterification as a beneficial strategy to enable PEC formation.

Overall, we see esterified peptide/polymer PEC formation as a complex yet tunable system, and plan to study different aspects of it over several future papers. First, we plan to assess how different molecular details of the esterified peptide and polymer affect PEC formation and release. Specifically, we aim to look at the effect of installed ester number, installed ester type, and polymer composition on PEC properties. As we have established esterification of αCT11 is necessary for supramolecular structures to form with PMAA, and that these structures are driven by electrostatic interactions between the 2, we look forward to probing how decreasing the net overall charge of the peptide affects PEC formation and release, where we imagine a tradeoff between the two as installed ester number increases or decreases. Further, by varying ester type, we can attempt to either vary the hydrophobicity of the esters or attempt to imbue the peptide with higher charge by using alcohol with cationic groups, such as ethanolamine. Finally, while our current

system uses electrostatics to drive complexation, we could use hydrophobic polymers, such as poly(butyl methacrylate) to form hydrophobic complexes, which could have an even more pronounced effect on peptide hydrolysis than those formed from electrostatics. In this case, using more hydrophobic esters with either increased alkyl chain length or aromatic groups could yield varying degrees of encapsulation and release. While we see these experiments as the next logical step after establishing PEC formation with esterified peptides, we also look forward to varying the charge ratio of peptide and polymers used as well as studying the formation of polyelectrolyte complex micelles (PCMs) with block copolymers to form nanoparticles with a hydrated outer shell to add both solubility and an added layer of protection from proteases *in vivo.*

3.5 Materials & Methods

3.5.1 *Materials*

Fluorenylmethoxycarbonyl(Fmoc)-protected amino acids and 2-chlorotrityl chloride resin (0.6 mmol/g) were purchased from Advanced ChemTech (Louisville, Kentucky). Diisopropyl carbodiimide (DIC, 99.8%), N,N'-dimethylformamide (DMF, 99%), Oxyma Pure (99%), piperidine (99%), N,N-Diisopropylethylamine (DIPEA, 99%), trifluoroacetic acid (TFA, 99%), triisopropyl silane (TIPS, 98%), 2,2'-(ethylenedioxy)diethanethiol (DODT, 95%), diethyl ether (99%), methanol (MeOH, 99.8%), methanol (MeOH, > 99%), acetonitrile (ACN, HPLC-grade, 99.9%), hydrochloric acid (HCl, 37% in H2O), deuterated dimethyl sulfoxide (DMSO-d6, 99.5%), sodium bicarbonate (99.7%), sodium carbonate (99.5%), potassium phosphate monobasic (99%), potassium phosphate dibasic (99%), Methacrylic acid (MAA, stabilized with monomethyl ether hydroquinone (MEHQ), > 99%), 4-Cyano-4-(phenylcarbonothioylthio)pentanoic acid (> 99%), 4-4'-Azobis(4-cyanovaleric acid)

(ACVA, ≥ 98.0%) was purchased from Sigma Aldrich. Potassium iodide (KI) were purchased from VWR. MAA was purified by passing the monomer through a MEHQ removal column (Scientific Polymer Products Inc.) to remove inhibitor prior to polymerization. All other chemicals were used as received. All water was purified by in house-reverse osmosis (RO). Ultrapure water refers to water purified by a Thermo Scientific Barnstead Smart2Pure water purification system (18.2 mΩxcm).

3.5.2 *Synthesis of poly(methacrylic acid) (PMAA)*

Poly(methacrylic acid) was synthesized via reversible-addition fragmentation-chain transfer (RAFT) polymerization. MAA (1.7 mL, 20 mmol), CTA (279.3 mg, 1 mmol), ACVA (28 mg, 0.1 mmol) and methanol (8.3 mL, monomer concentration of 2.4 M) were added synchronously to a 20 mL scintillation vial. The molar ratio of [MAA]:[CTA]:[ACVA] was held at 20:1:0.1 with the target degree of polymerization at 20. The solution was degassed with nitrogen for 30 min, then added to a silicone oil bath set to 60 °C for 24 h. The solution was purified via dialysis against 40/60 MeOH/water, then against water. Following lyophilization, the polymer molecular weight was determined using ^{1}H nuclear magnetic resonance (NMR) spectroscopy.

3.5.3 *Fischer Esterification of αCT11 with Methanol (MeOH)*

For each esterification, αCT11 (20 – 150 mg) was mixed at a 5000:1 molar ratio of MeOH:αCT11 in a 95:5 MeOH:HCl ratio (v/v). The solution was stirred for 24 h at 40 °C, after which it was precipitated into diethyl ether and the peptide was isolated by centrifugation (5 min, 2420 xg, 4 °C). The supernatant was decanted, and the peptide was washed with diethyl ether, isolated by centrifugation under the same conditions, and dried under vacuum for 1 h. The peptide was dissolved in 95/5 H_2O/ACN, both with 0.1% TFA (v/v), at 5 – 10 mg/mL and frozen with liquid N_2 immediately prior to lyophilization for

at least 48 h to produce a fluffy cake that was easy to manipulate. We achieved 50 – 70%

yield for each esterification, assuming all 4 COOHs were esterified and peptides all

contained 3 trifluoroacetic acid counterions.

Scheme 3.1. Fischer esterification of αCT11 (RPRPDDLEI)
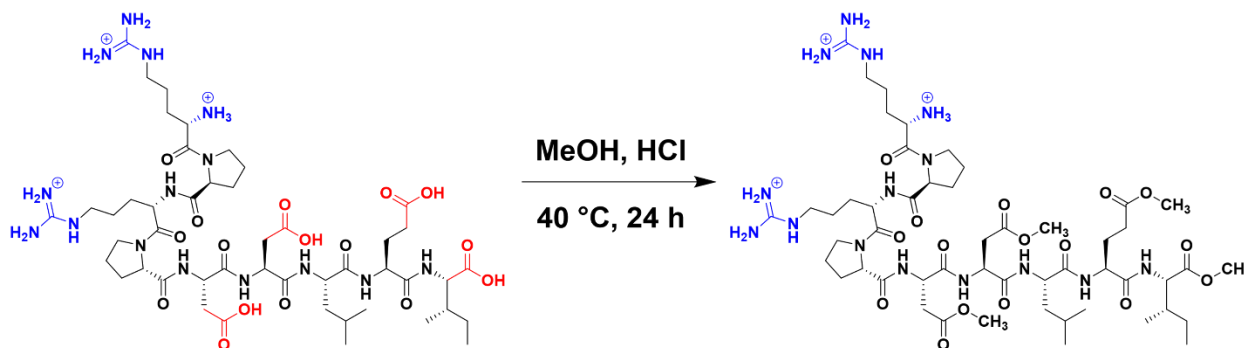
3.5.4 Analytical reverse-phase high-performance liquid chromatography (RP-HPLC)

Analytical RP-HPLC was performed at 35 °C with a flow rate of 1 mL/min on a

Waters e2695 Alliance Separations Module, equipped with a XBridge® C18

chromatographic separation column (4.6 mm x 50 mm, 3.5 µm beads) and a photodiode

array detector (Waters 2489 UV/Visible). The mobile phase consisted of ultrapure water

containing 0.1% TFA (A) and ACN containing 0.1% TFA (B), where TFA was included to

maintain pH. The mobile phase gradient was designed such that the peptide eluted

between 5 and 15 min (23 – 26% B) (**Table 3.1**). UV absorbance was monitored at 214

nm. For the hydrolysis experiments, the retention time of each sample was reported

relative to the αCT11 peak in the chromatogram measured at the initial timepoint, which

was set to a relative retention time of 0, and absorbance was normalized between 0 and

1 for each chromatogram. For a discussion of how the αCT11-4OMe peak was identified

and aligned in the chromatogram of each timepoint, see **Figure B5** in Appendix B. Peak

area (%) for αCT11-4OMe was calculated as the integration of the -4OMe peak relative

to the sum of the integrations of all αCT11-related peaks (αCT11$_i$) eluting between 5 and 15 min (Table 3.1 and **Equation 3.1**). Since the 38 mM phosphate buffer did not produce any features in the elution phase, we neglected solvent influence in the peak area calculations.

Equation 3.1) % αCT11-4OMe $= \dfrac{\int_{t_{4OMe,start}}^{t_{4OMe,end}} αCT11-4OMe}{\sum_i(\int_5^{15} αCT11_i)}$

Table 3.1. RP-HPLC mobile phase gradients

Run Time (min)		Mobile Phase Composition	
Analytical	Preparative	% Water + 0.1% TFA (A)	% Acetonitrile + 0.1% TFA (B)
0	0	95	5
0.5	2.6	95	5
5	25.2	77	23
15	50.2	74	26
15.1	50.7	5	95
16.1	60.0	5	95
16.2	60.6	95	5
22	70.0	95	5

3.5.5 *Preparative RP-HPLC*

To purify αCT11 and αCT11-4OMe and collect the isolated products, preparative RP-HPLC was performed at 25.52 mL/min at room temperature on a Waters Empower system, equipped with a XBridge® Prep C18 optimum bed density chromatographic separation column (30 mm x 150 mm, 5 µm beads) and a photodiode array detector (Waters 2489 UV/Visible). UV absorbance was monitored at 214 nm. The mobile phase consisted of ultrapure water containing 0.1% TFA (A) and ACN containing 0.1% TFA (B), where TFA was included to maintain pH. Mobile phase gradients can be found in Table 3.1. Like fractions were then combined and lyophilized to obtain solid, purified peptide. Between 30 – 80 mg of peptide were routinely injected, with 20 – 60% recovery achieved for each injection.

3.5.6 *Matrix-assisted laser desorption/ionization-time of flight (MALDI-TOF) mass spectrometry (MS)*

Molecular weights of each purified peptide sample were measured using a Shimadzu MALDI-8030 mass spectrometer with a 200 Hz solid-state laser (355 nm). The instrument was calibrated with a standard MALDI calibration kit (TOFMix and CHCA matrix, Shimadzu), for which samples were dissolved at 670 femtomoles/µL in 70% v/v ACN each with 0.1% v/v TFA. All samples were dissolved in 5% v/v ACN in ultrapure H_2O, each with 0.1% v/v TFA, at approximately 1 mg/mL and co-crystallized in a 1:1 ratio (v/v) with a α-cyano-4-hydroxycinnamic acid (CHCA) matrix solution (5 mg/mL in 70% v/v ACN with 0.1% v/v TFA). Peaks with less than 2% intensity or those that could be attributed to a CHCA blank were not reported.

3.5.7 *Preparation of PMAA and αCT11-4OMe mixtures*

PEC solutions and their relevant controls potassium phosphate buffer. First, we dissolved either esterified αCT11-4OMe or unesterified αCT11 (> 10 mg to enable accurate measurements) in 95/5 H_2O + 0.1% TFA/ACN + 0.1% TFA (v/v) at 1 mg/mL, aliquoted proper amounts required for the proposed charge ratio (~5 mg for αCT11 and αCT11-4OMe) for each solution, and then lyophilized the aliquots for at least 24 h. Prior to mixing, PMAA (> 10 mg) was weighed and dissolved into phosphate buffer at 1 mg/mL. PMAA solution (1 mL) was added to each of the lyophilized peptide samples, and these solutions were immediately vortexed for ~5 s to insure proper mixing. The same procedure was applied to the control samples with either PMAA or peptide alone, where PMAA solution (1 mL, 1 mg/mL) alone was used as the PMAA control and the phosphate buffer without PMAA (1 mL) was added to peptide aliquots to create the respective αCT11-4OMe and αCT11 control solutions.

3.5.8 Turbidimetry

Turbidimetry data was obtained using an Infinite 200 PRO (Tecan Group Ltd.) multimode plate reader. Each prepared solution (0.2 mL) was added to a well in a COR96fc UV transparent) – Corning 96 flat transparent well plate and absorbance within that well was measured through a kinetic cycle at 550 nm (25 flashes) every 30 min for 24 h.

Statistical analysis of turbidity data was performed using a one-tailed t-test assuming unequal variances with a confidence interval of 0.95. For the statistical analysis, we chose to use a one-tailed t-test as we were analyzing whether PMAA/4OMe solutions were specifically higher than PMAA/αCT11 solutions. We chose to assume unequal variances as differences between the computed variance of the PMAA/4OMe and PMAA/αCT11 solution turbidity were greater than an order of magnitude.

3.5.9 Phosphate buffer preparation

Phosphate buffer was prepared by dissolving solid potassium phosphate monobasic and potassium phosphate dibasic at various ratios in RO water. Buffer was prepared to contain 2 proton accepting units for the amount of proton donating units in solutions of αCT11 (4 proton donating units per mole) and PMAA (24 proton donating units per mole). Recipes for phosphate buffer variations with different concentration and pH were calculated using www.aatbio.com, and can be found in **Table 3.2.**

Table 3.2. Recipes for phosphate buffers with various pH and concentrations

Concentration (mM)	Concentration of proton accepting units (mM)	pH	potassium phosphate dibasic (proton accepting) (g)	potassium phosphate monobasic (g)	RO water (mL)
38	26	7.4	0.92	0.31	200
77	52	7.4	1.87	0.64	200
28	26	8	1.14	0.06	250

3.6 Acknowledgements.

I'd like to acknowledge Jack Dunleavy, Aditi S. Gourishankar and Kelly M. Bukovic for their contributions to this section. Jack Dunleavy assisted in finding conditions to increase the yield of fully esterified αCT11 from Fischer esterification. Aditi S. Gourishankar assisted with experimental design and collected the turbidity, pH, and RP-HPLC data disclosed in this section. Kelly M. Bukovic synthesized and characterized the PMAA.

3.7 References

(1)   Di, L. Strategic Approaches to Optimizing Peptide ADME Properties. *AAPS Journal* **2015**, *17* (1), 134–143. https://doi.org/10.1208/s12248-014-9687-3.

(2)   Werle, M.; Bernkop-Schnürch, A. Strategies to Improve Plasma Half Life Time of Peptide and Protein Drugs. *Amino Acids* **2006**, *30* (4), 351–367. https://doi.org/10.1007/S00726-005-0289-3.

(3)   Boöttger, R.; Hoffmann, R.; Knappe, D. Differential Stability of Therapeutic Peptides with Different Proteolytic Cleavage Sites in Blood, Plasma and Serum. *PLoS One* **2017**, *12* (6). https://doi.org/10.1371/journal.pone.0178943.

(4)   Lau, J. L.; Dunn, M. K. Therapeutic Peptides: Historical Perspectives, Current Development Trends, and Future Directions. *Bioorg Med Chem* **2018**, *26* (10), 2700–2707. https://doi.org/10.1016/j.bmc.2017.06.052.

(5)   Jiang, J.; Hoagland, D.; Palatinus, J. A.; He, H.; Iyyathurai, J.; Jourdan, L. J.; Bultynck, G.; Wang, Z.; Zhang, Z.; Schey, K.; Poelzing, S.; McGowan, F. X.; Gourdie, R. G. Interaction of α Carboxyl Terminus 1 Peptide With the Connexin 43 Carboxyl Terminus Preserves Left Ventricular Function After Ischemia-Reperfusion Injury. *J Am Heart Assoc* **2019**, *8* (16). https://doi.org/10.1161/JAHA.119.012385.

(6)   Grek, C. L.; Montgomery, J.; Sharma, M.; Ravi, A.; Rajkumar, J. S.; Moyer, K. E.; Gourdie, R. G.; Ghatnekar, G. S. A Multicenter Randomized Controlled Trial Evaluating a Cx43-Mimetic Peptide in Cutaneous Scarring HHS Public Access. *J Invest Dermatol* **2017**, *137* (3), 620–630. https://doi.org/10.1016/j.jid.

(7)   Tasdemiroglu, Y.; Council-Troche, M.; Chen, M.; Ledford, B.; Norris, R. A.; Poelzing, S.; Gourdie, R. G.; He, J. Q. Degradation of the α-Carboxyl Terminus 11 Peptide: In Vivo and Ex Vivo Impacts of Time, Temperature, Inhibitors, and Gender in Rat. *ACS Pharmacol Transl Sci* **2024**, *7* (5), 1624–1636. https://doi.org/10.1021/acsptsci.4c00120.

(8)   Meka, V. S.; Sing, M. K. G.; Pichika, M. R.; Nali, S. R.; Kolapalli, V. R. M.; Kesharwani, P. A Comprehensive Review on Polyelectrolyte Complexes. *Drug Discov Today* **2017**, *22* (11), 1697–1706. https://doi.org/10.1016/j.drudis.2017.06.008.

(9)   Kulkarni, A. D.; Vanjari, Y. H.; Sancheti, K. H.; Patel, H. M.; Belgamwar, V. S.; Surana, S. J.; Pardeshi, C. V. Polyelectrolyte Complexes: Mechanisms, Critical Experimental Aspects, and Applications. *Artif Cells Nanomed Biotechnol* **2016**, *44* (7), 1615–1625. https://doi.org/10.3109/21691401.2015.1129624.

(10)   Perry, S. L.; Leon, L.; Hoffmann, K. Q.; Kade, M. J.; Priftis, D.; Black, K. A.; Wong, D.; Klein, R. A.; Pierce, C. F.; Margossian, K. O.; Whitmer, J. K.; Qin, J.; De Pablo, J. J.; Tirrell, M. Chirality-Selected Phase Behaviour in Ionic Polypeptide Complexes. *Nat Commun* **2015**, *6*. https://doi.org/10.1038/ncomms7052.

(11)   Felgner, P. L.; Gadek, T. R.; Holm, M.; Roman, R.; Chan, H. W.; Wenz, M.; Northrop ¶, J. P.; Ringold § ¶, G. M. Lipofection: A Highly Efficient, Lipid-Mediated DNA-Transfection Procedure (Liposomes/Cationic Lipid Vesides/Gene Transfer). *Proc. Nati. Acad. Sci. USA* **1987**, *84*, 7413–7417.

(12)   Burke, R. S.; Pun, S. H. Synthesis and Characterization of Biodegradable HPMA-Oligolysine Copolymers for Improved Gene Delivery. *Bioconjug Chem* **2010**, *21* (1), 140–150. https://doi.org/10.1021/bc9003662.

(13)   Pack, D. W.; Hoffman, A. S.; Pun, S.; Stayton, P. S. Design and Development of Polymers for Gene Delivery. *Nat Rev Drug Discov* **2005**, *4* (7), 581–593. https://doi.org/10.1038/nrd1775.

(14)   Johnson, R. N.; Burke, R. S.; Convertine, A. J.; Hoffman, A. S.; Stayton, P. S.; Pun, S. H. Synthesis of Statistical Copolymers Containing Multiple Functional Peptides for Nucleic Acid Delivery. *Biomacromolecules* **2010**, *11* (11), 3007–3013. https://doi.org/10.1021/bm100806h.

(15)   Blocher McTigue, W. C.; Perry, S. L. Design Rules for Encapsulating Proteins into Complex Coacervates. *Soft Matter* **2019**, *15* (15), 3089–3103. https://doi.org/10.1039/C9SM00372J.

(16)   Blocher McTigue, W. C.; Perry, S. L. Protein Encapsulation Using Complex Coacervates: What Nature Has to Teach Us. *Small* **2020**, *16* (27). https://doi.org/10.1002/SMLL.201907671.

(17)   Obermeyer, A. C.; Mills, C. E.; Dong, X.-H.; Flores, R. J.; Olsen, B. D. Complex Coacervation of Supercharged Proteins with Polyelectrolytes †. *Soft Matter* **2016**, *12*, 3570. https://doi.org/10.1039/c6sm00002a.

(18)   Zervoudis, N. A.; Obermeyer, A. C. The Effects of Protein Charge Patterning on Complex Coacervation. *Soft Matter* **2021**, *17* (27), 6637–6645. https://doi.org/10.1039/D1SM00543J.

(19) Kapelner, R. A.; Obermeyer, A. C. Ionic Polypeptide Tags for Protein Phase Separation. *Chem Sci* **2019**, *10* (9), 2700–2707. https://doi.org/10.1039/C8SC04253E.

(20) Borro, B. C.; Malmsten, M. Complexation between Antimicrobial Peptides and Polyelectrolytes. *Adv Colloid Interface Sci* **2019**, *270*, 251–260. https://doi.org/10.1016/J.CIS.2019.07.001.

(21) Niece, K. L.; Vaughan, A. D.; Devore, D. I. Graft Copolymer Polyelectrolyte Complexes for Delivery of Cationic Antimicrobial Peptides. *J Biomed Mater Res A* **2013**, *101A* (9), 2548–2558. https://doi.org/10.1002/JBM.A.34555.

(22) Wang, C.; Feng, S.; Qie, J.; Wei, X.; Yan, H.; Liu, K. Polyion Complexes of a Cationic Antimicrobial Peptide as a Potential Systemically Administered Antibiotic. *Int J Pharm* **2019**, *554*, 284–291. https://doi.org/10.1016/J.IJPHARM.2018.11.029.

(23) Cui, Z.; Luo, Q.; Bannon, M. S.; Gray, V. P.; Bloom, T. G.; Clore, M. F.; Hughes, M. A.; Crawford, M. A.; Letteri, R. A. Molecular Engineering of Antimicrobial Peptide (AMP)-Polymer Conjugates. *Biomater Sci* **2021**, *9* (15), 5069–5091. https://doi.org/10.1039/d1bm00423a.

(24) Cummings, C. S.; Obermeyer, A. C. Phase Separation Behavior of Supercharged Proteins and Polyelectrolytes. *Biochemistry* **2018**, *57* (3), 314–323. https://doi.org/10.1021/acs.biochem.7b00990.

(25) Perry, S. L.; Leon, L.; Hoffmann, K. Q.; Kade, M. J.; Priftis, D.; Black, K. A.; Wong, D.; Klein, R. A.; Pierce, C. F.; Margossian, K. O.; Whitmer, J. K.; Qin, J.; De Pablo, J. J.; Tirrell, M. Chirality-Selected Phase Behaviour in Ionic Polypeptide Complexes. *Nat Commun* **2015**, *6*. https://doi.org/10.1038/ncomms7052.

(26) Chollakup, R.; Smitthipong, W.; Eisenbach, C. D.; Tirrell, M. Phase Behavior and Coacervation of Aqueous Poly(Acrylic Acid)-Poly(Allylamine) Solutions. *Macromolecules* **2010**, *43* (5), 2518–2528. https://doi.org/10.1021/ma902144k.

CHAPTER 4:
EXPANDING THE DESIGN SPACE OF POLYMER-METAL ORGANIC FRAMEWORK (MOF) GELS BY UNDERSTANDING POLYMER-MOF INTERACTIONS

4.1 Introduction

Metal-organic frameworks (MOFs), crystalline coordination networks containing organic linkers bridged by metal ions/clusters,[1] can be integrated with polymers to create polymer-MOF composite gels that enable advanced capabilities in optoelectronics,[2] wound healing,[3–6] and separations.[7–13] The functionality and versatility of these composite materials arise from enhanced sorptive capacity,[14] processability,[15] and mechanical stability[16,17] relative to the individual polymer and MOF constituents. For example, synthesizing MOF-808 within metal-cross-linked alginate gels increased methylene blue sorption by an order of magnitude compared to the alginate gels alone.[12] In another example, forming HKUST-1 MOFs within bentonite clay-cross-linked poly(vinyl alcohol) networks furnished 3D-printable MOF-laden inks.[18] Additionally, the synthesis of ZIF-8 within a gelatin matrix enhanced the storage modulus of the composite gels (5x) compared to the gelatin alone.[19] While interactions between MOFs and polymers that facilitate composite gel formation are quite beneficial in these examples, polymer-MOF interactions can also detract from the intended properties of composite gels.

MOF formation requires the coordination of organic linkers to metal ions/clusters, while gel formation in these systems generally relies on cross-linking of polymer chains by the same metal ions/clusters. Therefore, this competition between the organic linker and polymer for binding the metal ions/clusters can disrupt MOF crystallization in

composite gels. For example, synthesizing MOF-808 within Zr^{4+}-cross-linked alginate gels yielded composite gels with lower crystallinity than MOF-808 particles formed in the absence of alginate.[12] It is in turn possible that the linkers outcompete polymers for binding the metal ions/clusters, reducing cross-link density in the composite gels.[13] To gain control over polymer-MOF composite gel properties, we must further understand the competition between linkers and polymers for metal ions/clusters.

To date, many reported polymer-MOF composite gels rely on carboxylic acid (–COOH) containing polymers, such as alginate.[9,11,13,20–22] However, since many MOF linkers contain carboxylic acids, competition will likely occur between the carboxylic acids on the polymer and the linker for binding metal clusters. Using polymers more weakly metal binding functional groups (e.g., amines ($–NH_2$) or hydroxyl (–OH)) than carboxylic acid groups can permit crystalline MOF formation without preventing gelation. For example, four crystalline MOFs were formed within chitosan composite gels, suggesting that the chitosan hydroxyl and amine groups did not prevent MOF formation.[8] Encouragingly, this suggests that polymer molecular details can tune the MOF formation properties and the polymer-MOF interactions and, by extension, the properties of the resulting composites. On the other hand, the MIL-100 MOF did not form within the same chitosan networks,[8] highlighting that, in addition to the polymer functional groups, it is important to consider the effects of MOF chemistry on MOF crystallinity and formation within composite gels. Studies so far have mainly highlighted the benefits of polymer-MOF combinations. However, comparisons of composite structure and properties (e.g., MOF crystallinity, gel properties, sorption characteristics) with control materials lacking either polymer (i.e., MOF alone) or linker (i.e., metal-cross-linked polymer gels) are

needed for understanding the role of molecular details on the structure and properties of these composite gels.

Here, we investigate how the molecular details of polymers and MOFs affect the formation, gelation behavior, crystallinity, and sorption characteristics of their composite gels. Specifically, for these studies, we form composite gels using polymers with different types and densities of functional groups (i.e., carboxylic acids, hydroxyl groups, or neither) and a range of Zr-based MOFs. We then compare the ability of the composite gels, Zr-cross-linked polymer gels (control without MOF linker), and MOF (control without polymer) to sorb and release the small molecule dye methylene blue and the therapeutic peptide Angiotensin 1-7. By understanding the role of molecular details of polymers and MOFs on the properties of composite gels prepared by forming MOFs in the presence of polymers, we expand the design space of polymer-MOF composite gels.

4.2 Results and Discussion

We first studied the impact of polymer chemistry on MOF formation, and, in turn, the impact of MOF formation on polymer cross-linking. To probe the role of polymer chemistry in MOF formation, we formed MOFs in the presence and absence of poly(acrylic acid) (PAA), poly(acrylic acid-*co*-acrylamide) (PAAA), poly(vinyl alcohol) (PVA), and poly(ethylene glycol) (PEG), and assessed the crystallinity of the resulting MOFs. We note that aside from PEG, these polymers are all simple hydrocarbon chains with functional groups pendant to every other carbon, allowing us to isolate the effects of these functional groups. In turn, to investigate the extent to which MOF formation plays a role in polymer cross-linking, we compared the gelation behavior of Zr-cross-linked polymers, which were formed with in the absence of the organic MOF linker, to that of the polymer-MOF composites.

To evaluate the role of polymer chemistry, we selected the prototypical MOF UiO-66, featuring zirconium-oxide (Zr-oxo) clusters linked with benzene dicarboxylic acid (H$_2$BDC) linker. Previously finding that pre-forming Zr-oxo clusters before adding linker accelerates MOF formation,[23,24] we first synthesized the clusters by dissolving zirconium propoxide (70 wt% in 1-propanol) and acetic acid modulator in DMSO followed by heating at 130 °C for 2 h. Then, we added the H$_2$BDC linker as a powder to the Zr-oxo cluster solution, which is transparent (**Figure C.1a**), and stirred at room temperature (RT) for 24 h to form UiO-66 (**Figure 4.1a**). As is typical with UiO-66 formation,[25] the solution turned white within 4-6 h (**Figure C.1b**). We isolated the UiO-66 powder by dialyzing the suspension against DI water, followed by drying the particles at RT in ambient conditions. Scanning electron microscopy (SEM) images of the MOF powder revealed spherical particles ~30 to 80 nm in diameter, typical of this accelerated MOF formation protocol, [24] (**Figure C.2**). Grazing incidence X-ray diffraction (GIXD) from the powder shows characteristic diffraction peaks corresponding to scattering from the (111) and (200) planes of UiO-66 (**Figure 4.1a**). From the GIXD pattern, we used the Scherrer equation[26] to calculate the coherence length of UiO-66, reflective of the length scale over which crystalline order persists, as 40 nm.

To form composite gels, we added a MOF linker to the polymer solution before mixing with Zr-oxo clusters. We chose to pre-mix the polymer and linker to promote simultaneous formation of MOF and gel, since pre-mixing linker and Zr-oxo clusters prior to adding polymer might preferentially promote MOF formation and pre-mixing polymer and Zr-oxo clusters prior to adding linker might preferentially promote gelation. We first attempted to form composite gels with a 1:1 molar ratio of linker:metal similar to the MOF

alone, but obtained no gelation. In contrast, increasing the linker:metal molar ratio to 2:1 yielded gels (**Figure C.3**). A possible explanation is that doubling the linker concentration accelerates UiO-66 crystallization, generating defects (i.e., open metal sites) and availing open Zr-oxo cluster sites for polymers to bind and gel.[27] Thus, all polymer-UiO-66 composites gels were formed at a 2:1 linker:metal molar ratio. We have included a discussion in **Section C1.2** of Appendix C on why using a lower linker:metal ratio was not plausible.
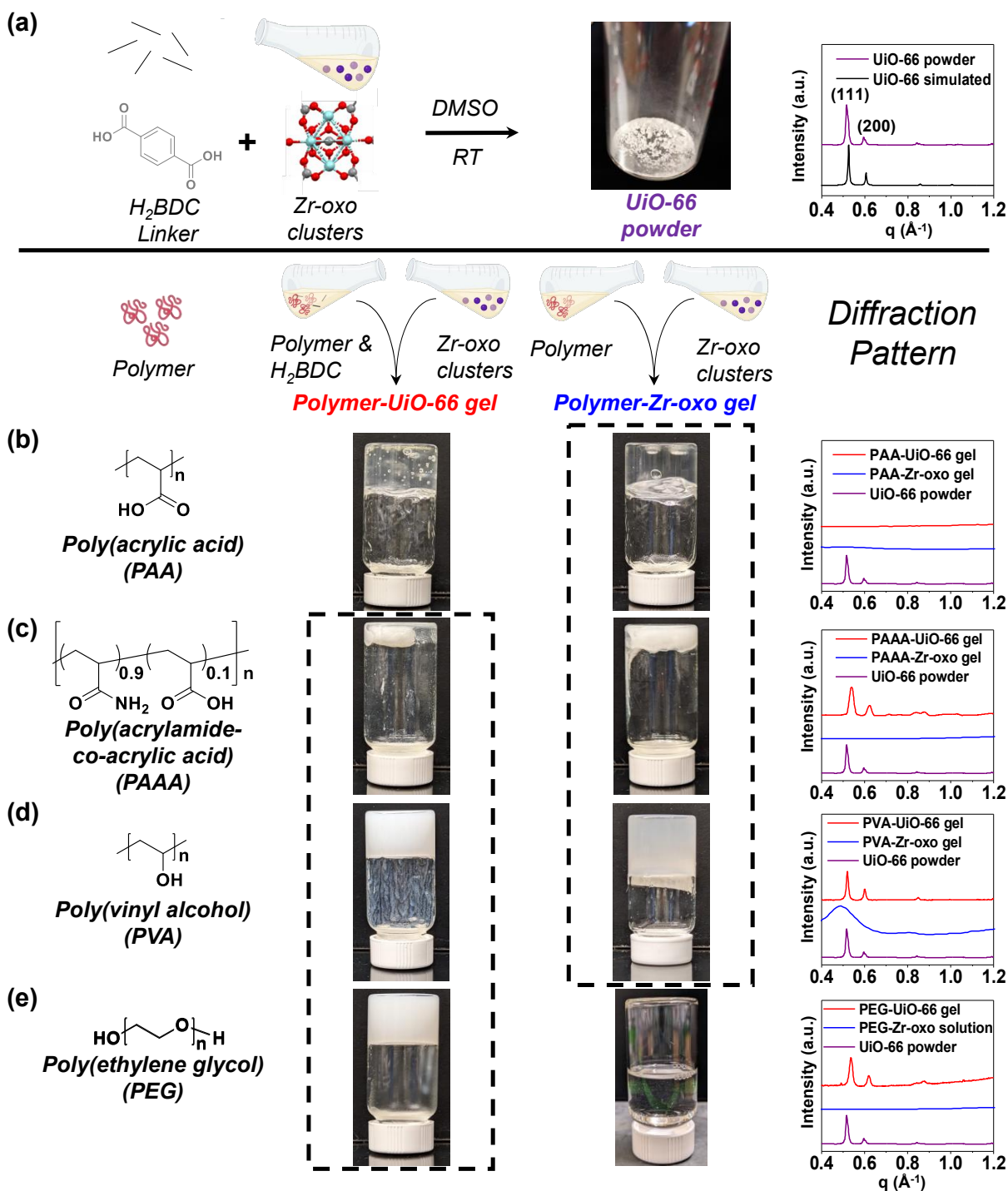
Figure 4.1. Polymer gelation and MOF formation within polymer-MOF composite gels, varying in polymer functional group chemistry and density. **(a)** Formation of UiO-66, with the corresponding grazing incidence X-ray diffraction (GIXD) pattern (purple) compared with the simulated pattern (black). In the structure of the Zr-oxo clusters, generated using Mercury,[28] Zr, O, and C atoms are colored cyan, red, and grey respectively. Gelation behavior (center) and GIXD patterns (right) of polymer-UiO-66 composite gels (red) and polymer-Zr-oxo gels (blue) synthesized with **(b)** poly(acrylic acid) (PAA), **(c)** poly(acrylamide-co-acrylic acid) (PAAA), **(d)** poly(vinyl alcohol) (PVA), and **(e)** poly(ethylene glycol) (PEG). For PAA, we form gel, but

not UiO-66. For PAAA and PVA, we form composite gels containing UiO-66, but those with carboxylic acid-containing PAAA show lower UiO-66 crystallinity, while hydroxyl-containing PVA maintains crystallinity. For PEG, we form composite gels containing UiO-66, but PEG-Zr-oxo mixtures lacking linker do not gel, indicating MOF formation is necessary for gelation. All samples were synthesized in dimethyl sulfoxide (DMSO). Image of Zr-oxo cluster is reproduced or adapted with permission from [28]. Copyright 2022 American Chemical Society. GIXD data and images were collected by Prince Verma.

4.2.1 *MOF and gel formation in carboxylic acid-containing polymer solutions:*

Anticipating that polymers with carboxylic acid groups would compete most strongly with the carboxylic acid-containing linkers for binding the Zr-oxo metal clusters, we first attempted to form PAA-UiO-66 composite gels. Adding a solution of Zr-oxo clusters to a solution containing H_2BDC linker and 2 wt% PAA (M_w~1,033,000 g/mol) in DMSO yielded a self-supporting gel after 24 h at room temperature (**Figure 4.1b, center left).** Yet, the gel was transparent, and since UiO-66 formation should produce particles that give the gel a white color, we suspected limited-to-no UiO-66 formation within the gel. Corroborating our visual assessment, GIXD patterns contained no peaks characteristic of the (111) or (200) planes of UiO-66 crystals **(Figure 4.1b, right)**. Furthermore, unlike UiO-66 alone, which forms spherical particles (Figure C.2), we observed no spherical particles in SEM images of the gels (**Figure C.4**). Suspecting that gelation was due to Zr-oxo clusters cross-linking PAA chains, we added a solution of Zr-oxo clusters to a PAA solution containing no linker, which also produced a self-supporting PAA-Zr-oxo gel (**Figure 4.1b, center right**). Since UiO-66 did not form in the presence of PAA, presumably due to PAA outcompeting the H_2BDC linker for binding the Zr-oxo clusters, we next sought to form composites by adding pre-formed UiO-66 to PAA. While we did observe a small amount of gelation of these physical mixtures of MOF and polymer, we did not observe the homogenous gelation necessary to pass an inversion

(**Figure C.5a**), a result we ascribe to the lower accessibility of Zr-oxo clusters needed for polymer cross-linking.

As PAA, with carboxylic acid groups pendent to every other carbon, inhibited UiO-66 formation, we reasoned that lowering the density of carboxylic acids on the polymer would permit MOF formation simultaneously with gelation. We next attempted composite gel formation with PAAA, a copolymer containing 10% acrylic acid groups randomly dispersed among acrylamide units with $M_w \sim 210,000$ g/mol (**Figure 4.1c, left**). Despite the lower density of carboxylic acids and the lower molecular weight of this polymer, mixtures of PAAA and Zr-oxo still formed gels in the absence of linker (**Figure 4.1c, center right**). In the presence of linker, we also observed the formation of a self-supporting gel (**Figure 4.1c, center left**). Yet in this case, the opaque white color of this gel was an encouraging indication of UiO-66 particle formation within the gel, which GIXD patterns (**Figure 4.1c, right**) and SEM confirmed (**Figure C.6**). While the coherence length of UiO-66 synthesized in the presence of PAAA (26 nm) was slightly lower than that of UiO-66 alone (40 nm), it is apparent that lowering the carboxylic acid density within the polymer permitted simultaneous MOF formation and gelation, suggesting functional group density can modulate MOF crystallinity.

4.2.2 MOF and gel formation in hydroxyl-containing polymer solutions:

Relative to carboxylic acids, hydroxyl groups interact less strongly with Zr-oxo clusters;[29] therefore, we expected that forming UiO-66 in the presence of poly(vinyl alcohol) (PVA, $M_w \sim 146,000-186,000$ g/mol, **Figure 4.1d, left**) would also furnish composite gels despite the anticipated lower binding affinity of PVA to Zr-oxo clusters. To this end, adding a Zr-oxo cluster solution to a PVA solution in the absence of H_2BDC linker yielded a self-supporting PVA-Zr-oxo gel (**Figure 4.1d, center right**). Upon adding

Zr-oxo solution to a mixture of PVA and H_2BDC linker, the resulting gel exhibited the opaque, white color characteristic of UiO-66 formation (**Figure 4.1d, center left)**. SEM (**Figure C.7**) and GIXD (**Figure 4.1d, right)** confirmed UiO-66 formation, showing UiO-66 particles within the composite, that had a similar coherence length (44 nm) to UiO-66 formed in the absence of polymer (40 nm).

Given that PVA yielded more crystalline UiO-66 within composite gels compared to both carboxylic acid-containing polymers, we next sought to determine the effects of PVA molecular weight and concentration on composite gelation behavior. Varying the concentration of PVA (M_w~146,000-186,000 g/mol) used to form PVA-UiO-66 composites from 0.1 to 3.0 wt%, we obtained self-supporting gels at and above 2.0 wt% (**Figure C.8**). Reducing PVA molecular weight to M_w~31,000-50,000 g/mol required a higher polymer concentration (3 wt%) for gelation (**Figure C.9**). Further reducing PVA molecular weight to M_w~9,000-10,000 g/mol did not result in gelation even at 4 wt% PVA (**Figure C.10**). Together, these results suggest that polymer chains must be long enough or at a high enough concentration in solution to bridge multiple MOF particles (or Zr-oxo clusters) for gelation to occur (**Figure C.11**).

4.2.3 Poly(ethylene glycol)-MOF composites

Since hydroxyl-containing PVA facilitated the formation of more crystalline UiO-66 compared to carboxylic acid-containing polymers, we next further reduced the interactions between polymer and Zr-oxo clusters by using poly(ethylene glycol) (PEG, M_v~100,000 g/mol), which only contains hydroxyls at the chain ends. Unlike the polymers with carboxylic acid and hydroxyl pendant groups, mixing PEG with Zr-oxo clusters did not produce gels (**Figure 4.1e, right center**). However, adding a solution of Zr-oxo clusters to a mixture of PEG and H_2BDC linker in DMSO did yield a self-supporting gel

with the opaque, white color characteristic of MOF formation (**Figure 4.1e, left center**).

SEM (**Figure C.12**) and GIXD (**Figure 4.1e**) revealed the presence of UiO-66 particles

with a comparable, yet slightly lower coherence length (32 nm) to UiO-66 synthesized in

the absence of polymer (40 nm). Since Zr-oxo does not cross-link PEG, the observation

of gelation during MOF formation suggested the exciting possibility that MOFs may cross-

link polymers by physically entrapping them as they form. To further probe the possibility

that PEG is simply entrapped in the composites, we heated the PVA- and PEG-based

composites to 40 °C for 24 hrs. After cooling back down to room temperature, the PEG-

UiO-66 composite gel flowed (**Figure C.13a**), while the PVA-UiO-66 composite gel

remained intact (**Figure C.13b**), suggesting PVA-based composites to be more thermally

stable than PEG-based composites, presumably due to the stronger interactions between

PVA and Zr-oxo sites.

4.2.4 *Extending PVA-MOF composite gel synthesis to other Zr-based MOFs and processibility of the composite gel*

To determine the generalizability of this composite gel formation process, we

attempted to form composite gels with PVA and different Zr-oxo-based MOFs (NU-901

(**Figure C.14**),[30] UiO-67,[31] and MOF-525[32]). We selected PVA as it facilitated the

formation of most crystalline UiO-66 crystals within the composite gels among the

polymers we studied. Just as in PVA-UiO-66 composite gel synthesis, we added a

solution of Zr-oxo clusters to a solution containing PVA and the corresponding organic

linker for each Zr-based MOF (**Table 4.1**).[23,33] For MOFs containing dicarboxylic acid

linkers, we used double the linker:Zr ratio used in the previous syntheses.[23] For MOFs

containing tetracarboxylic acid linkers, we used the same linker:Zr used in the previous

syntheses.[33] All formulations produced self-supporting gels, and SEM images (**Figure**

C.15-C.17) and GIXD patterns confirmed the presence of each MOF within their respective composite gels (**Figure 4.2a-c**). The thermal stability observed in the PVA-UiO-66 composte gels persisted across the PVA-NU-901, PVA-UiO-67, and PVA-MOF-525 composite gels, which all passed the inversion test after being heated to 40 °C (**Figure C.18**). Encouragingly, the examples presented here involving three different MOFs demonstrate the generalizability of this composite gel formation process.

After preparing composites from different MOFs, we sought to demonstrate that this composite gel formation procedure could be extended to preparing conformable gel films from PVA-UiO-66 composites. We heated the composite gel to make it liquid and amenable to spin-coating. Spin-coating the composite onto glass substrates, followed by allowing the sample to set in ambient conditions for 24 h yields a free-standing gel film (**Figure 4.2d**). The thin film contains UiO-66 particles as demonstrated by the diffraction pattern (**Figure 4.2e**) and is capable of conforming to objects (e.g., a pencil as shown in **Figure 4.2f**, showcasing the enhanced processability imparted to MOFs by incorporation into these composites.
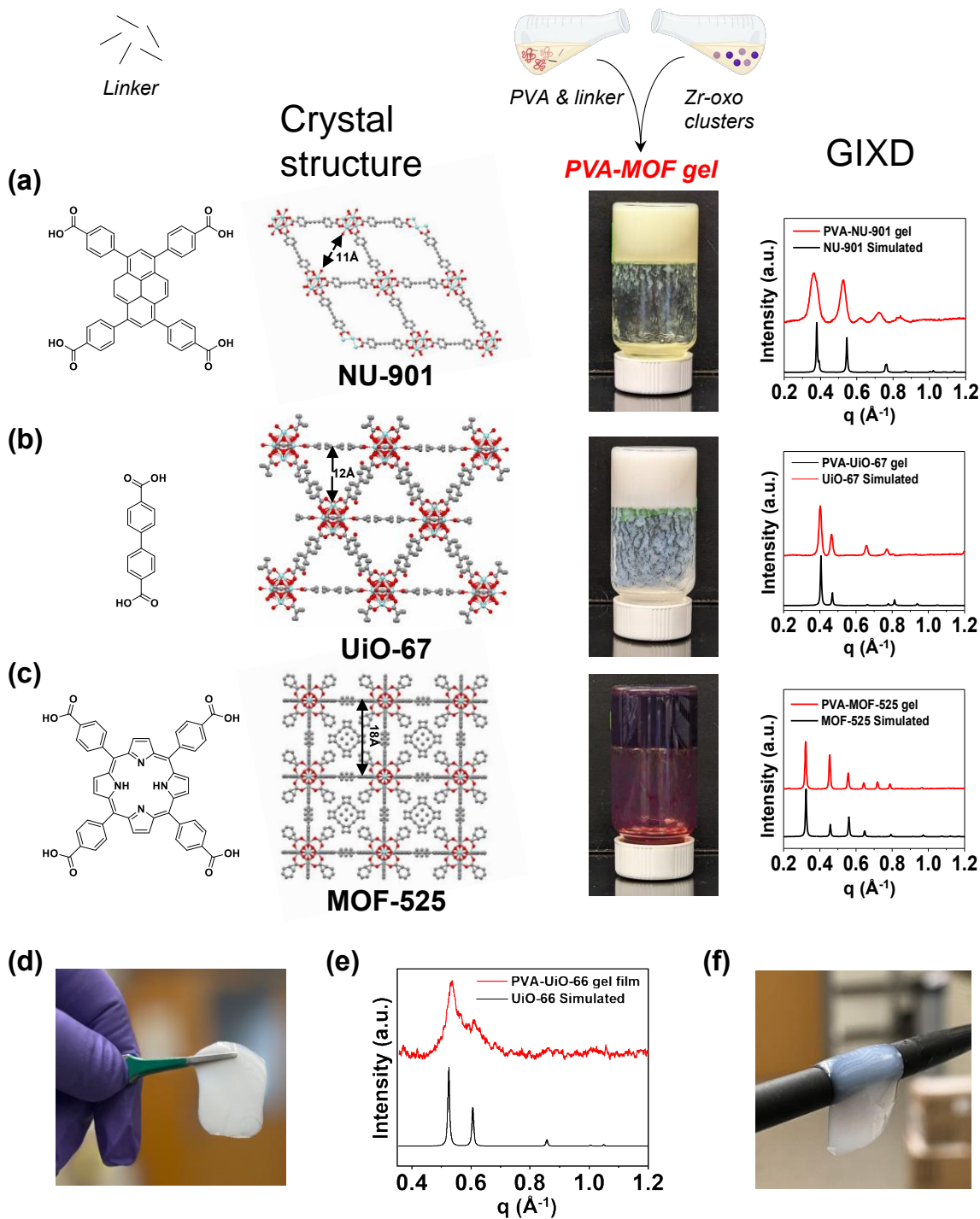
Figure 4.2. Extension of the composite gel synthesis process to different Zr-based MOFs and processibility of the PVA-UiO-66 composite gels. Formation and properties of PVA-based composite gels formed from **(a)** NU-901, with 4,4',4'',4'''-(1,3,6,8-pyrenetetrayl) tetrakis-benzoic acid) (H$_4$TBAPy) linker; **(b)** UiO-67, with biphenyl-4,4′-dicarboxylic acid (BPDC) linker; and **(c)** MOF-525, with tetrakis (4-carboxyphenyl porphyrin (TCPP) linker. For each formulation, we show the organic linker used in the synthesis, the crystal structures of each MOF obtained from Mercury software,[28] composite gelation behavior via inversion tests, and grazing incidence X-ray diffraction (GIXD) patterns comparing the crystal structures of the MOFs formed in each composite gel to the simulated patterns for the corresponding MOFs. **(d)** Image showing that the PVA-

UiO-66 composite gel thin film is free-standing. **(e)** Powder X-ray diffraction (PXRD) of the PVA-UiO-66 composite gel thin film. **(f)** Image showing that the PVA-UiO-66 composite gel thin film exhibits conformality. For the PVA-UiO-66 composite gel thin film, the PVA wt% is 2.5. Image of NU-901 crystal structure is reprinted (adapted) with permission from *Chem. Mater.* 2020, *32* (24), 10556–10565.[31] Copyright 2020 American Chemical Society. Image of UiO-67 crystal structure is reprinted (adapted) with permission from *Chem. Mater.* 2017, *27* (7), 3111-3117.[56] Copyright 2017 American Chemical Society. Image of MOF-525 crystal structure is reprinted (adapted) with permission from *Inorg. Chem.* 2012, *51* (12), 6443–6445.[33] Copyright 2012 American Chemical Society. GIXD data and images of the composite gels were collected by Prince Verma. GIXD data and images of the composite gel film were collected by Ankit Dhakal.

Sorptive Capacity and Sustained Release of PVA-MOF composite gels

We next sought to examine the sorptive properties of the composite gels relative to Zr-oxo-cross-linked polymer gels and MOF powder. For these experiments, we used composite and Zr-oxo-cross-linked PVA gels containing 3 wt% polymer, as they were easier to cut into uniform samples the gels containing 2 wt% polymer. Rather than performing these studies in DMSO, we opted for aqueous conditions more relevant to drug delivery and environmental remediation applications. We first attempted to synthesize the PVA-UiO-66 composite gels in aqueous conditions, and while the white, opaque color of the solution suggested MOF formation, we did not observe gelation, likely due to the high concentration of water hydroxyl groups saturating the binding sites on the Zr-oxo clusters and outcompeting PVA hydroxyl groups (**Figure C.19**). Therefore, we synthesized composite gels in DMSO and to transition the gels from DMSO into aqueous solvent, we instead dialyzed the DMSO-swollen PVA-UiO-66 composite gels and controls (i.e., MOF powder and PVA-Zr-oxo gels) against RO water. We confirmed the complete removal of DMSO from the composite gels using ^{1}H nuclear magnetic resonance spectroscopy (**Figure C.20, Table C.1**). UiO-66 crystallinity was also maintained after solvent exchange, suggesting no disruption of UiO-66 structure during dialysis (**Figure C.21b**). Since dialysis removes unincorporated organic linker and dissolved Zr-oxo clusters, we used thermal gravimetric analysis (TGA) to compare the compositions (i.e.,

wt% Zr) of the materials before and after solvent exchange (**Figures C.22-C25, Table C.2**). The Zr content in the PVA-Zr-oxo control gels decreased substantially from 7.8 to 1.2 wt% Zr during solvent exchange, indicating that dialysis removes much of the Zr-oxo that is cross-linking polymer chains, and the resulting samples are primarily PVA hydrogels. In contrast, the PVA-UiO-66 composite gels retained more of their Zr during solvent exchange, only decreasing from 7.3 to 4.3 wt% Zr. Since the composite gels retain more Zr than the PVA-Zr-oxo control gels during solvent exchange, it is likely that the Zr-oxo clusters in the composites are primarily incorporated into UiO-66. Though we could not calculate the % Zr in the UiO-66 powder prior to solvent exchange, as it did not precipitate in DMSO, it contained an appreciable amount of Zr (21.3 wt%) after dialysis.

After each formulation was switched into aqueous solvent, we first monitored the sorption of the small molecule dye methylene blue (MB, 320 g/mol) into each by measuring the decrease in MB absorbance (660 nm) in the surrounding solution. We elected to study sorption of MB into these materials to compare their sorptive characteristics in the hydrated state. After 7 days, when sorption plateaued in the gel formulations and each sample was saturated with MB, we compared the amounts sorbed into each formulation (**Figures C.26-C.29**). The PVA-UiO-66 composite hydrogels sorbed significantly more MB (0.16 +/- 0.02 mg MB/mg dry sample) than the PVA-Zr-oxo hydrogels (0.06 +/- 0.01 mg MB/mg dry sample), indicating that the MOF contributes appreciable sorption capacity to the composites (**Figure 4.3a**). The increased MB sorption capacity of the composite gels relative to the PVA-Zr-oxo hydrogels, extended to composites prepared with all other Zr-oxo MOFs described in **Figure 4.3** (PVA-MOF-525, PVA-UiO-67, and PVA-NU-901, all synthesized with 2 wt% PVA) (**Figure C.29**).

We next determined how the polymer impacts the sorption properties of MOFs by comparing MB sorption into PVA-UiO-66 composite hydrogels relative to UiO-66 MOF powder alone in ultrapure water. On a per mass of sorbent basis, our PVA-UiO-66 composite hydrogels MB sorptive capacities were on par with state-of-the art reported values for UiO-66.[34,35] However, rather than comparing these on a per mass of sorbent basis, we compared the samples on a per mass Zr basis to isolate the role of the polymer. On a per g of Zr basis, the composite hydrogels sorbed substantially more MB (3.71 +/- 0.39 mg MB/mg Zr) than UiO-66 (0.75 +/- 0.03 mg MB/mg Zr) after 7 days (**Figure 4.3b**, **Table C.3**). We suspect that forming UiO-66 in the presence of PVA disperses the UiO-66 particles within the hydrogel composite, leading to a greater UiO-66 surface area in the composite gels and the higher sorption per Zr relative to that of UiO-66 formed in the absence of polymer. Taken together, these sorptive studies highlight how forming MOFs in the presence of polymer boosts the sorption capacity relative to polymer networks without MOF, and also relative to MOF formed in the absence of polymer.
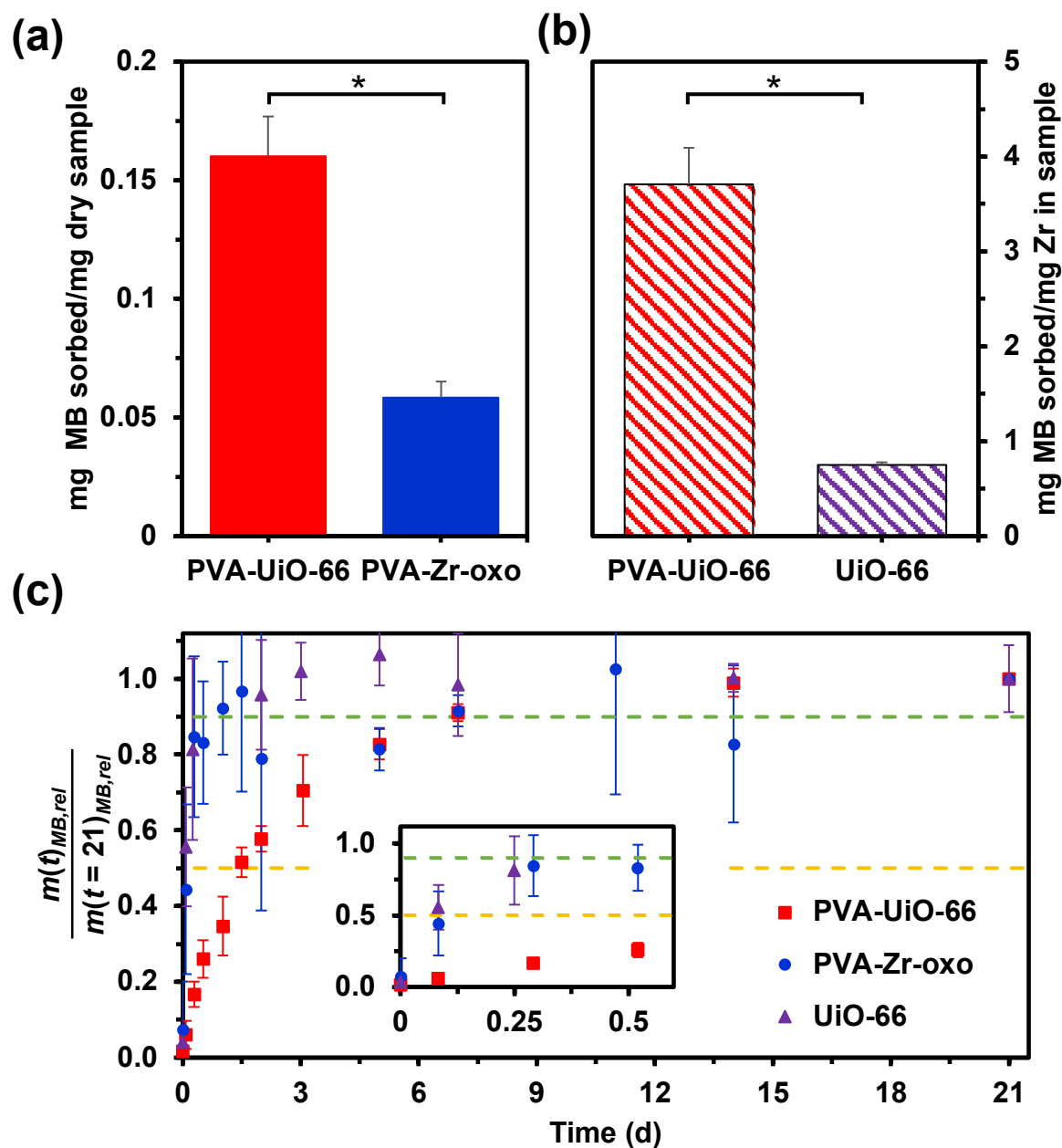
Figure 4.3. Sorptive capacity and release behavior of PVA-UiO-66 composite hydrogels (red) relative to that of PVA-Zr-oxo hydrogels (blue), and UiO-66 powder (purple) in ultrapure water. **(a)** Methylene blue (MB) sorption into PVA-UiO-66 composite hydrogels and PVA-Zr-oxo hydrogels after 7 days (mg MB/mg dry sorbent) shows UiO-66 incorporation into polymer increases MB sorption per mass of dry sorbent. **(b)** MB sorption into PVA-UiO-66 composite hydrogels and UiO-66 MOF (mg MB/mg Zr) after 7 days shows that forming UiO-66 in the presence of PVA increases MB sorption capacity on a per Zr basis. **(c)** Mass of MB released from each formulation at any given time ($m(t)_{MB,rel}$) relative to the mass released after 21 d ($m(t = 21)_{MB,rel}$), with the first 12 h (inset, bottom right) highlighted and lines included between points to guide the eye. Yellow and green dashed lines denote release of 50% and 90% MB relative to that released at 21 days, respectively. While the PVA-Zr-oxo hydrogels (blue, circles) and UiO-66 powder (purple, triangles) display burst release behavior, releasing 90% of their cargo within less than 24 h, the PVA-UiO-66 composite hydrogels (red, squares) do not release 90% of the loaded MB until day 7. Error bars

We next studied the release of MB from the composite gels relative to the PVA-Zr-oxo and UiO-66 control samples in ultrapure water. After allowing MB to load into each sample for 7 days, we replaced the surrounding solution with an equivalent volume of DI water and monitored the release of MB into the surrounding solution. We report the mass of MB released into the outer solution ($m(t)_{MB,rel}$) relative to the total amount released after 21 d ($m(t=21)_{MB,rel}$), specifically focusing on the time taken for each formulation to release 50% and 90% of their respective $m(t = 21)_{MB,rel}$ (**Figure 4.3c**). While the PVA-Zr-oxo hydrogel and UiO-66 controls exhibited burst release behavior, releasing 50% and 90% of their respective $m(t=21)_{MB,rel}$ in less than 3 and 24 h, respectively, the PVA-UiO-66 composite hydrogels showed a sustained MB release profile, releasing 50% and 90% of $m(=21)_{MB,rel}$ in 1.5 and 7 d, respectively. While there was a particularly large amount of error between the PVA-Zr-oxo samples, we ascribe this to the relatively low amounts of MB released into the solution, with MB concentrations approaching the limit of reliable absorbance detection of the instrument. Comparing the release profiles suggests that the combination of UiO-66 and PVA slows solute diffusion relative to their components.

After demonstrating the sorption and release of MB, we investigated the encapsulation and release of larger, therapeutically relevant cargo (*e.g.,* peptides). Despite their high potency, high selectivity, and low toxicity, therapeutic peptides[36–38] are often rapidly cleared from circulation by proteolytic degradation and renal clearance, leading to poor efficacy.[39] Angiotensin 1-7 (DRVYIHP, Ang 1-7), a therapeutic peptide with anti-tumor and cardioprotective properties, has an *in vivo* half-life of just 30 min.[40,41] Encapsulation and sustained release into a carrier such as polymer-MOF composite

hydrogels could offer a way to extend the half-life of Ang1-7. Because Ang 1-7 (899 g/mol) (**Figure C.30)** is larger than MB (320 g/mol) we first attempted to encapsulate it within UiO-67 and MOF-525, which have larger pores (12 Å and 18 Å, respectively) than UiO-66 (6 Å).[42] Though reverse-phase high-performance liquid chromatography showed little decrease in Ang 1-7 absorbance in the outer solution after incubation with UiO-67 after 27 h, there was no detectable trace of Ang 1-7 in the solution containing MOF-525, suggesting that Ang 1-7 sorbed into MOF-525, but not UiO-67 (**Figure C.31**). Therefore, we performed the Ang 1-7 encapsulation and release experiments using PVA-MOF-525 composite hydrogels. We also confirmed total removal of DMSO and that MOF-525 crystallinity is maintained in the PVA-MOF-525 composite hydrogels after dialysis (Figure C.20-C.21).
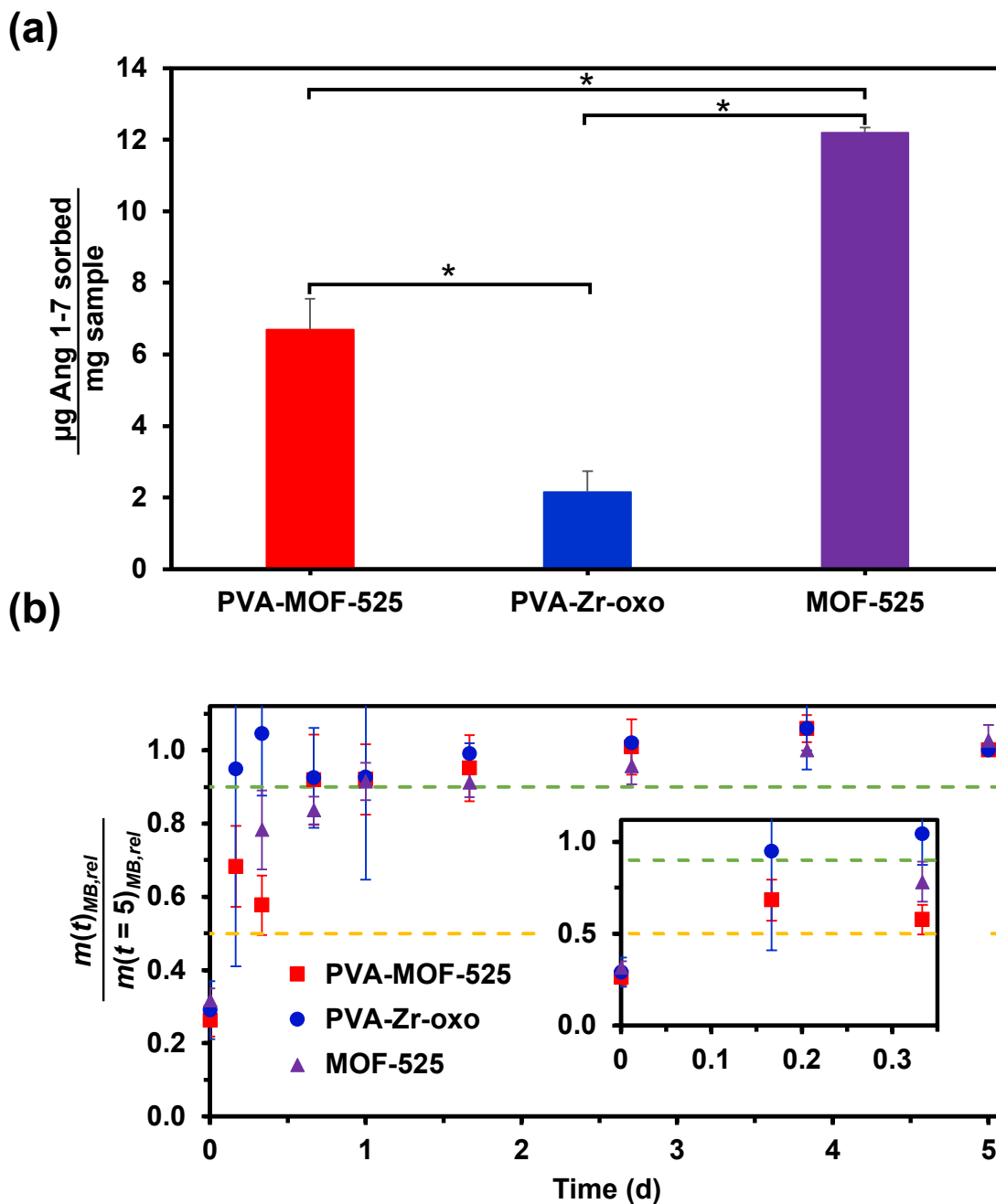
Figure 4.4. Sorptive capacity and release behavior of PVA-MOF-525 composite hydrogels (red), PVA-Zr-oxo hydrogels (blue), and MOF-525 powder (purple) for the therapeutic peptide Ang 1-7 in ultrapure water. **(a)** Mass of Ang 1-7 (μg) sorbed into each sample after 7 days, normalized relative to the mass of each sample (mg), showing more Ang 1-7 to sorb into the MOF-525 powder than into the PVA-Zr-oxo and PVA-MOF-525 composite hydrogels on a per mass basis. **(b)** Mass of Ang 1-7 released from each formulation at any given time ($m(t)_{Ang\ 1-7,rel}$) relative to the mass released after 5 d ($m(t = 5)_{Ang\ 1-7,rel}$), with the first 6 h (inset, bottom right) highlighted and lines included between points to guide the eye. Yellow and green dashed lines denote release of 50% and 90% MB relative to that released at 5 days, respectively. The PVA-MOF-525 composite hydrogels (red, squares), PVA-Zr-oxo hydrogels (blue, circles), and MOF-525 powder (purple, triangles) all display burst release behavior, releasing 90% of their cargo within less than 24 h.

106

Error bars represent the standard deviation between three separately synthesized samples, with * in (a) and (b) indicating an equal variances two sample t-test giving p < 0.05.

To encapsulate Ang 1-7 into PVA-MOF-525 composite hydrogels, PVA-Zr-oxo hydrogels, and MOF-525 powder, we incubated each sample in a solution of Ang 1-7 in ultrapure water. Here, we normalized the sorption data by the overall weight of each sample (mg Ang 1-7 sorbed/mg material. After 7 days, when the samples were found to be saturated (**Figure C.32**), the MOF-525 powder sorbed significantly more Ang 1-7 (12.2 +/- 0.2 μg Ang 1-7/mg sample) than both the PVA-Zr-oxo (2.2 +/- 0.6 μg Ang 1-7/mg sample) and PVA-MOF-525 composite hydrogels (6.7 +/- 0.9 μg Ang 1-7/mg dry sample) (**Figure 4.4a**, **Table C.5**). On a dry weight basis, the PVA-MOF-525 composite hydrogel sorbed significantly more Ang 1-7 (79.7 +/- 10.2 μg Ang 1-7/mg dry sample) than the PVA-Zr-oxo hydrogel (45.3 +/- 12.5 μg Ang 1-7/mg dry sample) and MOF-525 powder (12.2 +/- 0.2 μg Ang 1-7/mg dry sample) (**Figure C.33**, **Table C.5**). The release profiles of the 3 formulations in ultrapure water, however, were fast and indistinguishable, with all formulations plateauing in less than 1 day **(Figure 4.4b)**. The burst release observed in the PVA-MOF-525 composite gels could be due to the larger pore size of MOF-525; however, given that the PVA-MOF-525 composite gel only released 28.8% +/- 3.3% of the encapsulated Ang 1-7 (**Figure C.34**, **Table C.6**), it is also possible that the Ang 1-7, which has 2 carboxylic acids, is interacting with the open Zr-oxo sites, and these interactions prevent any bound peptide from being released. While future optimization of PVA-MOF composite hydrogels for larger peptide cargo is still needed; however, the enhanced sorption capacity of the composite hydrogels for Ang1-7 relative to the PVA-Zr-oxo hydrogel and MOF-525 controls is certainly encouraging.

4.3 Conclusion

In this work, we found that polymer molecular details dictate the formation and properties of polymer-MOF composite gels prepared by forming MOF in the presence of the polymeric component. While we found that polymers with groups that bind the Zr-oxo nodes of MOFs without outcompeting the organic linkers allowed for concurrent gelation and MOF formation, our experiments with PEG suggest that polymer entrapment within MOFs by alone is sufficient to facilitate gelation within composites, expanding the polymeric options available for future polymer-MOF composite formulations. Through simulations, we found that both chemical interactions between polymers and metal nodes as well as physical entrapment of polymers within MOF pores play a role in polymer-MOF composite gel formation. Composite gel formation with various PVA-Zr-based MOF composite gels demonstrated the generalizability of the composite gel formation technique to other MOFs, and the fabrication of films suggests the ability to extend this composite formation process to conformable gel films. PVA-UiO-66 composite hydrogels demonstrated higher sorption and sustained release of MB relative to UiO-66 powder and/or PVA-Zr-oxo hydrogels, showcasing the composites as beneficial materials for various sorption applications. While forming MOF-525 in the presence of PVA yielded increased sorptive capacity for Ang 1-7 relative to the metal cross-linked PVA hydrogels, the sorptive capacity of the PVA-MOF-525 composite hydrogels (8 wt%) was significantly lower than those reported for insulin, another therapeutic peptide, into either MIL-100, NU-1000, or MOF-545 (34 – 63 wt%).[43,44] Further, unlike the PVA-UiO-66 composites, we observed a burst release of Ang 1-7 from the PVA-MOF-25 composite gels. To that end, we expect both sorptive capacity and release profiles to highly depend on the compatibility of both the solute and the adsorbent being used, and we look forward to

exploring different combinations of MOFs and polymers to optimize these properties for larger peptide cargo. By understanding the role of molecular details of polymers and MOFs on the properties of composite gels prepared by forming MOFs in the presence of polymers, this study expands the design space of polymer-MOF gels, and offers a method to increase the processability and performance of MOFs for applications ranging from separations to medicine.

4.4 Future Directions

While our studies in this chapter provided much needed context on the individual effects of the polymer and MOF on both formation and sorptive/release performance of polymer-MOF composite gels, future studies will focus on improving their ability to encapsulate and release therapeutic peptides, such as Angiotensin 1-7 (Ang 1-7). One such direction is to incorporate our work with peptide esterification to increase the encapsulation efficiency of these composite gels for therapeutic peptides. One of the drawbacks of our PVA-MOF-525 composite hydrogels was that it only encapsulated less than 10% of the available Ang 1-7. A solution to overcoming this low encapsulation efficiency is to synthesize the composite gels in a solution containing Ang 1-7, which could theoretically lead to a 100% encapsulation efficiency, as we see complete gelation of solutions of polymer, Zr-oxo clusters, and organic linkers. However, as Ang 1-7, like most peptides, has carboxylic acids, we could imagine competition with carboxylic acids on the organic linkers creating either defective MOFs or preventing MOF formation all together, as seen with the PAA-UiO-66 composite gels (Figure 4.1). Additionally, bonds between Ang 1-7 carboxylic acids and the Zr-oxo clusters could prevent release from the composite gels upon encapsulation. Therefore, future studies will focus on the encapsulation and release of esterified peptide into and from polymer-MOF composite

gel carriers to increase encapsulation efficiency without affecting MOF crystallinity within the hydrogels. Further, we aim to perform systematic studies to determine the sorptive capacity and release behaviors of different polymer-MOF composite gel systems for Ang 1-7. By affording higher drug encapsulation efficiencies, higher MOF crystallinity, higher sorptive capacity, and tunable release profiles, these experiments will allow for the potential of polymer-MOF composite gels for reversible peptide encapsulation to be fully realized.

4.5 Materials & Methods

4.5.1 Materials

Zirconium (IV) propoxide solution (70 wt% in 1-propanol, Zr(OnPr)$_4$), N,N-dimethylformamide (DMF, ≥99.8%), poly(vinyl alcohol) (PVA: M_w ~ 146000 – 186000 g/mol & 99%+ hydrolyzed; M_w ~ 31000 – 50000 g/mol & 98-99% hydrolyzed; and M_w ~ 9000 – 10000 g/mol & 80% hydrolyzed), poly(ethylene glycol) (PEG, M_v ~ 100000 g/mol), poly(acrylic acid) (PAA, M_w ~ 1033000 g/mol), terephthalic acid (H$_2$BDC, 98%), 2-aminoterephthalic acid (H$_2$ATA, 99%), biphenyl-4,4'-dicarboxylic acid (BPDC, 97%), 4,4',4'',4'''-(porphine-5,10,15,20-tetrayl)tetrakis(benzoic acid) (TCPP, dye content 75%), dimethyl sulfoxide-d6 (deuteration ≥ 99.8%), acetic acid (≥99.7%), 4-ethoxycarbonylphenylboronic acid (95%), dioxane (99%), 1,3,6,8-tetrabromopyrene (97%), potassium phosphate tribasic (98%), tetrakis-(triphenylphosphine)palladium(0) (99%), potassium hydroxide (90%), chloroform (99%), dichloromethane (99.8%), methylene blue (certified by the Biological Stain Commission, dye content ≥82%) diisopropyl carbodiimide (DIC, 99.8%), N,N'-dimethylformamide (DMF, 99%), Oxyma Pure (99%), piperidine (99%), N,N-Diisopropylethylamine (DIPEA, 99%), trifluoroacetic acid (TFA, 99%), triisopropyl silane (TIPS) (98%), 2,2'-(ethylenedioxy)diethanethiol

(DODT) (95%), diethyl ether (99%), and acetonitrile (ACN, HPLC grade, 99.8%) were purchased from Sigma Aldrich. Dimethyl sulfoxide (DMSO, $\geq$99.9%), methanol (99.9%), and hydrochloric acid (HCl, 36.5−38%) were purchased from Fisher Scientific. Potassium iodide (KI, >99%) was purchased from VWR. Poly (acrylamide-*co*-acrylic acid) (PAAA, AMD: AA = 9:1, M_w ~ 210000 g/mol) was purchased from Polymer Source Inc. Fluorenylmethoxycarbonyl(Fmoc)-protected amino acids and 2-chlorotrityl chloride resin (0.6 mmol/g) were purchased from Advanced ChemTech (Louisville, Kentucky). 4,4',4'',4'''-(pyrene-1,3,6,8-tetrayl)tetrabenzoic acid (H_4TBAPy), the organic linker for NU-901, was synthesized following a previously published procedure, and characterized using ^{1}H nuclear magnetic resonance spectroscopy (**Figure C.14**).[45] All water was purified by in-house reverse osmosis (RO). Ultrapure water refers to water purified by a Thermo Scientific Barnstead Smart2Pure water purification system (18.2 mΩxcm).

4.5.2 Synthesis of Zr-oxo clusters in DMSO

Synthesis conditions were adapted from a previously published procedure.[23] Briefly, in a 20 mL glass vial, Zr(O*n*Pr)$_4$ (355 µL, 0.792 mmol, stored under N_2(g) until use) and acetic acid (4.00 mL, 69.9 mmol) were added to solvent (DMSO, 7.00 mL). The solution was sonicated for 10 min, placed in an oven at 130 °C for 2 h, and cooled to room temperature to yield Zr-oxo clusters for use in further synthesis.

4.5.3 Synthesis of Zr-oxo cluster in DI water

Synthesis conditions were adapted from ref. [24]. In a 20 mL glass vial, $ZrOCl_2$.8H2O (1.288 g) and acetic acid (5.00 mL) were dissolved in DI water (12.00 mL) via bath sonication. Then, the solution was heated at 70 °C for 2 h, and cooled to room temperature to yield Zr-oxo clusters for use in further synthesis.

4.5.4 Synthesis of UiO-66 powder in DMSO

Into a Zr-oxo cluster solution in DMSO (10.0 mL, 0.697 mmol of Zr), H_2BDC (120.0 mg, 0.722 mmol) was added and dissolved using sonication. The solution was stirred for 24 h at room temperature. The particles produced from this synthesis were not isolatable by centrifugation, and therefore were isolated by dialysis against deionized water in a 3.5 kDa molecular weight cut-off regenerated cellulose dialysis membrane (Spectra/Por). Each water change was allowed to equilibrate for ≥ 3h. After dialysis, the UiO-66 particles were allowed to settle in DI water and the sediment was dried at room temperature for 48 h in a fume hood to obtain the dried UiO-66 powder.

4.5.5 Synthesis of UiO-67 powder in DMSO

Into a Zr-oxo cluster solution in DMSO (10.0 mL, 0.697 mmol of Zr), BPDC (175.0 mg, 0.722 mmol) was added and sonicated for 10 min. The solution was heated at 130 °C for 24 h. Then the UiO-67 was separated from the supernatant by centrifugation (10 min, 9000 x g, 4 °C), and washed three times with DMSO and three times with acetone by centrifugation (10 min, 9000 x g, 4 °C). The UiO-67 sample was dried at 80 °C for 24 h to obtain the dried UiO-67 powder.

4.5.6 Synthesis of MOF-525 powder in DMSO

Into a Zr-oxo cluster solution in DMSO (10.0 mL, 0.697 mmol of Zr), TCPP (60.0 mg, 0.076 mmol) was added and sonicated for 10 min. The solution was heated at 130 °C for 24 h. Then the MOF-525 was separated from the supernatant by centrifugation (10 min, 9000 x g, 4 °C), and washed three times with DMSO and three times with acetone by centrifugation (10 min, 9000 x g, 4 °C). The MOF-525 sample was dried at 80 °C for 24 h to obtain the dried MOF-525 powder.

4.5.7 Synthesis of polymer-UiO-66 composite gels

In a 20 mL scintillation vial, 220.0 mg of polymer (PAA, PAAA, PVA, or PEO) was dissolved in DMSO (5.00 mL) by stirring at 120 °C for up to 45 min, then cooling to room temperature, where the polymers remained soluble. H_2BDC (120.0 mg, 0.722 mmol) was then added to the polymer solution. Next, the Zr-oxo cluster solution (5.00 mL in DMSO, 0.349 mmol of Zr) was added to the polymer-H_2BDC solution (5.00 mL in DMSO) and the mixture was shaken for 1 min and allowed to stand at room temperature for 24 h. After 24 h, the gelation of the mixture was evaluated using an inversion test (*i.e.*, inverting the vial). The polymer-UiO-66 composite gels with different wt% of polymer were synthesized by varying the polymer amount in a constant volume of DMSO (5.00 mL). The gels were stored at ambient temperature until further use.

4.5.8 Synthesis of polymer-Zr-oxo gels

In a 20 mL scintillation vial, 220.0 mg of polymer (PAA, PAAA, PVA, or PEO) was dissolved in DMSO (5.00 mL) by stirring at 120 °C for up to 45 min, then cooling to room temperature, where it remained soluble. Zr-oxo cluster solution (5.00 mL in DMSO, 0.349 mmol of Zr) was added to the polymer solution (5.00 mL in DMSO) and the mixture was shaken for 1 min and allowed to stand at room temperature for 24 h. After 24 h, the gelation of the mixture was evaluated using an inversion test. The gels were stored at ambient temperature until further use.

4.5.9 Synthesis of polymer-UiO-66 physical mixture

In a 20 mL scintillation vial, 220.0 mg of polymer (PAA, PAAA, PVA, or PEO) was dissolved in DMSO (5.00 mL) by stirring at 120 °C for up to 45 min, then cooling to room temperature, where it remained soluble. UiO-66 powder (95.0 mg, synthesized in DMSO) was added to the polymer solution (5.00 mL in DMSO) and the mixture was shaken for 1 min and allowed to stand at room temperature for 24 h. After 24 h, the gelation of the

mixture was evaluated using an inversion test. These mixtures were stored at ambient

temperature until use for characterization.

4.5.10 Synthesis of PVA-Zr-MOFs composite gels

In a 20 mL scintillation vial, 220.0 mg of PVA was dissolved in DMSO (5.00 mL)

by stirring at 120 °C for up to 45 min, then cooling to room temperature, where it remained

soluble. Organic linkers (**Table 4.1**) were then added to the PVA solution. Next, the Zr-

oxo clusters solution (5.00 mL in DMSO, 0.349 mmol of Zr) was added to PVA-linker

solution (5.00 mL) and the mixture was shaken for 1 min and allowed to stand at room

temperature for 24 h, after which the gelation of the mixture was evaluated using an

inversion test. The linker amount was determined based on the molar ratio of linker:Zr

used in the previously published syntheses to make MOFs (**Table 1**). The composite gels

were stored at ambient temperature until further use.

Table 4.1. Organic linkers used in the synthesis of PVA-Zr-MOF composite gels

Composite gel	Organic linker used to obtain the composite gel	Amount of organic linker used in composite gel synthesis	Molar ratio of linker:Zr in the composite gel	Molar ratio of linker:Zr in the literature
PVA-UiO-66[2]	H_2BDC	120.0 mg	2:1	1:1
PVA-NU-901[33]	H_4TBAPy	50.0 mg	1:5	1:5
PVA-UiO-67[23]	BPDC	175.0 mg	2:1	1:1
PVA-MOF-525*	TCPP	60.0 mg	1:5	--

*Since MOF-525, like NU-901, contains a tetratropic organic linker, we used the same linker:Zr ratio for MOF-525 composites as for the PVA-NU-901 composites.

4.5.11 Synthesis of PVA-UiO-66 composite gel film

The PVA-UiO-66 composite gel film synthesis procedure has been illustrated in

Scheme 4.1. First, a PVA-UiO-66 composite gel (2.5 wt%) in a vial was heated in the

oven at 80 °C for 2 h. Due to heating, the gel yielded a viscous liquid which was removed via syringe (0.5 mL) and spin coated on a glass substrate at 150 rpm for 30 s. The spin coated liquid film was then left covered in a petri dish overnight to yield a free-standing gel film. To record the diffraction pattern of the gel film, it was left uncovered to dry at room temperature for 3 d. Afterward, we recorded the diffraction of the dried gel film.

Scheme 4.1. Synthesis procedure to process the PVA-UiO-66 composite gel into a film

| Liquifying the gel in oven 80 °C | Spin coating the liquified gel | Gelation | Free-standing gel film |
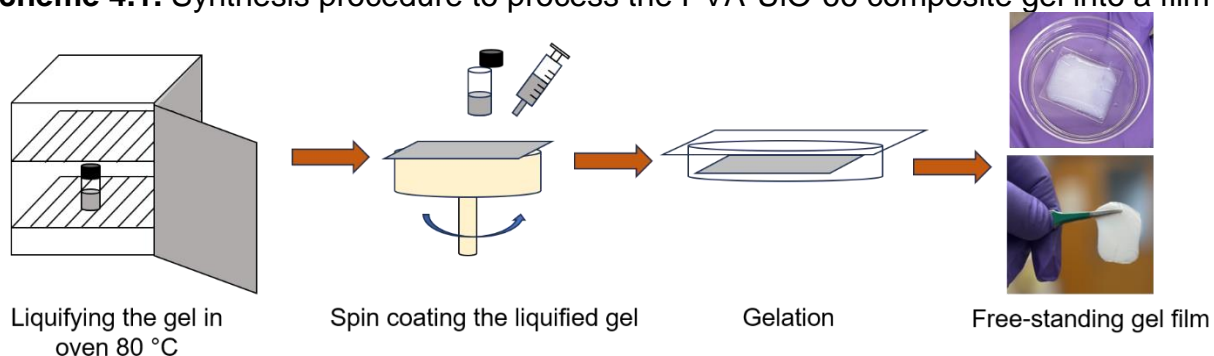
4.5.12 Synthesis trial of PVA-UiO-66 composite in DI water

In a 20 mL glass vial, 220.0 mg of PVA (M_w ~ 146000 – 186000 g/mol) was dissolved in DI water (5.00 mL) by stirring at 130 °C for up to 120 min, then cooling to room temperature, where the polymer remained soluble. H_2BDC (181.0 mg) and NaOH (80.0 mg) were added to the PVA solution. Next, Zr-oxo cluster solution (5.00 mL in DI water) was added to the polymer-H_2BDC solution (5.00 mL in DI water) and the mixture was shaken for 1 min and allowed to stand at room temperature for 24 h. After 24 h, the gelation of the mixture was evaluated using an inversion test (i.e., inverting the vial).

4.5.13 Synthesis of Angiotensin 1-7

Angiotensin 1-7 (DRVYIHP) was prepared using Fmoc-solid phase peptide synthesis with a CEM Liberty Blue microwave peptide synthesizer. To prepare the peptide with a carboxylic acid C-terminus, 2-chlorotrityl chloride resin (0.6 mmol/g) was used, and the entire synthesis was conducted at 25 °C to prevent premature cleavage of the ester

115

bond connecting the peptide to the resin, which was observed above 50 °C. DIC (1 M in DMF) and Oxyma Pure (1 M in DMF) were used to mediate amino acid coupling, except for the first amino acid, which was coupled to the resin using KI (0.125 M in DMF) and DIPEA (1 M in DMF). 20% piperidine in DMF (v/v) was used to deprotect Fmoc groups preceding amino acid additions. After synthesis, the peptide was cleaved from the resin using a deprotection cocktail comprised of 92.5% TFA, 2.5% RO water, 2.5% TIPS and 2.5% DODT by volume for 3 h at room temperature under constant stirring. Following deprotection, the peptide solution was separated from the resin by gravity filtration, and the peptide solution was precipitate into cold diethyl ether (5-8 mL of peptide solution in 30 mL ether), and centrifuged (5 min, 2420 x g, 4 °C) using a Thermo Scientific Haraeus Multifuge X3R. The supernatant was then decanted and the precipitated peptide pellet was washed again with the same volume diethyl ether and isolated by centrifugation under the same conditions and the supernatant decanted. The peptide pellet was dried under vacuum for 1 h, dissolved in 5% ACN in ultrapure water (v/v) and frozen with liquid nitrogen immediately prior to lyophilization for 48 h to produce a fluffy cake that was easy to manipulate. 60-70% yield was achieved for each synthesis.

4.5.14 Reverse-phase high-performance liquid chromatography (RP-HPLC)

Analytical RP-HPLC was performed at 35 °C with a flow rate of 1 mL/min on a Waters e2695 Alliance Separations Module, equipped with a XBridge® C18 chromatographic separation column (4.6 mm x 50 mm, 3.5 µm beads) and a photodiode array detector (Waters 2489 UV/Visible). The mobile phase consisted of ultrapurified water and ACN, both with 0.1% TFA by volume for pH maintenance. Peptide purification was completed using preparative scale RP-HPLC, which was performed at 25.52 mL/min at room temperature on a Waters Empower system,

equipped with a XBridge® Prep C18 optimum bed density chromatographic separation column (30 mm x 150 mm, 5 μm beads) and a photodiode array detector (Waters 2489 UV/Visible). UV absorbance was monitored at 214 nm for both systems. Mobile phase gradients for Ang 1-7 on each system are detailed in **Table 4.2**. The preparative scale mobile phase gradients were derived from those used at the analytical scale using the Waters Gradient Chromatography Calculator online tool.

Table 4.2. RP-HPLC mobile phase gradients

Time (m)		Gradient	
Analytical	**Preparative**	**% Water + 0.1% TFA (A)**	**% ACN + 0.1% TFA (B)**
0	0	95	5
0.5	2.22	82	18
3.5	15.07	80	20
3.7	15.93	5	95
4.2	18.07	5	95
4.8	20.65	95	5
6.0	25.79	95	5

4.5.15 Electrospray ionization mass spectrometry (ESI)

For mass spectrometry, Angiotensin 1-7 was dissolved at a concentration of 50 μg/mL in DI water. The experiment was performed on an Agilent G7104C LC system equipped with an Agilent G1958-65268 Dual AJS electrospray ionization source and Agilent 6545B QTOF mass spectrometer. The sample (0.2 μL) was eluted on a linear gradient of 0.1% formic acid in water and 0.1% formic acid in methanol, from 5% methanol

at 0 min to 100% methanol at 3 min. Separation was achieved using an Agilent InfinityLab

Poroshell 120 EC-C18 (3.0 mm ID x 100 mm, 2.7 µm pore size). Mass spectrometry data

was collected in negative ionization mode with the following ESI parameters: capillary

voltage = 4000 V; nozzle voltage = 250 V; fragmentor voltage = 90 V; drying gas flow = 5

L/min; drying gas temperature = 325 °C; and nebulizer gas pressure = 60 psig.

4.5.16 Solvent Exchange from DMSO to Water

All samples were placed in 3.5 kDa molecular weight cut-off regenerated cellulose

dialysis membranes (Spectra/Por 7) containing 15-20 mL of water and dialyzed against

DI H_2O. After allowing the solution to equilibrate for ≥ 3 h, the dialysate was replaced with

fresh DI H_2O. After four total dialysate replacements, the samples were removed and

stored in DI H_2O at room temperature prior to use.

4.5.17 Encapsulating solutes into MOF-based carriers

To measure the mass (m, in mg) of a solute, s (either methylene blue (MB) or the

peptide Angiotensin 1-7 (Ang1-7)), encapsulated into the MOF-based carriers at any

given time, t, or $m(t)_{s,\ carrier}$, we first prepared an aqueous solution of solute s (0.05 mg/mL

for MB or 0.57 mg/mL for Ang 1-7). This solution was termed the "outer solution", os, and

each sample carrier was added to a specific volume, V_{os} (mL). For consistency, we added

70 – 80 mg of each gel or 10 – 12 mg of UiO-66 powder to 17.5 – 20 mL of MB solution

(4 mg gel/mL MB solution, 0.16 mg UiO-66/mL MB solution), and ~100 – 120 mg gels

and/or MOF-525 to 10 – 12 mL of Ang 1-7 solution (10 mg carrier/mL Ang 1-7 solution)

for the encapsulation experiments. To calculate the sorption of a given solute s into each

sample at time t, we started with a mass balance on the solute in the vial. Specifically, we

considered $m(t)_{s,\ carrier}$ would be the difference between the total mass of s in the vial at

time t ($m(t)_{s,\ vial}$) and that in the outer solution at time t ($m(t)_{s,\ os}$) (**Equation 4.1**).

Equation 4.1) $m(t)_{s, carrier} = m(t)_{s, vial} - m(t)_{s, os}$

Rewriting Equation 4.1 in terms of the concentration (c, in mM) of s in the outer solution gives **Equation 4.2**.

Equation 4.2) $m(t)_{s, carrier} = m(t)_{s, vial} - c(t)_{s, os}V_{os}$

In Equation 4.2, we assume V_{os} to be constant, as the carriers are swollen when they enter the vial and therefore are unlikely to absorb appreciable amounts water from the outer solution upon incubation. As we are measuring the absorbance of the outer solution ($A(t)_{s,os}$) at the absorbance maximum wavelength (λ) specific to s (660 nm for MB and 277 nm for Ang 1-7), we convert it to a corresponding concentration ($c(t)_{s, os}$) using the Beer-Lambert law (**Equation 4.3**),

Equation 4.3) $A(t)_{s,os} = (\varepsilon_s b)c(t)_{s, os}$

where ε_s is the molar absorptivity of s and b is the optical path length in the configuration used (in this case a Biotek Synergy 4 plate reader), which we lump into one term determined from calibration curves for MB (Figure C.26a) and Ang 1-7 (Figure C.26b), fitting the data linearly to determine the ($\varepsilon_s b$) term for each solute s ($5 - 6 \times 10^{-3}$ absorbance units/μM MB and 7×10^{-4} absorbance units/μM Ang 1-7). To account for absorbance due to the carrier rather than to s (*e.g.*, linker that leaches into the outer solution), we placed each sample in two aqueous solutions, one containing s and the other containing only RO water. Once we subtracted the absorbance of water alone, which was often negligible relative to the absorbances of s, from that measured for each

sample, we accounted for any absorbance from the carrier at λ by subtracting the absorbance of the control (*cntrl*) sample outer solution ($A(t)_{cntrl,os}$) from that of the solution containing s ($A(t)_{s,os}$) to calculate a corrected absorbance of s in the outer solution ($A(t)^*_{s,os}$) (**Equation 4.4**).

Equation 4.4) $A(t)^*_{s,os} = A(t)_{s,os} - A(t)_{cntrl,os}$

Using our calibration curve for s, we then converted $A(t)^*_{s,os}$ to $c(t)_{s,\ os}$ Equation 4.3, and solved for $m(t)_{s,\ os}$ (**Equation 4.5**).

Equation 4.5) $m(t)_{s,\ os} = \frac{A(t)^*_{s,os}}{(\varepsilon_s b)} V_{os} MW_s$

where MW_s is the molecular weight of s. To measure $A(t)^*_{s,os}$, we removed an aliquot (with a volume V_a) of the outer solution at each timepoint (V_a = 0.6 mL for MB and V_a = 0.1 mL for Ang 1-7); however, removing these aliquots also $m(t)_{s,\ vial}$. To accurately calculate $m(t)_{s,\ vial}$, we need to calculate the mass of s in each aliquot ($m(t)_{s,\ aliquot}$) that we are removing from the vial using **Equation 4.6**.

Equation 4.6) $m(t)_{s,\ aliquot} = \frac{A(t)^*_{s,os}}{(\varepsilon_s b)} V_a MW_s$

After every aliquot, we replaced the volume removed in each aliquot (V_a) with the same volume of DI water (not containing s) to keep V_{os} constant. We then calculated $m(t)_{s,\ vial}$ by subtracting the sum of the mass of the aliquots removed before the time t ($\sum_{i=0}^{t-1} m(t)_{s,aliquot}$) from the initial mass of s added to the vial ($m(0)_{s,\ vial}$) (**Equation 4.7**).

Equation 4.7) $m(t)_{s,\ vial} = m(0)_{s,\ vial} - \sum_{i=0}^{t-1} m(t=i)_{s,aliquot}$

120

As s is only present in the outer solution at $t = 0$, $m(0)_{s, vial} = m(0)_{s, os}$, and we can rewrite Equation 4.7 as **Equation 4.8.**

Equation 4.8) $m(t)_{s, vial} = m(0)_{s, os} - \sum_{i=0}^{t-1} m(t = i)_{s,aliquot}$

Rewriting Equation 4.8 in terms of absorbance gives us a mass balance on the vial in terms of measured and/or known variables (**Equation 4.9**).

Equation 4.9) $m(t)_{s, vial} = \left[\frac{A(0)^*_{s,os}}{(\varepsilon_s b)} V_{os} - \sum_{i=0}^{t-1} \frac{A(t=i)^*_{s,os}}{(\varepsilon_s b)} V_{aliquot} \right] MW_s$

As we now know $m(t)_{s, os}$ and $m(t)_{s, vial}$ in terms of measured values, we can rearrange Equation 1 to solve for $m(t)_{s, carrier}$ using the $A(t)^*_{s,os}$ in the outer solution (**Equation 4.10**).

Equation 4.10) $m(t)_{s, carrier} = \left[\left(A(0)^*_{s,os} - A(t)^*_{s,os} \right) V_{os} - \sum_{i=0}^{t-1} \left(A(t = i)^*_{s,os} \right) V_{aliquot} \right] \frac{MW_s}{(\varepsilon_s b)}$

After calculating $m(t)_{s, carrier}$, we normalized these values relative to either the total weight of the carrier, dry weight of the carrier, or the weight of Zr in the carrier, as indicated. To calculate the dry weight of the carriers we weighed one sample of each of the hydrogels and MOF powder used in the encapsulation experiments and dried it at room temperature for 24 h. We then weighed the mass of the dried carriers and calculated a dry/wet weight ratio for each sample (dry weight of hydrogel/wet weight of hydrogel). The dry mass of each hydrogel used in the encapsulation experiment was calculated by multiplying the wet weight of the gel by this ratio, assuming similar swelling ratios across each of the hydrogel samples. As the MOF powder was added into each vial as a dry solid, its dry:wet mass ratio was 1. The Zr weight of each gel was calculated by multiplying the dry weight

of each hydrogel or MOF powder used for encapsulation by the Zr wt%, as determined by TGA (Figure C.22, Table C.2).

4.5.18 Release of solutes from MOF-based carriers

After encapsulation was complete, the outer solution of each sample (*s* and *cntrl*) was pipetted out and replaced with an equal amount of RO water. To account for the lower molar absorptivity of Ang 1-7 at 277 nm relative to MB at 660 nm, the outer solution was replaced with half of the volume of RO water (20 mg carrier/mL) in the Ang 1-7 experiments to increase $A(t)^*_{Ang\ 1-7,os}$. In these experiments, we were interested in determining the mass of solute released into the outer solution as a function of time, or $m(t)_{s,\ rel}$. To determine $c(t)_{s,\ os}$, we measured $A(t)^*_{s,os}$ at each timepoint *t*. We can directly measure $m(t)_{s,rel}$ through equation 5; however, we still have to account for $m_{s,aliquot}$, as we are removing a mass of *s* from our system for each measurement. Taken together, we can use **Equation 4.11** to calculate $m(t)_{s,rel}$ from a measured $A(t)^*_{s,os}$.

Equation 4.11) $m(t)_{s,rel} = \left[\left(A(t)^*_{s,os}\right)V_{os} + \sum_{i=0}^{t-1}\left(A(t=i)^*_{s,os}\right)V_{aliquot}\right]\frac{MW_s}{(\varepsilon_s b)}$

Here, we report the mass of *s* released into the outer solution ($m(t)_{MB,rel}$) relative to the total amount of MB released from the carriers after 21 d ($m(t=21)_{MB,\ rel}$) and the total amount of Ang 1-7 released from the carriers after 5 d ($m(t=5)_{Ang\ 1-7,\ rel}$) to better visualize and compare differences in the release profiles over time between each sample.

4.5.19 Statistics for encapsulation and release experiments

Each measurement represents an average of three independently synthesized samples, meaning 3 *s* and 3 *cntrl* samples from separate synthetic batches. Error bars represent the standard deviation between these three measurements. Each absorbance measurement represents the average of three individual measurements of one sample, and the standard deviation between these measurements was negligible.

4.5.20 Plate reader absorbance measurements

The absorbance of MB and Ang 1-7 were measured at 660 nm and 277 nm, respectively, on a Biotek Synergy 4 plate reader. All measurements were conducted in RO H_2O. Calibration curves were developed in triplicate through serial dilution of the MB and Ang 1-7 stock solutions.

4.5.21 Grazing incidence X-ray Diffraction (GIXD)

GIXD experiments were performed at beamline 11-3 of the Stanford Synchrotron Radiation Lightsource at SLAC National Accelerator Laboratory with a fixed beam energy of 12.7 keV. The two-dimensional (2D) GIXD diffraction patterns were recorded using a Rayonix MX225 CCD area detector. Wet gel samples and dry UiO-66 powder were put on a metal substrate holder to collect the 2D diffraction patterns. The sample-to-detector distance was 316 mm. Fast Azimuthal Integration (pyFAI) using python was used to obtain one-dimensional (1D) diffraction patterns from 2D GIXD diffraction patterns.

4.5.22 Coherence length calculation

Coherence length was calculated using the Scherrer equation[46] **(Equation 4.12)**:

Equation 4.12) $L = \frac{K*2\pi}{\Delta q}$

where L is coherence length, Δq is the full width at half maximum (FWHM) of the most intense peak in the diffraction pattern, and K is a dimensionless shape factor that depends on the shape of the crystallites. For spherical particles, K = 0.93. All calculated coherence lengths of UiO-66 particles synthesized in the presence of polymers are reported in Table 4.3.

Table 4.3. Coherence length of UiO-66 particles synthesized in the presence of polymers in DMSO

Sample name	Coherence length (nm)
PVA-UiO-66 gel	44

PEG-UiO-66 gel	32
PAAA-UiO-66 gel	26

4.5.23 Powder X-ray Diffraction (PXRD) for analysis of the gel film

To determine the presence of UiO-66 within the composite gel film spun on a glass substrate, PXRD patterns were collected using an Empyrean multipurpose X-ray diffractometer. Before the PXRD analysis, the gel film was dried at room temperature for 72 h. X-rays were generated using a water-cooled sealed X-ray tube with line focus Cu-anode (λ = 1.54 Å) operating at 45 keV and 40 mA. The one-dimensional (1D) PXRD diffraction patterns were recorded using a GaliPIX3D detector.

4.5.24 Scanning Electron Microscopy-energy dispersive x-ray spectroscopy (SEM-EDS)

The gels were dried at room temperature on a glass slide prior to characterization. The dry gel was sputter coated with a layer of Au/Pd using a Gatan 682 Precision Etching and Polishing System (PECS). SEM Images of the dry gel were obtained using a FEI quanta 650 field-emission secondary electron microscope. The accelerating voltage of the primary beam was kept between 5 kV and 15 kV, and the spot size was kept below 4. EDS analysis was performed using the same instrument at the voltage between 10 – 15 kV and spot size at 4.

4.5.25 Thermogravimetric analysis (TGA)

TGA was performed using a TA instruments Q50 thermogravimetric analyzer. The DMSO-swollen gels and the hydrogel samples were dried at room temperature, the former in a fume hood, for 48-72 h before analysis. The sample gas was air (flowrate = 60 mL/min) and the balance gas was N_2 (flowrate = 40 mL/min). Samples were heated from room temperature to 1000 °C at a rate of 10 °C/min on a platinum pan.

124

4.5.26 Calculating Zr content from TGA profiles

The Zr wt% in each sample was calculated from the final wt% of each sample at 1000 °C, as determined by TGA (**Figure C.22-C.25, Table C.2**). Since TGA was run in air, we assumed the inorganic fraction to be ZrO_2,[47] and calculated the wt% Zr in each sample by multiplying the final wt% (at 1000 °C) by the molecular weight fraction of Zr (91 g/mol) to ZrO_2 (123 g/mol) (**Table C.2**). The Zr wt% of each sample was calculated before and after solvent exchange, to track the loss of Zr throughout the process. As UiO-66 powder did not form large enough particles in DMSO to be separated from the supernatant, we could not analyze it using TGA. So, we could only analyze the UiO-66 powder after the dialysis.

4.5.27 [1]H Nuclear Magnetic Resonance Spectroscopy

^{1}H NMR spectroscopy was conducted on a 400 MHz Varian NMR spectrometer. To quantify the DMSO content in the composite gels before and after dialysis, we digested the 3 wt% PVA-UiO-66 composite gels in 1 M sodium deuteroxide in deuterium oxide (D_2O) at 10 mg/mL before and after dialysis. We then spiked the samples with 10 μL of methanol and used ^{1}H NMR spectroscopy to quantify the amount of DMSO, comparing the integration of the DMSO proton resonances to those of methanol to determine their wt% within the composite gels and hydrogels.

4.6 Acknowledgments

4.7 References

(1)   Peterson, G. W.; Au, K.; Tovar, T. M.; Epps, T. H. Multivariate Cubtc Metal-Organic Framework with Enhanced Selectivity, Stability, Compatibility, and Processability. *Chemistry of Materials* **2019**, *31* (20), 8459–8465. https://doi.org/10.1021/acs.chemmater.9b02756.

(2)   Sharma, P.; Goswami, R.; Neogi, S.; Shahi, V. K. Devising Ultra-Robust Mixed-Matrix Membrane Separators Using Functionalized MOF-Poly(Phenylene Oxide) for High-Performance Vanadium Redox Flow Batteries. *J Mater Chem A Mater* **2022**, *10* (20), 11150–11162. https://doi.org/10.1039/d1ta10715a.

(3)   Wang, M.; Huang, H.; Ma, X.; Huang, C.; Peng, X. Copper Metal-Organic Framework Embedded Carboxymethyl Chitosan-g-Glutathione/Polyacrylamide Hydrogels for Killing Bacteria and Promoting Wound Healing. *Int J Biol Macromol* **2021**, *187* (May), 699–709. https://doi.org/10.1016/j.ijbiomac.2021.07.139.

(4)   Nie, W.; Huang, Y.; Wang, Y.; Kengla, C.; Scott Copus, J.; Sun, J.; Shao, Z.; Dai, X.; Shen, Y. Temperature Sensitive PolyMOF Hydrogel Formed by in Situ Open-Ring Polymerization for Infected Chronic Wound Treatment. *Chemical Engineering Journal* **2022**, *446* (P2), 136948. https://doi.org/10.1016/j.cej.2022.136948.

(5)   Gwon, K.; Han, I.; Lee, S.; Kim, Y.; Lee, D. N. Novel Metal-Organic Framework-Based Photocrosslinked Hydrogel System for Efficient Antibacterial Applications. *ACS Appl Mater Interfaces* **2020**, *12* (18), 20234–20242. https://doi.org/10.1021/acsami.0c03187.

(6)   Javanbakht, S.; Nabi, M.; Shadi, M.; Amini, M. M.; Shaabani, A. Carboxymethyl Cellulose/Tetracycline@UiO-66 Nanocomposite Hydrogel Films as a Potential Antibacterial Wound Dressing. *Int J Biol Macromol* **2021**, *188* (May), 811–819. https://doi.org/10.1016/j.ijbiomac.2021.08.061.

(7)   Denny, M. S.; Cohen, S. M. In Situ Modification of Metal-Organic Frameworks in Mixed-Matrix Membranes. *Angewandte Chemie - International Edition* **2015**, *54* (31), 9029–9032. https://doi.org/10.1002/anie.201504077.

(8)   Zhao, R.; Ma, T.; Zhao, S.; Rong, H.; Tian, Y.; Zhu, G. Uniform and Stable Immobilization of Metal-Organic Frameworks into Chitosan Matrix for Enhanced Tetracycline Removal from Water. *Chemical Engineering Journal* **2020**, *382* (June 2019), 122893. https://doi.org/10.1016/j.cej.2019.122893.

(9)   Mahmoud, M. E.; Mohamed, A. K. Novel Derived Pectin Hydrogel from Mandarin Peel Based Metal-Organic Frameworks Composite for Enhanced Cr(VI) and Pb(II) Ions Removal. *Int J Biol Macromol* **2020**, *164*, 920–931. https://doi.org/10.1016/j.ijbiomac.2020.07.090.

(10)   Allegretto, J. A.; Giussi, J. M.; Moya, S. E.; Azzaroni, O.; Rafti, M. Synthesis and Characterization of Thermoresponsive ZIF-8@PNIPAm-: Co-MAA Microgel Composites

with Enhanced Performance as an Adsorption/Release Platform. *RSC Adv* **2020**, *10* (5), 2453–2461. https://doi.org/10.1039/c9ra09729e.

(11)   Lim, J.; Lee, E. J.; Choi, J. S.; Jeong, N. C. Diffusion Control in the in Situ Synthesis of Iconic Metal-Organic Frameworks within an Ionic Polymer Matrix. *ACS Appl Mater Interfaces* **2018**, *10* (4), 3793–3800. https://doi.org/10.1021/ACSAMI.7B17662/ASSET/IMAGES/LARGE/AM-2017-17662F_0006.JPEG.

(12)   Klein, S. E.; Sosa, J. D.; Castonguay, A. C.; Flores, W. I.; Zarzar, L. D.; Liu, Y. Green Synthesis of Zr-Based Metal-Organic Framework Hydrogel Composites and Their Enhanced Adsorptive Properties. *Inorg Chem Front* **2020**, *7* (24), 4813–4821. https://doi.org/10.1039/d0qi00840k.

(13)   Zhu, H.; Zhang, Q.; Zhu, S. Alginate Hydrogel: A Shapeable and Versatile Platform for in Situ Preparation of Metal-Organic Framework-Polymer Composites. *ACS Appl Mater Interfaces* **2016**, *8* (27), 17395–17401. https://doi.org/10.1021/acsami.6b04505.

(14)   Pastore, V. J.; Cook, T. R.; Rzayev, J. Polymer-MOF Hybrid Composites with High Porosity and Stability through Surface-Selective Ligand Exchange. *Chemistry of Materials* **2018**, *30* (23), 8639–8649. https://doi.org/10.1021/acs.chemmater.8b03881.

(15)   Hess, S. C.; Grass, R. N.; Stark, W. J. MOF Channels within Porous Polymer Film: Flexible, Self-Supporting ZIF-8 Poly(Ether Sulfone) Composite Membrane. *Chemistry of Materials* **2016**, *28* (21), 7638–7644. https://doi.org/10.1021/acs.chemmater.6b02499.

(16)   Palomba, J. M.; Wirth, D. M.; Kim, J. Y.; Kalaj, M.; Clarke, E. M.; Peterson, G. W.; Pokorski, J. K.; Cohen, S. M. Strong, Ductile MOF-Poly(Urethane Urea) Composites. *Chemistry of Materials* **2021**, *33* (9), 3164–3171. https://doi.org/10.1021/acs.chemmater.0c04874.

(17)   Unnikrishnan, V.; Zabihi, O.; Ahmadi, M.; Li, Q.; Blanchard, P.; Kiziltas, A.; Naebe, M. Metal-Organic Framework Structure-Property Relationships for High-Performance Multifunctional Polymer Nanocomposite Applications. *J Mater Chem A Mater* **2021**, *9* (8), 4348–4378. https://doi.org/10.1039/d0ta11255k.

(18)   Lawson, S.; Alwakwak, A. A.; Rownaghi, A. A.; Rezaei, F. Gel-Print-Grow: A New Way of 3D Printing Metal-Organic Frameworks. *ACS Appl Mater Interfaces* **2020**, *12* (50), 56108–56117. https://doi.org/10.1021/acsami.0c18720.

(19)   Garai, A.; Shepherd, W.; Huo, J.; Bradshaw, D. Biomineral-Inspired Growth of Metal-Organic Fra(1) Garai, A.; Shepherd, W.; Huo, J.; Bradshaw, D. Biomineral-Inspired Growth of Metal-Organic Frameworks in Gelatin Hydrogel Matrices. J. Mater. Chem. B 2013, 1 (30), 3678–3684. Https://Doi.Org/10.1039/C3tb2. *J Mater Chem B* **2013**, *1* (30), 3678–3684. https://doi.org/10.1039/c3tb20814a.

(20) Zhuang, Y.; Kong, Y.; Wang, X.; Shi, B. Novel One Step Preparation of a 3D Alginate Based MOF Hydrogel for Water Treatment. *New Journal of Chemistry* **2019**, *43* (19), 7202–7208. https://doi.org/10.1039/c8nj06031b.

(21) Wang, Y.; Peng, H.; Wang, H.; Zhang, M.; Zhao, W.; Zhang, Y. In-Situ Synthesis of MOF Nanoparticles in Double-Network Hydrogels for Stretchable Adsorption Device. *Chemical Engineering Journal* **2022**, *450* (P3), 138216. https://doi.org/10.1016/j.cej.2022.138216.

(22) Tang, L.; Gong, L.; Xu, Y.; Wu, S.; Wang, W.; Zheng, B.; Tang, Y.; Zhang, D.; Tang, J.; Zheng, J. Mechanically Strong Metal–Organic Framework Nanoparticle-Based Double Network Hydrogels for Fluorescence Imaging. *ACS Appl Nano Mater* **2022**, *5* (1), 1348–1355. https://doi.org/10.1021/acsanm.1c03034.

(23) Destefano, M. R.; Islamoglu, T.; Garibay, S. J.; Hupp, J. T.; Farha, O. K. Room-Temperature Synthesis of UiO-66 and Thermal Modulation of Densities of Defect Sites. **2017**, 6–10. https://doi.org/10.1021/acs.chemmater.6b05115.

(24) Huelsenbeck, L.; Luo, H.; Verma, P.; Dane, J.; Ho, R.; Beyer, E.; Hall, H.; Geise, G. M.; Giri, G. Generalized Approach for Rapid Aqueous MOF Synthesis by Controlling Solution PH. *Cryst Growth Des* **2020**, *20* (10), 6787–6795. https://doi.org/10.1021/acs.cgd.0c00895.

(25) Somjit, V.; Thinsoongnoen, P.; Waiprasoet, S.; Pila, T.; Pattanasattayavong, P.; Horike, S.; Kongpatpanich, K. Processable UiO-66 Metal-Organic Framework Fluid Gel and Electrical Conductivity of Its Nanofilm with Sub-100 Nm Thickness. *ACS Appl Mater Interfaces* **2021**, *13* (26), 30844–30852. https://doi.org/10.1021/acsami.1c07262.

(26) Patterson, A. L. The Scherrer Formula for X-Ray Particle Size Determination. *Physical Review* **1939**, *56* (10), 978–982. https://doi.org/10.1103/PhysRev.56.978.

(27) Dighe, A. V.; Huelsenbeck, L.; Bhawnani, R. R.; Verma, P.; Stone, K. H.; Singh, M. R.; Giri, G. Autocatalysis and Oriented Attachment Direct the Synthesis of a Metal-Organic Framework. *JACS Au* **2022**, *2* (2), 453–462. https://doi.org/10.1021/jacsau.1c00494.

(28) MacRae, C. F.; Sovago, I.; Cottrell, S. J.; Galek, P. T. A.; McCabe, P.; Pidcock, E.; Platings, M.; Shields, G. P.; Stevens, J. S.; Towler, M.; Wood, P. A. Mercury 4.0: From Visualization to Analysis, Design and Prediction. *J Appl Crystallogr* **2020**, *53*, 226–235. https://doi.org/10.1107/S1600576719014092.

(29) Deblock, L.; Goossens, E.; Pokratath, R.; De Buysser, K.; De Roo, J. Mapping out the Aqueous Surface Chemistry of Metal Oxide Nanocrystals: Carboxylate, Phosphonate, and Catecholate Ligands. *JACS Au* **2022**, *2* (3), 711–722. https://doi.org/10.1021/JACSAU.1C00565/ASSET/IMAGES/LARGE/AU1C00565_0009. JPEG.

(30) Verma, P. K.; Huelsenbeck, L.; Nichols, A. W.; Islamoglu, T.; Heinrich, H.; Machan, C. W.; Giri, G. Controlling Polymorphism and Orientation of NU-901/NU-1000 Metal-

Organic Framework Thin Films. *Chemistry of Materials* **2020**, *32* (24), 10556–10565. https://doi.org/10.1021/acs.chemmater.0c03539.

(31)   Chavan, S.; Vitillo, J. G.; Gianolio, D.; Zavorotynska, O.; Civalleri, B.; Jakobsen, S.; Nilsen, M. H.; Valenzano, L.; Lamberti, C.; Lillerud, K. P.; Bordiga, S. H 2 Storage in Isostructural UiO-67 and UiO-66 MOFs. *Physical Chemistry Chemical Physics* **2012**, *14* (5), 1614–1626. https://doi.org/10.1039/c1cp23434j.

(32)   Morris, W.; Volosskiy, B.; Demir, S.; Gándara, F.; McGrier, P. L.; Furukawa, H.; Cascio, D.; Stoddart, J. F.; Yaghi, O. M. Synthesis, Structure, and Metalation of Two New Highly Porous Zirconium Metal-Organic Frameworks. *Inorg Chem* **2012**, *51* (12), 6443–6445. https://doi.org/10.1021/ic300825s.

(33)   Islamoglu, T.; Farha, O. K. Revisiting the Structural Homogeneity of NU-1000, a Zr-Based Metal–Organic Framework. **2018**, *20* (39). https://doi.org/10.1039/c8ce00455b.

(34)   Song, X.; Yang, P.; Wu, D.; Zhao, P.; Zhao, X.; Yang, L.; Zhou, Y. Facile Synthesis of Metal-Organic Framework UiO-66 for Adsorptive Removal of Methylene Blue from Water. *Chem Phys* **2020**, *531*. https://doi.org/10.1016/j.chemphys.2019.110655.

(35)   Mohammadi, A. A.; Alinejad, A.; Kamarehie, B.; Javan, S.; Ghaderpoury, A.; Ahmadpour, M.; Ghaderpoori, M. Metal-Organic Framework Uio-66 for Adsorption of Methylene Blue Dye from Aqueous Solutions. *International Journal of Environmental Science and Technology* **2017**, *14* (9), 1959–1968. https://doi.org/10.1007/s13762-017-1289-z.

(36)   Muttenthaler, M.; King, G. F.; Adams, D. J.; Alewood, P. F. Trends in Peptide Drug Discovery. *Nature Reviews Drug Discovery,* **2021**, *20* (4), 309-325 https://doi.org/10.1038/s41573-020-00135-8.

(37)   Fosgerau, K.; Hoffmann, T. Peptide Therapeutics: Current Status and Future Directions. *Drug Discov Today* **2015**, *20* (1), 122–128. https://doi.org/10.1016/J.DRUDIS.2014.10.003.

(38)   Lau, J. L.; Dunn, M. K. Therapeutic Peptides: Historical Perspectives, Current Development Trends, and Future Directions. *Bioorg Med Chem* **2018**, *26* (10), 2700–2707. https://doi.org/10.1016/j.bmc.2017.06.052.

(39)   Di, L. Strategic Approaches to Optimizing Peptide ADME Properties. *AAPS Journal* **2015**, *17* (1), 134–143. https://doi.org/10.1208/s12248-014-9687-3.

(40)   Petty, W. J.; Miller, A. A.; McCoy, T. P.; Gallagher, P. E.; Tallant, E. A.; Torti, F. M. Phase I and Pharmacokinetic Study of Angiotensin-(1-7), an Endogenous Antiangiogenic Hormone. *Clinical Cancer Research* **2009**, *15* (23), 7398–7404. https://doi.org/10.1158/1078-0432.CCR-09-1957.

(41)   Jiang, F.; Yang, J.; Zhang, Y.; Dong, M.; Wang, S.; Zhang, Q.; Liu, F. F.; Zhang, K.; Zhang, C. Angiotensin-Converting Enzyme 2 and Angiotensin 1-7: Novel Therapeutic

Targets. *Nature Reviews Cardiology*, **2014**, *11* (7), 413 - 426.
https://doi.org/10.1038/nrcardio.2014.59.

(42) Morris, W.; Volosskiy, B.; Demir, S.; Gándara, F.; McGrier, P. L.; Furukawa, H.; Cascio, D.; Stoddart, J. F.; Yaghi, O. M. Synthesis, Structure, and Metalation of Two New Highly Porous Zirconium Metal-Organic Frameworks. *Inorg Chem* **2012**, *51* (12), 6443–6445. https://doi.org/10.1021/ic300825s.

(43) Zhou, Y.; Liu, L.; Cao, Y.; Yu, S.; He, C.; Chen, X. A Nanocomposite Vehicle Based on Metal-Organic Framework Nanoparticle Incorporated Biodegradable Microspheres for Enhanced Oral Insulin Delivery. *ACS Appl Mater Interfaces* **2020**, *12* (20), 22581–22592. https://doi.org/10.1021/acsami.0c04303.

(44) Wang, S.; Chen, Y.; Wang, S.; Li, P.; Mirkin, C. A.; Farha, O. K. DNA-Functionalized Metal-Organic Framework Nanoparticles for Intracellular Delivery of Proteins. *J Am Chem Soc* **2019**, *141* (6), 2215–2219. https://doi.org/10.1021/jacs.8b12705.

(45) Wang, T. C.; Vermeulen, N. A.; Kim, I. S.; Martinson, A. B. F.; Stoddart, J. F.; Hupp, J. T.; Farha, O. K. Scalable Synthesis and Post-Modification of a Mesoporous Metal-Organic Framework Called NU-1000. *Nat Protoc* **2016**, *11* (1), 149–162. https://doi.org/10.1038/nprot.2016.001.

(46) Patterson, A. L. The Scherrer Formula for X-Ray Particle Size Determination. *Physical Review* **1939**, *56* (10), 978–982. https://doi.org/10.1103/PhysRev.56.978.

(47) Athar, M.; Rzepka, P.; Thoeny, D.; Ranocchiari, M.; Anton Van Bokhoven, J. Thermal Degradation of Defective High-Surface-Area UiO-66 in Different Gaseous Environments. *RSC Adv* **2021**, *11* (61), 38849–38855. https://doi.org/10.1039/d1ra05411b.

CHAPTER 5:
CONCLUSIONS AND PERSPECTIVES ON THE FIELD

In this thesis, we establish esterification as a method to increase the cell membrane permeability of therapeutic peptides and enable their encapsulation into relevant delivery vehicles, such as PECs. Additionally, we design polymer-metal organic framework (MOF) composite gels as potential delivery vehicles for therapeutic peptides. Taken together, the work presented in this thesis serves to further the design of therapeutic peptides and their carriers to realize their potential as therapeutics and increase their implementation into the clinic.

In **Chapter 2**, we found that both the number and, more importantly, position of esters installed onto therapeutic peptides affect hydrophobicity and hydrolytic stability. For αCT11, esters installed on the C-terminus yielded the largest increase in both properties, and we look forward to see if this is more indicative of amino acid position within the sequence (i.e., 5, 6, 8, C-terminus) or type (I,e,. D, E, I, etc.) to establish general design rules for therapeutic peptide esterification. While we did not observe any significant differences in scratched human dermal fibroblasts treated with either αCT11-3OMe(D5,D6,E8) or αCT11-4OMe, treatment with both formulations produced a significant difference in scratched fibroblasts relative to those treated with unesterified αCT11, suggesting that esterifying αCT11 assists with wound healing, possibly through increased cell internalization and access to intracellular targets.

Building upon the conclusion that esterification can successfully cap anionic carboxylic acids on therapeutic peptides and increase their overall net charge, we next used esterification as a tool to make net-cationic αCT11-4OMe amenable to complexation with anionic PMAA and subsequent reversible encapsulation within PECs in **Chapter 3**.

In this chapter we found that esterification not only enables PEC formation not observed with unesterified peptide, but ensuing ester hydrolysis also coincided with a decrease in turbidity and assumed PEC dissociation. As we see esterification as a general strategy to reversibly encapsulate a wide range of therapeutic peptides (such as Ang 1-7), we look forward to expanding upon this initial proof of concept to probe esterified peptide complexation with different polymers (i.e., hydrophobic polymers) and use what we learned from Chapter 2 to determine the effect of ester number, position, and even type on PEC formation and subsequent release profiles.

Finally, **Chapter 4** develops design rules for polymer-MOF composite gels, leveraging the high sorptive capacity of MOFs within processable polymer gel templates to form beneficial carriers for therapeutic peptides. We learned that polymer chemistry can significantly affect the formation of polymer-MOF composite gels, as interactions between the polymer and MOF metal node are necessary to form robust, stable gels, but these interactions cannot be too strong to outcompete organic linkers and prevent MOF formation. Interestingly, we saw that the sorptive properties and release profiles of polymer-MOF composite gels are highly dependent on MOF chemistry and the solute itself. While PVA-UiO-66 composite hydrogels had increased sorptive capacities and extended release profiles relative to the polymer gel or MOF powder alone for methylene blue, polymer-MOF composite gels with the large-pore MOF MOF-525 enabled only increased sorptive capacity for the peptide angiotensin 1-7 relative to the polymer gels alone, and instead exhibited burst release profiles. This suggests that further engineering and synergistic matching of the MOF carrier and solute are required for optimum performance, which we look forward to studying in the future.

The field of therapeutic peptides has been rapidly growing for the past few decades, with relevant publications growing from less than 100 in 1990 to over 5000 in 2022 (**Figure 5.1**). While insulin continues to dominate the pharmaceutical market, drugs such as semaglutide are gaining traction due to their potency. As issues with peptide cell membrane permeability and *in vivo* half-lives are still prevalent and a defining characteristic of most peptides, well known strategies such as peptide cyclization, *N*-methylation, and appending either cell penetrating peptide or lipophilic tags remain the gold standard for increasing the bioavailability of peptides. Esterification could very well replace these strategies as a mechanism to increase bioavailability; however, it remains to be seen how esterification itself *in vivo* half-life. As esterification doesn't significantly change the therapeutic size in solution to counteract renal clearance, and it stands to be seen whether esters can protect peptides from proteolytic degradation, esterified peptides would likely still require a delivery vehicle to avoid rapid clearance and realize their full therapeutic potential *in vivo*. Therefore, we see the primary impact of esterification to likely be its ability to tailor therapeutic peptides for delivery, either through encapsulation into relevant delivery carriers, such as PECs or polymer-MOF composite hydrogels. Additionally, the increase in lipid bilayer membrane permeability could be specifically relevant to encapsulation inside of lipid vesicles, such as liposomes or exosomes. In all, multi-site esterification offers a tunable and reversible strategy to modify therapeutic peptides without a related sacrifice in activity as usually seen with comparable permanent modifications, and provides the potential to enable the widespread implementation of this beneficial class of therapeutics.

Publications containing "Therapeutic Peptide"
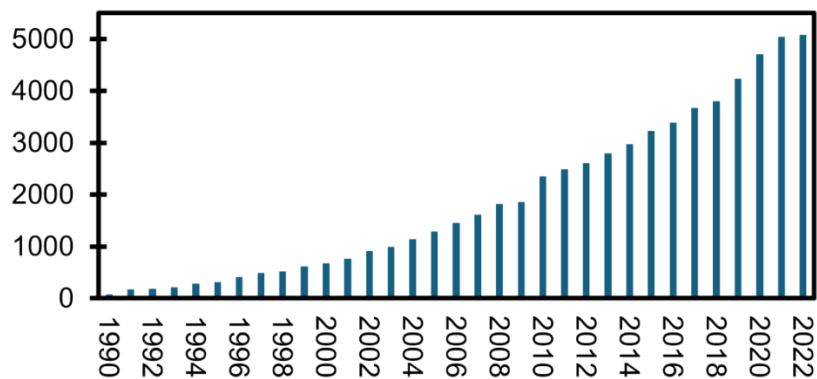
Figure 5.1. Publications containing the term "therapeutic peptide" since 1990. Plot was generated using data from www.webofscience.com.

CHAPTER A:
SUPPLEMENTARY INFORMATION FOR CHAPTER 2: MULTI-SITE ESTERIFICATION: A TUNABLE, REVERSIBLE STRATEGY TO TAILOR A THERAPEUTIC PEPTIDE FOR DELIVERY

LIST OF FIGURES

LIST OF TABLES

A.1 Fischer Esterification of αCT11

Figure A.1. RP-HPLC chromatograms of αCT11 Fischer esterification replicates, showing 3 independently set up reaction mixtures. The peptide eluted between 25% and 40% acetonitrile in each different reaction, with the produced peaks overlapping each other. Mobile phase composition (% ACN, gray) is plotted against normalized retention time in each RP-HPLC chromatogram.

Table A.1. RP-HPLC mobile phase gradients

Mobile Phase Stages	Time (min)		Mobile Phase Composition	
	Analytical	Preparative	% Water + 0.1% TFA (A)	% Acetonitrile + 0.1% TFA (B)
Warm up	0	0	95	5
Ramp up	0.5	2.6	95	5
Elution	5	25.2	77	23
	15	50.2	74	26
Purge	15.1	50.7	5	95
	16.1	60.0	5	95
Equilibration	16.2	60.6	95	5
	22	70.0	95	5

In this study, our RP-HPLC mobile phase gradients had five stages. First was the warm-up stage, where the system was equilibrated for 30 s with a mobile phase composition of 95% water + 0.1% trifluoroacetic acid (TFA) (mobile phase A) and 5% acetonitrile + 0.1% TFA (mobile phase B). During the ramp-up stage, the % B in the mobile phase was increased linearly to 23% over 4.5 min. In the elution stage, the % B was further increased linearly to 26% over 10 min to elute the sample from the column. To remove any bound solute from the column, we then increased the % B to 95% linearly and held at that

composition for 1 min, in the purge phase of the elution. Finally, the equilibration phase was used to prepare the system for the next injection, where the % B was reset to 5% and held there for 5.8 min. The flowrates of mobile phase in the analytical and preparative-scale RP-HPLC systems were 1 mL/min and 25.52 mL/min, respectively.
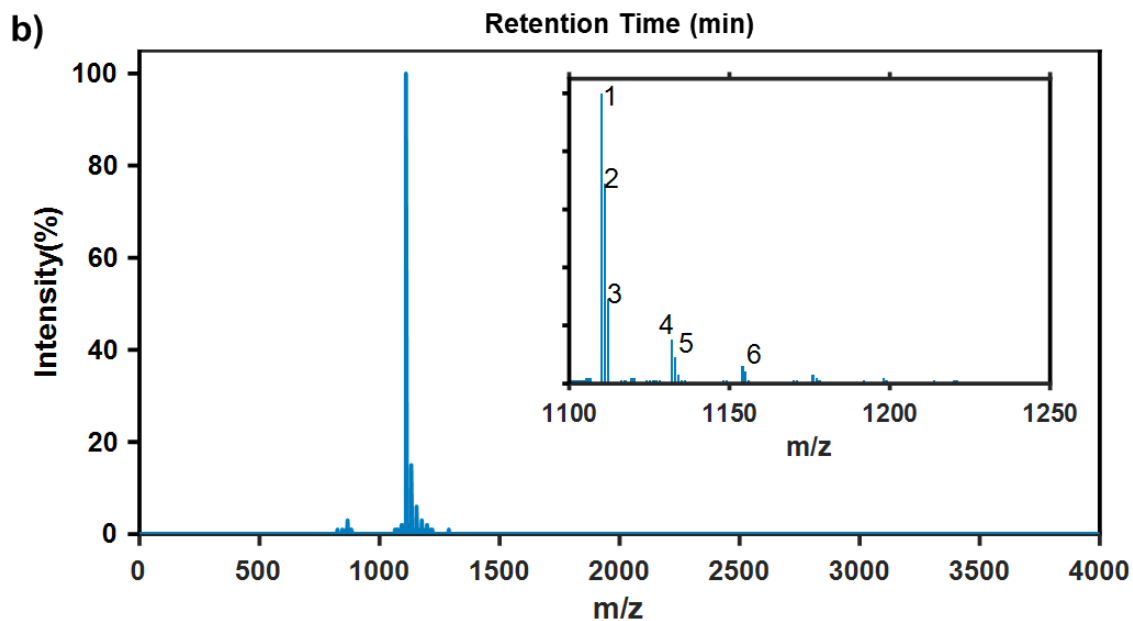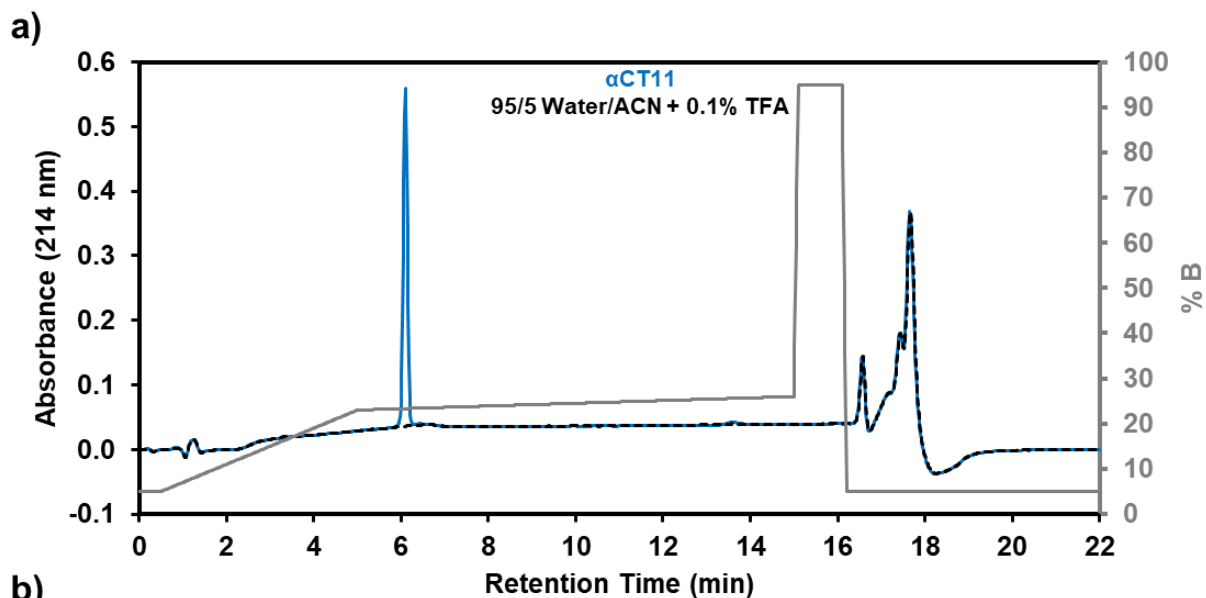
label	Mass (Da)	Intensity (%)	Species
1	1110	100	
2	1111.1	69	[αCT11 + H]+
3	1112.1	29	
4	1132.1	15	[αCT11 + Na]+
5	1133.1	9	
6	1154.1	6	[αCT11 + 2Na - H]+

Figure A.2 a) RP-HPLC chromatogram and **b)** MALDI-TOF MS of αCT11. In MALDI-TOF, [αCT11+2Na-H]$^+$ indicates that one of the originally protonated carboxylic acids now carries a sodium counterion.

Table A.2. Installed methyl ester number and position, normalized retention times of the products in each gradient, and percent peak area of αCT11 and its esterified products

αCT11 Product	# of methyl esters installed	Esterified Residues	COOH Residues	Normalized Retention Time (τ)	Percent Peak Area
αCT11	0	N/A	D5, D6, E8, I9	0	N/A
2OMe	2	*Not Determined		0.22	1
3OMe(A)	3	D5, D6, E8	I9	0.35	19
3OMe(B)	3	D5, D6, I9	E8	0.69	4
3OMe(C)	3	D6, E8, I9	D5	0.70	
3OMe(D)	3	D5, E8, I9	D6	0.75	
4OMe	4	D5, D6, E8, I9	N/A	1.00	74

*Ester positions were not able to be determined by ^{1}H NMR spectroscopy (insufficient amounts isolated)

Table A.3. Calculated molecular mass of αCT11 with various numbers of esters, charge (z) = 1

Sample:	αCT11	αCT11-1OMe	αCT11-2OMe	αCT11-3OMe	αCT11-4OMe
Exact Mass:	1109.6	1123.6	1137.6	1151.6	1165.7
[M + H]+	1110.6	1124.6	1138.6	1152.6	1166.7
[M + Na]+	1132.6	1146.6	1160.6	1174.6	1188.7
[M + K]+	1148.6	1162.6	1176.6	1190.6	1204.7
[M + 2Na - H]+	1154.6	1168.6	1182.6	1196.6	
[M + K + Na - H]+	1170.6	1184.6	1198.6	1212.6	
[M + 1 imide + H]+	1092.6	1106.6	1120.6	1134.6	
[M + 1 imide + Na]+	1114.6	1128.6	1142.6	1156.6	
[M + 1 imide + K]+	1130.6	1144.6	1158.6	1172.6	
[M + 2 imide + H]+	1074.6	1088.6	1102.6		
[M + 2 imide + Na]+	1096.6	1110.6	1124.6		
[M + 2 imide + K]+	1112.6	1126.6	1140.6		
[M + 3 imide + H]+	1056.6	1070.6			
[M + 3 imide + Na]+	1078.6	1092.6			
[M + 3 imide + K]+	1094.6	1108.6			
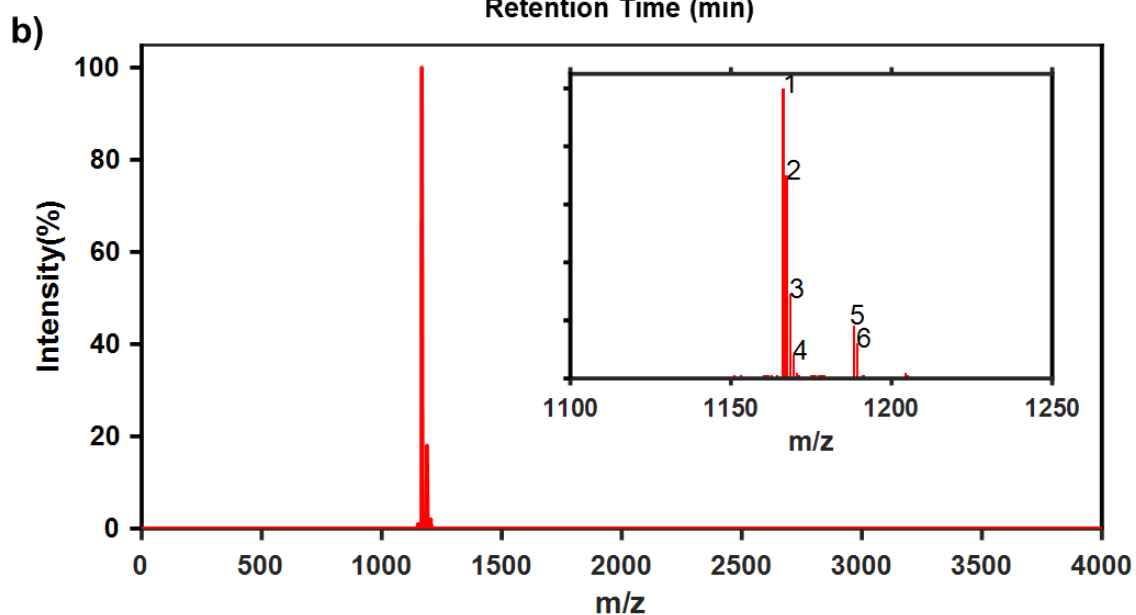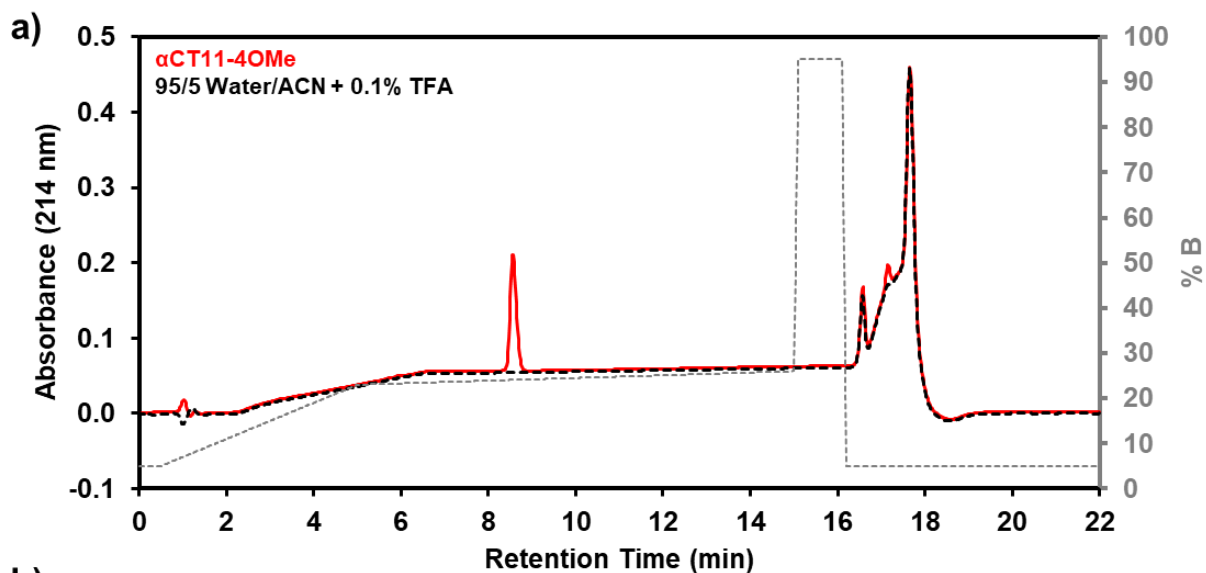
label	Mass (Da)	Intensity (%)	Species
1	1166.3	100	[αCT11-4OMe + H]+
2	1167.3	70	
3	1168.4	29	
4	1169.4	8	
5	1188.3	18	[αCT11-4OMe + Na]+
6	1189.3	12	

Figure A.3. a) RP-HPLC chromatogram and **b-c)** MALDI-TOF MS of αCT11-4OMe.

label	Mass (Da)	Intensity (%)	Species
1	1151.6	100	[αCT11-3OMe + H]+
2	1152.6	59	[αCT11-3OMe + H]+
3	1153.6	20	[αCT11-3OMe + H]+
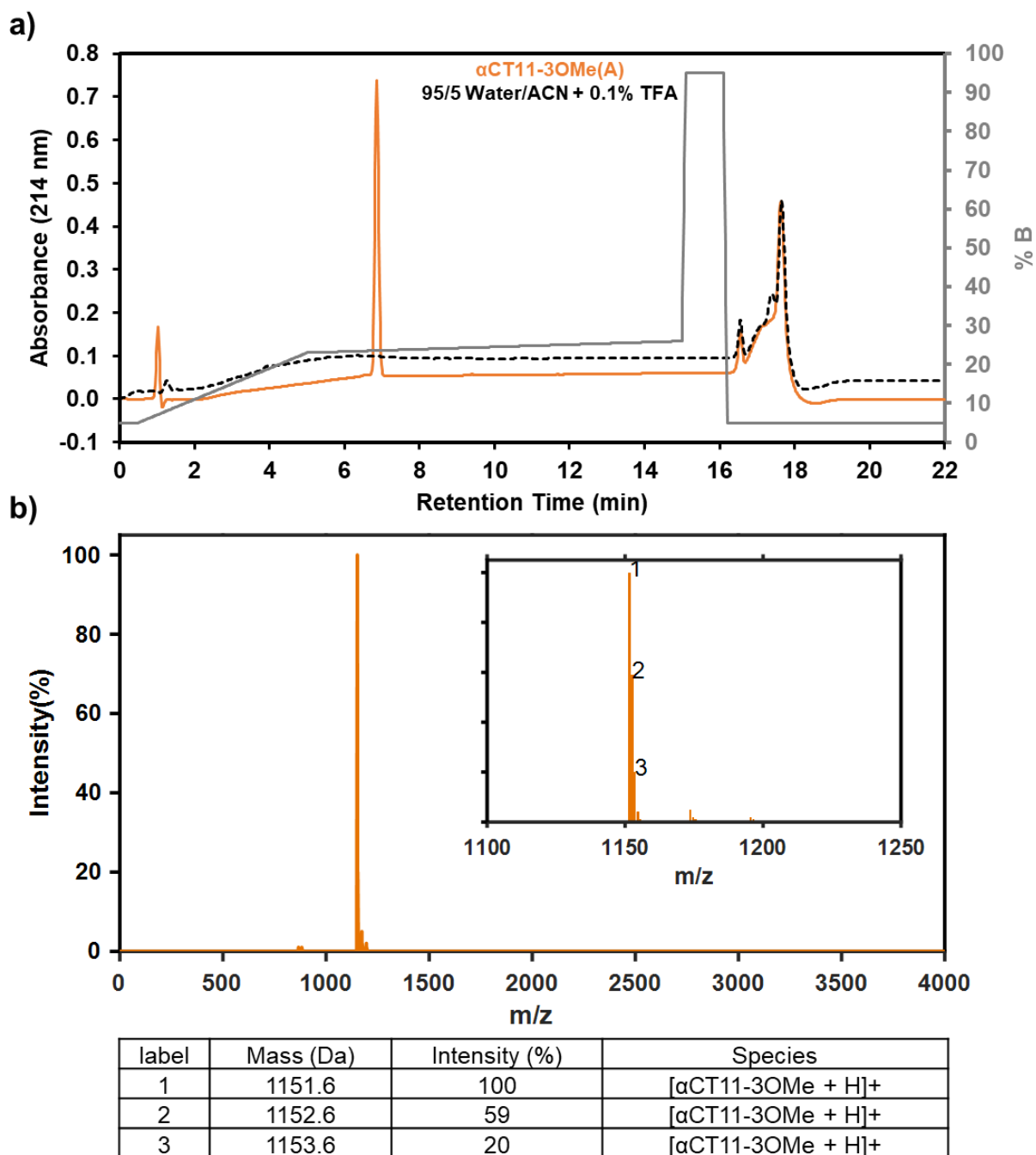
Figure A.4. a) RP-HPLC chromatogram and **b)** MALDI-TOF MS of αCT11-3OMe(A), with [3OMe+2Na-H]+ indicating that one of the originally protonated carboxylic acids now carries a sodium counterion.
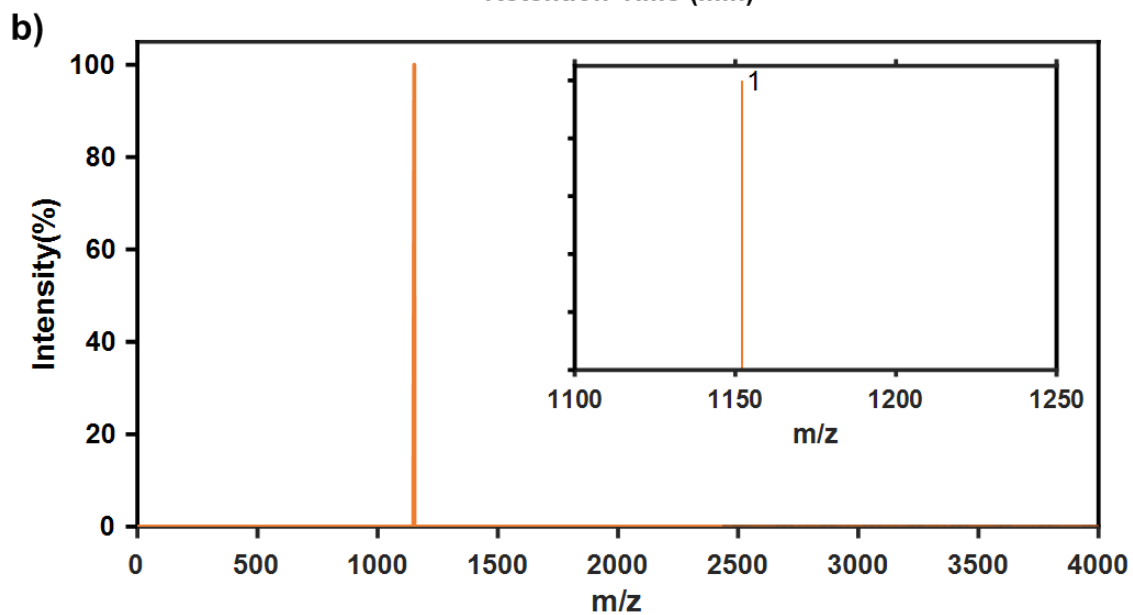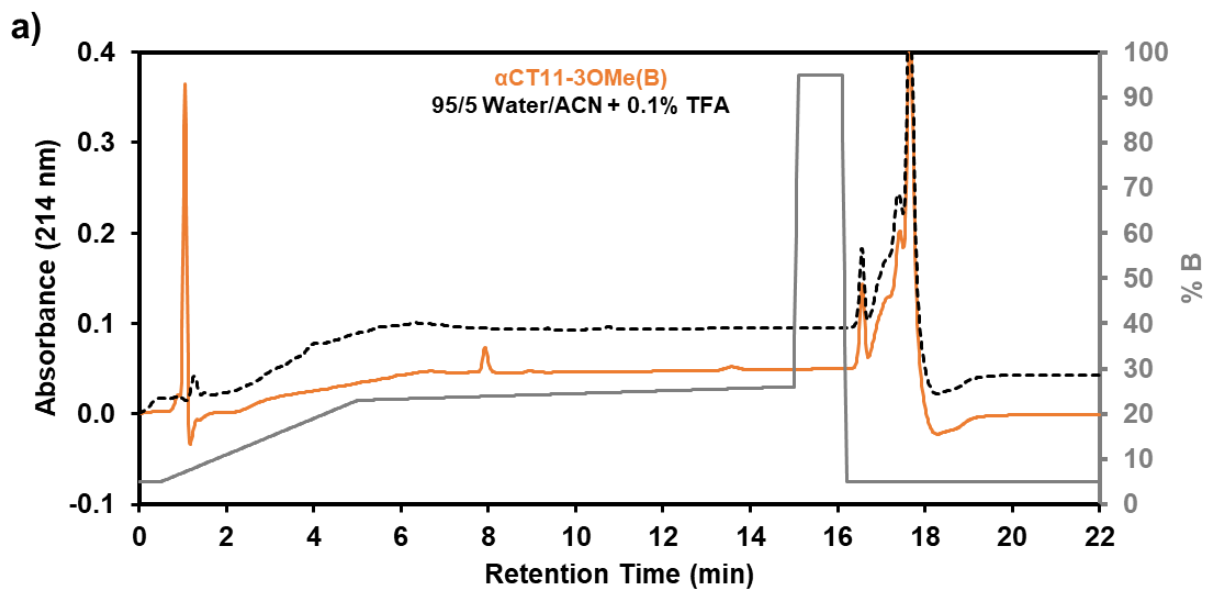
label	Mass (Da)	Intensity (%)	Species
1	1152.2	100	[αCT11-3OMe + H]+

Figure A.5. a) RP-HPLC chromatogram and **b)** MALDI-TOF MS of αCT11-3OMe(B).

label	Mass (Da)	Intensity (%)	Species
1	1152.3	65	
2	1153.3	51	[αCT11-3OMe + H]+
3	1154.3	29	
4	1174.4	20	
5	1175.2	18	[αCT11-3OMe + Na]+
6	1176.2	10	
7	1196.3	13	
8	1197.2	11	[αCT11-3OMe + 2Na - H]+
9	1198.2	6	
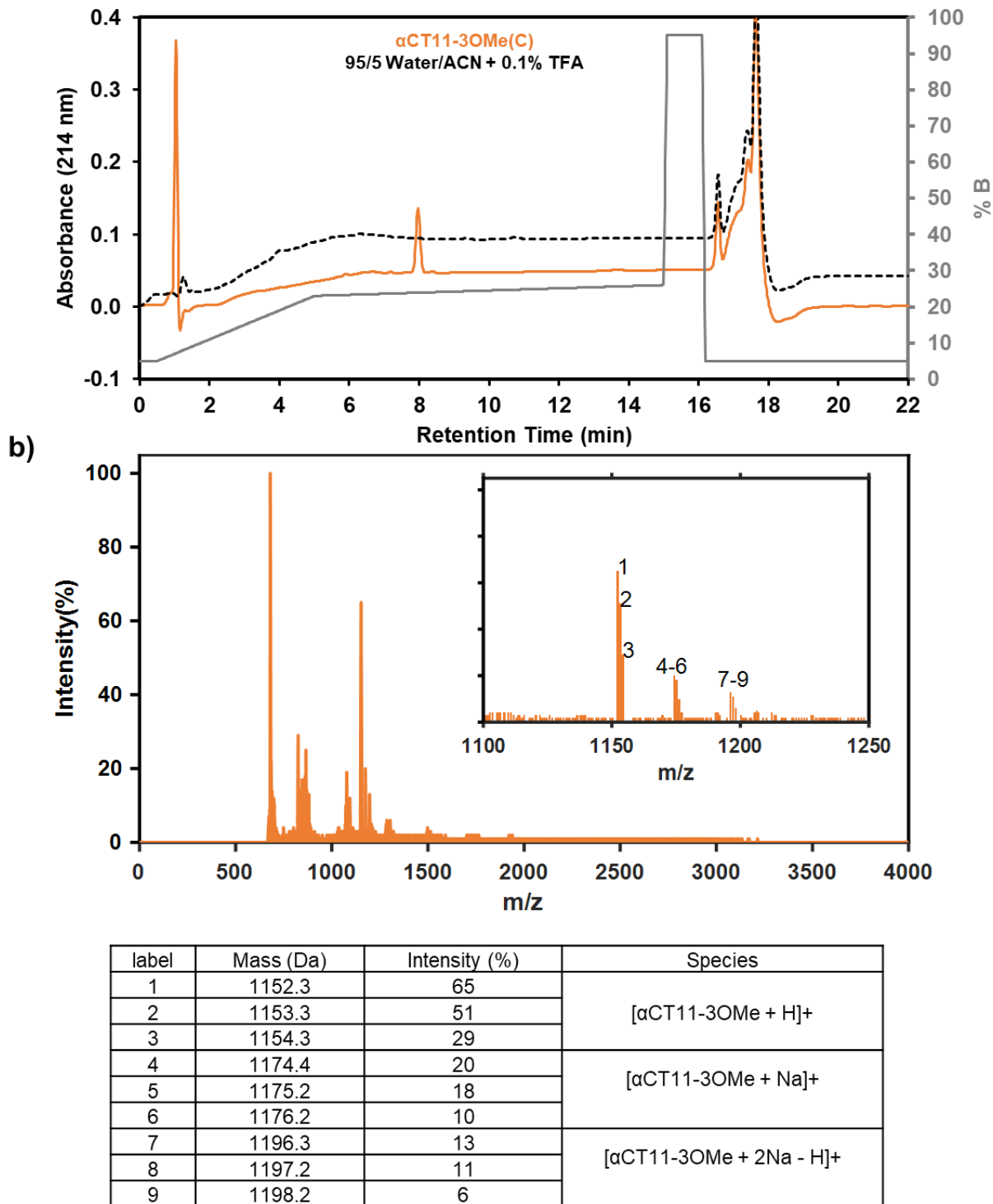
Figure A.6. a) RP-HPLC chromatogram (gradient 2) and **b)** MALDI-TOF MS plot of αCT11-3OMe(C).
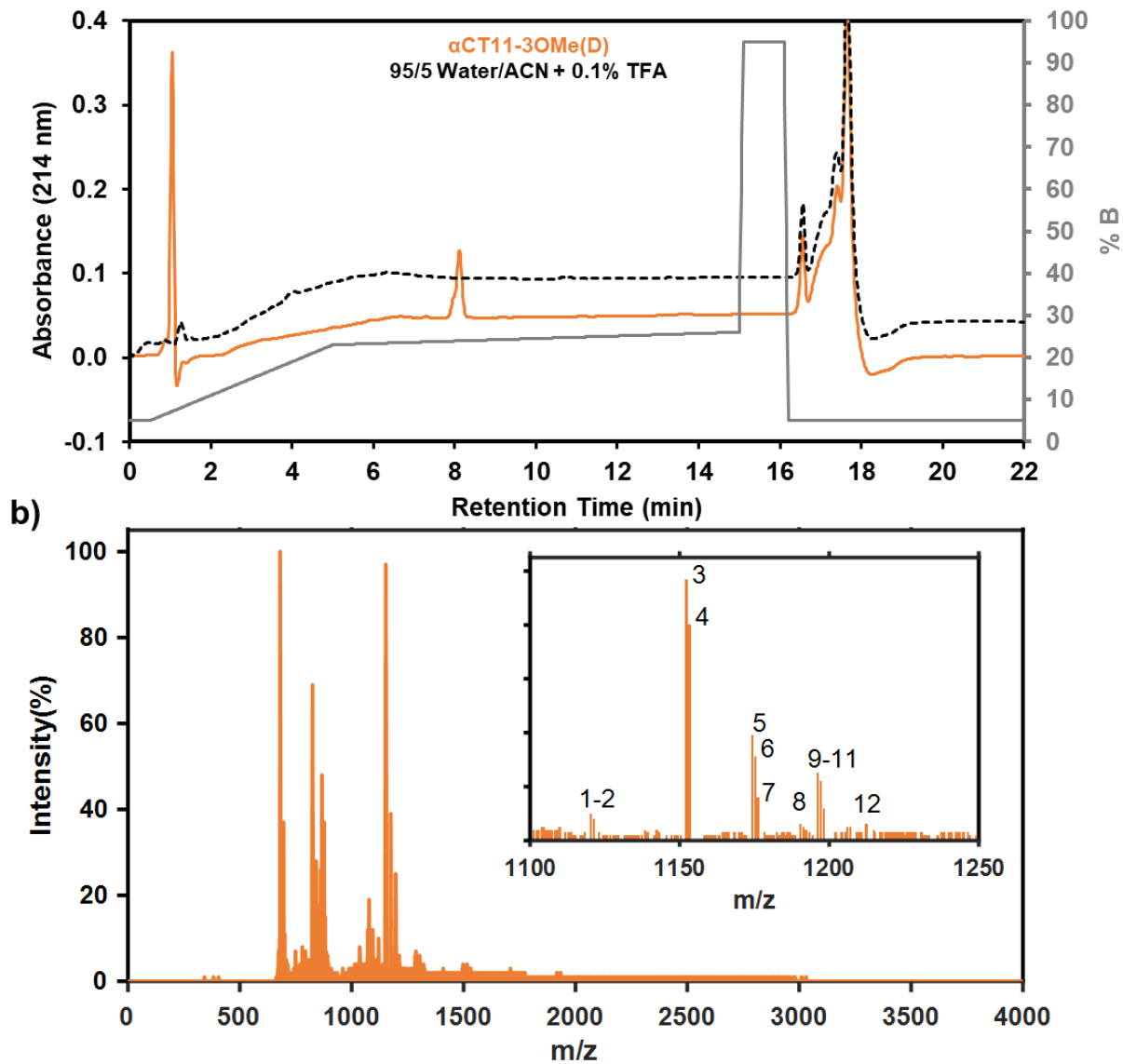
label	Mass (Da)	Intensity (%)	Species
1	1120.3	10	[αCT11-2OMe + 1 imide + H]+
2	1121.3	8	
3	1152.3	97	[αCT11-3OMe + H]+
4	1153.3	80	
5	1174.4	39	[αCT11-3OMe + Na]+
6	1175.3	31	
7	1176.2	16	
8	1190.3	6	[αCT11-3OMe + K]+
9	1196.3	25	[αCT11-3OMe + 2Na - H]+
10	1197.3	22	
11	1198.2	12	
12	1212.4	6	[αCT11-3OMe + K + Na - H]+

Figure A.7. a) RP-HPLC chromatogram (gradient 2) and **b)** MALDI-TOF MS of αCT11-3OMe(D).

label	Mass (Da)	Intensity (%)	Species
1	1138.5	100	[αCT11-2OMe + H]+
2	1139.5	87	
3	1160.8	18	[αCT11-2OMe + Na]+
4	1161.6	18	
5	1182.8	8	[αCT11-2OMe + 2Na - H]+
6	1183.7	8	
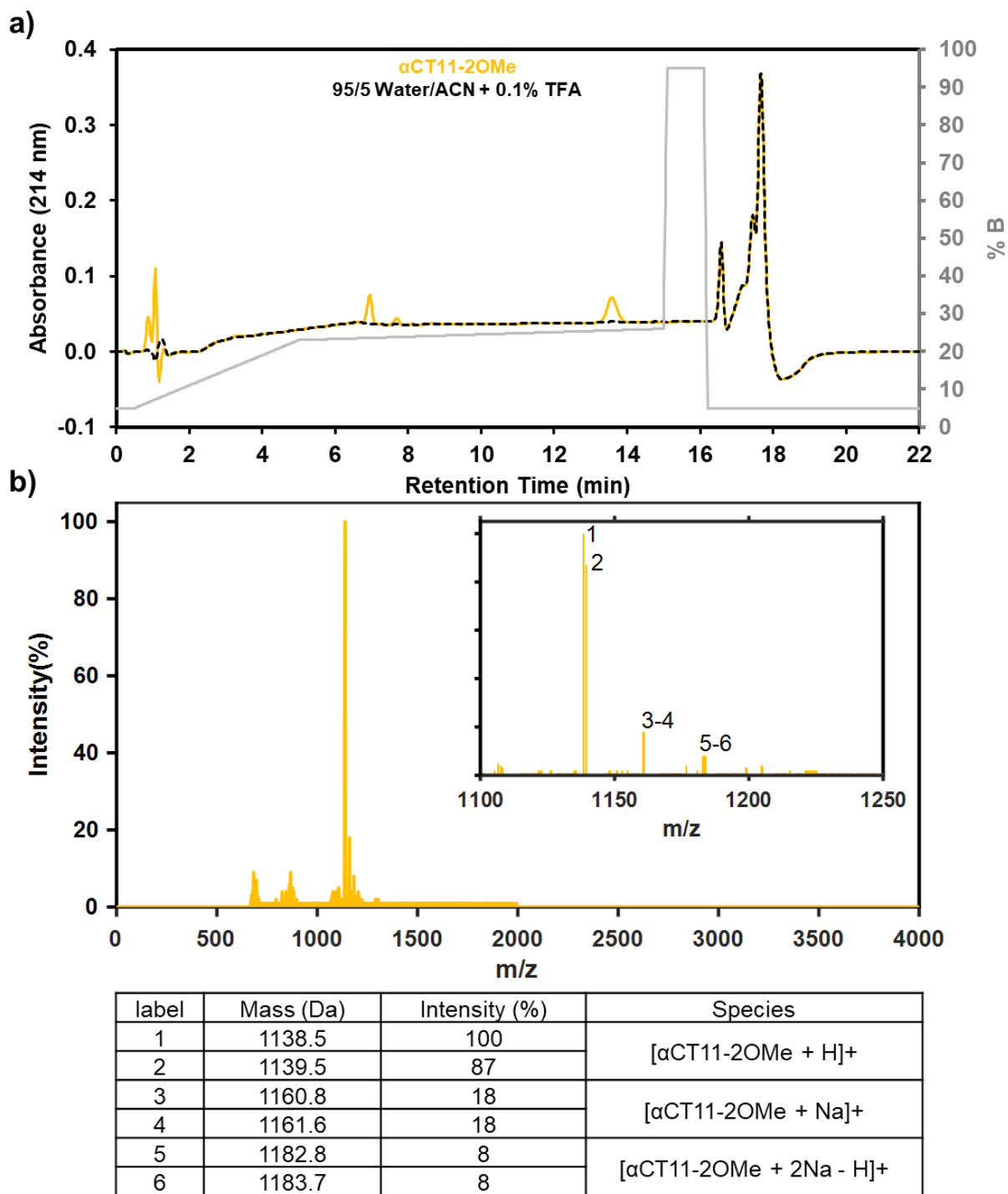
Figure A.8. a) RP-HPLC chromatogram and **b)** MALDI-TOF MS of αCT11-2OMe.

A.2 Establishing ester position with 2D nuclear magnetic resonance (NMR) spectroscopy

To assign the methyl ester αCT11-4OMe protons and carbons (**Figure A.9**), we used 1D ^{1}H (**Figure A.10-A.12**) and ^{13}C (**Figure A.13**) spectra together with 2D H-H total correlation spectroscopy (TOCSY, **Figures A.14-A.15**), H-H nuclear Overhauser effect spectroscopy (NOESY, **Figure A.16**), H-H clean in-phase correlation spectroscopy (CLIP-COSY, **Figures A.17-A.20**), and H-C selective heteronuclear multiple bond correlation (selHMBC, **Figures A.21-A.24**). For reference, the H and C chemical shifts and the H integrations and numbers are listed in **Table A.4**. Towards assigning the D5 and D6 Cγ, E8 Cδ, and I9 C carbonyls in the ^{13}C spectrum for correlation with the methyl ester proton resonances, we first used TOCSY to separate each H resonance into their individual spin system, which contains all the H resonances connected in a continuous chain of protonated nuclei. For example, the D5 C backbone carbonyl is not bound to a proton and therefore serves as a spin system boundary, separating the D5 and D6 spin systems. Conveniently, the H resonances within a given amino acid are in the same spin system. **Therefore, we assigned some of the amide/amine proton resonances (*H*N, Hε, 7.7 – 8.3 ppm) as belonging to either a R, D, E, or L/I residue spin system by considering the number of backbone-sidechain correlations with H resonances between 0 – 4.7 ppm** (**Figure A.14**). For example, we found the E8 *H*N (7.91 ppm) to have 4 unique correlations: 1 in the Hα region (4.0 – 4.7 ppm), 1 around the expected shift of the E8 Hγ resonance (2.32 ppm), and 2 around the expected shifts of the E8 Hδ resonances (~1.8 ppm). **However, we were unable to distinguish between R1 and R3, D5 and D6, or L7 and I9 resonances due to the similar number and chemical shifts of these correlations in the TOCSY spectrum. We assigned the R1 *H*N (8.17 ppm) because the amine-water H exchange caused it to appear as a broad singlet instead of a doublet split by the adjacent Hα. The TOCSY spectrum also showed *H*N - Hε correlations for both R1 and R3 in the amide/amine region of the spectrum, allowing us to assign the R1 and R3 *H*N (8.17 and 8.24 ppm) and Hε (7.83 and 7.71 ppm) resonances (Figure A.15).**

To assign the D5, D6, L7, and I9 Hs, we next used NOESY, which shows correlations between protons that are close to each other in space, suspecting it would reveal interactions between amide/amine protons on adjacent amino acids. We observed a correlation in the amide/amine (*H*N and R Hε) region (7.7 – 8.3 ppm) of the NOESY spectrum (**Figure A.16**) between what TOCSY showed to be either the D5 or D6 *H*N and either the L7 or I9 *H*N. Because D6 is next to L7 in the peptide sequence, this correlation allowed us to assign the D6 and L7 *H*N, and by the process of elimination D5 and I9 Hs. **In all, NOESY revealed D5-D6, D6-L7, L7-E8, and E8-I9 HN-HN correlations, which allowed us to assign the remaining *H*N resonances.**

With the *H*Ns and Hε resonances assigned, we next moved to COSY, which displays correlations between protons on adjacent nuclei, with the goal of assigning the I9 Hα (4.17 ppm) and the D5/D6 Hßs (2.57 – 2.75 ppm), which were each 3 bonds away from their respective methyl ester carbonyl Cs, and could therefore be used to assign

said carbonyl Cs with selHMBC. To enhance the signal intensities, we used CLIP COSY. **To assign the Hα resonances, we plotted the now assigned *H*N and Hε region (7.7 – 8.3 ppm) against the Hα region (4.0 – 4.7 ppm) (Figure A17), where correlations allowed us to assign the D5 Hα (4.54 ppm), D6 Hα (4.58 ppm), E8 Hα (4.32 ppm), and I9 Hα (4.17 ppm) resonances. We also used CLIP-COSY correlations to assign the D5/D6 Hßs (2.57 – 2.75 ppm) through their respective correlations with the now-assigned Hα region (4.0 - 4.7 ppm) (Figure A.18).** The D5 and D6 Hα protons split the adjacent Hß resonances, and CLIP-COSY showed each of part of the split D5 and D6 Hß resonances to correlate with the respective Hα resonances. **After assigning the E8 Hα resonance, we were able to assign the E8 Hß resonances (1.767 and 1.904 ppm) (Figure A.19) and, subsequently, the E8 Hγ resonance (2.319 ppm) (Figure A20) through their respective correlations.**

Finally, to assign the carbonyl Cs in the ^{13}C spectrum of αCT11-4OMe, we used selHMBC, which measures correlations between protons and carbons separated by 2-4 bonds within a specified region of the spectrum, as HMBC did not offer enough resolution in the ^{13}C dimension to confidently assign each peak, specifically the D5 and D6 Cγ resonances (**Figure A.21**). As a reference for the αCT11-4OMe selHMBC spectrum, which was collected only in the carbonyl region (165 – 175 ppm), we used the L7 Hα-carbonyl C correlation (4.25-171.61 ppm) (**Figure A.22**). As we had already assigned the relevant I9 Hα resonance, the D5/D6 Hß resonances, and the E8 Hγ resonances, we used observed correlations in selHMBC to assign the respective carbonyl Cs, specifically the D5/D6 Cγ, E8 Cδ, and I9 Cs. **Plotting the Hα region of the ^{1}H spectrum (4.0 – 4.7 ppm) against carbonyl C region of the ^{13}C spectrum, in which we observed Hα - C correlations, allowed us to assign the D5 C (170.23 ppm), D5 Cγ (170.68 ppm), D6 C (169.75), D6 Cγ (170.68 ppm), and I9 C (171.76) resonances (Figure A.23).** The observed methyl ester -OC*H$_3$* - Cγ correlations (**Figure 2.2**) allowed us to distinguish the D6 backbone and side chain carbonyls, the former of which was 6 bonds away from the methyl ester -OC*H$_3$*, and would not have produced a selHMBC correlation. **We then used the E8 Hγ - Cδ correlation to assign the E8 Cδ resonance (Figure A.24).** After assigning all the relevant carbonyl C resonances, we were then able to use their selHMBC correlations with their respective D5, D6, E8, and I9 methyl ester -OC*H$_3$* resonances to assign each singlet in the αCT11-4OMe ^{1}H spectrum (Figure 2.2).
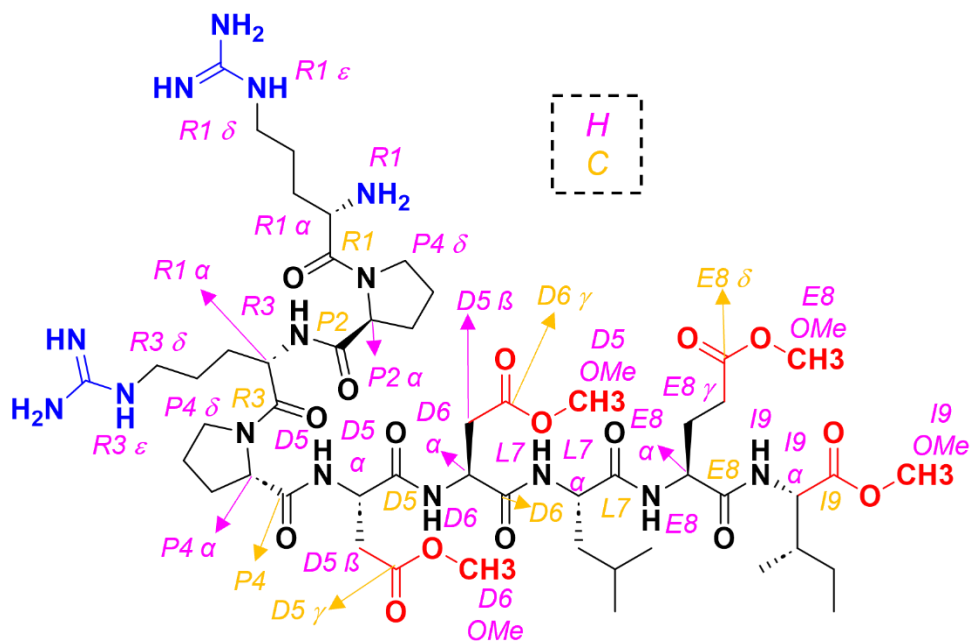
Figure A.9. Chemical structure of αCT11-4OMe. Relevant ¹H (pink) and ¹³C (yellow) atoms are labeled within the structure, and ester groups (red) and positively charged groups (blue) are also highlighted.
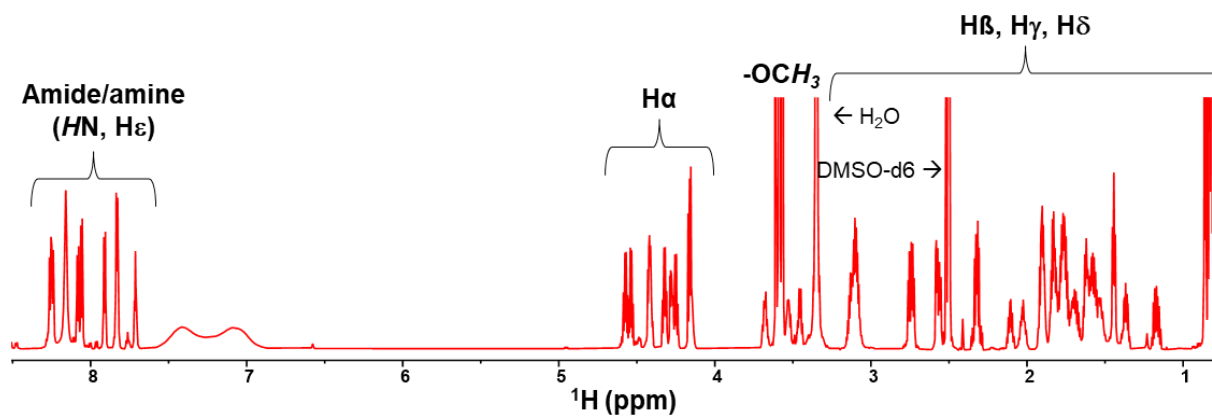
Figure A.10. ¹H NMR spectrum of αCT11-4OMe (0.75 – 8.50 ppm).
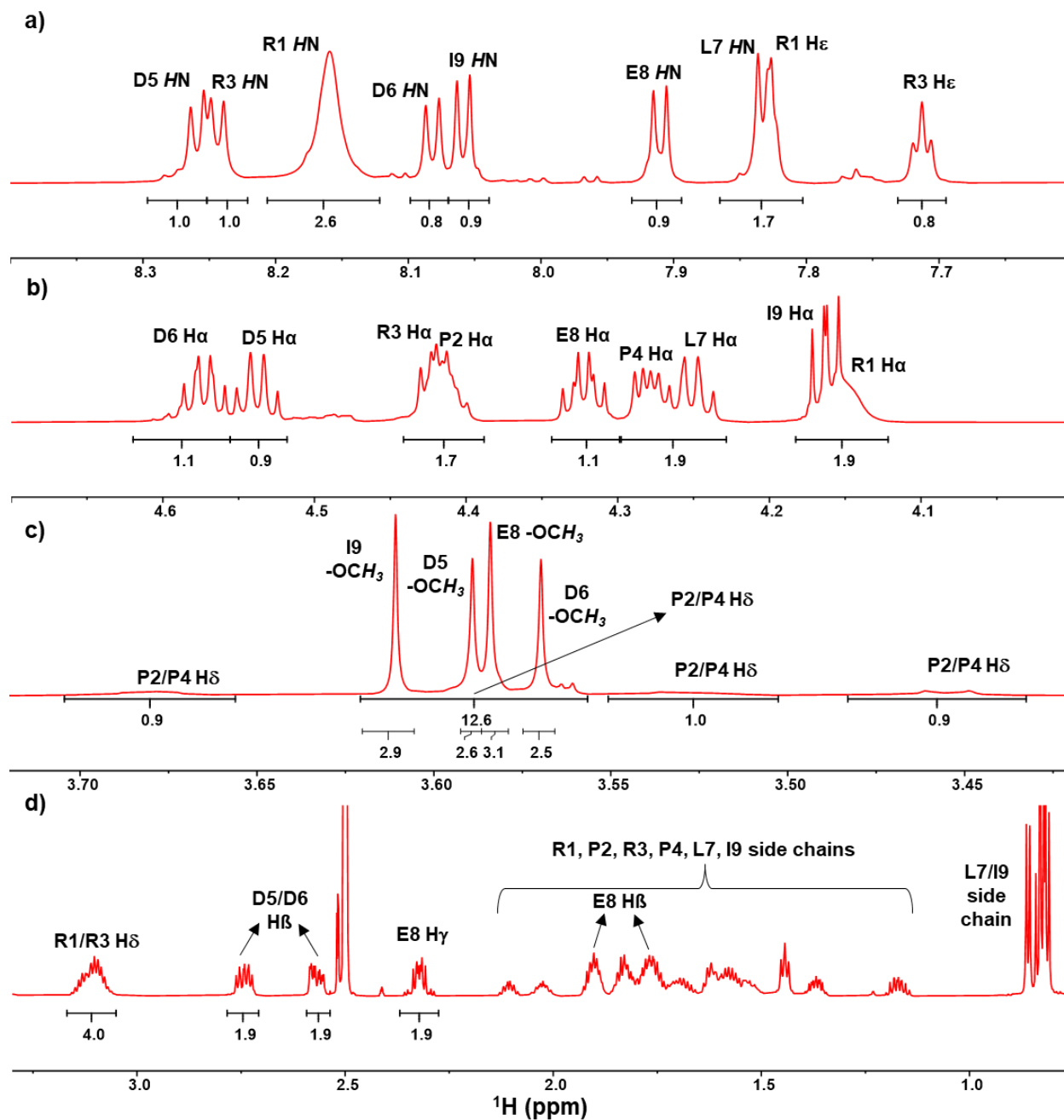
Figure A.11. Expanded select regions of the αCT11-4OMe ^{1}H NMR spectrum. The **a)** amide/amine (*H*N, Hε) (7.6 – 8.4 ppm), **b)** Hα (4.0 – 4.7 ppm), **c)** methyl ester H (-OC*H₃*) and proline Hδ (3.4 – 3.7 ppm), and **d)** the Hß, Hγ, and Hδ (0.75 – 3.50 ppm) regions are shown.
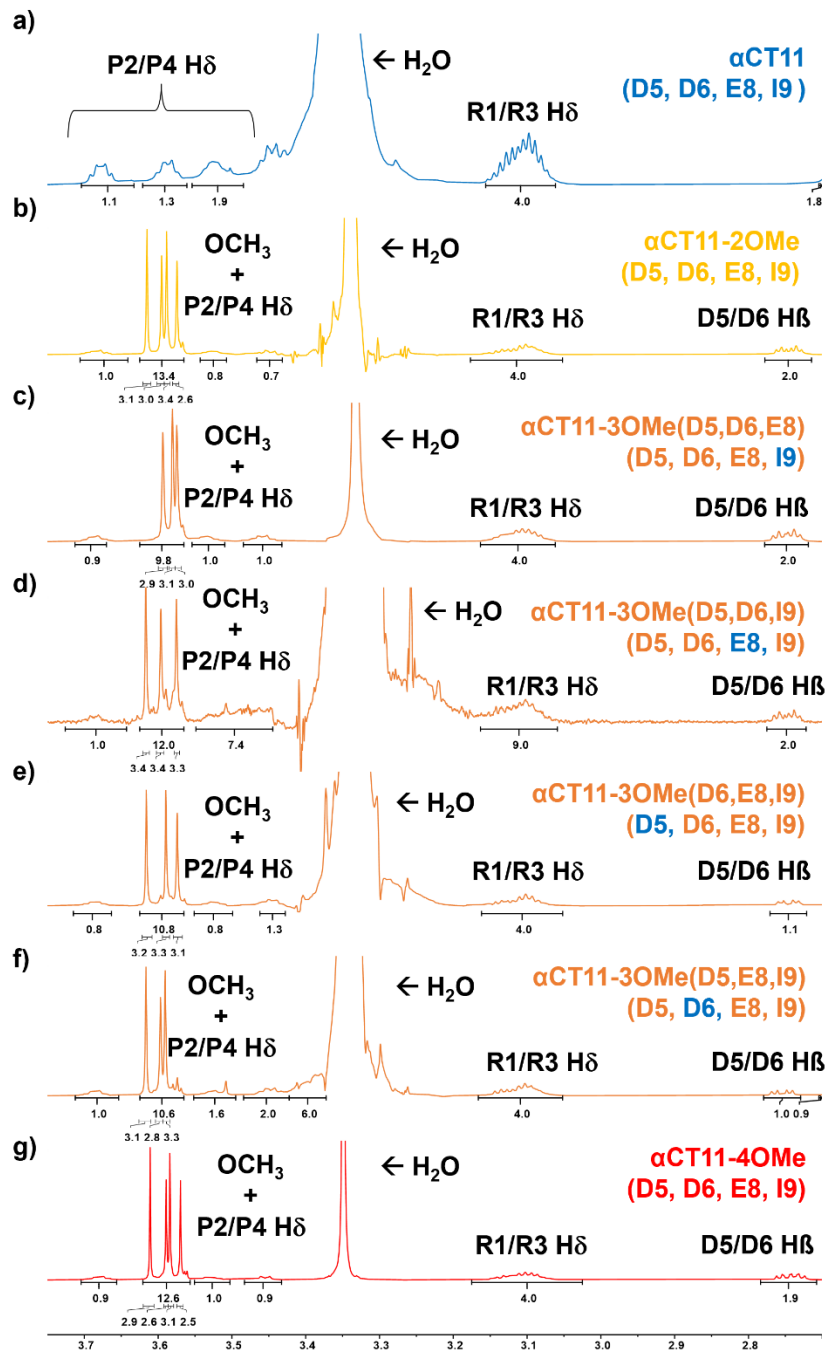
Figure A.12. ^{1}H NMR spectrum of **a)** αCT11 and **b-g)** esterified variants (2.7 – 3.75 ppm). Only proline Hδ resonances were observed in the region that methyl ester H singlets were observed in the esterified ^{1}H spectra (3.55 – 3.64 ppm). For each esterified spectrum, both the total methyl ester H region and the individual peaks were integrated to show the presence of the proline Hδ proline, which is overlapped by the methyl ester H singlets. All methyl ester peaks integrate to 3 protons; however, in (d-f) the αCT11-3OMe samples with an esterified I9 residue, lower concentrations of sample led to higher baseline noise and slightly higher integrals than expected (9 methyl ester Hs + 1 proline Hδ = 10 Hs). The αCT11-2OMe spectrum contained peaks from all the possible esterified methyl esters, suggesting this product is a mixture of αCT11 with different combinations of 2 methyl esters esterified.
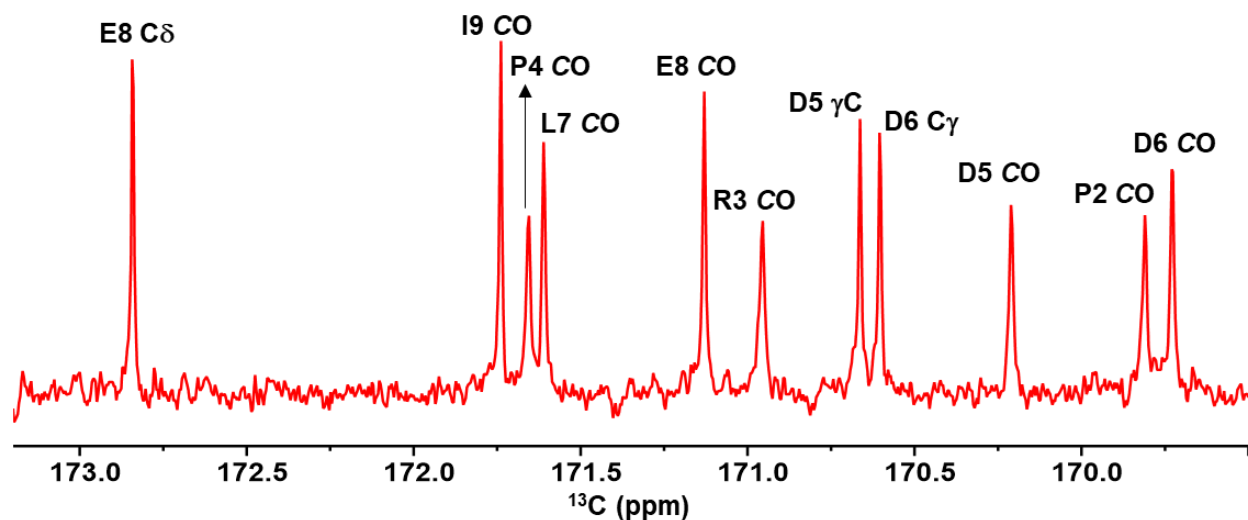
Figure A.13. Carbonyl carbon region of the αCT11-4OMe ^{13}C NMR spectrum (169.5 – 173.2 ppm).

Table A.4. Chemical shifts of relevant ^{1}H and ^{13}C in αCT11-4OMe

Amino Acid	Atom	Chemical Shift (ppm)	Integral	# of protons
R1	HN	8.17	2.6	3
	Hα	4.17	1.0	1
	Hδ	3.11	2*	
	Hε	7.83	0.9	1
P2	Hα	4.41	0.9	1
	Hδ	3.68 - 3.45	Not isolatable**	2
	CO	169.83	N/A	N/A
R3	HN	8.24	1.0	1
	Hα	4.41	0.9	1
	Hδ	3.11	2*	
	Hε	7.71	0.8	1
	CO	170.98	N/A	
P4	Hα	4.29	1.0	1
	Hδ	3.68 - 3.45	Not isolatable**	2
	CO	171.68	N/A	N/A
D5	HN	4.54	1.0	1
	Hα	4.54	0.9	1
	Hß	2.75	1.0	1
		2.57	1.0	1
	CO	170.23	N/A	
	Cγ	**170.68**	**N/A**	
	OCH₃	**3.59**	**2.6**	**3**
D6	HN	8.08	0.8	1
	Hα	4.58	1.1	1
	Hß	2.75	1.0	1
		2.57	1.0	1

	CO	169.75	N/A	
	Cγ	**170.62**	**N/A**	
	OCH₃	**3.57**	**2.5**	**3**
L7	HN	7.83	0.9	1
	Hα	4.24	1.0	1
	CO	171.63	N/A	
E8	HN	7.91	0.9	1
	Hα	4.32	1.1	1
	Hγ	2.32	1.9	2
	Hß	1.90	Not isolatable***	-
		1.77	Not isolatable***	-
	CO	171.15	N/A	
	Cδ	**172.86**	N/A	
	OCH₃	**3.58**	**3.1**	**3**
I9	HN	8.06	0.9	1
	Hα	4.17	1.0	1
	CO	**171.76**	**N/A**	
	OCH₃	**3.61**	**2.9**	**3**

*Set as the reference integration
**Peak was either not able to be individually assigned (P2/P4 Hδ)
***Peaks were not able to be integrated separately from neighboring peaks (E8 Hß)
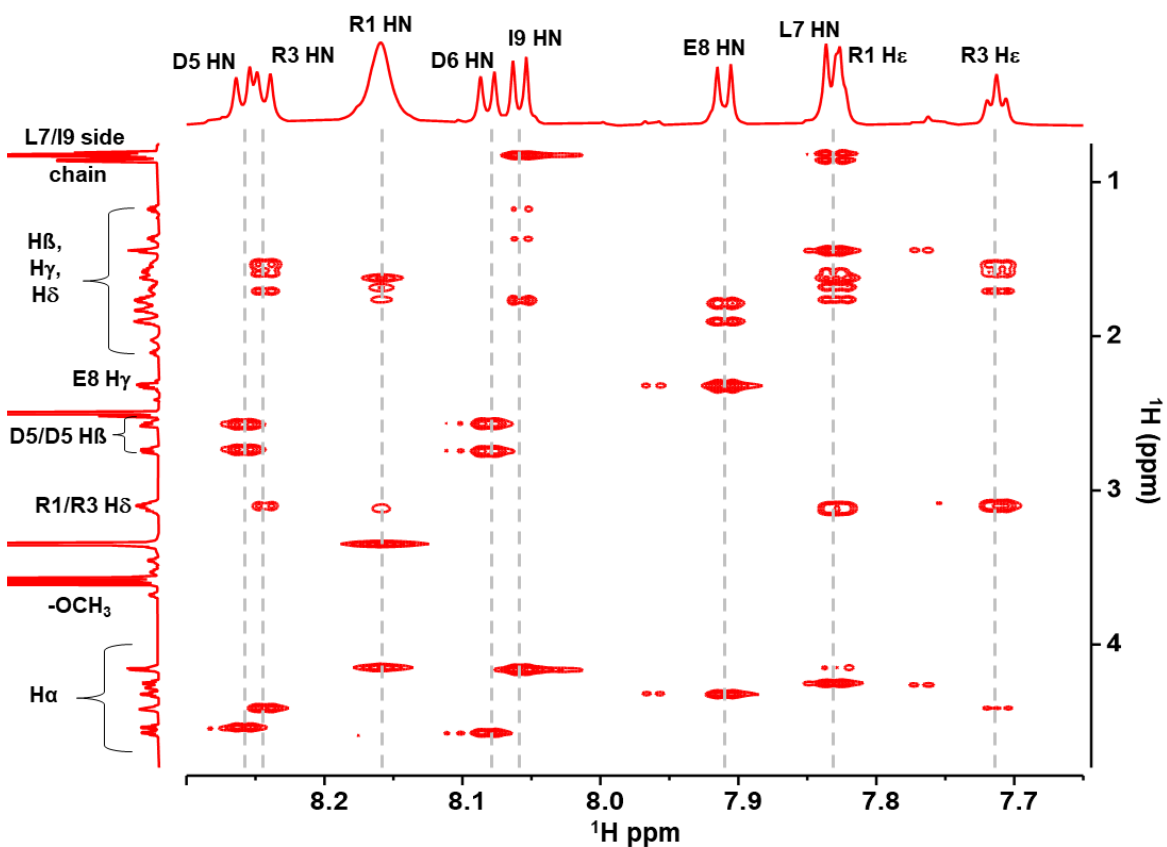
Figure A.14. Total correlation spectroscopy (TOCSY) of αCT11-4OMe: HN & Hε region (7.65 – 8.3 ppm) x Hα, Hß, Hγ, Hδ, and methyl ester H region (0.75 – 4.7 ppm). Dashed vertical lines are shown to guide the eye along the spin systems of the peptide, which were used to assign the HN and Hε resonances (x-axis).
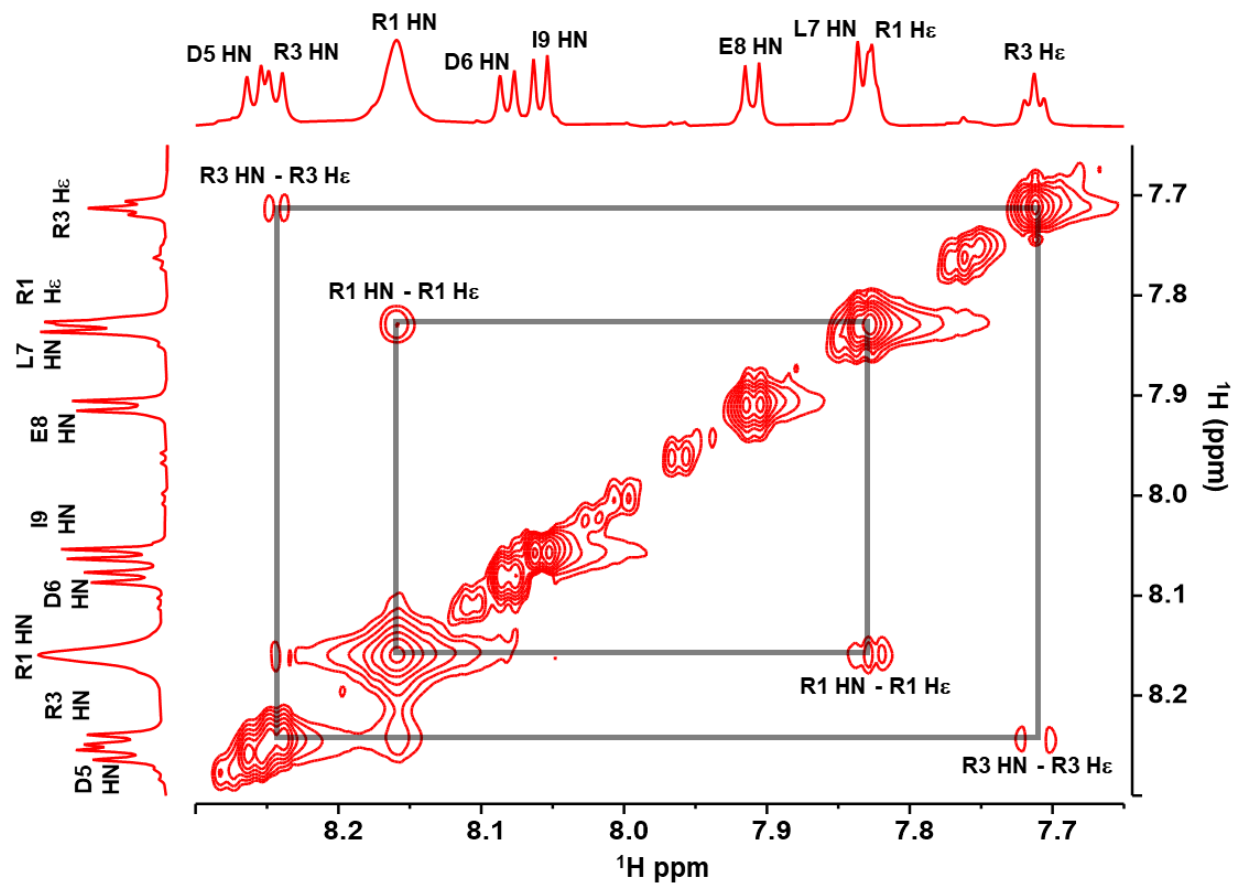
Figure A.15. TOCSY spectrum of αCT11-4OMe: HN & Hε region (7.65 – 8.3 ppm) x HN & Hε region. Correlations between the R1/R3 HN – Hε correlations were used to assign R1 and R3 HN and Hε resonances.
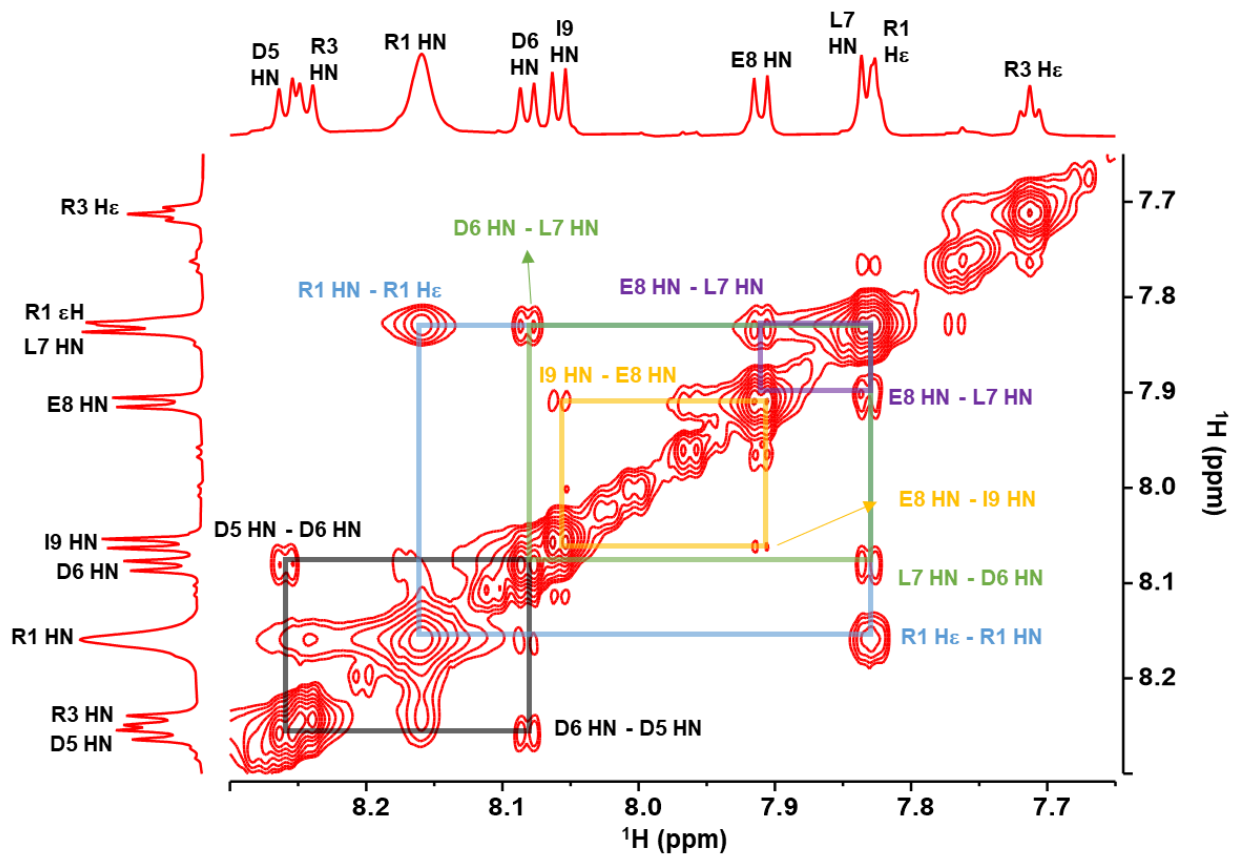
Figure A.16. Nuclear Overhauser spectroscopy (NOESY) of αCT11-4OMe: HN & Hε region (7.65 – 8.3 ppm) x HN & Hε region. R1 HN - R1 Hε (blue), D6 HN - L7 HN (green), and D5 HN - D6 HN (black) correlations were observed, with the latter 2 correlations being used assign the D5, D6, L7, and I9 HNs.
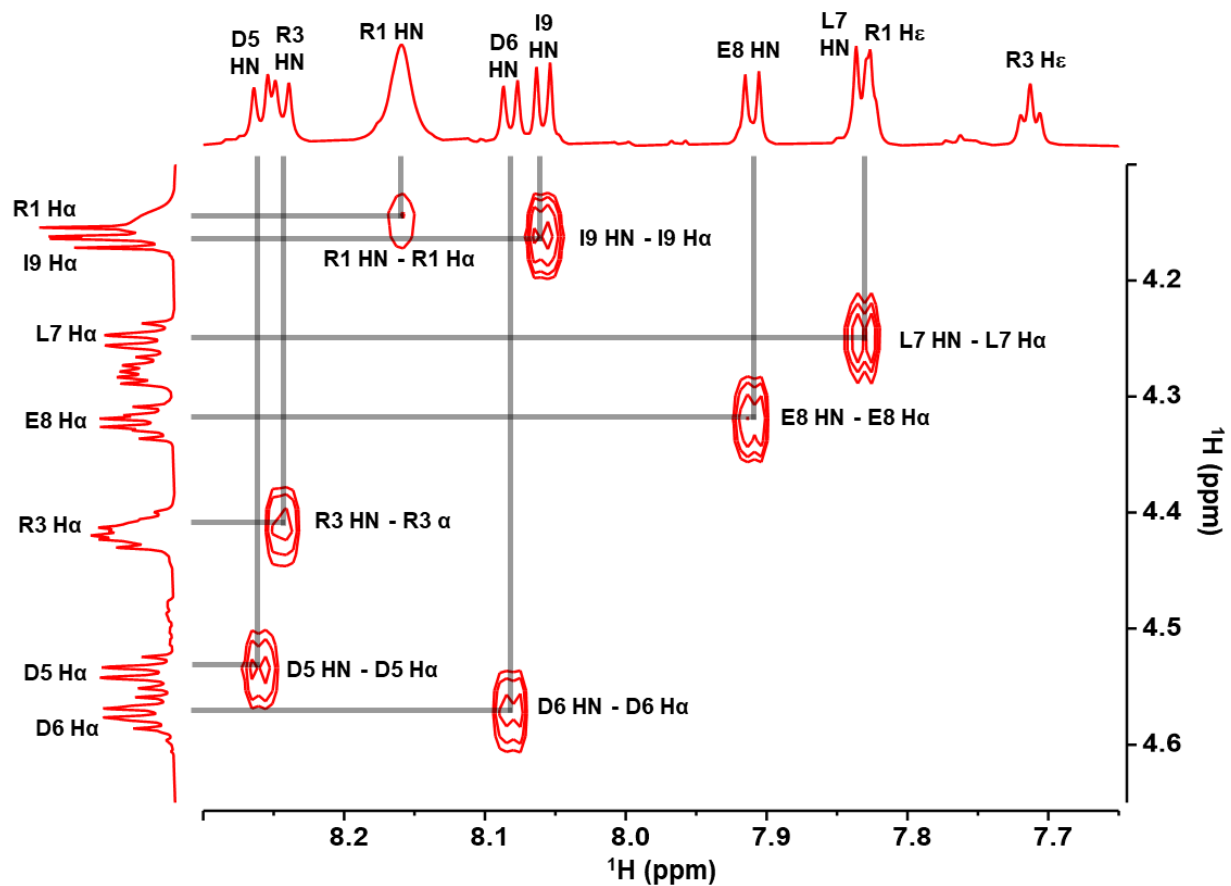
Figure A.17. Clean in-phase correlation spectroscopy (CLIP COSY) of αCT11-4OMe: *H*N & Hε region (7.65 – 8.3 ppm) x Hα region (4.1 – 4.65 ppm). *H*N – Hα correlations were used to assign the Hα resonances.
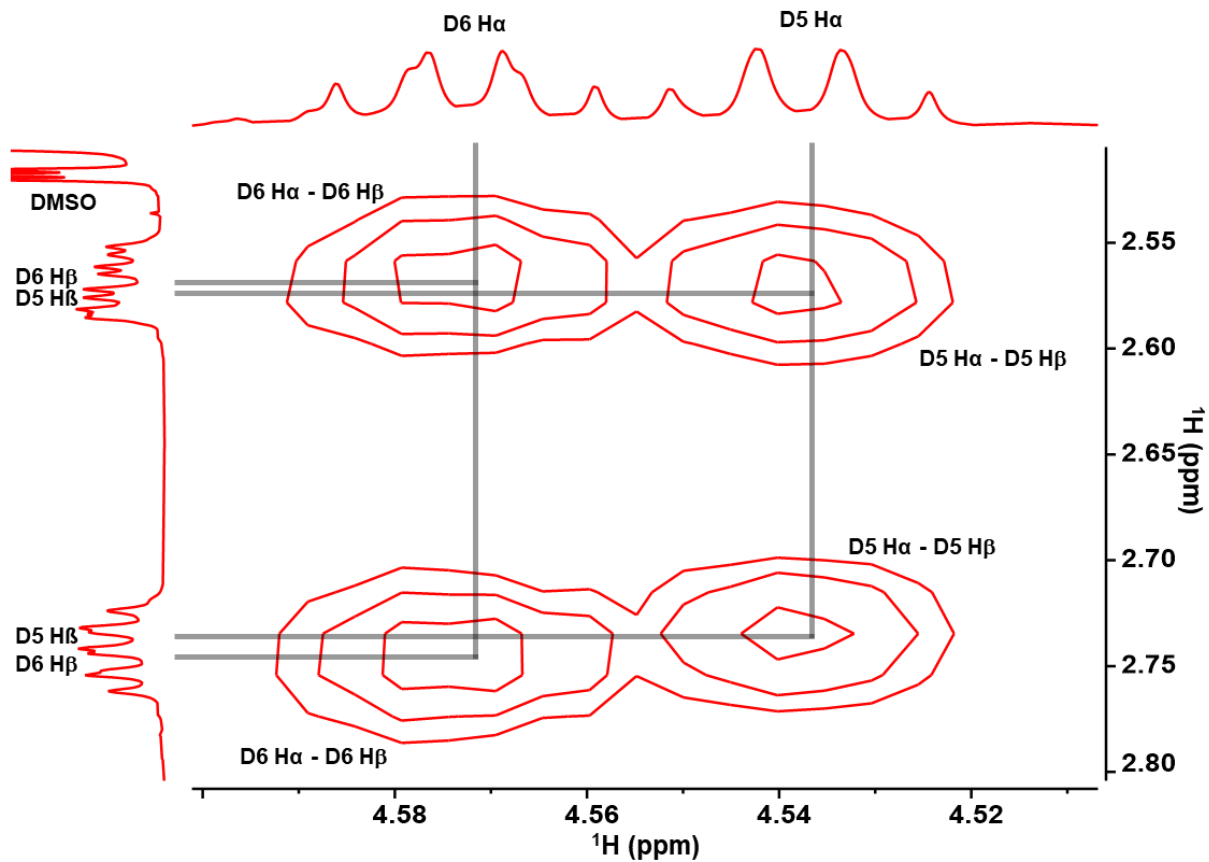
Figure A.18. CLIP COSY of αCT11-4OMe: D5 & D6 Hα resonance region (4.5 – 4.6 ppm) x D5 & D6 Hß resonance region (2.5 – 2.8 ppm). The D5 and D6 Hα protons split the adjacent Hß resonances, and this CLIP-COSY spectrum showed each of part of the split D5 and D6 Hß resonances to correlate with the respective Hα resonances.
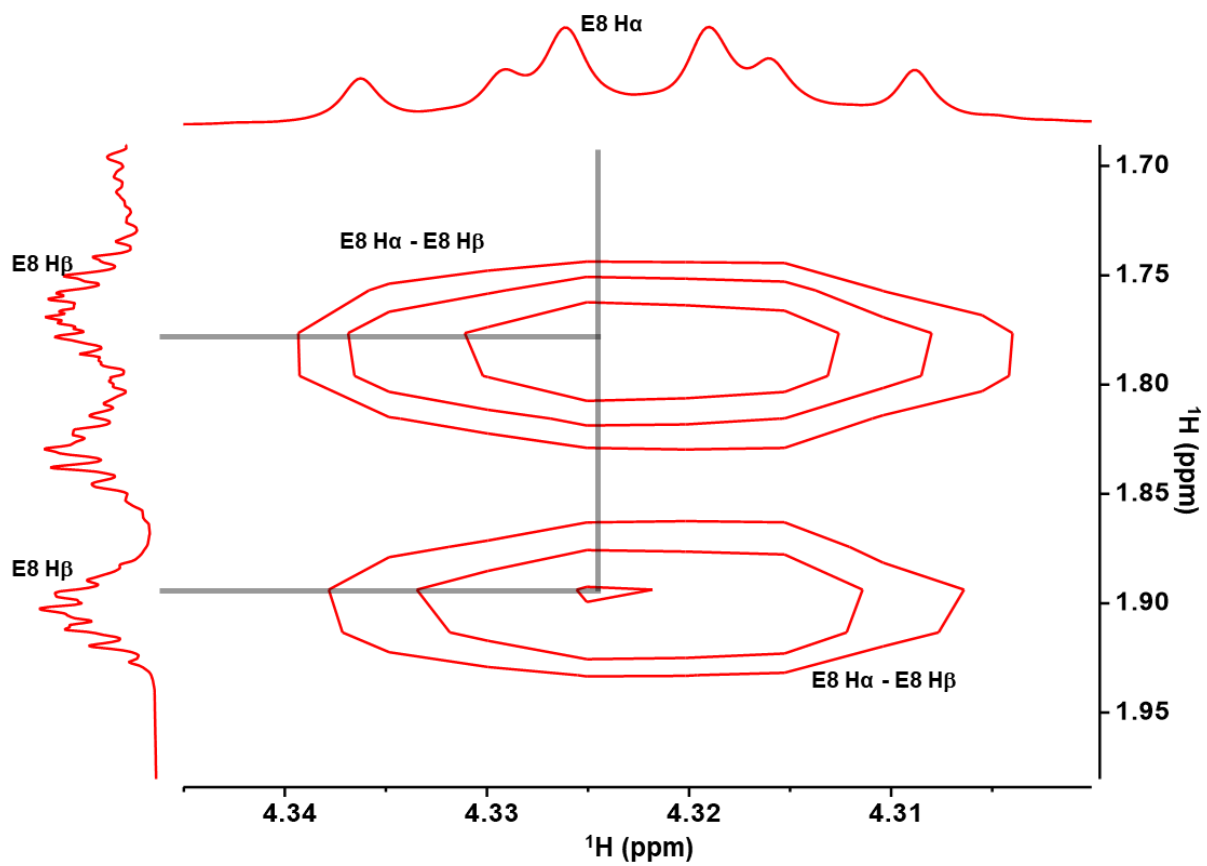
Figure A.19. CLIP COSY of αCT11-4OMe: E8 Hα resonance region (4.31-4.34 ppm) x the E8 Hß region (1.7-1.95 ppm), with E8 Hα – Hß correlations allowing for the assignment of the 2 E8 Hß resonances.
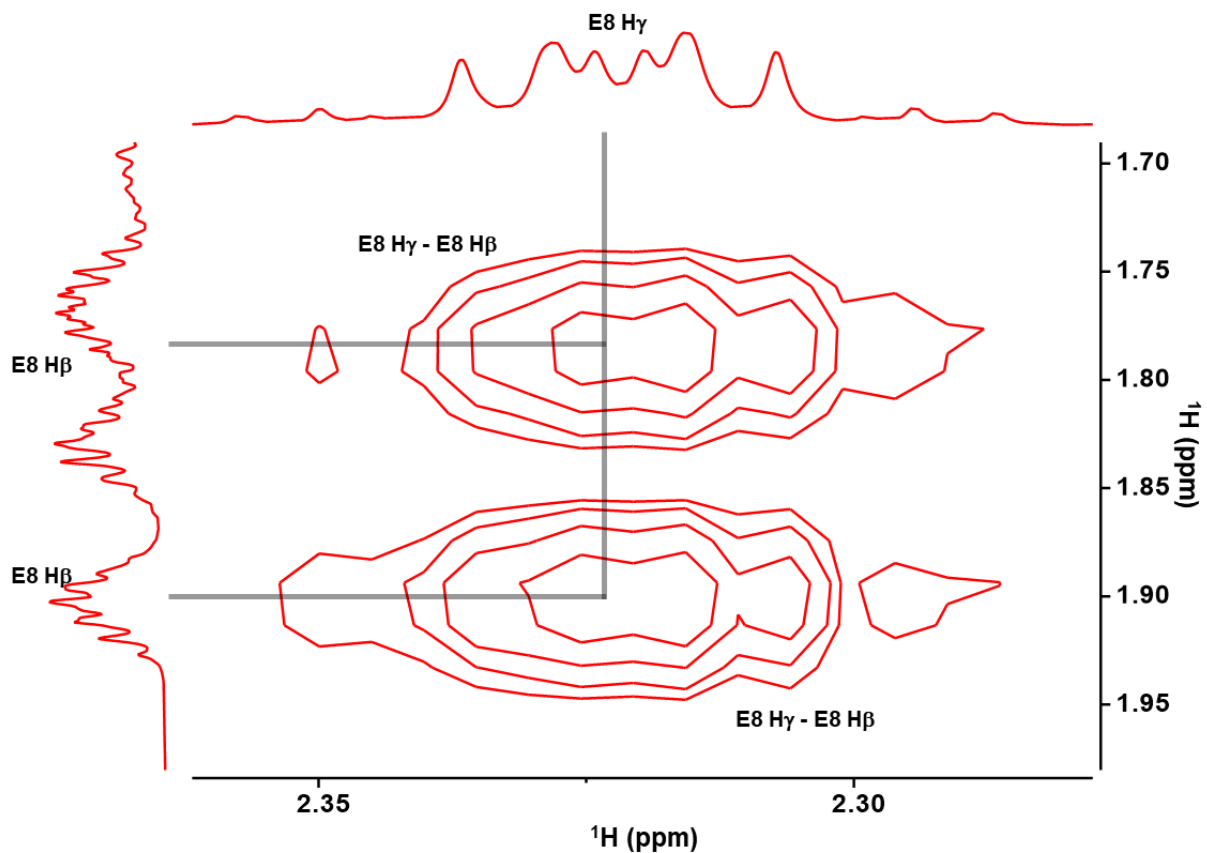
Figure A.20. CLIP COSY of αCT11-4OMe: E8 Hγ resonance region (2.30-2.35 ppm) x E8 Hß resonance region (1.70-1.95 ppm), with the E8 Hγ - Hß correlations allowed for the assignment of the E8 Hγ resonance.
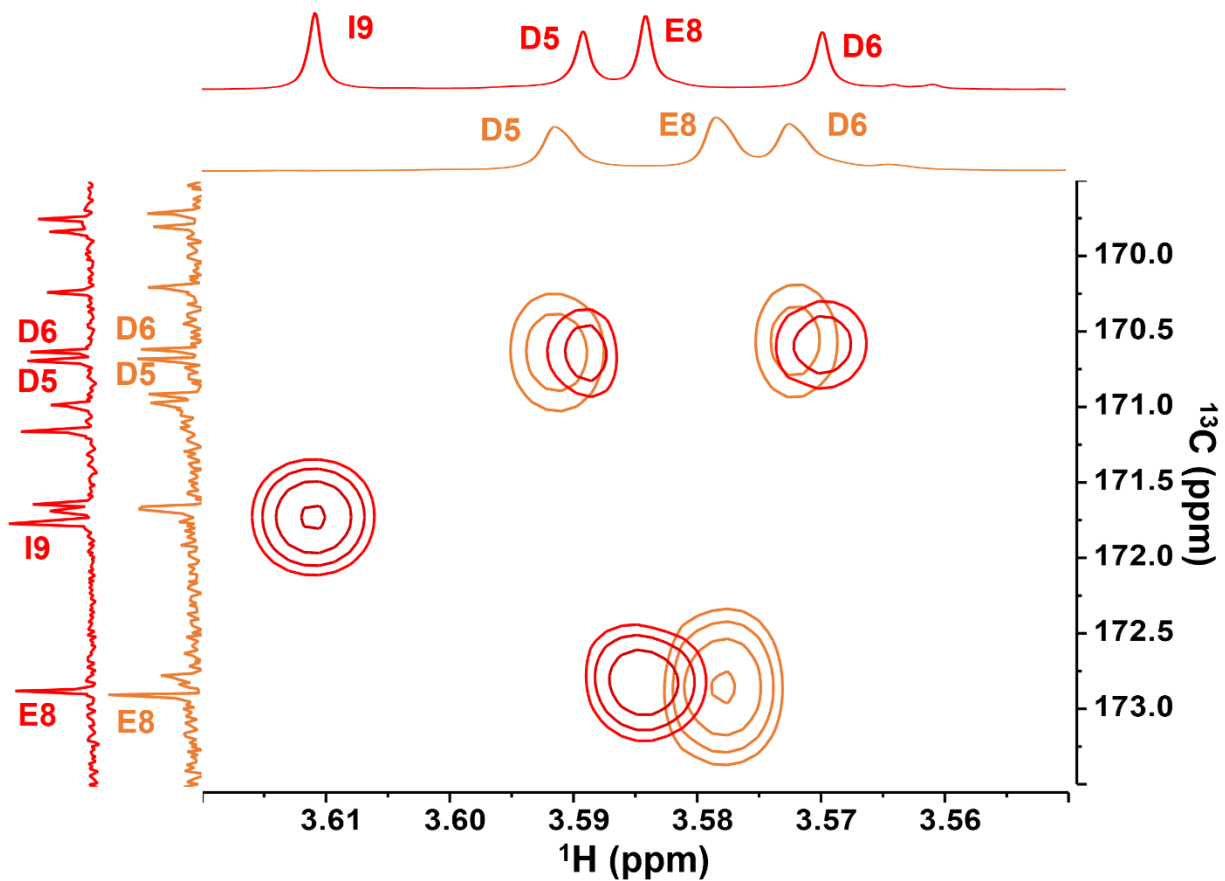
Figure A.21. Heteronuclear multiple bond correlation (HMBC) of αCT11-4OMe: methyl ester H singlet region (3.55 – 3.62 ppm) x carbonyl C region (169 – 173 ppm). Correlations did not have high enough resolution in the ^{13}C region to discern between methyl ester H correlations with the D5 and D6 Cγ resonances.
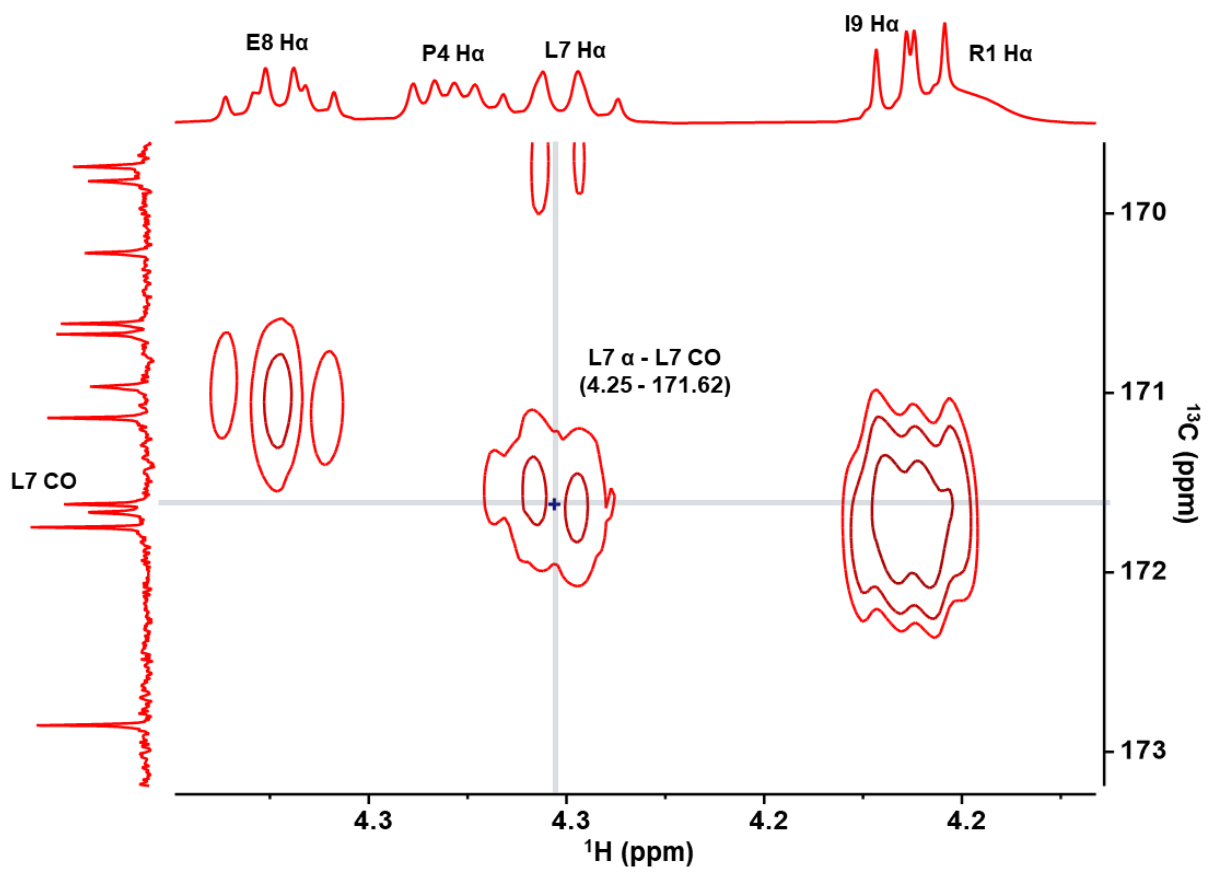
Figure A.22. HMBC of αCT11-4OMe: Hα region (4.1 – 4.4 ppm) x carbonyl C region (169 – 173 ppm). The L7 Hα – L7 CO correlation (at 4.25 –171.62 ppm) is highlighted, and was used to reference all of the selective HMBC (selHMBC) spectra.
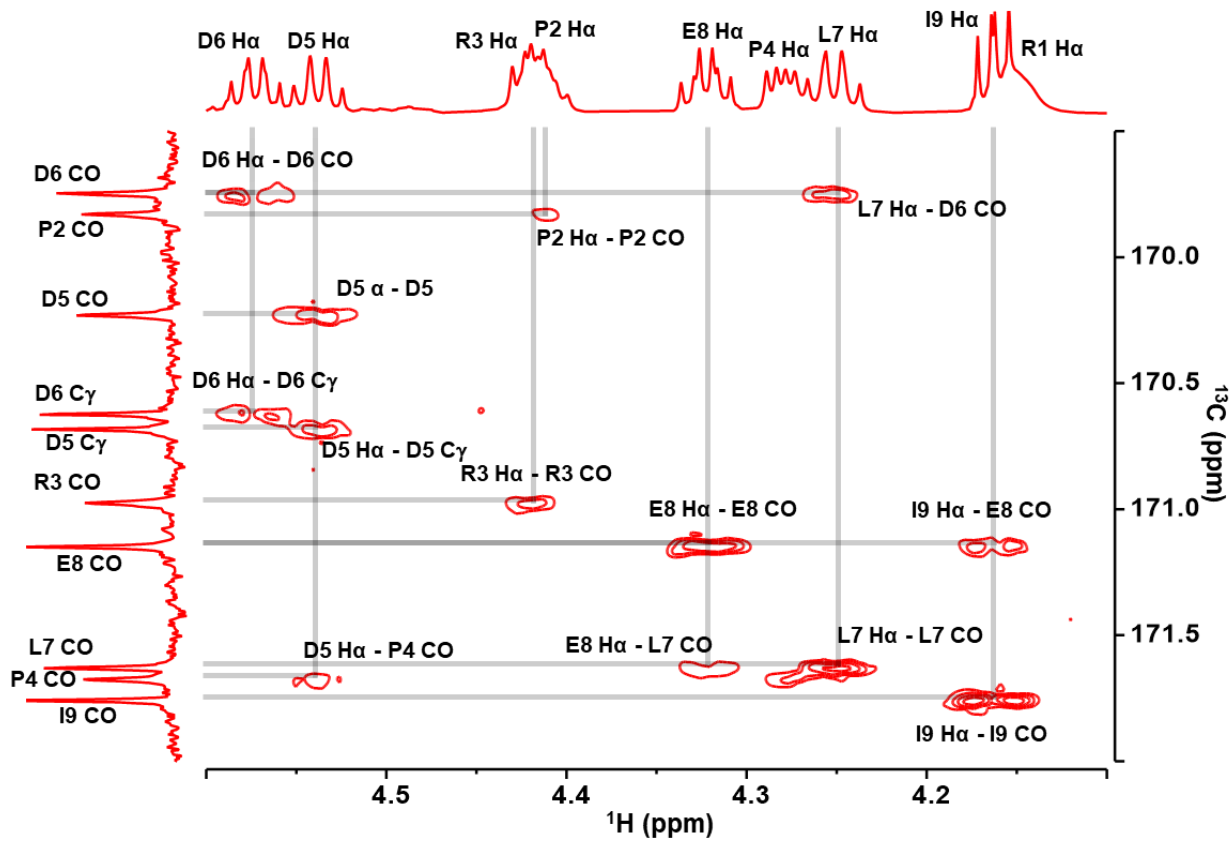
Figure A.23. selHMBC of αCT11-4OMe: Hα region (4.1 – 4.6 ppm) x carbonyl C region (169 – 172 ppm). Hα – CO and D5/D6 Hα – Cγ correlations were used to assign relevant CO and Cγ resonances.
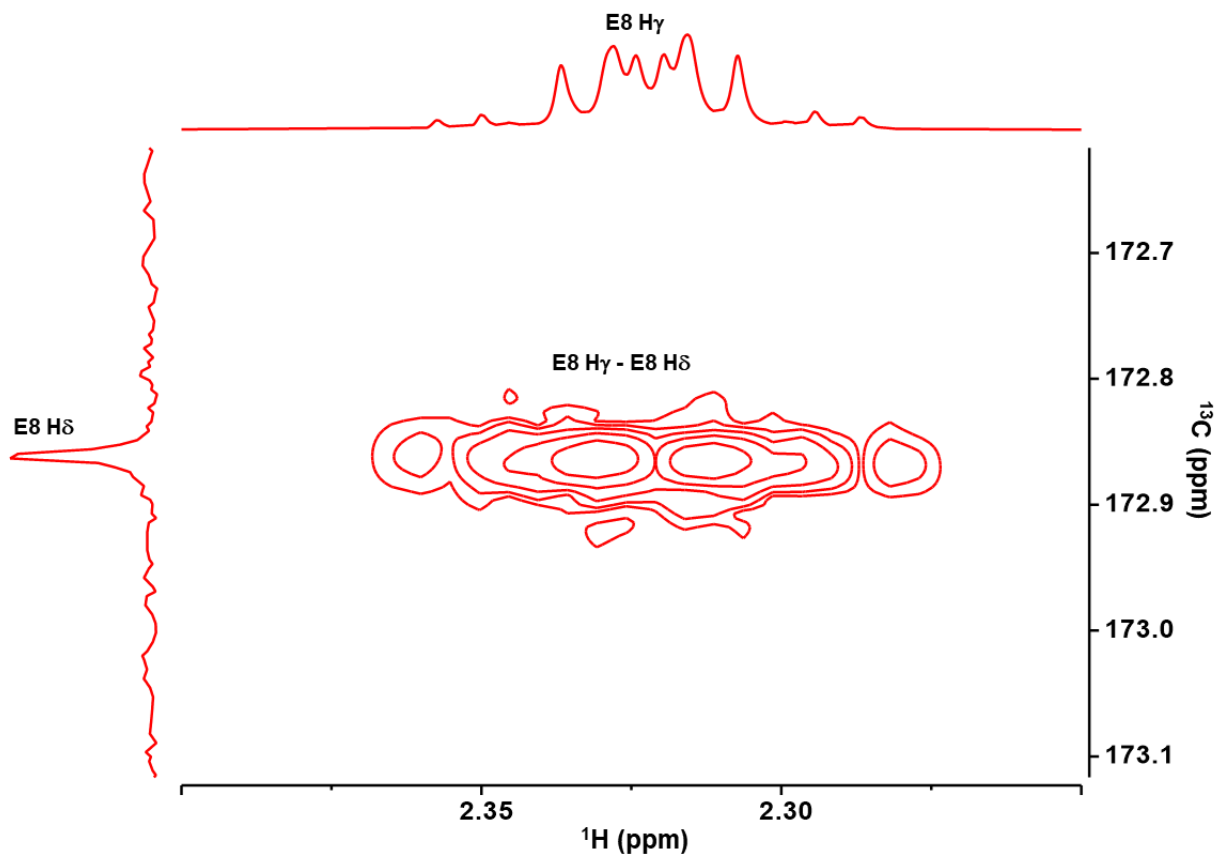
Figure A.24. selHMBC of αCT11-4OMe: E8 Hγ resonance region (2.30-2.35 ppm) x E8 Cδ region (172.7-173.1 ppm), with the E8 Hγ (pink)- Cδ (yellow) correlation used to identify the E8 Cδ resonance.
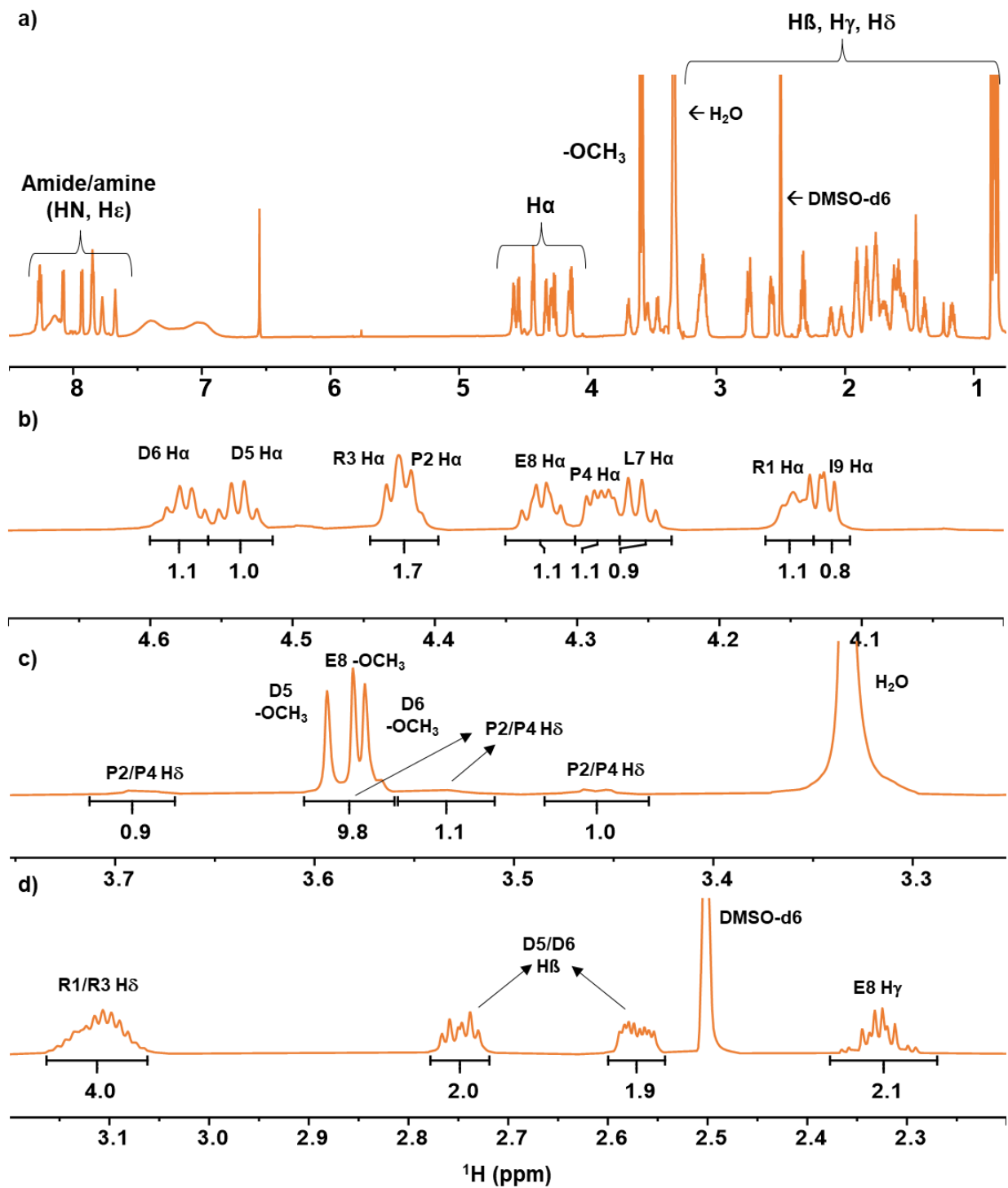
Figure A.25. Expanded select regions of the αCT11-3OMe(D5/D6/E8) ^{1}H NMR spectrum. Besides a) the full spectrum (0.75 – 8.5 ppm), the b) Hα region (4.0 – 4.7 ppm), c) methyl ester H and proline Hδ region (3.3 – 3.8 ppm), and d) the R1/R3 Hδ, D5/D6 Hß, and E8 Hγ region H (2.2 – 3.2 ppm) regions are expanded with the corresponding resonances labeled.
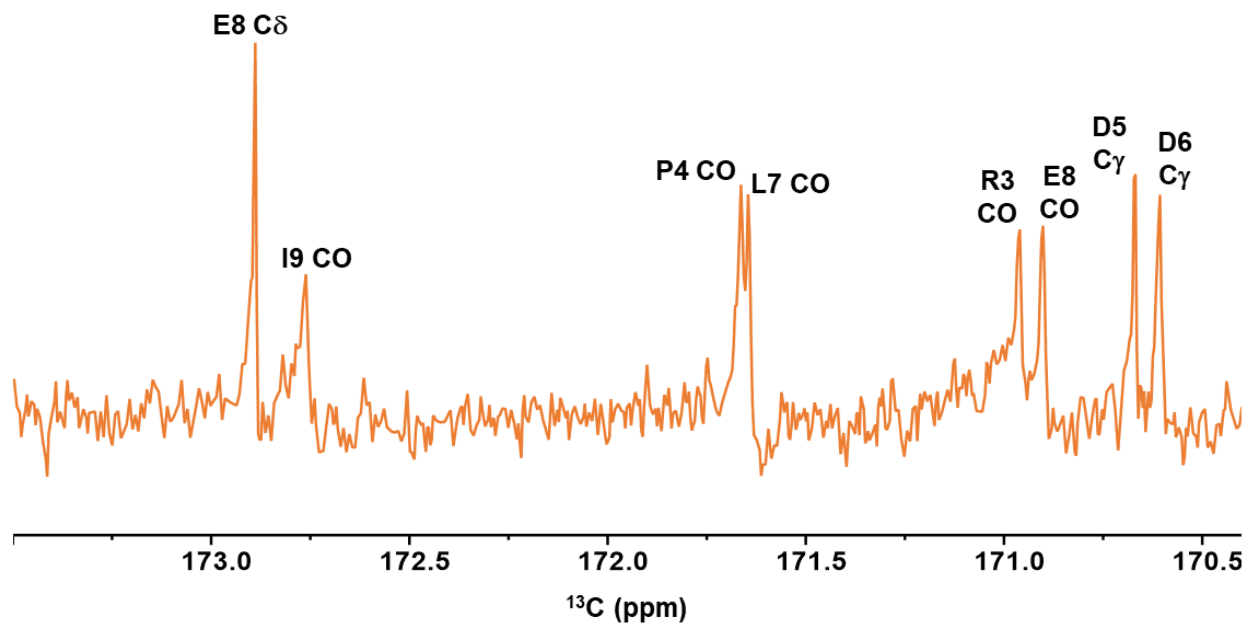
Figure A.26. Carbonyl carbon region of the αCT11-3OMe(D5/D6/E8) ^{13}C NMR spectrum (170.4 – 173.5 ppm).
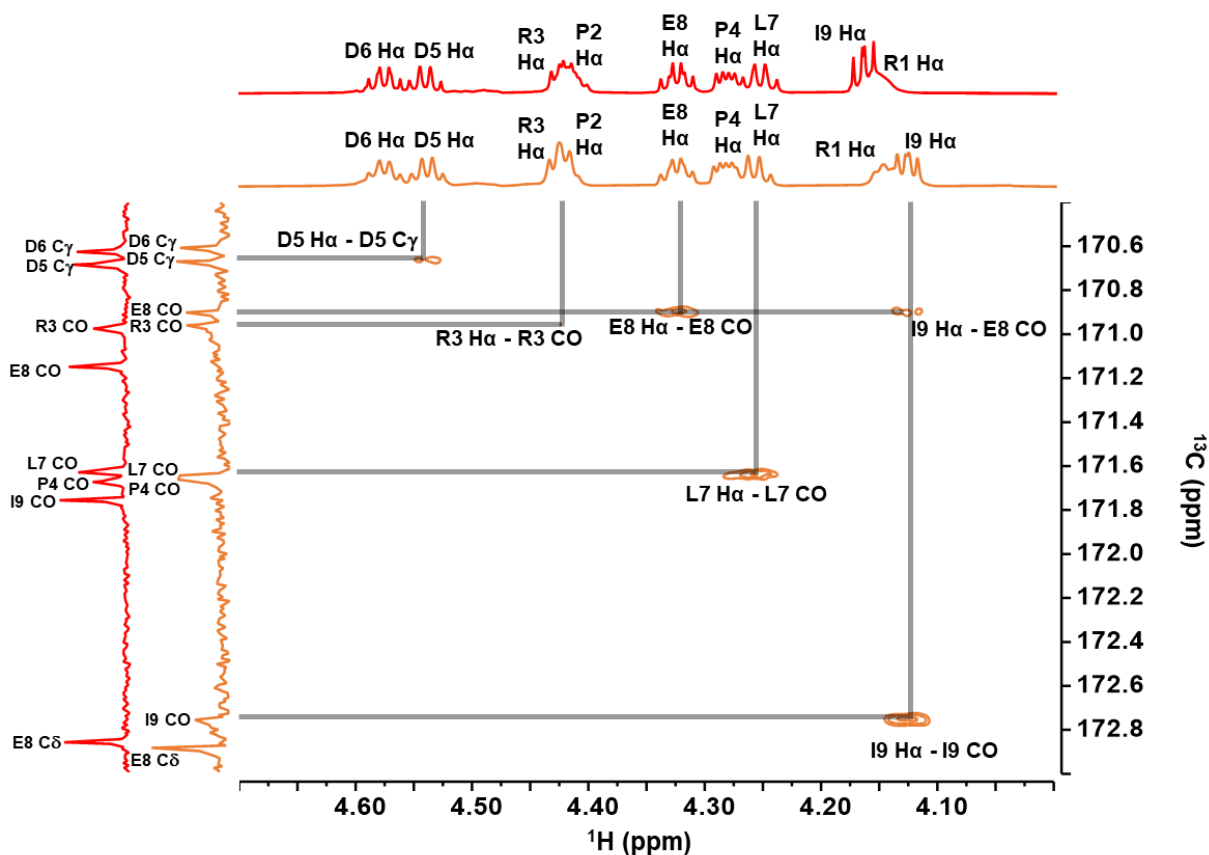
Figure A.27. selHMBC of αCT11-3OMe(D5/D6/E8): Hα region (4.0 – 4.7 ppm) x carbonyl C region (170.4 – 173.2 ppm). Hα – C correlations and the D5 Hα - Cγ correlation were used to assign αCT11-3OMe(D5/D6/E8) carbonyl C resonances. Corresponding αCT11-4OMe ^{1}H and ^{13}C spectra (red) are stacked above the corresponding -3OMe(D5/D6/E8) spectra (orange) as a comparison, specifically highlighting the upfield shift in the I9 Hα resonance and the upfield/downfield shifts in the E8/I9 carbonyl C resonances observed in the -3OMe(D5/D6/E8) spectra relative to the 4OMe spectra.
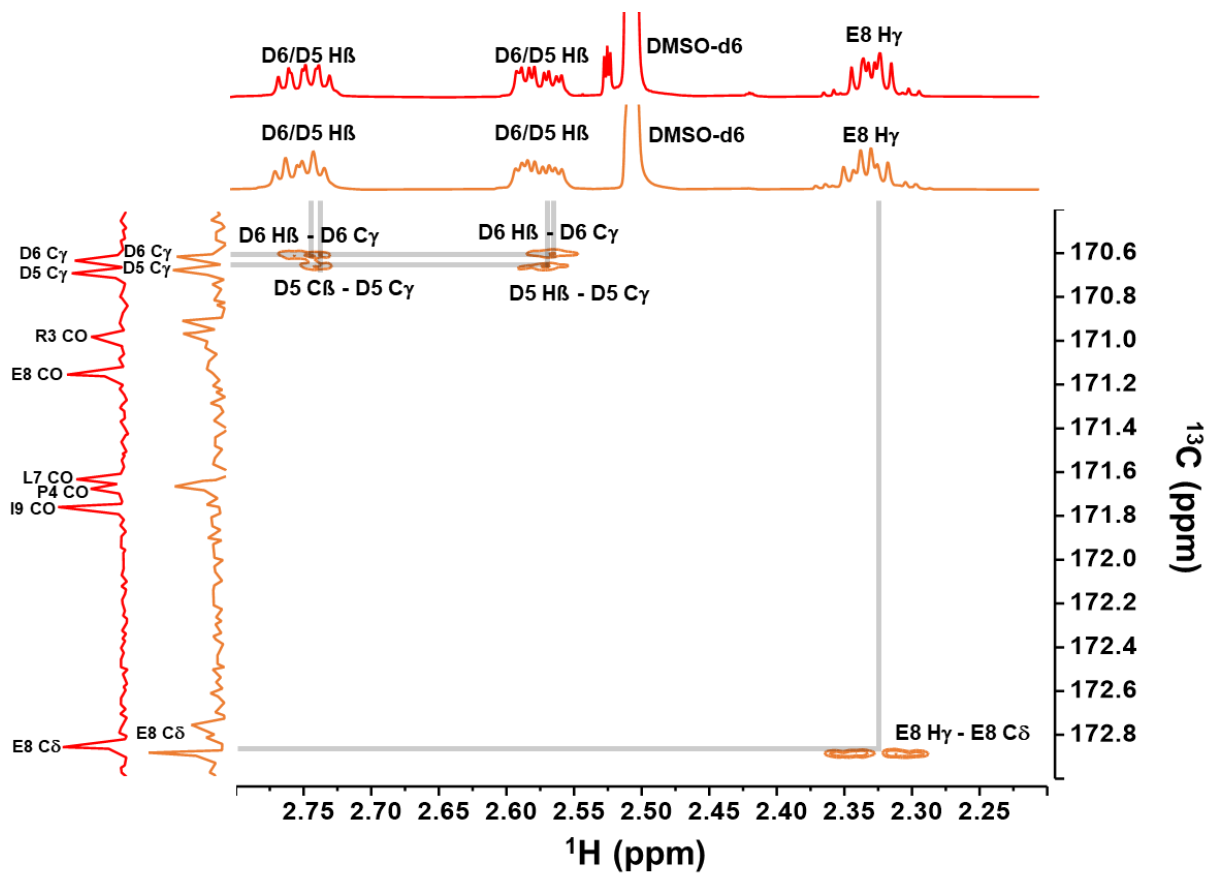
Figure A.28. selHMBC of αCT11-3OMe(D5/D6/E8): D5/D6 Hß and E8 Hγ resonance region (2.2 – 2.8 ppm) x carbonyl C region (170.4 – 173.2 ppm). The D5/D6 Hß - Cγ and E8 Hγ - Cδ correlations were used to assign the D5/D6 Cγ and E8 Cδ resonances, respectively. Corresponding αCT11-4OMe ^{1}H and ^{13}C spectra (red) are stacked above the corresponding -3OMe(D5/D6/E8) spectra (orange), where shifts in the E8 C and its correlation with the E8 Hγ were observed.

A.3 Hydrolysis of installed αCT11 methyl esters.
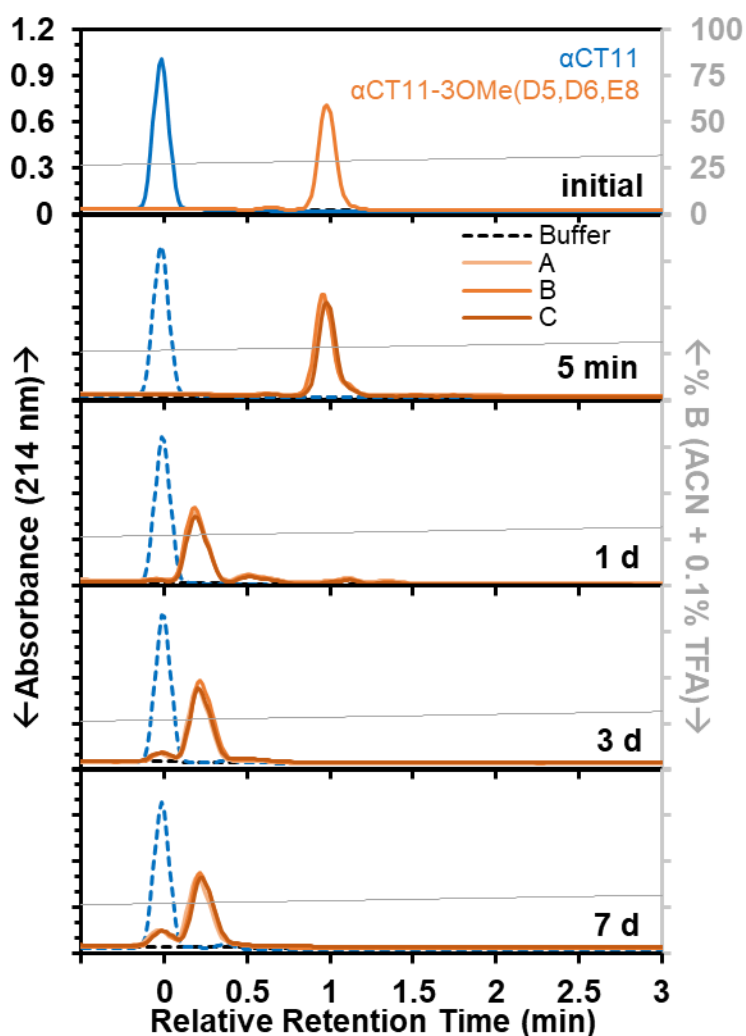
Figure A.29. Hydrolysis of αCT11-3OMe(D5/D6/E8) in 1X PBS (pH 7.4). RP-HPLC chromatograms of αCT11-3OMe(D5/D6/E8) (orange solid lines) are shown compared to unmodified αCT11 (blue dashed lines) standards run at each timepoint. Standards were stored in 5 % ACN in which no hydrolysis was expected to occur. Significant hydrolysis in PBS was observed only in the first 24 h, but with little subsequent hydrolysis or activation occurring over the remainder of the 14-d experiment. This experiment was repeated in triplicate, with each replicate plotted as a solid line with varying shades of orange (A, B, C). Retention time for each esterified sample was reported relative to that of αCT11, which was set to a retention time of 0. Mobile phase composition (% ACN + 0.1% TFA, gray) was plotted against the retention time in each RP-HPLC chromatogram.
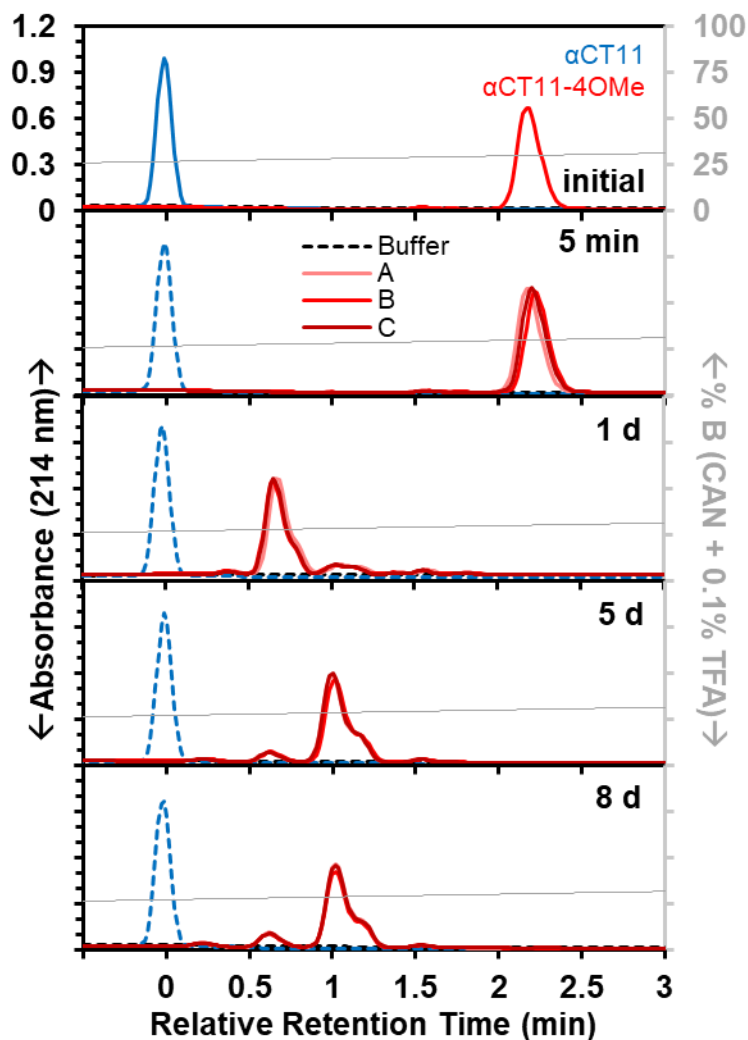
Figure A.30. Hydrolysis of αCT11-4OMe in 1X PBS (pH 7.4). RP-HPLC chromatograms of αCT11-4OMe (red solid lines) are shown compared to unmodified αCT11 (blue dashed lines) standards run at each timepoint. Standards were stored in 5 % ACN in which no hydrolysis was expected to occur. Significant hydrolysis in PBS was observed only in the first 24 h, but with little subsequent hydrolysis or activation occurring over the remainder of the 8-d experiment. This experiment was repeated in triplicate, with each replicate plotted as a solid line with varying shades of red (A, B, C). Retention time for each esterified sample was reported relative to that of αCT11, which was set to a retention time of 0. Mobile phase composition (% ACN + 0.1% TFA, gray) was plotted against the retention time in each RP-HPLC chromatogram.
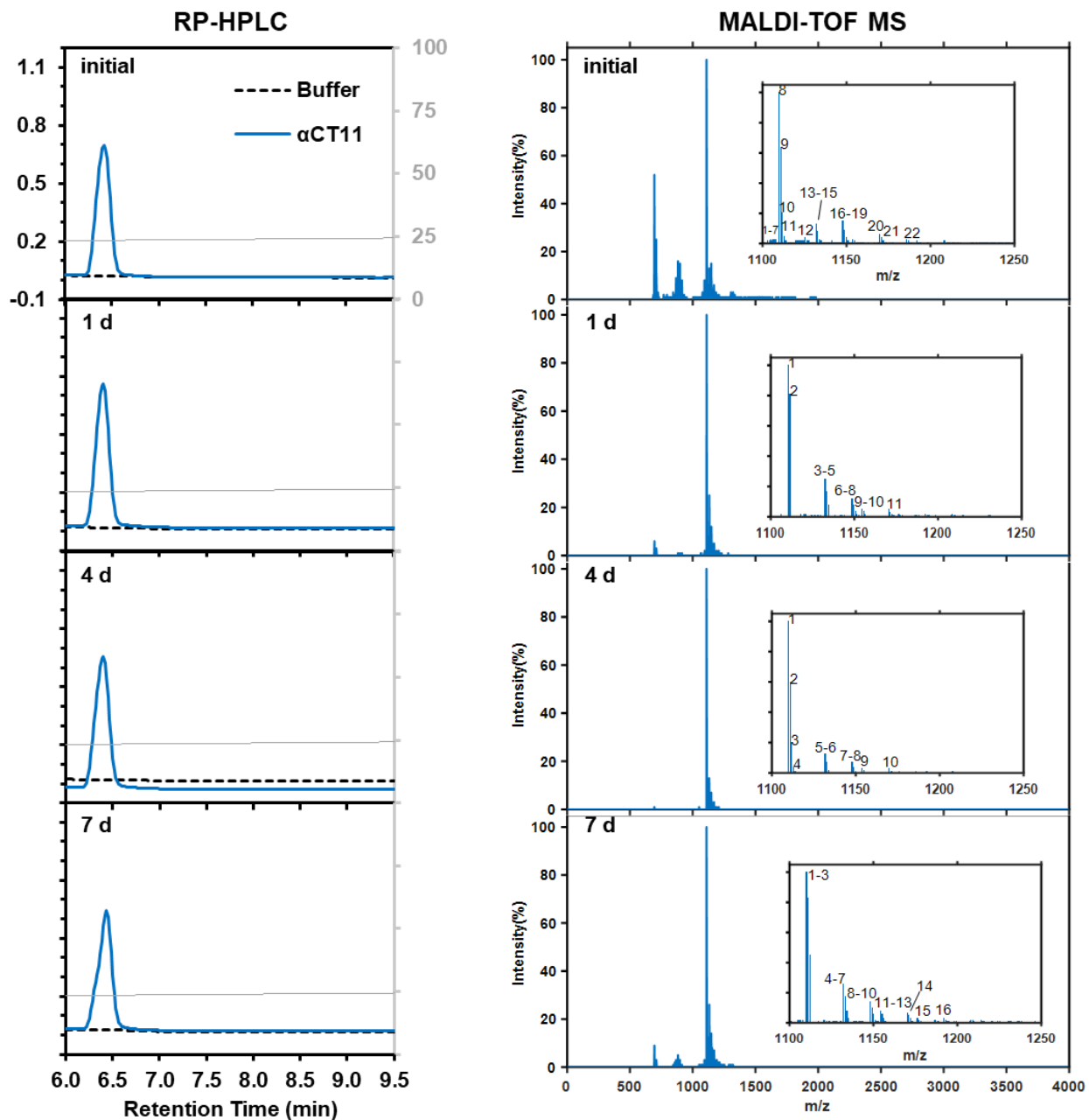
Figure A.31. RP-HPLC chromatograms and MALDI-TOF spectra of αCT11 in 1X PBS (pH 7.4) over 1 week. No changes were seen in either the chromatograms or MALDI-TOF mass spec over 7 d. Mobile phase composition (% ACN + 0.1% TFA, gray) was plotted against the retention time in each RP-HPLC chromatogram. MALDI-TOF measurements were obtained through co-crystallization in a CHCA matrix. Data between 1100 and 1250 m/z are shown inset of each plot, with each peak is numerically labeled. Labels are defined in Table A.5.

Table A.5. Molecular weights of peaks observed in MALDI-TOF MS data measuring the incubation of αCT11 in 1X PBS, as shown in Figure A.31.

Time	label	Mass (Da)	Intensity (%)	Species
initial	1	1104.742	3	?
	2	1104.897	3	?
	3	1106.055	3	?
	4	1106.595	3	?
	5	1107.136	3	?
	6	1107.6	3	?
	7	1107.909	3	?
	8	1109.919	100	[αCT11 + H]+
	9	1110.925	64	
	10	1111.931	21	
	11	1113.016	5	?
	12	1125.367	4	?
	13	1131.919	13	[αCT11 + Na]+
	14	1132.935	8	
	15	1133.951	3	
	16	1147.833	15	[αCT11 + K]+
	17	1148.856	9	
	18	1149.879	4	
	19	1153.898	3	[αCT11 + 2Na - H]+
	20	1169.806	6	[αCT11 + K + Na - H]+
	21	1170.839	4	[αCT11 + K + Na - H]+
	22	1185.743	3	?

	23	1321.423	3	?
1 d	1	1110.4	100	[αCT11 + H]+
	2	1111.5	81	
	3	1132.6	25	[αCT11 + Na]+
	4	1133.6	17	
	5	1134.6	8	
	6	1148.6	12	[αCT11 + K]+
	7	1149.6	8	
	8	1150.6	4	
	9	1154.7	5	[αCT11 + 2Na - H]+
	10	1155.6	4	
	11	1171.5	3	[αCT11 + K + Na - 2H]+
4 d	1	1109.8	100	[αCT11 + H]+
	2	1110.9	60	
	3	1111.9	20	
	4	1112.9	4	
	5	1131.8	13	[αCT11 + Na]+
	6	1132.9	7	
	7	1147.8	7	[αCT11 + K]+
	8	1148.9	4	
	9	1153.8	3	[αCT11 + 2Na - H]+
	10	1169.8	3	[αCT11 + K + 2Na - 2H]+
7 d	1	1110.1	100	[αCT11 + H]+
	2	1111.2	83	
	3	1112.2	45	

	4	1132.3	26	[αCT11 + Na]+
	5	1133.3	18	
	6	1134.2	8	
	7	1135.2	3	
	8	1148.2	14	[αCT11 + K]+
	9	1149.2	10	
	10	1150.2	6	
	11	1154.2	8	[αCT11 + 2Na - H]+
	12	1155.3	6	
	13	1156.218	3	
	14	1170.238	7	[αCT11 + K + Na - H]+
	15	1176.204	3	[αCT11 + 3Na - 2H]+
	16	1192.188	3	[αCT11 + K + 2Na - 2H]+

Table A.6. Percent activation of αCT11-3OMe(D5,D6,E8) and -4OMe in 1X PBS (pH 7.4) and 100 mM carbonate buffer (pH 10.0) over 8 d.

Time (d)	3OMe(D5,D6,E8)				4OMe			
	1X PBS (pH 7.4)		100 mM carbonate buffer (pH 10)		1X PBS (pH 7.4)		100 mM carbonate buffer (pH 10)	
	Average	StDev	Average	StDev	Average	StDev	Average	StDev
0.00	0.00	0.00	0.22	0.11	0.00	0.00	0.62	0.08
0.25			54.65	2.42			15.20	0.36
0.50			66.94	0.87			35.81	0.32
1.00	3.37	1.03	88.14	0.46	0.00	0.00	62.33	1.09
1.50			96.15	0.74			76.36	0.55
2.00			98.33	0.27			84.41	0.13
3.00	5.77	1.91	100.32	0.08			93.82	0.18
5.00			99.99	0.15	0.00	0.00	98.50	0.28
7.00	10.45	2.26						
8.00					1.13	0.30		
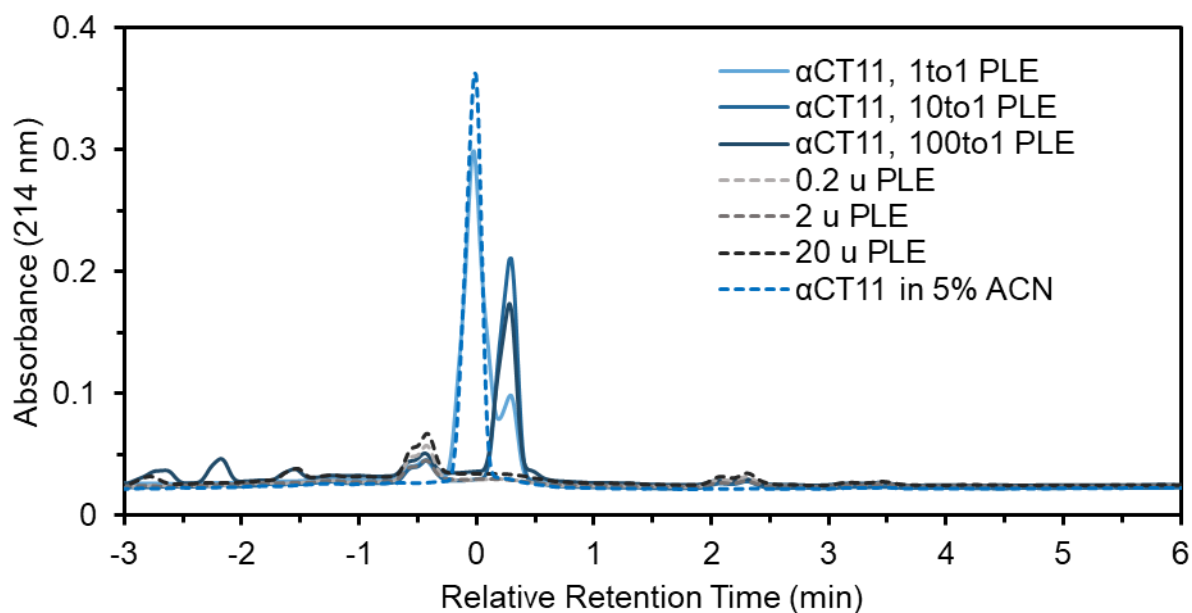
Figure A.32. PLE-catalyzed hydrolysis of αCT11. Hydrolysis was performed at a 1:1 (light blue), 10:1 (blue), and 100:1 (navy blue) ratios of PLE enzyme units:μmol αCT11. PLE controls for each condition (gray, dashed lines) and an αCT11 only control (blue dashed line) are also pictured. The appearance of a second peak in αCT11 + PLE samples and the disappearance of αCT11 were observed with increasing PLE concentration. Retention time of each sample is reported relative to an αCT11 control, which was set to 0.
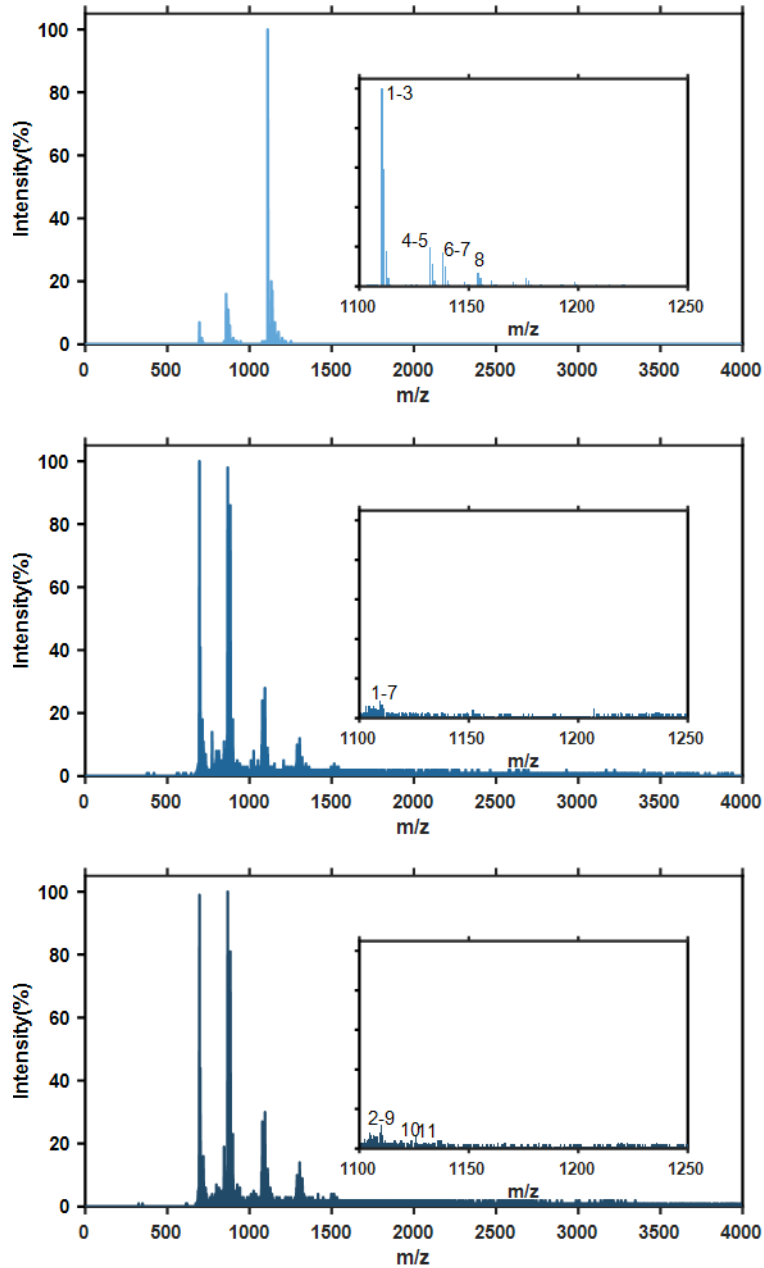
Figure A.33. MALDI-TOF MS results of PLE-catalyzed hydrolysis of αCT11, depicted in Figure S32. Hydrolysis was performed at a 1:1 (light blue), 10:1 (blue), and 100:1 (navy blue) ratios of PLE enzyme units:μmol αCT11. Results between 1100-1250 m/z, where αCT11 is expected to appear in MALDI-TOF MS, is inset. αCT11-related peaks disappeared with increasing PLE concentration. Peak labels are defined in Table A.7.

Table A.7. MALDI-TOF MS results of PLE-catalyzed hydrolysis of αCT11

PLE:αCT11 ratio (enzyme units: μmol peptide)	label	Mass (Da)	Intensity (%)	Species
1:1	1	1110.28	100	[αCT11 + H]+
	2	1111.28	59	[αCT11 + H]+
	3	1112.37	18	[αCT11 + H]+
	4	1132.36	20	[αCT11 + Na]+
	5	1133.38	11	[αCT11 + Na]+
	6	1138.31	17	[2OMe + H]+
	7	1139.32	10	[2OMe + H]+
	8	1154.34	7	[αCT11 + 2Na - H]+
10:1	1	1103.25	6	N/A
	2	1104.48	6	N/A
	3	1106.64	6	N/A
	4	1107.42	5	N/A
	5	1109.5	9	N/A
	6	1110.43	7	N/A
	7	1112.6	3	N/A
100:1	1	1100.86	3	N/A
	2	1104.64	8	N/A
	3	1105.25	7	N/A
	4	1106.64	7	N/A
	5	1106.95	6	N/A
	6	1107.96	6	N/A
	7	1109.5	8	N/A
	8	1109.97	12	N/A
	9	1110.82	7	N/A
	10	1118.65	3	N/A
	11	1125.81	6	N/A

*N/A refers to a sample that cannot be reliably attributed to either matrix or αCT11.
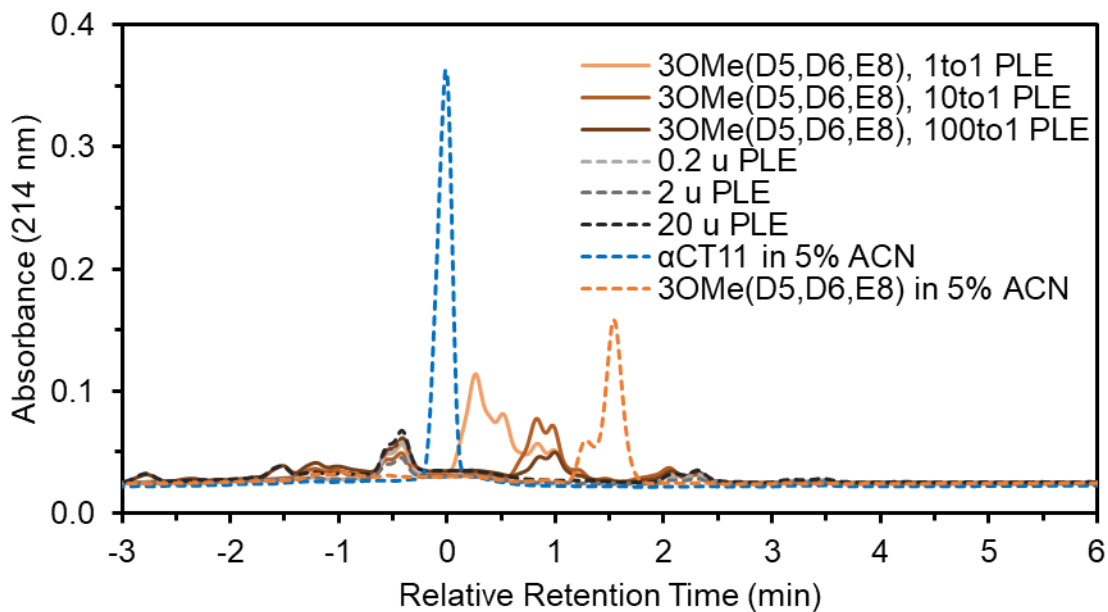
Figure A.34. RP-HPLC chromatogram of PLE-catalyzed hydrolysis of αCT11-3OMe(D5,D6,E8). Hydrolysis was performed at a 1:1 (light orange), 10:1 (dark orange), and 100:1 (brown) ratios of PLE enzyme units:μmol αCT11. PLE controls for each condition (gray, dashed lines) and an αCT11-3OMe(D5,D6,E) control (orange dashed line) and αCT11 control (blue dashed line) are also pictured. The appearance of an unaccounted-for peak in αCT11-3OMe(D5,D6,E8) + PLE samples and the disappearance of αCT11 were observed with increasing PLE concentration. Retention time of each sample is reported relative to an αCT11 control, which was set to 0.
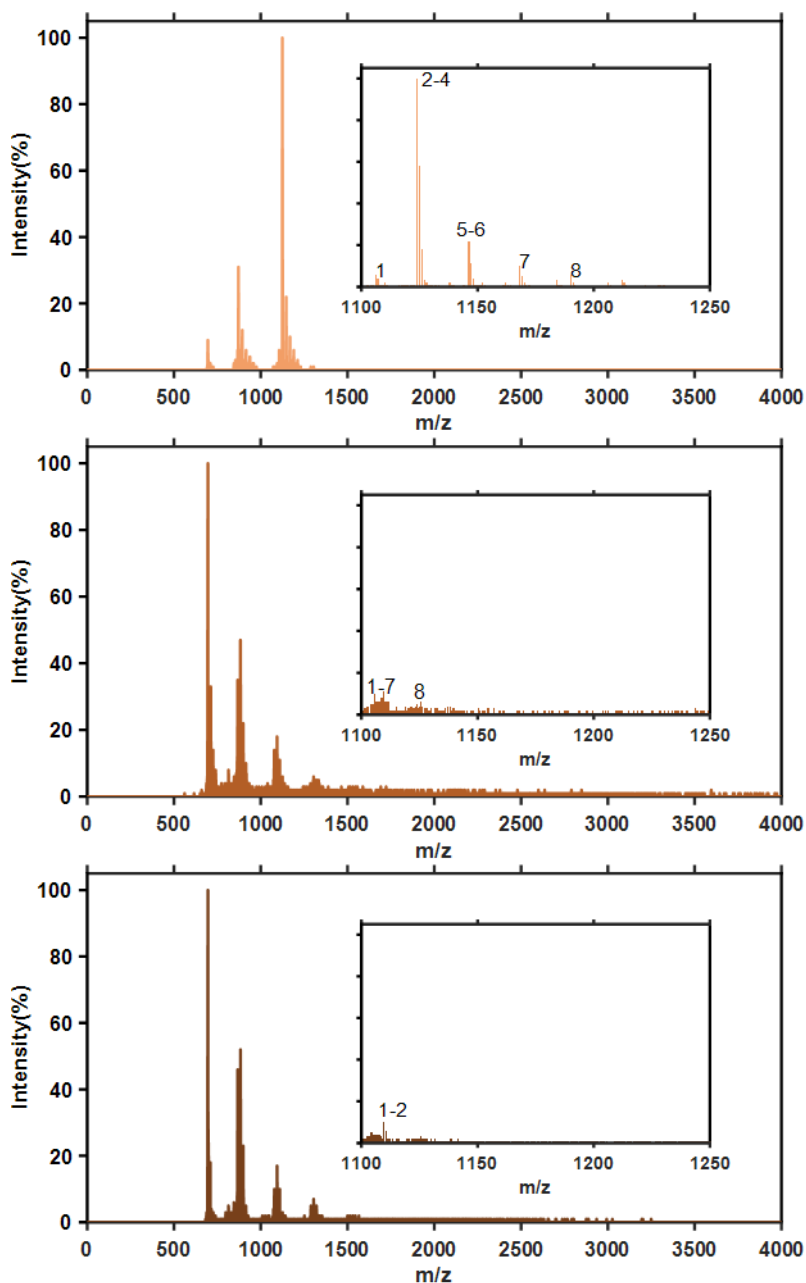
Figure A.35. MALDI-TOF MS results of PLE-catalyzed hydrolysis of αCT11-3OMe(D5,D6,E8), depicted in Figure S34. Hydrolysis was performed at a 1:1 (light orange), 10:1 (dark orange), and 100:1 (brown) ratios of PLE enzyme units:μmol αCT11. Results between 1100-1250 m/z, where αCT11 is expected to appear in MALDI-TOF MS, is inset. αCT11-related peaks disappeared with increasing PLE concentration. Peak labels are defined in Table A.8.

Table A.8. MALDI-TOF MS results of PLE-catalyzed hydrolysis of αCT11-3OMe(D5,D6,E8).

PLE:αCT11 ratio (enzyme units: μmol peptide)	label	Mass (Da)	Intensity (%)	Species
1:1	1	1106.103	6	[1OMe + 1 imide + H]+
	2	1124.092	100	[1OMe + H]+
	3	1125.104	58	[1OMe + H]+
	4	1126.117	18	[1OMe + H]+
	5	1146.152	22	[1OMe + Na]+
	6	1147.175	11	[1OMe + Na]+
	7	1168.19	10	[1OMe + 2Na - H]+
	8	1190.196	6	[3OMe + K]+
10:1	1	1105.794	10	N/A
	2	1106.489	6	[1OMe +1 imide + H]+
	3	1107.648	6	[1OMe +1 imide + H]+
	4	1108.653	8	[1OMe +1 imide + H]+
	5	1109.581	11	PLE
	6	1110.509	6	[αCT11 + H]+
	7	1111.593	6	[αCT11 + H]+
	8	1125.493	6	N/A
100:1	1	1109.735	10	PLE
	2	1110.741	6	PLE

*N/A refers to a sample that cannot be reliably attributed to either matrix or αCT11.
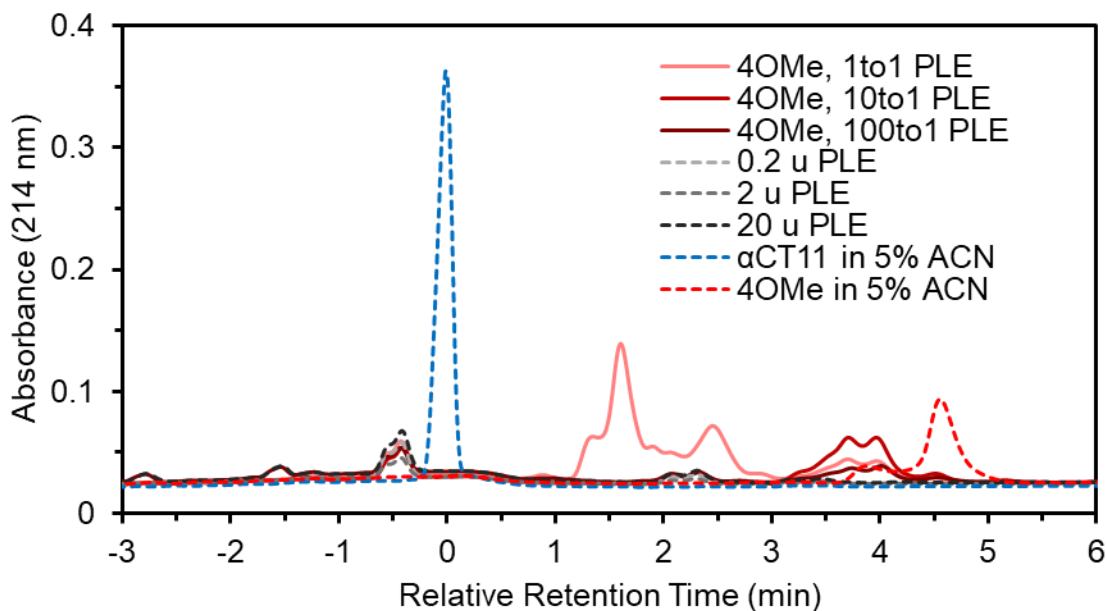
Figure A.36. RP-HPLC chromatogram of PLE-catalyzed hydrolysis of αCT11-4OMe. Hydrolysis was performed at a 1:1 (pink), 10:1 (red), and 100:1 (dark red) ratios of PLE enzyme units:μmol αCT11. PLE controls for each condition (gray, dashed lines) and an αCT11-4OMe control (red dashed line) and αCT11 control (blue dashed line) are also pictured. The appearance of an unaccounted-for peak in αCT11-4OMe + PLE samples were observed with increasing PLE concentration. Retention time of each sample is reported relative to an αCT11 control, which was set to 0.
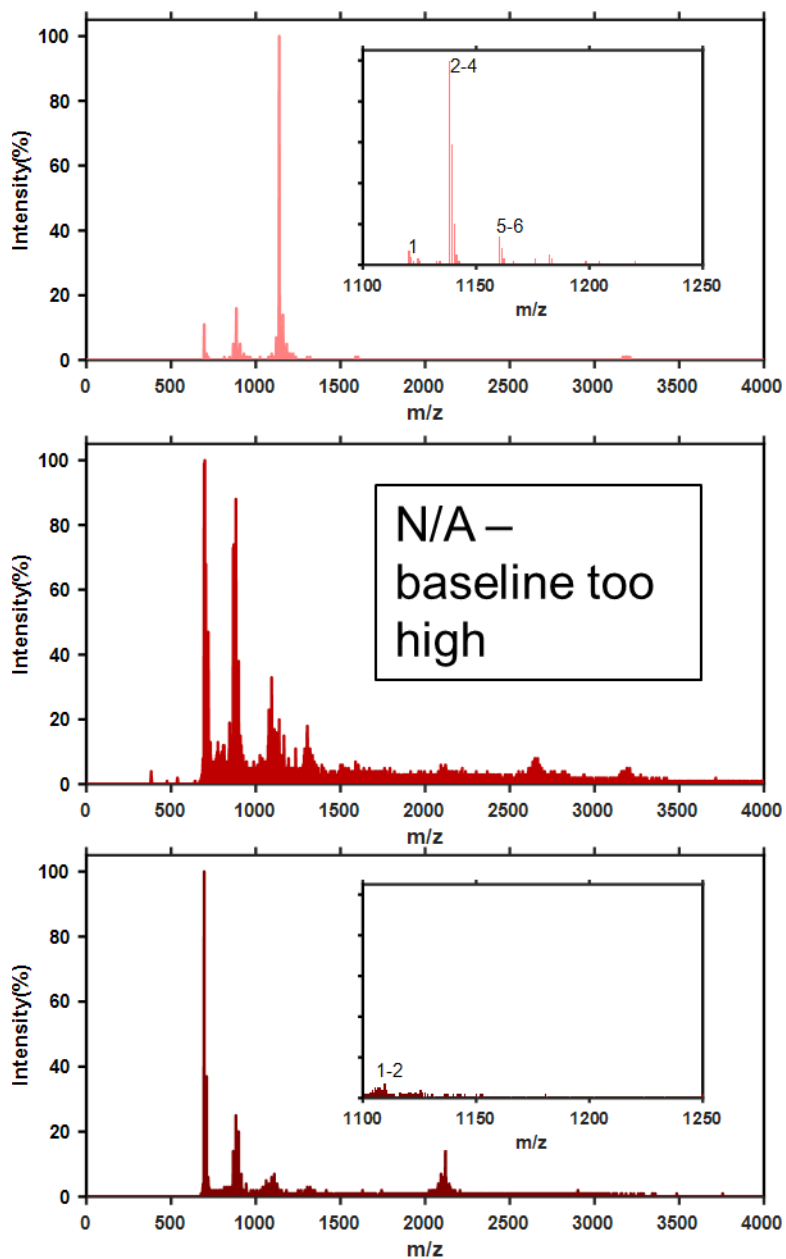
Figure A.37. MALDI-TOF MS results of PLE-catalyzed hydrolysis of αCT11-4OMe, depicted in Figure S36. Hydrolysis was performed at a 1:1 (pink), 10:1 (red), and 100:1 (dark red) ratios of PLE enzyme units:μmol αCT11. Results between 1100-1250 m/z, where αCT11 is expected to appear in MALDI-TOF MS, is inset. αCT11-related peaks disappeared with increasing PLE concentration. Peak labels are defined in Table A.9.

Table A.9. MALDI-TOF MS results of PLE-catalyzed hydrolysis of αCT11-3OMe(D5,D6,E8).

PLE:αCT11 ratio (enzyme units: μmol peptide)	label	Mass (Da)	Intensity (%)	Species
1:1	1	1120.358	7	[2OMe + 1 imide + H]+
	2	1138.383	100	[2OMe + H]+
	3	1139.402	59	[2OMe + H]+
	4	1140.421	20	[2OMe + H]+
	5	1160.425	14	[2OMe + Na]+
	6	1161.454	8	[2OMe + Na]+
100:1	1	1107.493	5	?
	2	1109.658	7	PLE

*N/A refers to a sample that cannot be reliably attributed to either matrix or αCT11.

We varied the PLE concentration between 1:1, 10:1, and 100:1 enzyme units:μmol peptide and stirred the solution at 37 °C over 24 h. At all ratios, we observed the appearance of a new peak in the αCT11 RP-HPLC chromatogram, which eluted later (xxx) than the αCT11 peak, grew with increasing PLE concentration, and were not associated with any esterase peaks (**Figure A.32**). Further, while MALDI-TOF MS confirmed the presence of αCT11 in the 1:1 PLE:αCT11 sample, we could identify no αCT11 peaks in the 10:1 and 100:1 MALDI-TOF spectra (**Figure A.33, Table A.7**). Similar trends were observed for the -3OMe(D5,D6,E8) and -4OMe samples, where the 1:1 PLE:peptide MALDI-TOF spectra revealed species similar to those present in samples incubated in only 1X PBS after 1 d (**Figures A.34-A.37, Table A.8-A.9**), but a loss of αCT11-related signal in both RP-HPLC chromatograms and MALDI-TOF MS spectra in both 10:1 and 100:1 PLE:peptide samples.
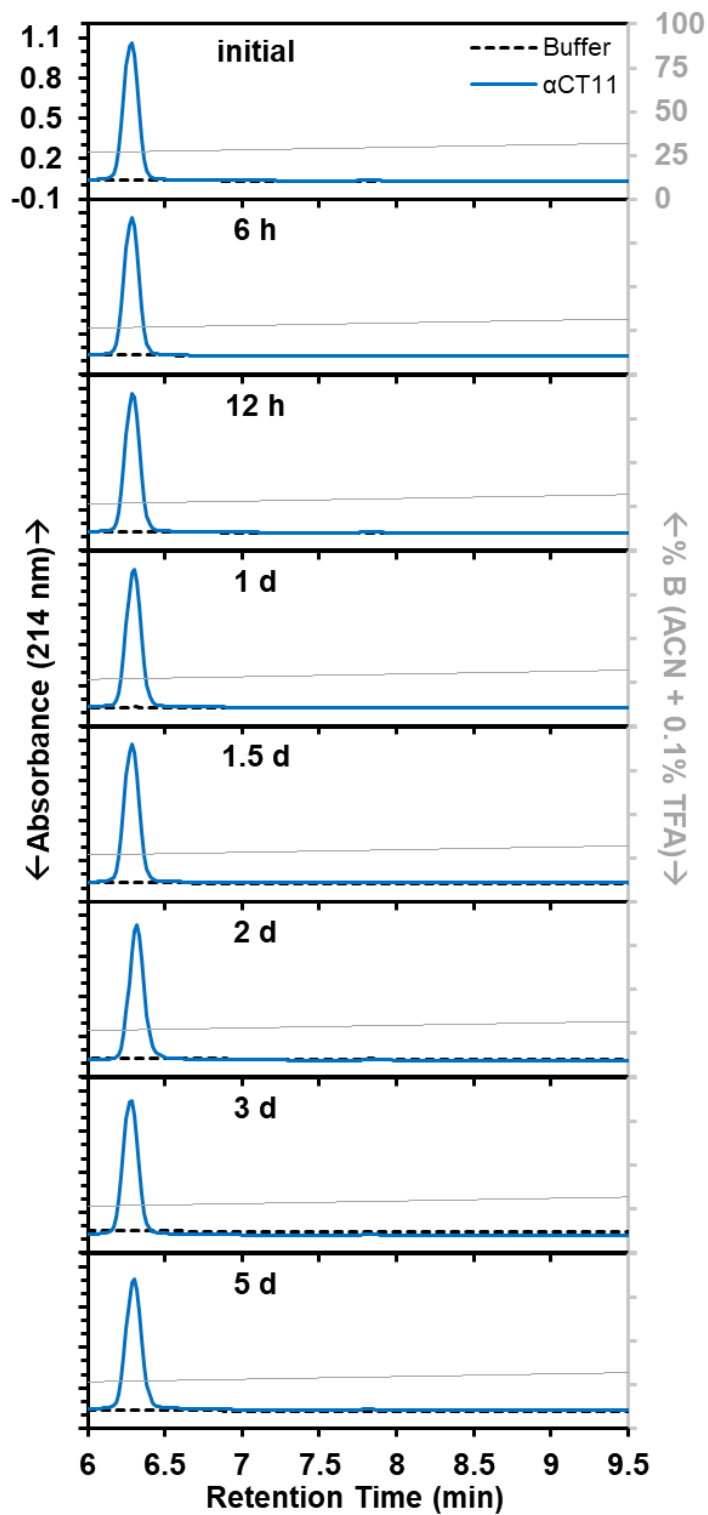
Figure A.38. RP-HPLC chromatograms αCT11 in 100 mM carbonate buffer (pH 10) over 1 week. No changes were seen in RP-HPLC chromatograms at each tested timepoint, suggesting stability of αCT11 under the basic conditions tested. Mobile phase composition (% ACN + 0.1% TFA, gray) was plotted against the retention time in each RP-HPLC chromatogram.
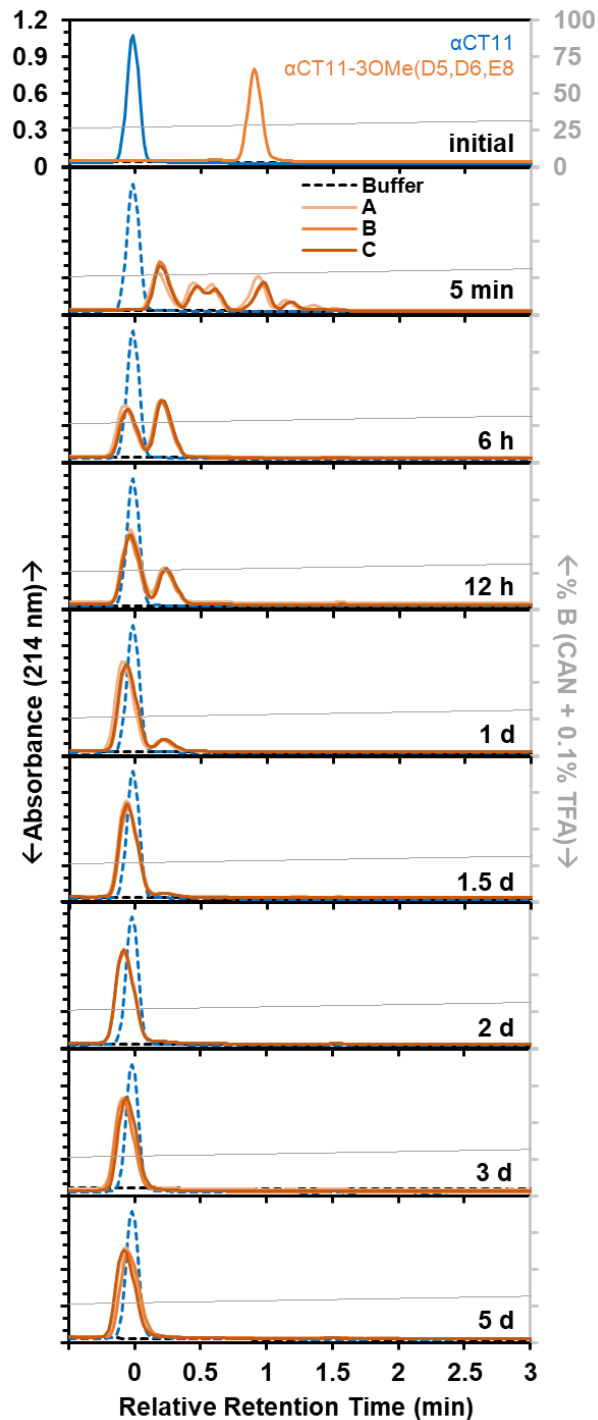
Figure A.39. Hydrolysis of αCT11-3OMe(D5/D6/E8) in 100 mM carbonate buffer (pH 10.0). RP-HPLC chromatograms of αCT11-3OMe(D5/D6/E8) (orange solid lines) are shown compared to unmodified αCT11 (blue dashed lines) standards run at each timepoint. Standards were stored in 5 % ACN in which no hydrolysis was expected to occur. Full esterified peptide hydrolysis was observed after 3 d and was confirmed by LC-MS (Figure A.41). The experiment was repeated in triplicate, with each replicate plotted as a solid line with varying shades of orange (A, B, C). Retention time for each esterified sample was reported relative to that of αCT11, which was set to a retention time of 0. Mobile phase composition (% ACN + 0.1% TFA, gray) was plotted against the retention time in each RP-HPLC chromatogram.
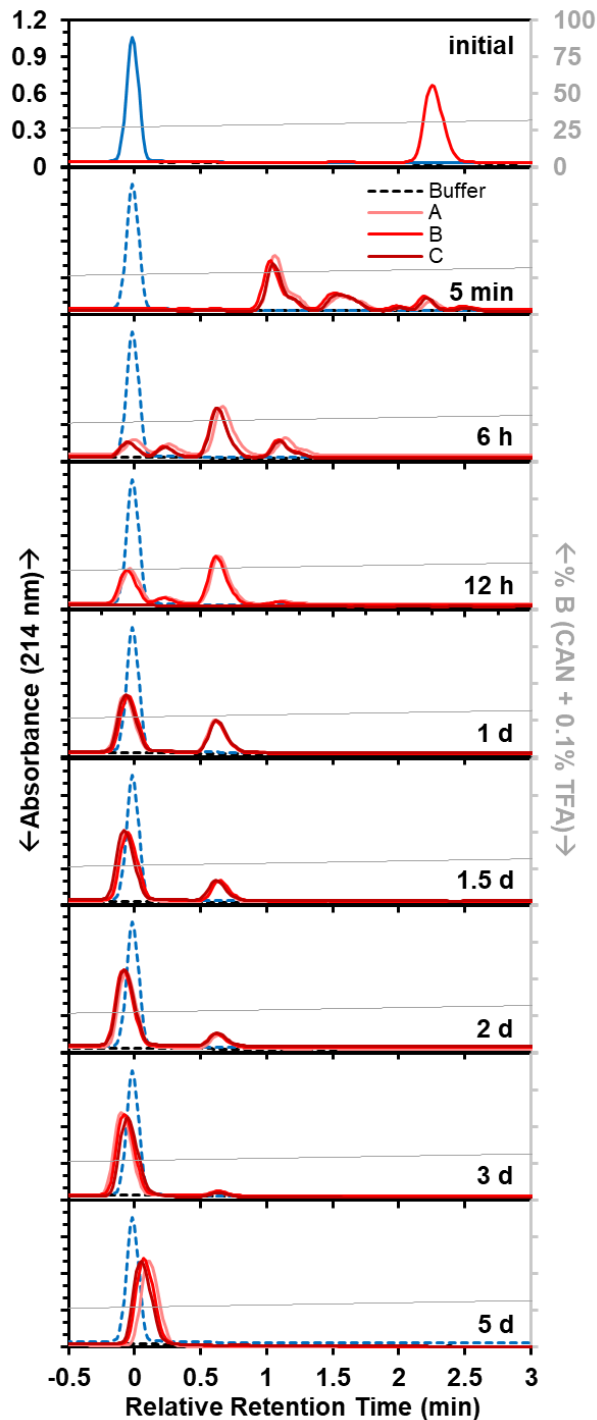
Figure A.40. Hydrolysis of αCT11-4OMe in 100 mM carbonate buffer (pH 10.0). RP-HPLC chromatograms of αCT11-4OMe (red solid lines) are shown compared to unmodified αCT11 (blue dashed lines) standards run at each timepoint. Standards were stored in 5 % ACN in which no hydrolysis was expected to occur. Full esterified peptide activation was observed after 5 d and was confirmed by LC-MS (Figure A.42). The experiment was repeated in triplicate, with each replicate plotted as a solid line with varying shades of red (A, B, C). Retention time for each esterified sample was reported relative to that of αCT11, which was set to a retention time of 0. Mobile phase composition (% ACN + 0.1% TFA, gray) was plotted against the retention time in each RP-HPLC chromatogram.
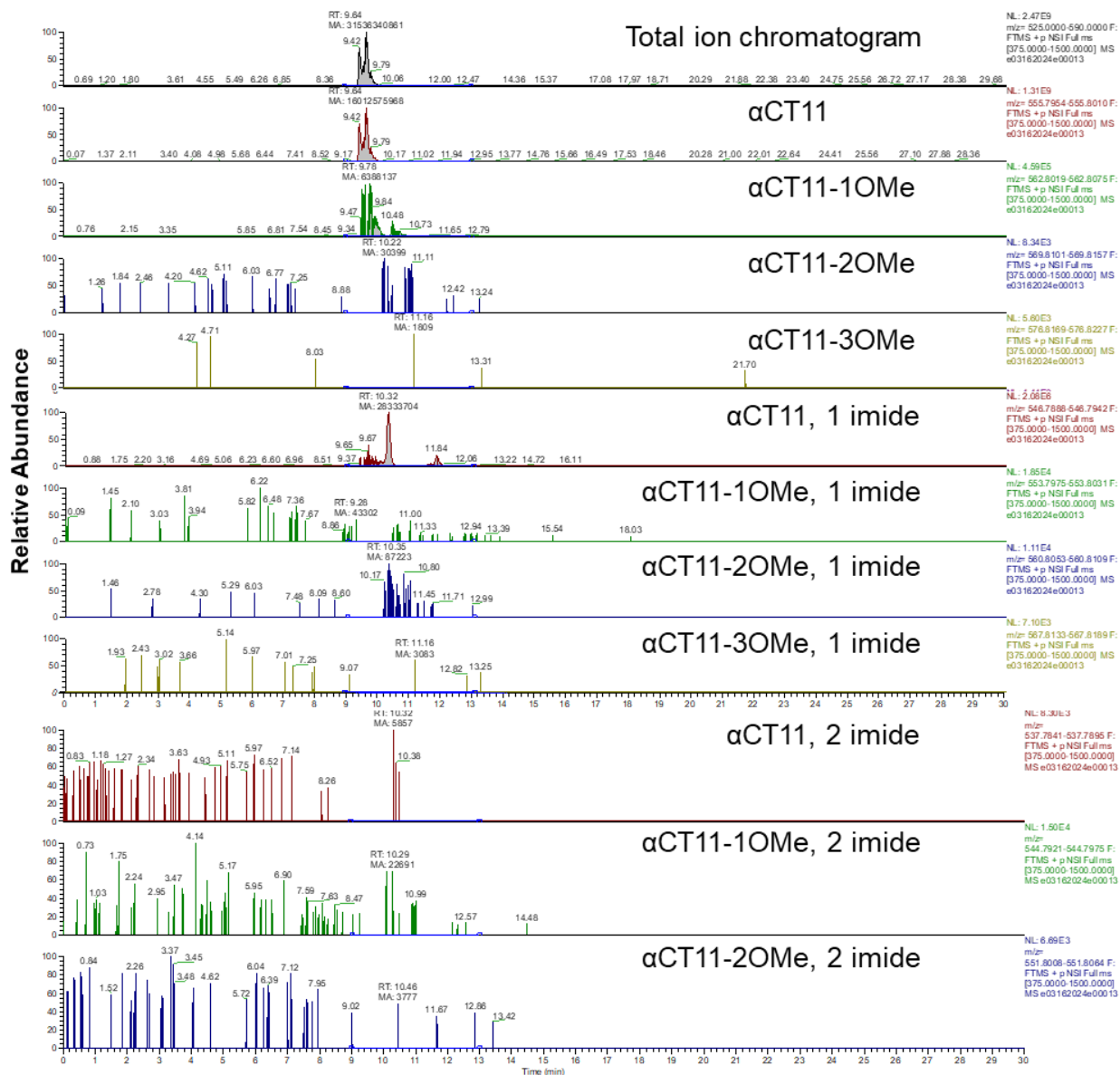
Figure A.41. LC-MS chromatograms of αCT11-3OMe(D5,D6,E8) after 3 d of stirring in 100 mM carbonate buffer (pH 10.0) at 37 °C. Total ion chromatogram (top, gray) and selective ion chromatograms for αCT11 with different numbers of esters and/or imides.
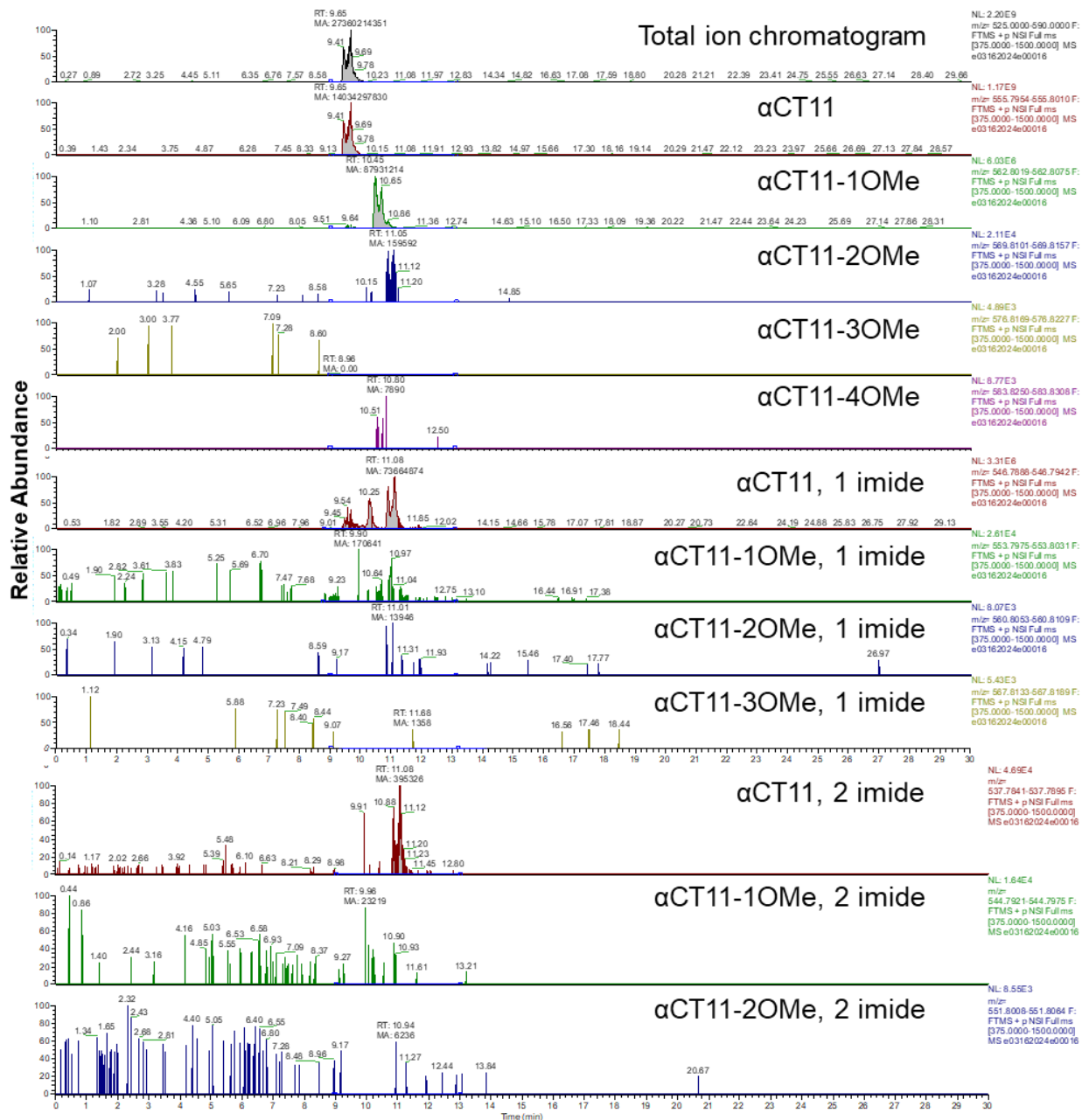
Figure A.42. LC-MS chromatograms of αCT11-4OMe after 5 d of stirring in 100 mM carbonate buffer (pH 10.0) at 37 °C. Total ion chromatogram (top, gray) and selective ion chromatograms for αCT11 with different numbers of esters and/or imides.

Table A.10. % Abundance and retention times (RT, min) of αCT11-based formulations produced by the hydrolysis of αCT11-3OMe(D5,D6,E8) in 100 mM carbonate buffer (pH 10) after 3 d, quantified by LC-MS.

		Ester #										Total
		0		1		2		3		4		
		% Abundance	RT (min)	% Abundance	RT (min)	% Abundance	RT (min)	% Abundance	RT (min)	% Abundance	RT (min)	% Abundance
	no imides	96.47	9.42 9.64 9.79	0.04	-	0.00	-	0.00	-	N/A	N/A	96.68
3 d	1 imide	0.17	-	0.00	-	0.00	-	0.00	-	N/A	N/A	0.17
	2 imides	0.00	-	0.00	-	0.00	-	N/A	N/A	N/A	N/A	0.00

Table A.11. % Abundance and retention times (RT, min) of αCT11-based formulations produced by the hydrolysis of αCT11-4OMe in 100 mM carbonate buffer (pH 10) after 5 d, quantified by LC-MS.

| | | Ester # | | | | | | | | | | Total |
| | | 0 | | 1 | | 2 | | 3 | | 4 | | |
		% Abundance	RT (min)	% Abundance	RT (min)	% Abundance	RT (min)	% Abundance	RT (min)	% Abundance	RT (min)	% Abundance
	no imides	97.46	9.41 / 9.65 / 9.69	0.61	-	0.00	-	0.00	-	0.00	-	0.00
5 d	1 imide	0.51	-	0.00	-	0.00	-	0.00	-	N/A	N/A	0.51
	2 imides	0.00	-	0.00	-	0.00	-	N/A	N/A	N/A	N/A	0.00
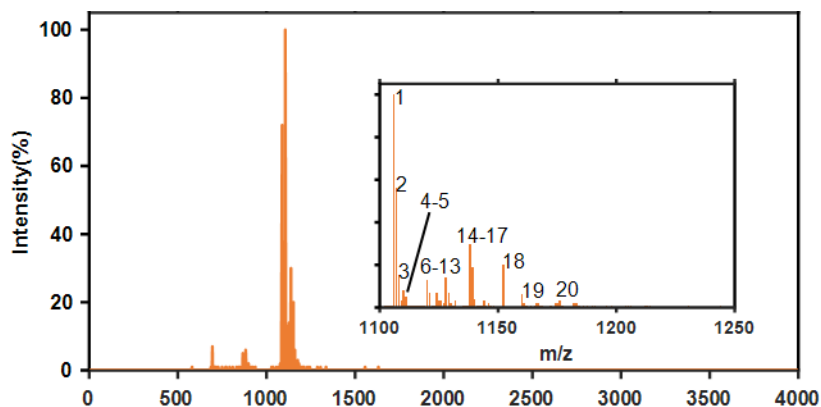
label	Mass (Da)	Intensity (%)	Species
1	1106.1	100	
2	1107.1	56	$[\alpha CT11\text{-}1OMe - H_2O + H]+$
3	1108.1	15	
4	1110.1	8	$[\alpha CT11 + H]+$
5	1111.1	5	
6	1120.2	13	$[\alpha CT11\text{-}2OMe - H_2O + H]+$
7	1121.1	7	
8	1124.1	7	
9	1125.1	3	$[\alpha CT11\text{-}1OMe + H]+$
10	1126.0	3	
11	1128.0	14	$\alpha CT11\text{-}1OMe - H_2O + Na]+$
12	1129.1	7	
13	1132.0	3	$[\alpha CT11 + Na]+$
14	1138.1	30	
15	1139.2	19	$[\alpha CT11\text{-}2OMe + H]+$
16	1140.1	4	
17	1144.1	3	$[\alpha CT11\text{-}1OMe - H_2O + K]+$
18	1152.2	20	$[\alpha CT11\text{-}3OMe + H]+$
19	1160.1	6	$[\alpha CT11\text{-}2OMe + Na]+$
20	1176.1	3	$[\alpha CT11\text{-}2OMe + K]+$

Figure A.43. MALDI-TOF MS of αCT11-3OMe(D5,D6,E8) after 2 h of incubation into 1X PBS. Peaks related to esterified αCT11 with the loss of either 1 or 2 H_2O molecules suggest the formation of intramolecular imides/amides.
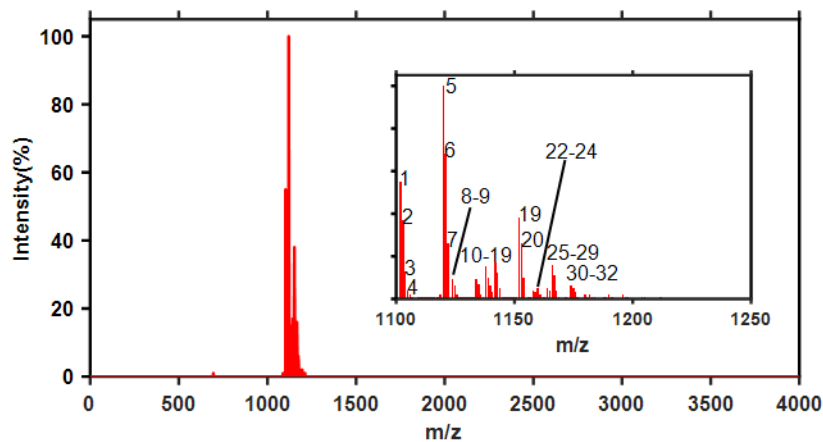
label	Mass (Da)	Intensity (%)	Species
1	1101.9	55	[αCT11-2OMe – 2 H_2O + H]+
2	1102.9	37	
3	1103.8	13	
4	1104.8	4	
5	1119.9	100	[αCT11-2OMe – H_2O + H]+
6	1120.9	68	
7	1121.9	26	
8	1123.9	9	[αCT11-1OMe H]+ or [αCT11-2OMe – 2 H_2O + Na]+
9	1124.8	6	
10	1133.9	9	[αCT11-3OMe – H_2O + H]+
11	1134.9	7	
12	1137.9	15	[αCT11-2OMe + H]+
13	1138.9	10	
14	1139.9	6	[αCT11-2OMe – 2 H_2O + K]+
15	1140.7	3	
16	1141.9	17	[αCT11-2OMe – H_2O + Na]+
17	1142.9	12	
18	1143.8	5	
19	1151.9	38	[αCT11-3OMe + H]+
20	1153.0	26	
21	1153.8	10	
22	1157.9	4	[αCT11-2OMe – H_2O + K]+
23	1158.8	3	
24	1159.9	5	[αCT11-2OMe + Na]+
25	1163.9	5	[αCT11-2OMe – H_2O + 2 Na - H]+
26	1164.9	4	
27	1166.0	16	[αCT11-4OMe + H]+
28	1166.9	11	
29	1167.8	4	
30	1173.9	6	[αCT11-3OMe + Na]+
31	1174.9	5	
32	1175.9	3	

Figure A.44. MALDI-TOF MS of αCT11-4OMe after 2 h of incubation into 1X PBS. Peaks related to esterified αCT11 with the loss of either 1 or 2 H_2O molecules suggest the formation of intramolecular imides/amides.
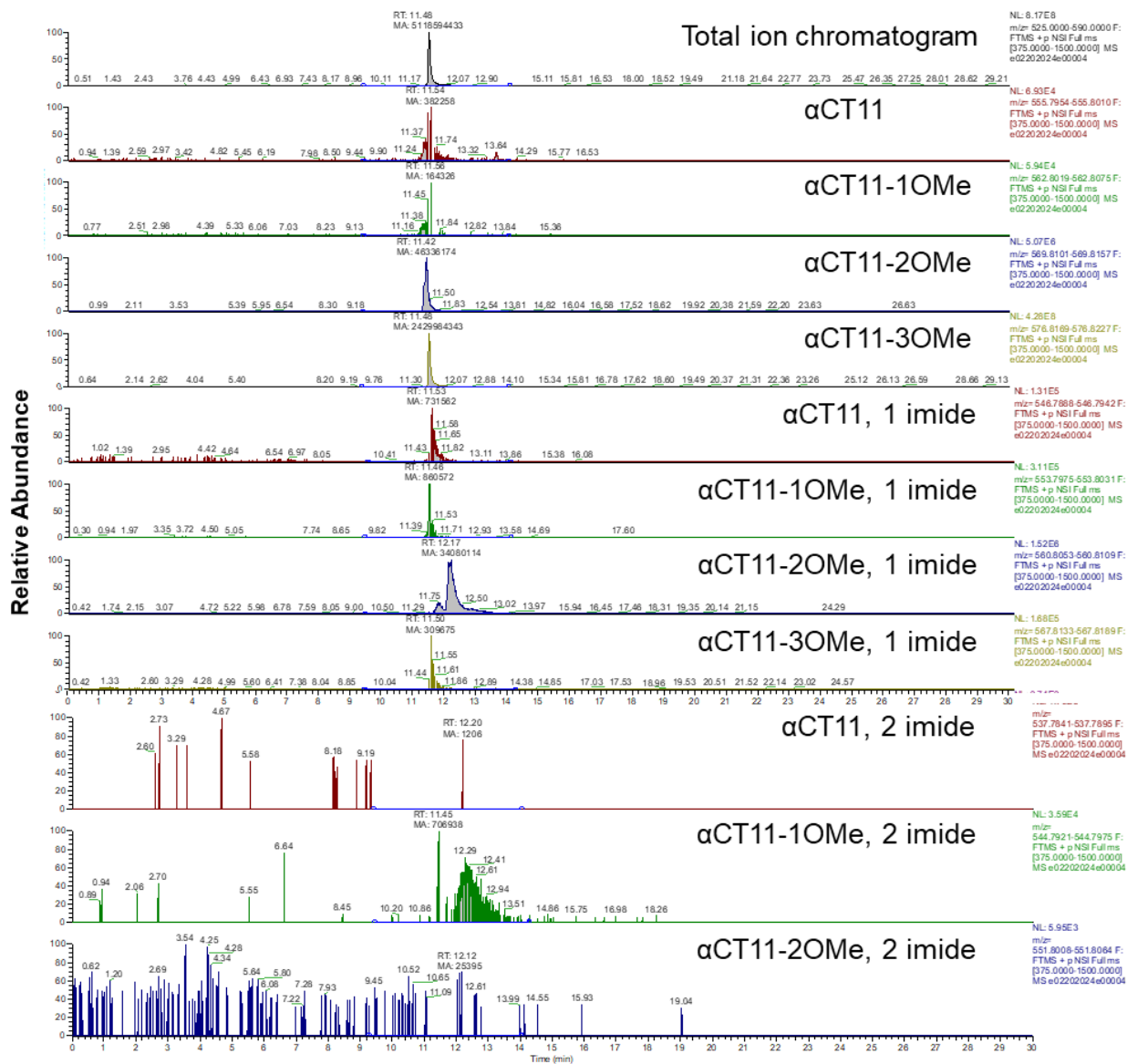
Figure A.45. LC-MS chromatograms of αCT11-3OMe(D5,D6,E8) after 5 min of incubation in 1X PBS (pH 7.4). Total ion chromatogram (top, gray) and selective ion chromatograms for αCT11 with different numbers of esters and/or imides.
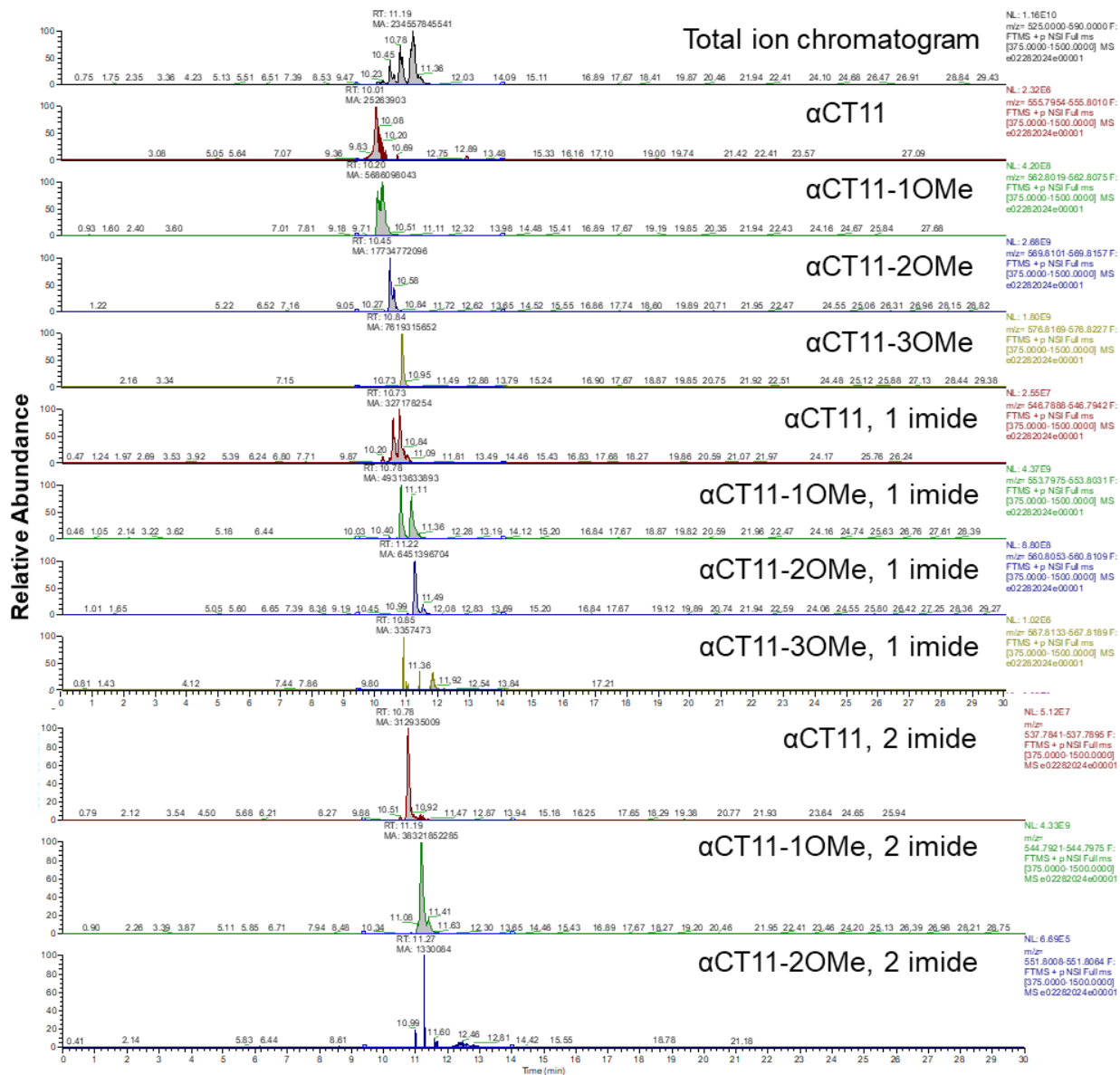
Figure A.46. LC-MS chromatograms of αCT11-3OMe(D5,D6,E8) after 2 h of stirring in 1X PBS (pH 7.4) at 37 °C. Total ion chromatogram (top, gray) and selective ion chromatograms for αCT11 with different numbers of esters and/or imides.
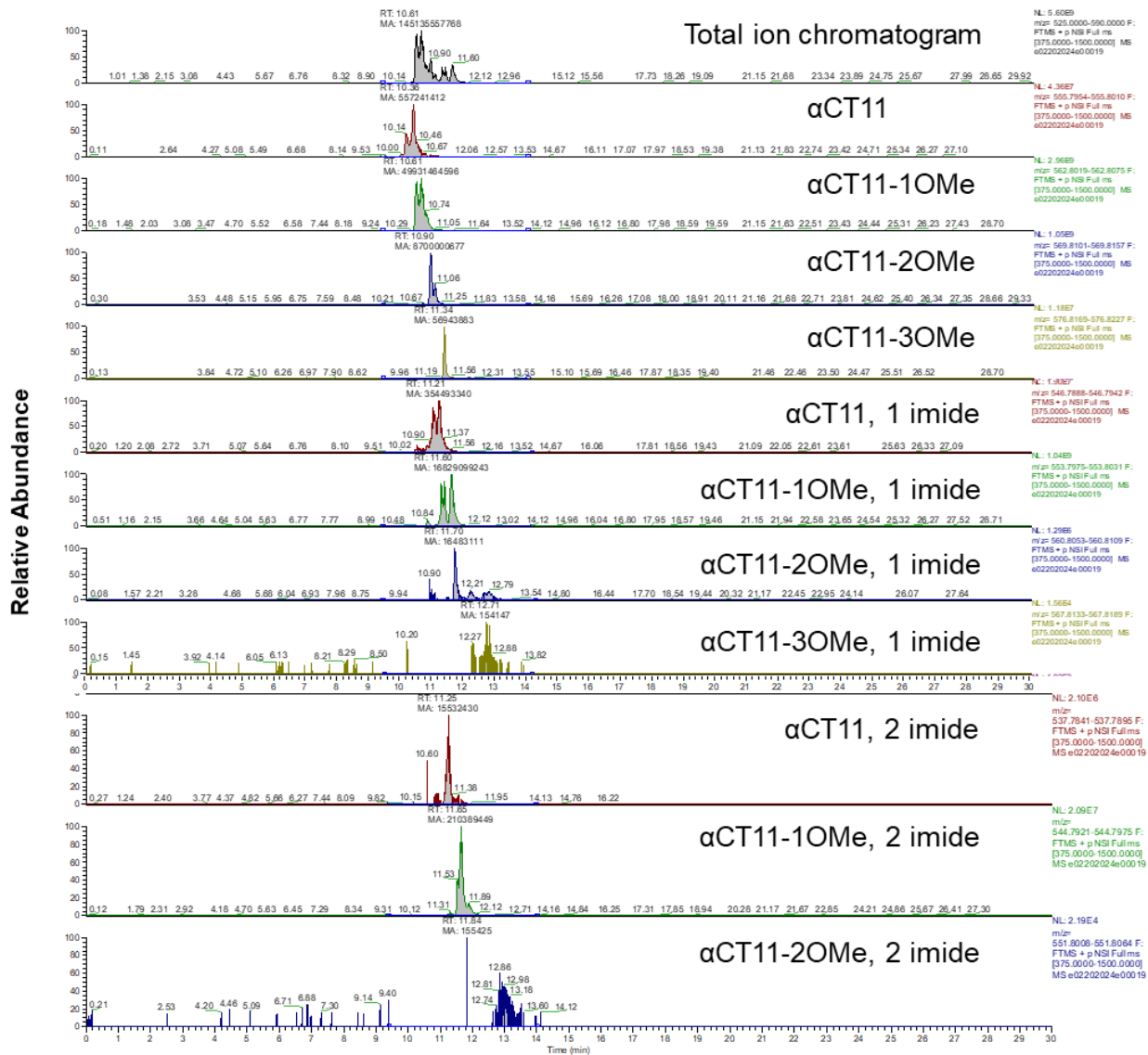
Figure A.47. LC-MS chromatograms of αCT11-3OMe(D5,D6,E8) after 6 h of stirring in 1X PBS (pH 7.4) at 37 °C. Total ion chromatogram (top, gray) and selective ion chromatograms for αCT11 with different numbers of esters and/or imides.
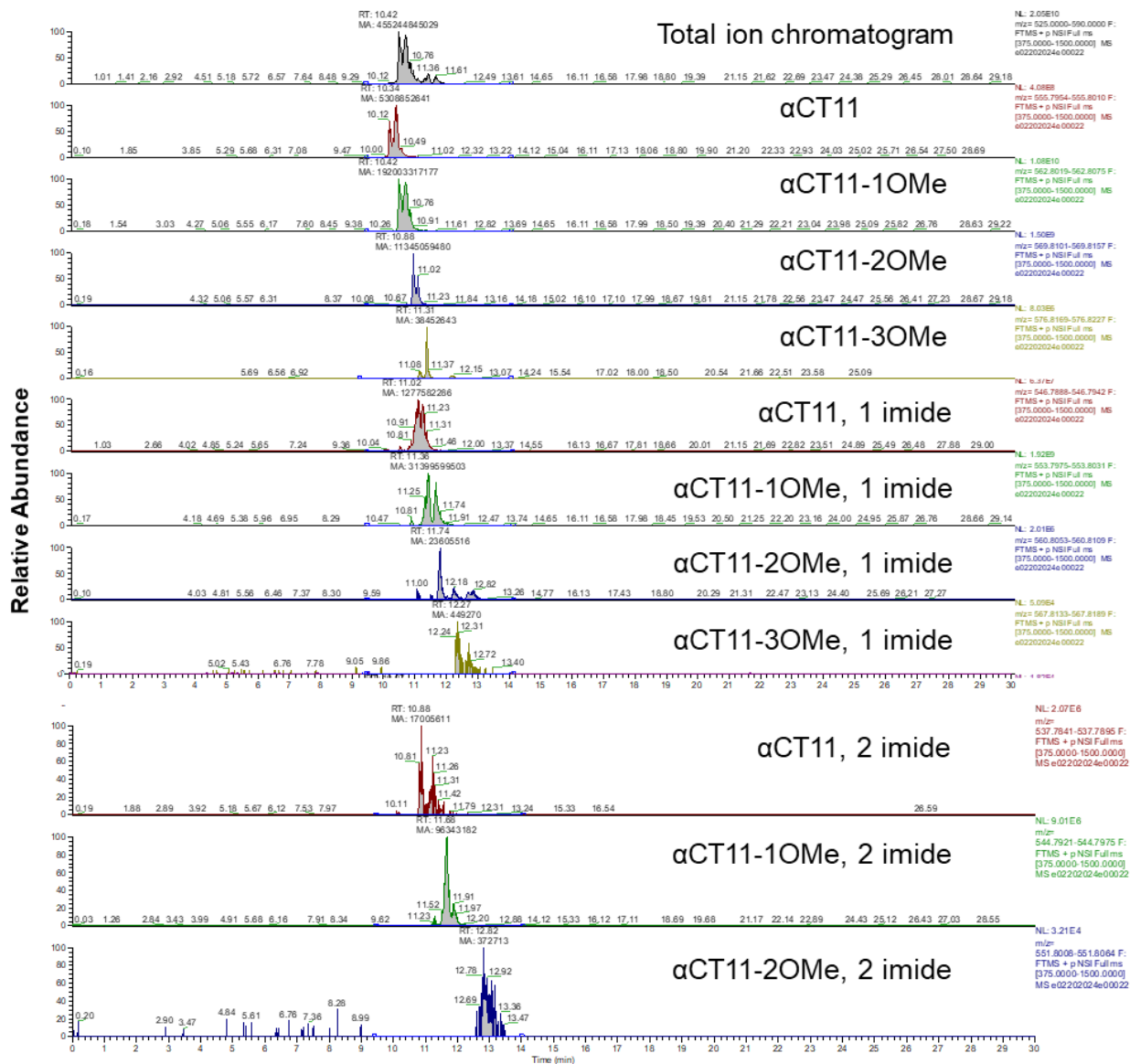
Figure A.48. LC-MS chromatograms of αCT11-3OMe(D5,D6,E8) after 12 h of stirring in 1X PBS (pH 7.4) at 37 °C. Total ion chromatogram (top, gray) and selective ion chromatograms for αCT11 with different numbers of esters and/or imides.
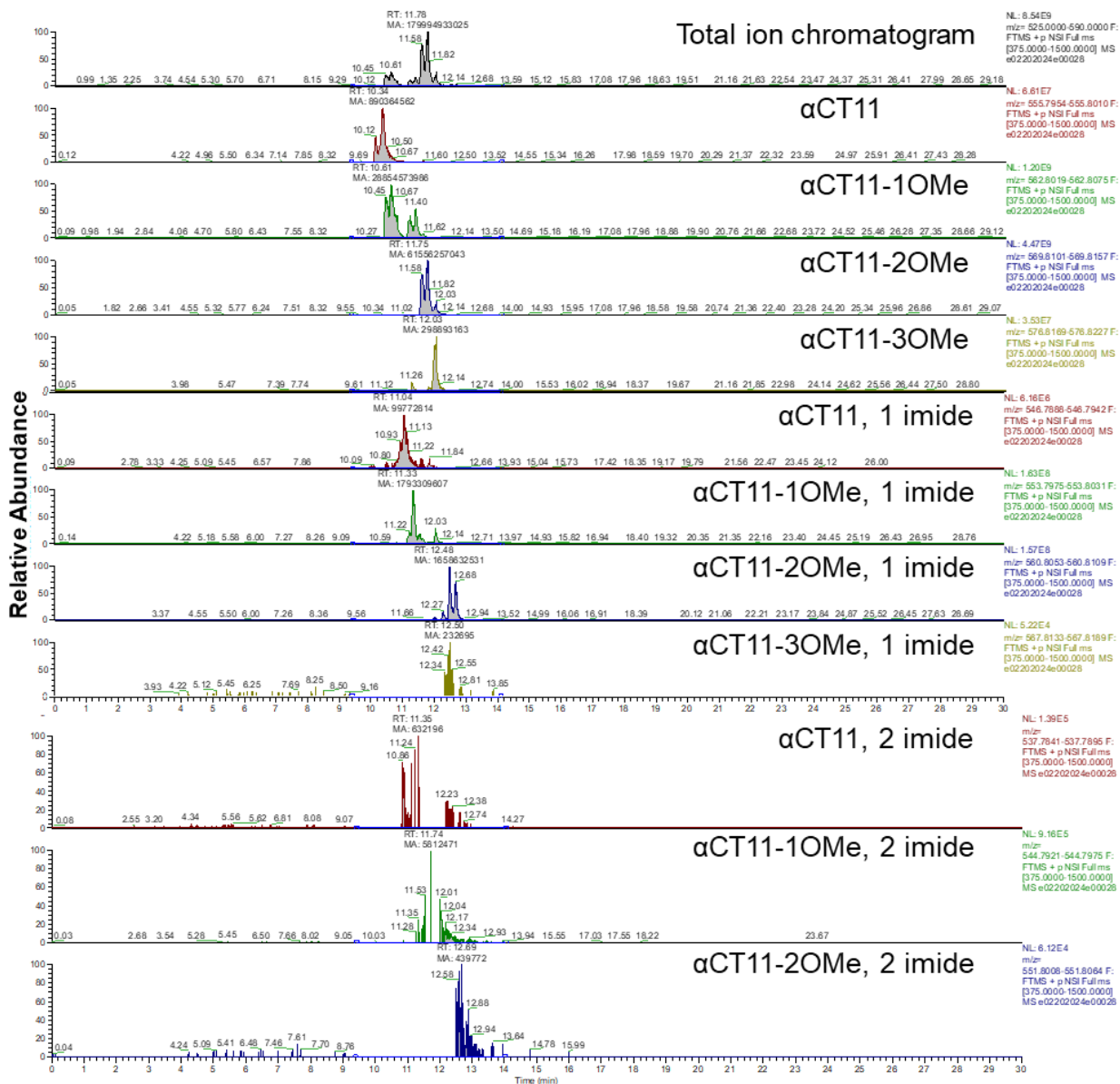
Figure A.49. LC-MS chromatograms of αCT11-3OMe(D5,D6,E8) after 24 h of stirring in 1X PBS (pH 7.4) at 37 °C. Total ion chromatogram (top, gray) and selective ion chromatograms for αCT11 with different numbers of esters and/or imides.
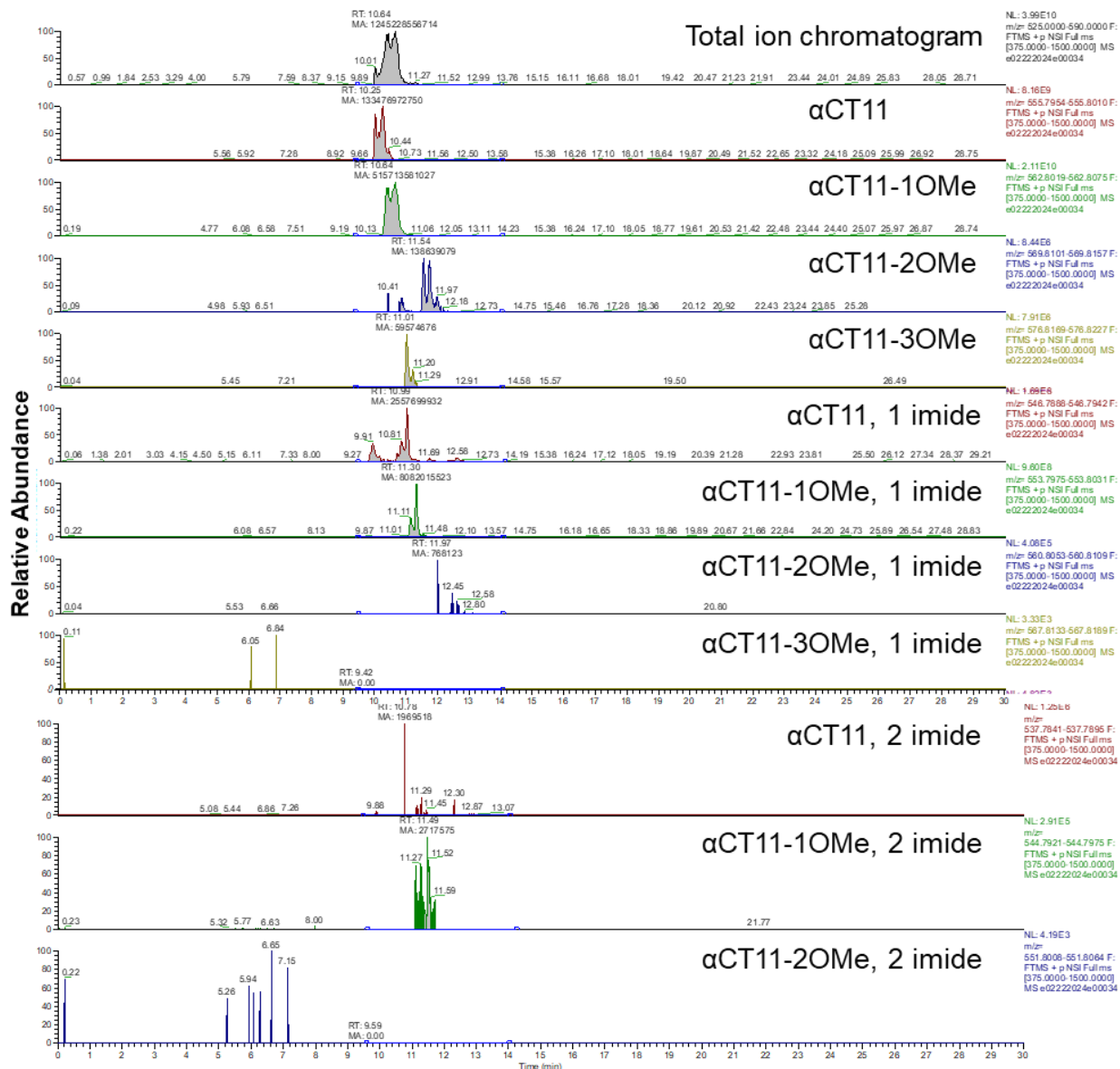
Figure A.50. LC-MS chromatograms of αCT11-3OMe(D5,D6,E8) after 1 week of stirring in 1X PBS (pH 7.4) at 37 °C. Total ion chromatogram (top, gray) and selective ion chromatograms for αCT11 with different numbers of esters and/or imides.
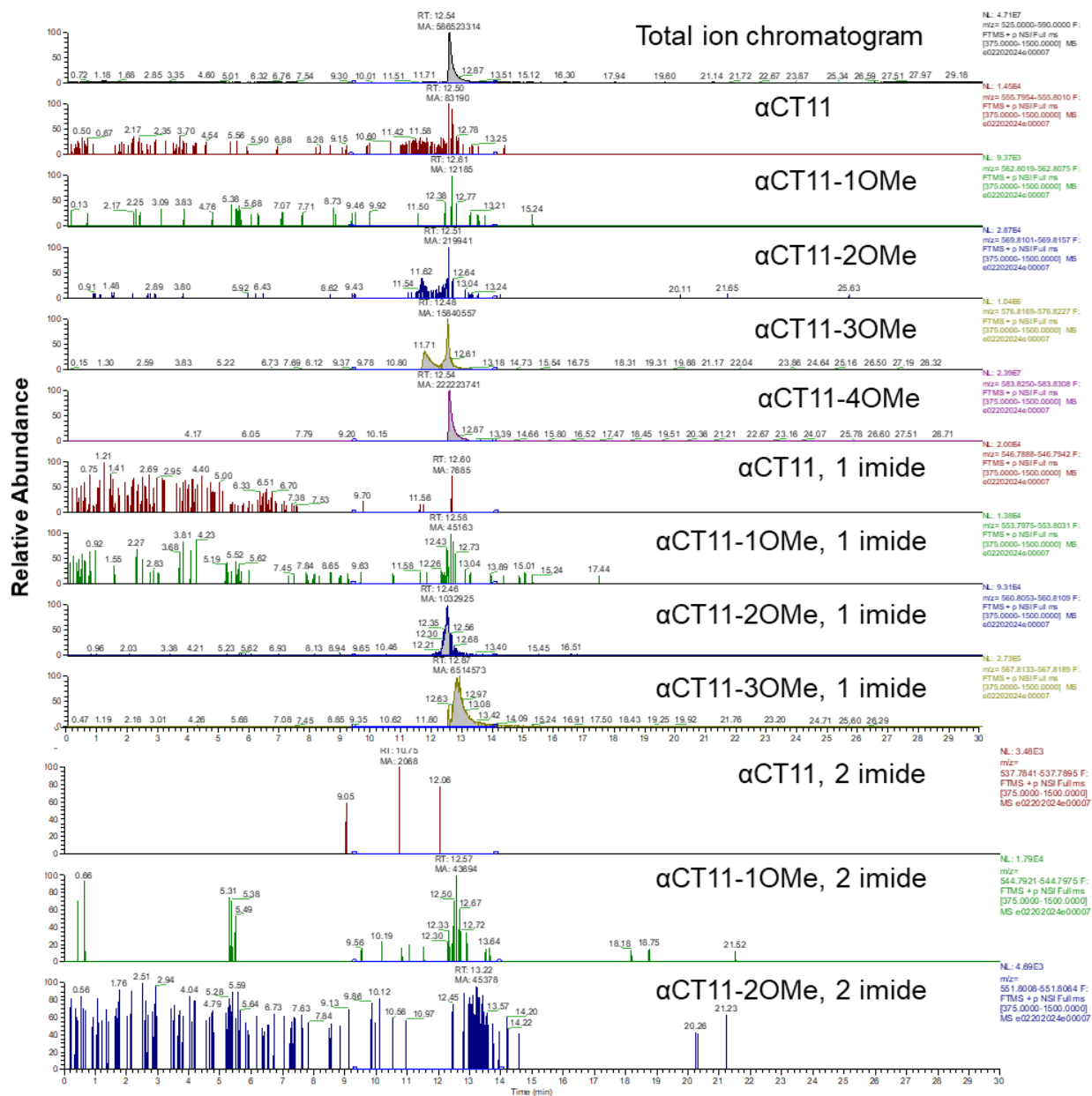
Figure A.51. LC-MS chromatograms of αCT11-4OMe after 5 min of incubation in 1X PBS (pH 7.4). Total ion chromatogram (top, gray) and selective ion chromatograms for αCT11 with different numbers of esters and/or imides.
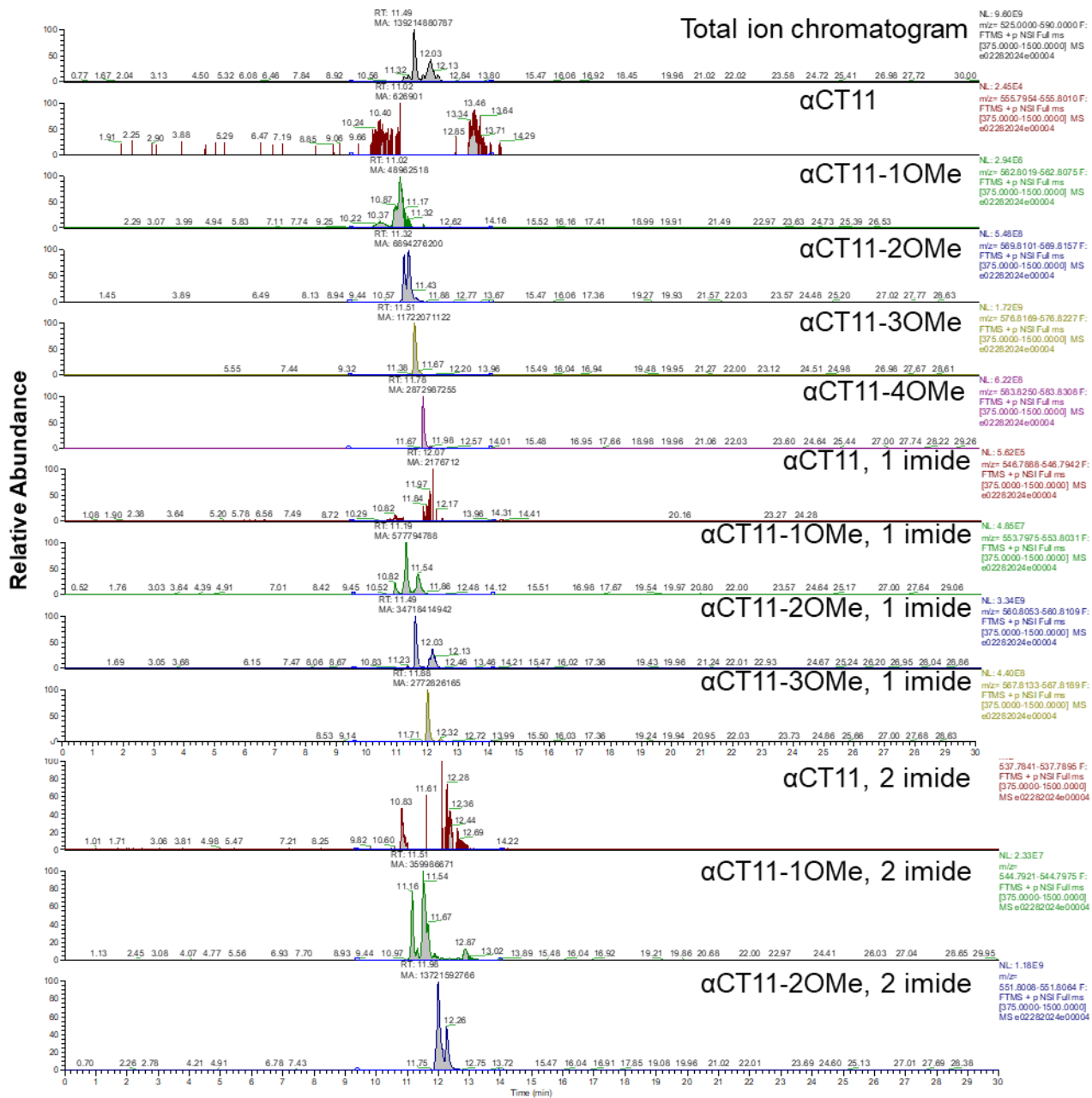
Figure A.52. LC-MS chromatograms of αCT11-4OMe after 2 h of stirring in 1X PBS (pH 7.4) at 37 °C. Total ion chromatogram (top, gray) and selective ion chromatograms for αCT11 with different numbers of esters and/or imides.
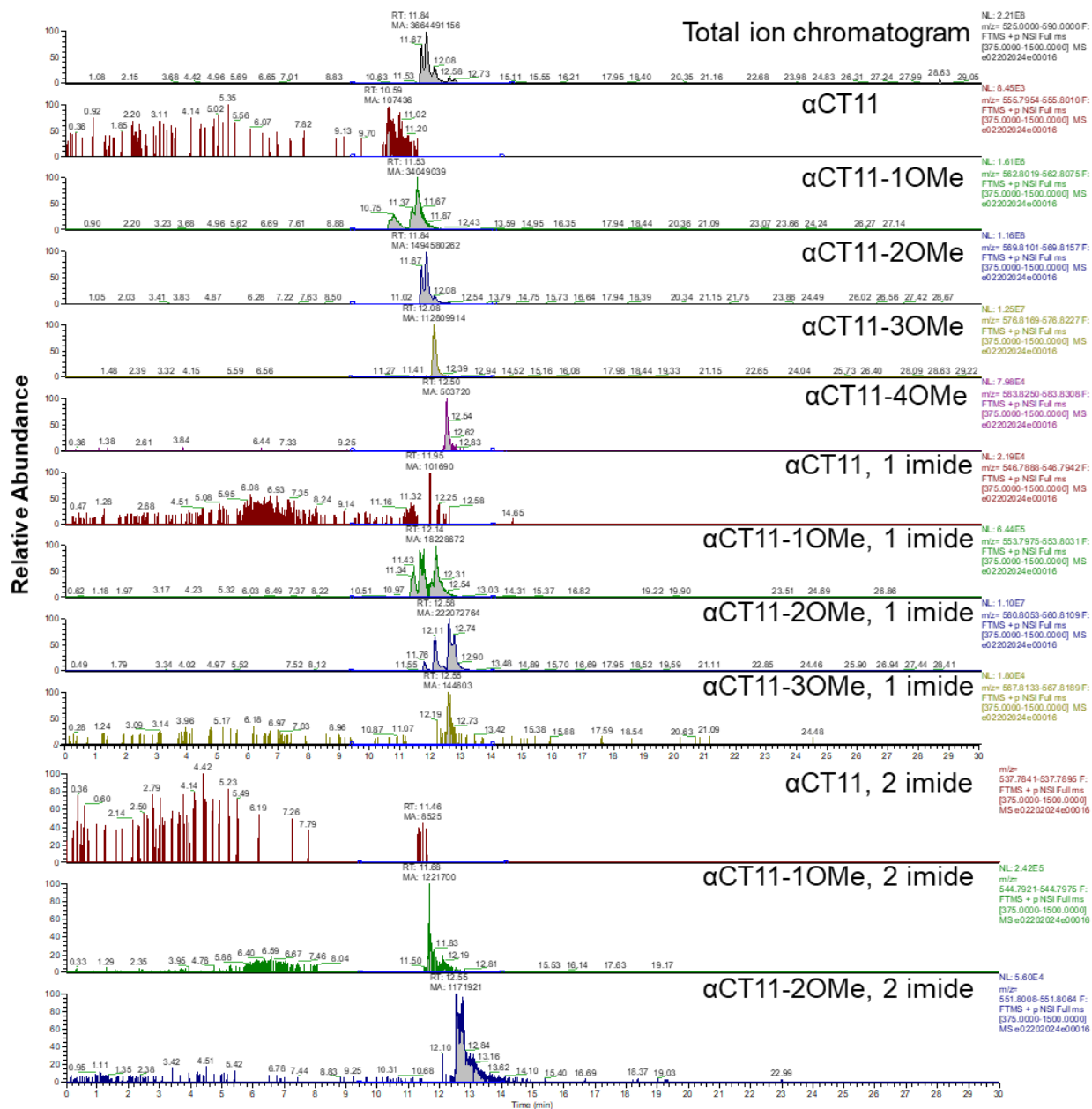
Figure A.53. LC-MS chromatograms of αCT11-4OMe after 6 h of stirring in 1X PBS (pH 7.4) at 37 °C. Total ion chromatogram (top, gray) and selective ion chromatograms for αCT11 with different numbers of esters and/or imides.
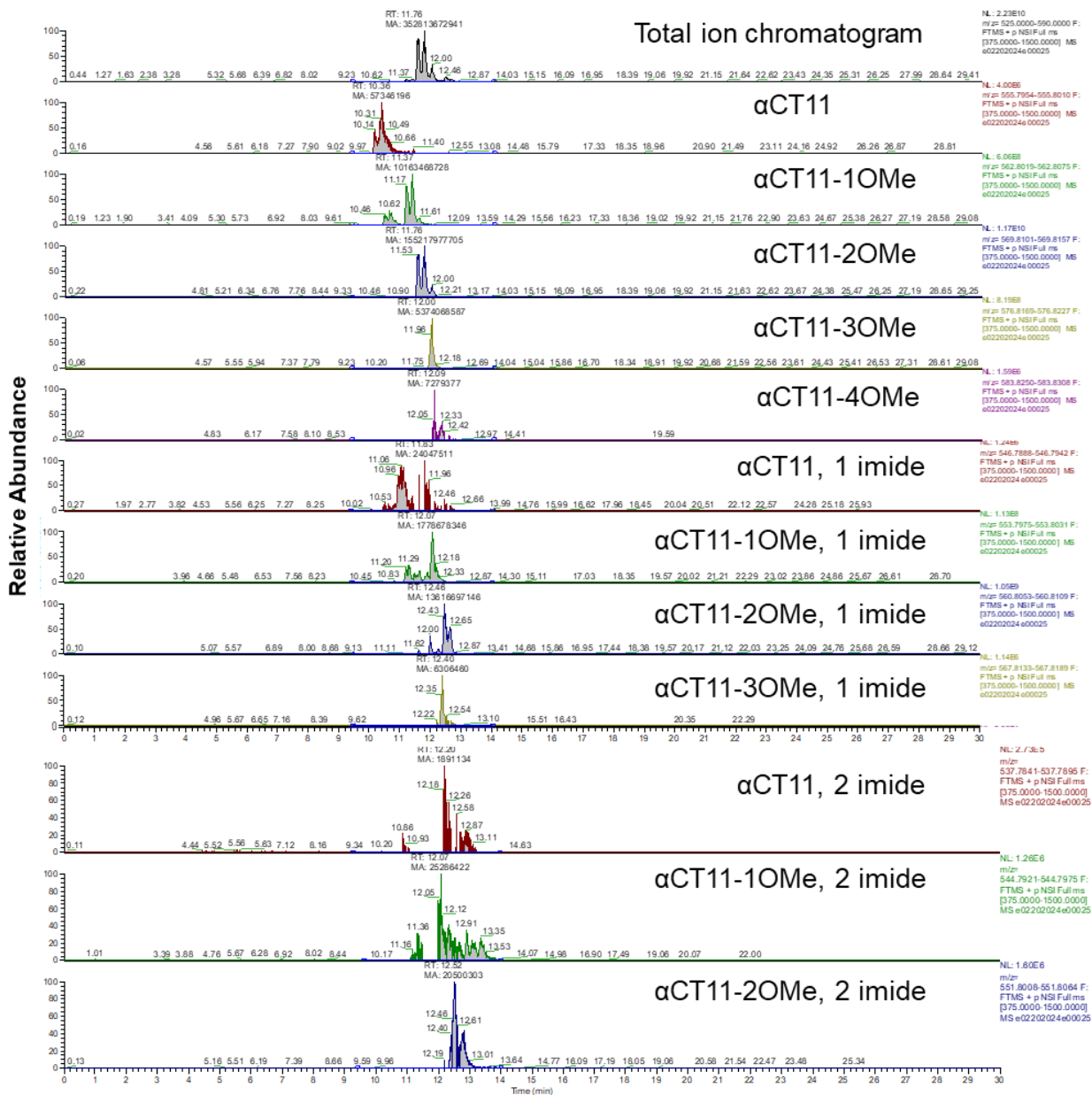
Figure A.54. LC-MS chromatograms of αCT11-4OMe after 12 h of stirring in 1X PBS (pH 7.4) at 37 °C. Total ion chromatogram (top, gray) and selective ion chromatograms for αCT11 with different numbers of esters and/or imides.
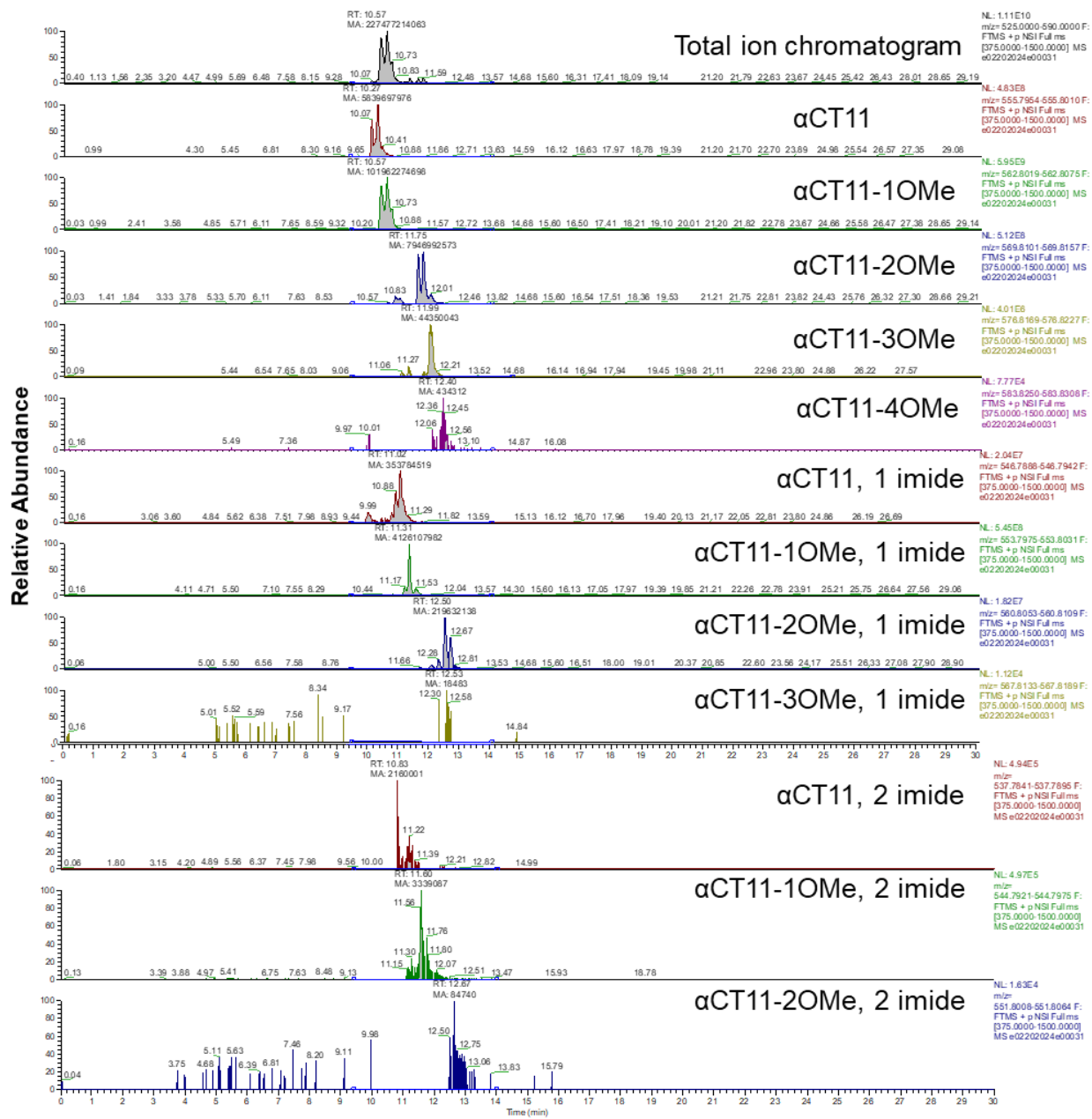
Figure A.55. LC-MS chromatograms of αCT11-4OMe after 24 h of stirring in 1X PBS (pH 7.4) at 37 °C. Total ion chromatogram (top, gray) and selective ion chromatograms for αCT11 with different numbers of esters and/or imides.
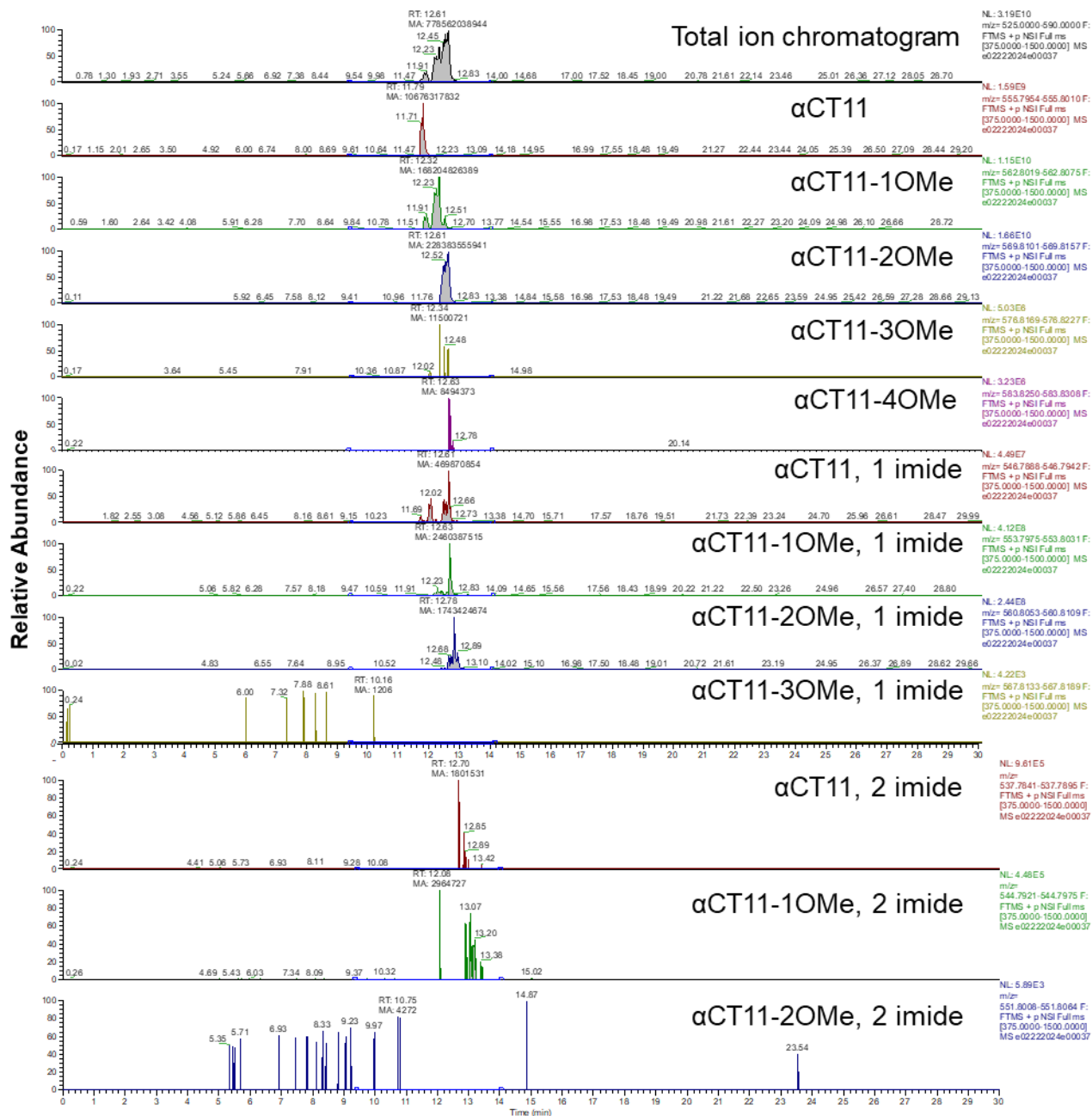
Figure A.56. LC-MS chromatograms of αCT11-4OMe after 1 week of stirring in 1X PBS (pH 7.4) at 37 °C. Total ion chromatogram (top, gray) and selective ion chromatograms for αCT11 with different numbers of esters and/or imides.

A-78
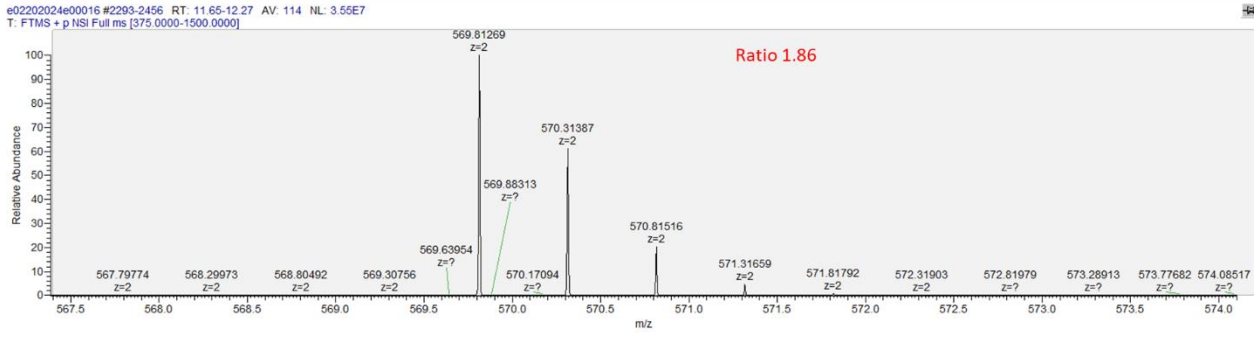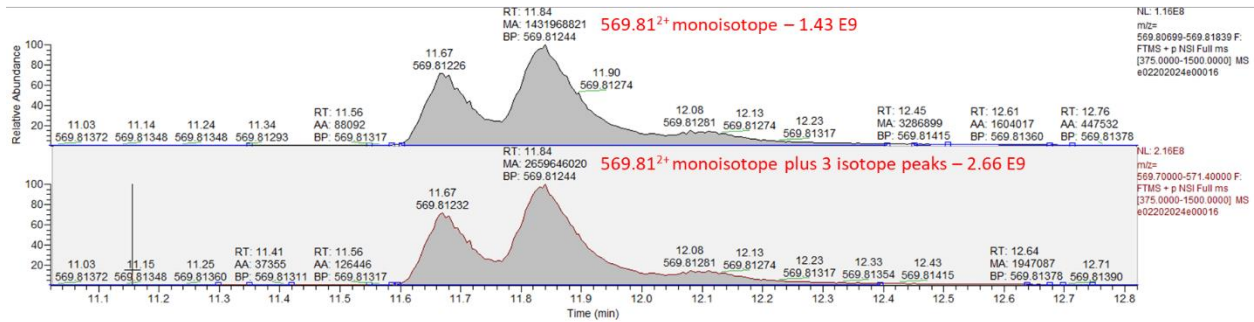
Figure A.57. LC-MS chromatograms of relevant isotopes of αCT11-3OMe(D5,D6,E8) after 5 min of incubation in 1X PBS (pH 7.4). The ratio of the area of the monoisotope (569.81) and 3 additional isotope peaks in the chromatogram to just the area of the monoisotope is 1.86; thus, all monoisotope selective ion chromatogram areas were multiplied by 1.9 to account for the additional isotopes.
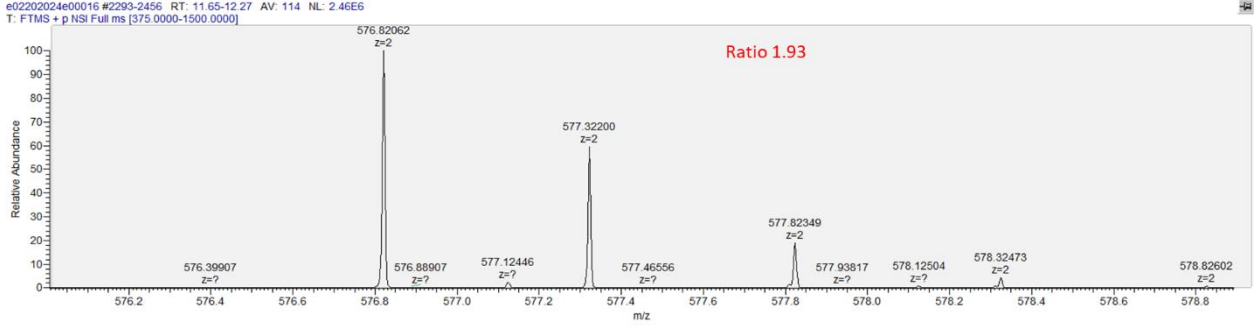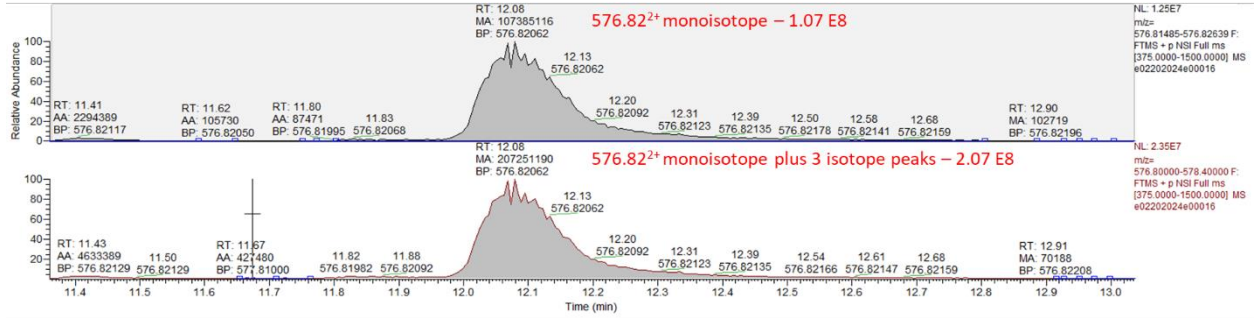
Figure A.58. LC-MS chromatograms of relevant isotopes of αCT11-4OMe after 5 min of incubation in 1X PBS (pH 7.4). The ratio of the area of the monoisotope (576.82) and 3 additional isotope peaks in the chromatogram to just the area of the monoisotope is 1.93; thus, all monoisotope selective ion chromatogram areas were multiplied by 1.9 to account for the additional isotopes.

Table A.12. % Abundance and retention time (RT, min) of αCT11-based formulations produced by the hydrolysis of αCT11-3OMe(D5,D6,E8) in 1X PBS over 7 d, quantified by LC-MS.

| | | Ester # | | | | | | | | | | Total |
| | | 0 | | 1 | | 2 | | 3 | | 4 | | |
		% Abundance	RT (min)	% Abundance	RT (min)	% Abundance	RT (min)	% Abundance	RT (min)	% Abundance	RT (min)	% Abundance
Initial	no imides	0.01	-	0.01	-	1.72	*11.40*	90.20	11.48	N/A	N/A	**91.94**
	1 imide	0.03	-	0.03	-	0.01	-	0.01	-	N/A	N/A	**0.08**
	2 imides	0.00	-	0.03	-	0.00	-	N/A	N/A	N/A	N/A	**0.03**
2 h	no imides	0.02	-	4.61	10.20 10.10	14.37	10.45 10.58	6.17	10.84	N/A	N/A	**25.16**
	1 imides	0.27	-	39.95	10.78 11.11	5.23	11.22 11.49	0.00	-	N/A	N/A	**45.44**
	2 imides	0.25	-	31.04	11.19	0.00	-	N/A	N/A	N/A	N/A	**31.30**
6 h	no imides	0.73	-	65.37	10.61 10.74	11.39	10.09 11.06	0.01	-	N/A	N/A	**77.49**
	1 imide	0.46	-	22.03	11.20 11.40 11.60	0.02	-	0.00	-	N/A	N/A	**22.52**
	2 imides	0.20	-	0.28	-	0.00	-	N/A	N/A	N/A	N/A	**0.48**
12 h	no imides	2.22	10.12 10.34	80.13	10.42 10.60	4.73	10.88 11.02	0.02	-	N/A	N/A	**87.10**
	1 imide	0.53	-	13.10	11.36 11.60	0.01	-	0.00	-	N/A	N/A	**13.65**
	2 imides	0.01	-	0.04	-	0.00	-	N/A	N/A	N/A	N/A	**0.05**
1 d	no imides	4.88	10.12 10.34	85.16	10.45 10.61 11.20	6.64	11.58 11.75 12.03	0.04	-	N/A	N/A	**96.72**
	1 imide	0.30	-	3.45	11.22 11.33 12.03	0.18	-	0.00	-	N/A	N/A	**3.93**
	2 imides	0.00	-	0.00	-	0.00	-	N/A	N/A	N/A	N/A	**0.00**
7 d	no imides	20.37	10 10.25	78.69	10.40 10.64	0.21	-	0.01	-	N/A	N/A	**99.28**
	1 imide	0.39	-	1.23	11.11 11.30	0.00	-	0.00	-	N/A	N/A	**1.62**
	2 imides	0.00		0.00		0.00		N/A	N/A	N/A	N/A	**0.00**

*Only retention times for products over 1% abundance were reported

Table A.13. % Abundance and retention times (RT, min) of αCT11-based formulations produced by the hydrolysis of αCT11-3OMe4OMe in 1X PBS over 7 d, quantified by LC-MS

		Ester # 0		Ester # 1		Ester # 2		Ester # 3		Ester # 4		Total
		% Abundance	RT (min)	% Abundance	RT (min)	% Abundance	RT (min)	% Abundance	RT (min)	% Abundance	RT (min)	% Abundance
Initial	no imides	0.03	-	0.00	-	0.07	-	5.13	12.48	71.99	12.54	**77.22**
	1 imide	0.00	-	0.01	-	0.33	-	2.11	12.87	N/A	N/A	**2.46**
	2 imides	0.00	-	0.01	-	0.01	-	N/A	N/A	N/A	N/A	**0.03**
2 h	no imides	0.00	-	0.07	-	9.41	11.20 11.32	16.00	11.51	3.92	11.78	**29.40**
	1 imides	0.00	-	0.79	-	47.38	11.49 12.03	3.78	11.88	N/A	N/A	**51.96**
	2 imides	0.00	-	0.49	11.19	18.73	11.98 12.26	N/A	N/A	N/A	N/A	**19.22**
6 h	no imides	0.01	-	1.77	10.75 11.37 11.53	77.49	11.87 11.84 12.08	5.85	12.08	0.03	-	**85.14**
	1 imide	0.01	-	0.95	-	11.51	12.11 12.58 12.74	0.01	-	N/A	N/A	**12.47**
	2 imides	0.00	-	0.06	-	0.06	-	N/A	N/A	N/A	N/A	**0.12**
12 h	no imides	0.03	-	5.47	11.17 11.37	83.59	11.53 11.76	2.89	12.00	0.00	-	**91.99**
	1 imide	0.01	-	0.96	-	7.33	12.46 12.65	0.00	-	N/A	N/A	**8.31**
	2 imides	0.00	-	0.01	-	0.01	-	N/A	N/A	N/A	N/A	**0.03**
1 d	no imides	0.94	-	30.46	10.40 10.57 10.73	64.98	11.60 11.75 12.01	0.32	-	0.01	-	**96.70**
	1 imide	0.11	-	1.89	11.17 11.31 11.53	1.75	12.50 12.67 12.81	0.00	-	N/A	N/A	**3.75**
	2 imides	0.00	-	0.01	-	0.00	-	N/A	N/A	N/A	N/A	**0.00**
7 d	no imides	2.61	11.79	41.05	11.91 12.23 12.32 12.51	55.73	12.52 12.61	0.00	-	0.00	-	**99.39**
	1 imide	0.11	-	0.60	-	0.43	-	0.00	-	N/A	N/A	**1.14**
	2 imides	0.00	-	0.00	-	0.00	-	N/A	N/A	N/A	N/A	

*Only retention times for products over 1% abundance were reported

A.4 Activity of Esterified αCT11
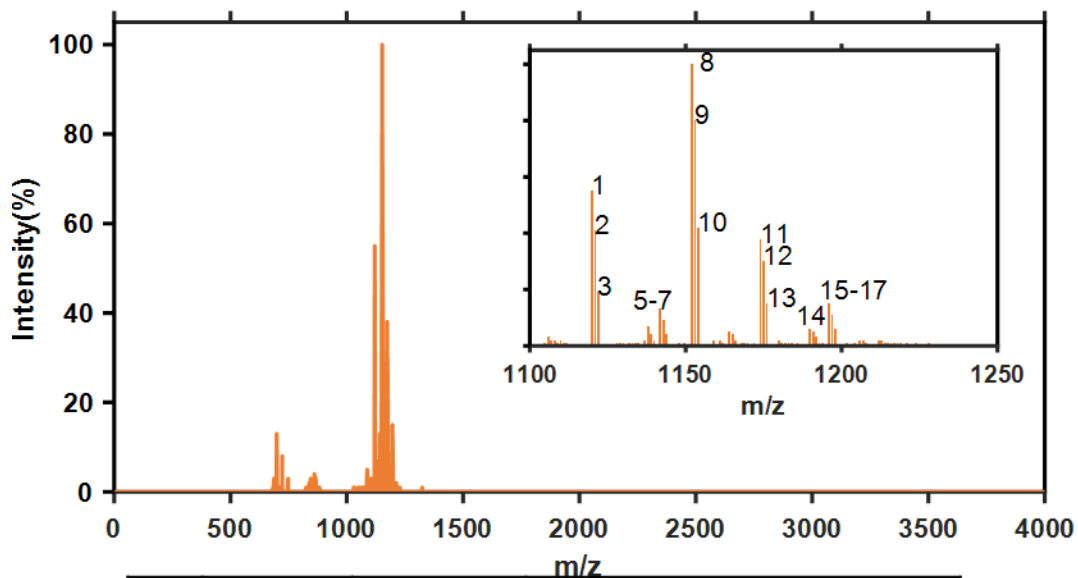
label	Mass (Da)	Intensity (%)	Species
1	1119.9	55	[αCT11-2OMe + 1 imide + H]+
2	1121	41	[αCT11-2OMe + 1 imide + H]+
3	1122	19	[αCT11-2OMe + 1 imide + H]+
4	1138	7	[αCT11-2OMe + H]+
5	1141.9	13	[αCT11-2OMe + 1 imide + Na]+
6	1142.8	9	[αCT11-2OMe + 1 imide + Na]+
7	1151.9	100	[αCT11-3OMe + H]+
8	1153	80	[αCT11-3OMe + H]+
9	1154	42	[αCT11-3OMe + H]+
10	1174	38	[αCT11-3OMe + Na]+
11	1174.9	30	[αCT11-3OMe + Na]+
12	1176	15	[αCT11-3OMe + Na]+
13	1189.9	6	[αCT11-3OMe + K]+
14	1196	15	[αCT11-3OMe + 2Na - H]+
15	1197	11	[αCT11-3OMe + 2Na - H]+
16	1198	6	[αCT11-3OMe + 2Na - H]+

Figure A.59. MALDI-TOF MS of αCT11-3OMe(D5/D6/E8) after the trifluoroacetate counterion exchange. Multiple esterified αCT11 species, but no activated αCT11, were detected, suggesting a small amount of hydrolysis over the counterion exchange.
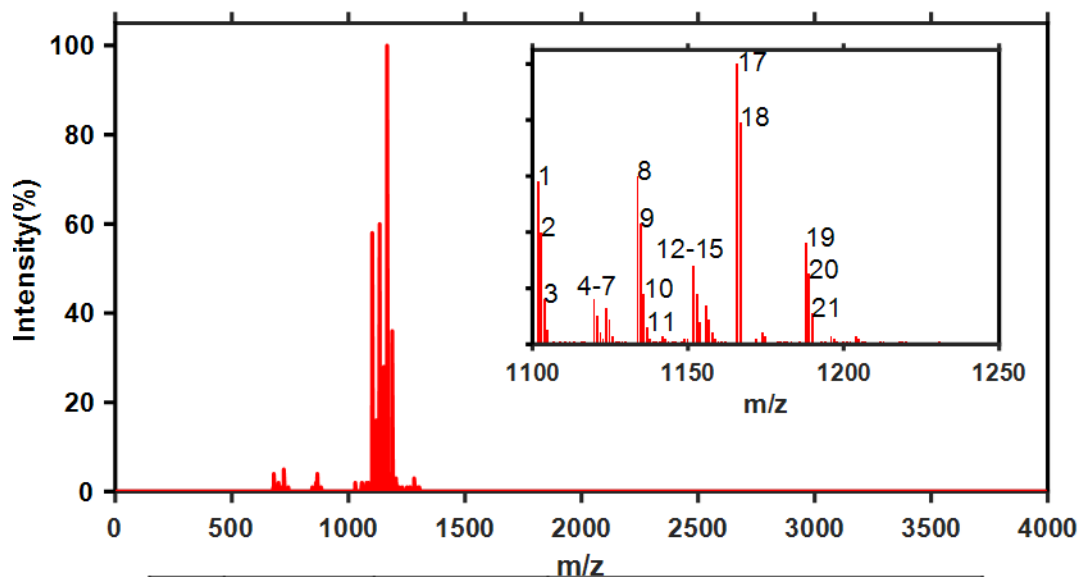
label	Mass (Da)	Intensity (%)	Species
1	1101.8	58	[αCT11-2OMe + 2 imide + H]+
2	1102.8	40	[αCT11-2OMe + 2 imide + H]+
3	1103.9	16	[αCT11-2OMe + 2 imide + H]+
4	1119.8	16	[αCT11-2OMe + 1 imide + H]+
5	1120.8	10	[αCT11-2OMe + 1 imide + H]+
6	1123.8	13	[αCT11-1OMe + H]+
7	1124.8	9	[αCT11-1OMe + H]+
8	1133.8	60	[αCT11-3OMe + 1 imide + H]+
9	1134.8	43	[αCT11-3OMe + 1 imide + H]+
10	1135.8	18	[αCT11-3OMe + 1 imide + H]+
11	1136.9	6	[αCT11-3OMe + 1 imide + H]+
12	1151.8	28	[αCT11-3OMe + H]+
13	1152.9	18	[αCT11-3OMe + H]+
14	1153.8	8	[αCT11-3OMe + H]+
15	1155.9	14	[αCT11-3OMe + 1 imide + Na]+
16	1156.8	9	[αCT11-3OMe + 1 imide + Na]+
17	1165.8	100	[αCT11-4OMe + H]+
18	1166.9	79	[αCT11-4OMe + H]+
19	1187.9	36	[αCT11-4OMe + Na]+
20	1188.9	25	[αCT11-4OMe + Na]+
21	1189.9	11	[αCT11-4OMe + Na]+

Figure A.60. MALDI-TOF MS of αCT11-4OMe after the trifluoroacetate counterion exchange. Multiple esterified αCT11 species, but no activated αCT11, were detected, suggesting a small amount of hydrolysis over the counterion exchange.

Table A.14. Scratch wound assay results: relative migration indices (Rel. Mis) and standard deviation for each individual scratched cell culture and their averages.

Cell Culture:	Vehicle		αCT11		3OMe(D5,D6,E8)		4OMe	
	Rel. MI	StDev	Rel. MI	StDev	Rel. MI	StDev	Rel. MI	StDev
1	1.0	0.3	1.7	1.2	6.0	1.7	8.1	0.9
2	1.0	0.3	1.4	0.5	5.3	1.4	6.6	0.7
3	1.0	0.8	1.0	0.4	3.1	0.5	4.0	0.5
Average	**1.0**	**0.0**	**1.4**	**0.4**	**4.8**	**1.5**	**6.2**	**2.1**

Table A.15. Statistical analysis of scratch wound assays: one-tailed paired t-tests assuming unequal variances (confidence interval = 0.95).

Treatment	Vehicle	αCT11	3OMe(D5,D6,E8)	4OMe
Vehicle		0.11	0.02	0.02
αCT11			0.03	0.03
3OMe(D5,D6,E8)				0.19
4OMe				
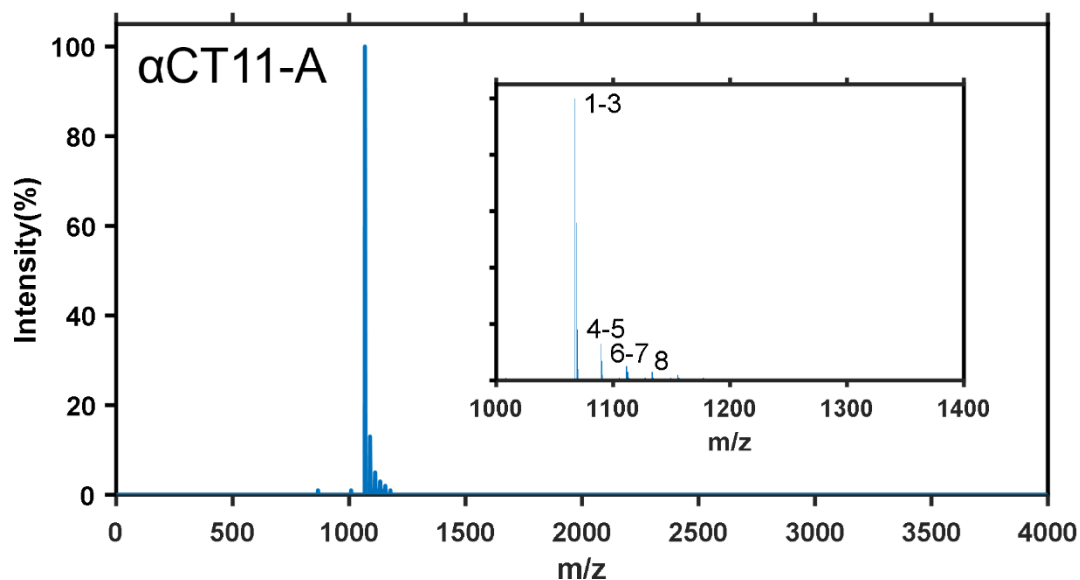
Figure A.61. MALDI-TOF MS of RPRPDDLEA (αCT11-A). Sample was cocrystallized with CHCA matrix and measured using a Shimadzu MALDI-8020 spectrometer after purification of the sample by preparative scale RP-HPLC. Numerical labels are defined in Table A.16.

Table A.16. MALDI-TOF MS results of αCT11-A. Labels correspond to Figure A.61.

label	Mass (Da)	Intensity (%)	Species
1	1067.453	100	
2	1068.516	56	[αCT11-A + H]+
3	1069.503	18	
4	1089.497	13	[αCT11-A + Na]+
5	1090.494	7	
6	1111.457	5	[αCT11-A + 2Na - H]+
7	1112.463	3	
8	1133.4	3	[αCT11-A + 3Na - 2H]+
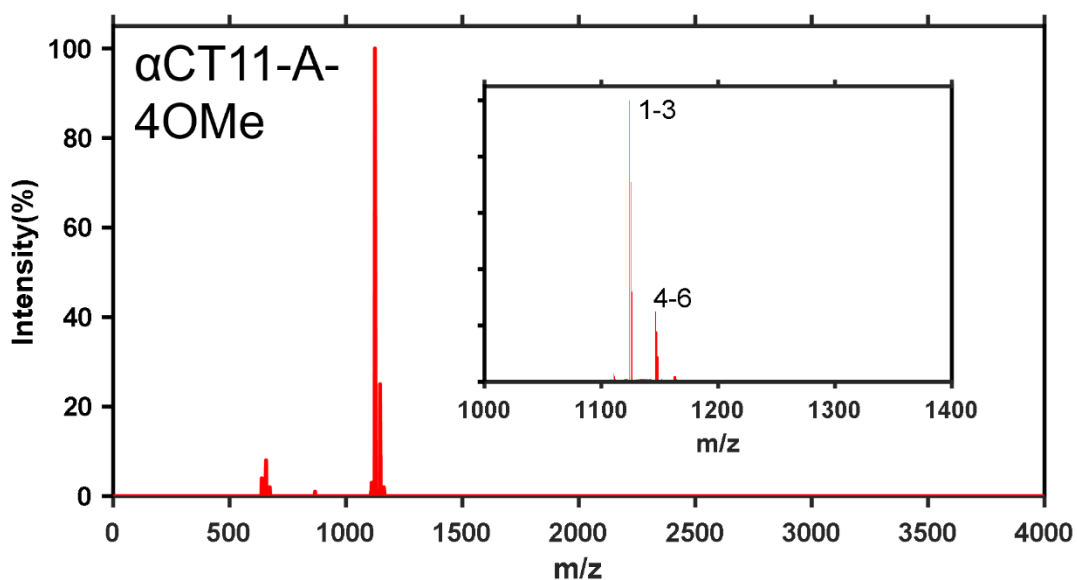
Figure A.62. MALDI-TOF MS of RPRPDDLEA with 4 methyl esters installed (αCT11-A-4OMe). Sample was cocrystallized with CHCA matrix and measured using a Shimadzu MALDI-8020 spectrometer after purification of the sample by preparative scale RP-HPLC. Numerical labels are defined in Table A.17.

Table A.17. MALDI-TOF MS results of αCT11-A-4OMe. Labels correspond to Figure A.62.

label	Mass (Da)	Intensity (%)	Species
1	1124.331	100	
2	1125.421	71	[αCT11-A-4OMe + H]+
3	1126.434	32	
4	1146.392	25	
5	1147.414	18	[αCT11-A-4OMe + Na]+
6	1148.358	9	
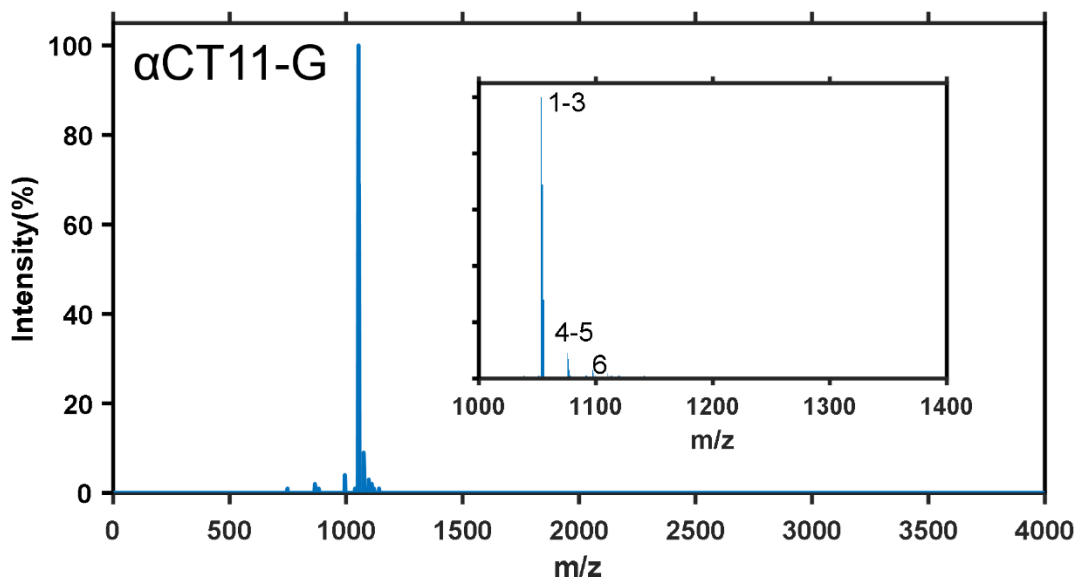
Figure A.63. MALDI-TOF MS of RPRPDDLEG (αCT11-G). Sample was cocrystallized with CHCA matrix and measured using a Shimadzu MALDI-8020 spectrometer after purification of the sample by preparative scale RP-HPLC. Numerical labels are defined in table A.18.

Table A.18. MALDI-TOF MS results of αCT11-G. Labels correspond to Figure A.63.

label	Mass (Da)	Intensity (%)	Species
1	1053.31	100	[αCT11-G + H]+
2	1054.365	69	
3	1055.422	28	
4	1075.36	9	[αCT11-G + Na]+
5	1076.351	7	
6	1097.331	3	[αCT11-G + 2Na - H]+
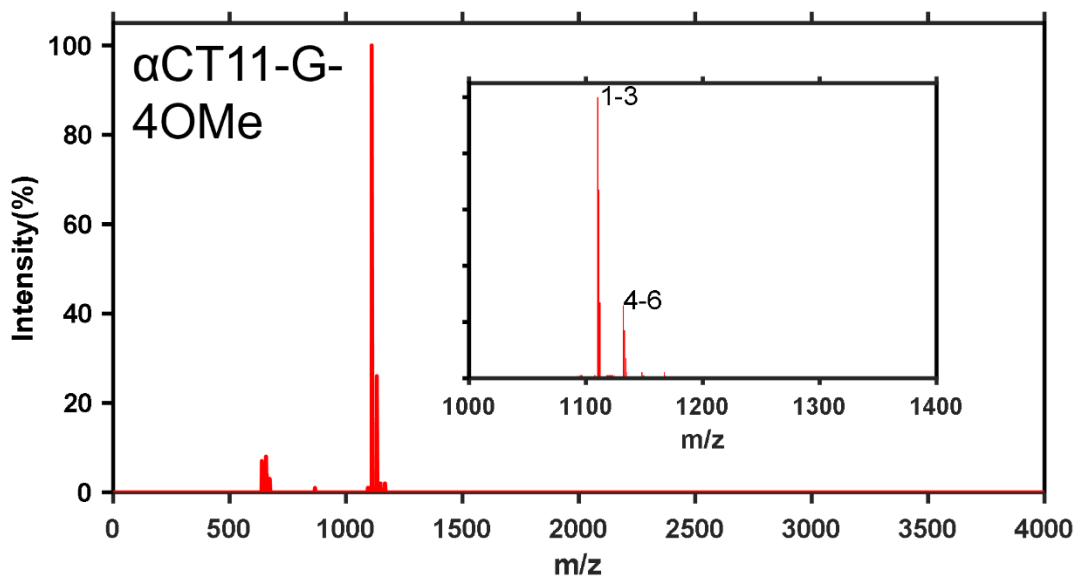
Figure A.64. MALDI-TOF MS of RPRPDDLEG with 4 methyl esters installed (αCT11-G-4OMe). Sample was cocrystallized with CHCA matrix and measured using a Shimadzu MALDI-8020 spectrometer after purification of the sample by preparative scale RP-HPLC. Numerical labels are defined to Table A.19.

Table A.19. MALDI-TOF MS results of αCT11-A-4OMe. Labels correspond to Figure A.64.

label	Mass (Da)	Intensity (%)	Species
1	1110.052	100	
2	1111.135	67	[αCT11-G-4OMe + H]+
3	1112.141	27	
4	1132.129	26	
5	1133.145	17	[αCT11-G-4OMe + Na]+
6	1134.161	7	
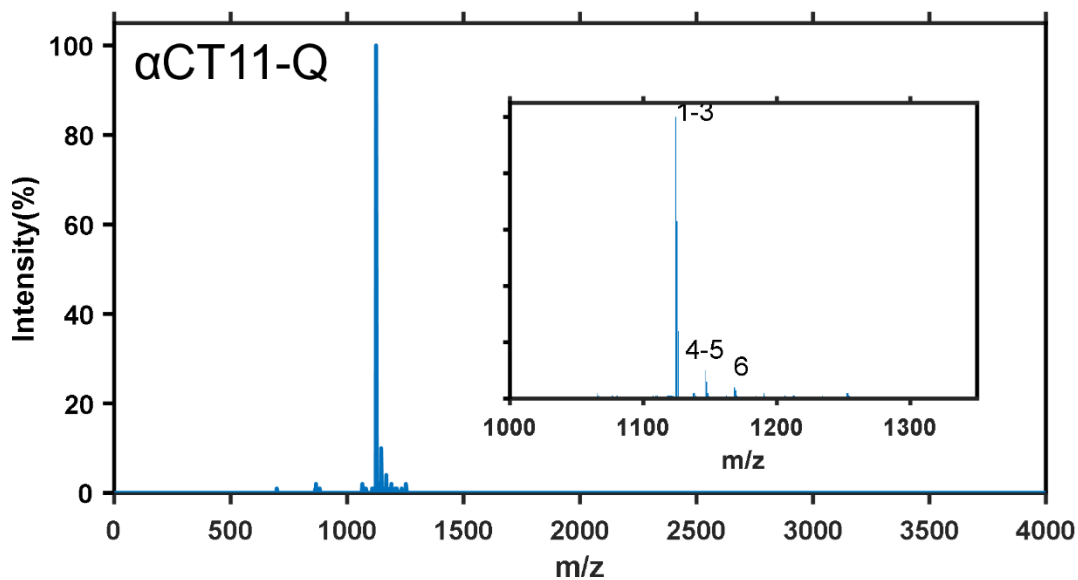
Figure A.65. MALDI-TOF MS of RPRPDDLEQ (αCT11-Q). Sample was cocrystallized with CHCA matrix and measured using a Shimadzu MALDI-8020 spectrometer after purification of the sample by preparative scale RP-HPLC. Numerical labels are defined in Table A.20.

Table A.20. MALDI-TOF MS results of αCT11-Q. Labels correspond to Figure A.65.

label	Mass (Da)	Intensity (%)	Species
1	1124.27	100	
2	1125.283	63	[αCT11-Q + H]+
3	1126.296	24	
4	1146.339	10	
5	1147.283	6	[αCT11-Q + Na]+
6	1168.306	4	
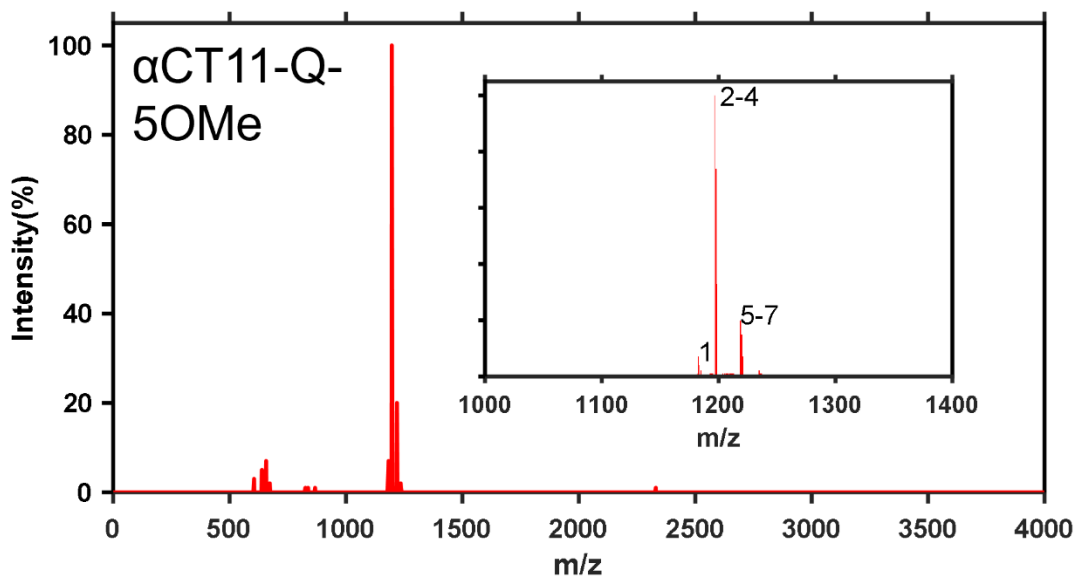
Figure A.66. MALDI-TOF MS of RPRPDDLEQ with 5 methyl esters installed (αCT11-Q-5OMe). Sample was cocrystallized with CHCA matrix and measured using a Shimadzu MALDI-8020 spectrometer after purification of the sample by preparative scale RP-HPLC. Numerical labels are defined in Table A.21.

Table A.21. MALDI-TOF MS results of αCT11-Q-5OMe. Labels correspond to Figure A.66.

label	Mass (Da)	Intensity (%)	Species
1	1182.598	7	[αCT11-Q-4OMe/1COOH + H]+
2	1196.531	100	[αCT11-5OMe + H]+
3	1197.656	74	
4	1198.62	33	
5	1218.638	20	[αCT11-5OMe + Na]+
6	1219.611	15	
7	1220.584	7	
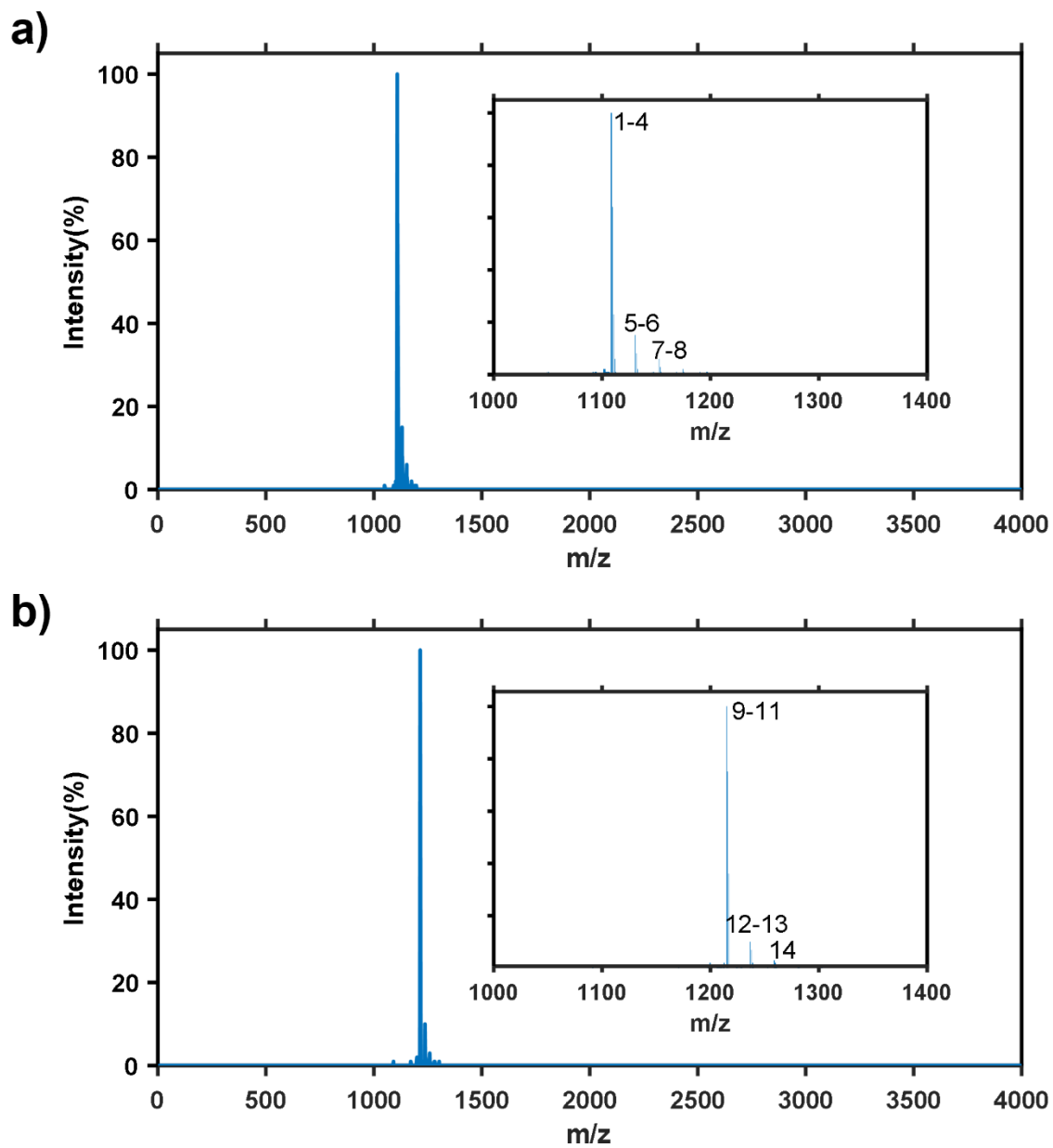
Figure A.67. MALDI-TOF MS of crude αCT11 with a C-terminal I9 amide (αCT11-1NH$_2$(I9)), as shown in **Figure 2.7**. 2 major peaks were collected through purification, with **a)** showing MALDI-TOF MS of the peak eluting at 11.2 min and **b)** showing the peak at 14.0 min. Samples were cocrystallized with CHCA matrix and measured using a Shimadzu MALDI-8020 spectrometer after purification of the sample by preparative scale RP-HPLC. Numerical labels are defined in Table A.22.

Table A.22. MALDI-TOF MS of crude αCT11-1NH$_2$(I9). Labels correspond to Figure A.67.

label	Mass (Da)	Intensity (%)	Species
1	1108.671	100	
2	1109.754	64	[αCT11-1NH2 + H]+
3	1110.76	23	
4	1111.766	6	
5	1130.665	15	[αCT11-1NH2 + Na]+
6	1131.681	8	
7	1152.639	6	[αCT11-1NH2 + 2Na - H]+
8	1153.664	3	
9	1214.806	100	
10	1215.939	75	[αCT11-1NH2 + 105 + H]+
11	1216.992	36	
12	1236.925	10	[αCT11-1NH2 + 105 + Na]+
13	1237.905	7	
14	1258.914	3	[αCT11-1NH2 + 105 + 44]+
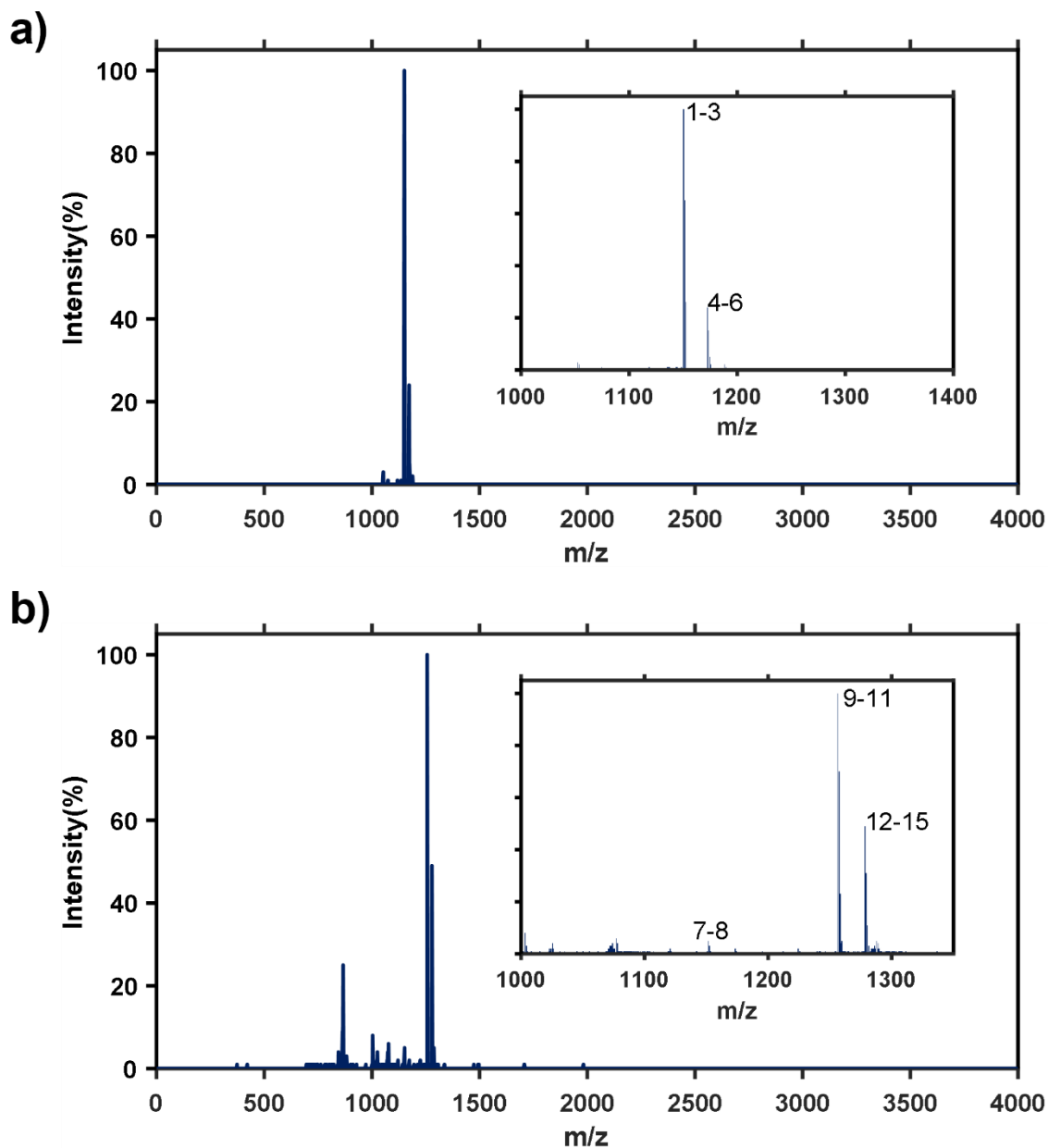
Figure A.68. MALDI-TOF MS of crude esterified αCT11-1NH$_2$(I9) (αCT11-1NH$_2$(I9)-OMe), as shown in Figure 5.2. Crude αCT11-1NH$_2$(I9) (Figure 2.7, A.67, Table A.22) was esterified at a 5000:1 MeOH:αCT11 ratio, with a solvent of 95:5 MeOH:HCl (v/v), for 24 h at 40 °C. 2 major peaks were collected through purification, with **a)** showing MALDI-TOF MS of the peak eluting at 14.0 min and **b)** showing the peak at 16.6 min. Samples were cocrystallized with CHCA matrix and measured using a Shimadzu MALDI-8020 spectrometer after purification of the sample by preparative scale RP-HPLC. Numerical labels are defined in Table A.23.

Table A.23. MALDI-TOF MS of crude αCT11-1NH2(I9)-OMe. Labels correspond to Figure A.68.

label	Mass (Da)	Intensity (%)	Species
1	1150.511	100	[αCT11-1NH2/3OMe + H]+
2	1151.614	65	
3	1152.56	26	
4	1172.517	24	[αCT11-1NH2/3OMe + Na]+
5	1173.631	15	
6	1174.506	5	
7	1151.457	5	[αCT11-1NH2/3OMe + H]+
8	1152.481	3	
9	1256.443	100	[αCT11-1NH2/3OMe + 105 + H]+
10	1257.514	70	
11	1258.502	23	
12	1278.439	49	[αCT11-1NH2/3OMe + 105 + Na]+
13	1279.435	31	
14	1280.433	11	
15	1281.43	3	
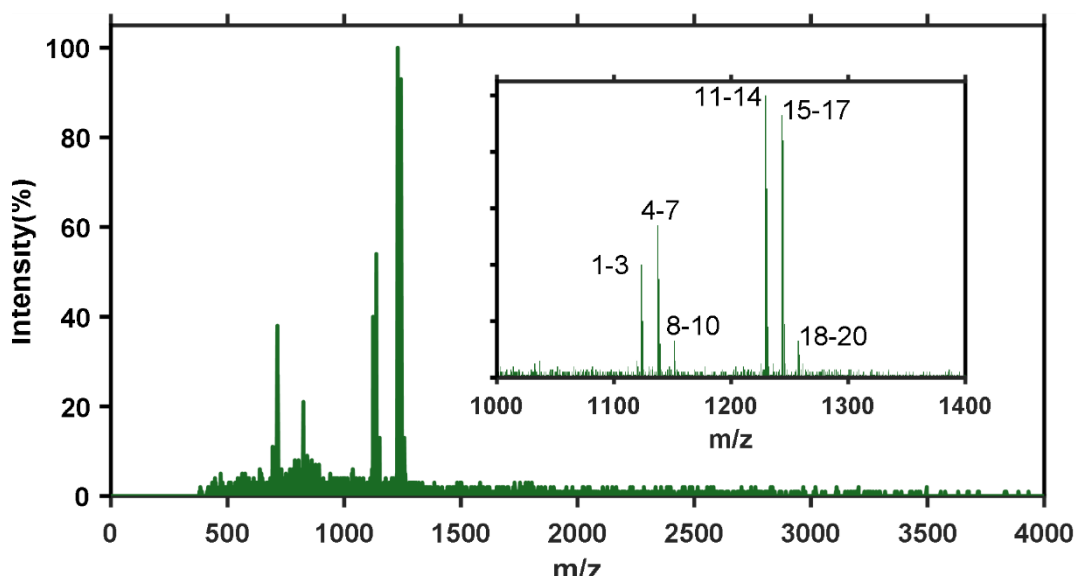
Figure A.69. MALDI-TOF MS of crude esterified αCT11-1NH2(I9) (αCT11-1NH2(I9)-OMe), as shown in Figure 5.2. Crude αCT11-1NH2(I9) (Figure 2.7, A.67, Table D.22) was esterified at a 10000:1 MeOH:αCT11 ratio, with a solvent of 47.5:47.5:5 MeOH:DMF:HCl (v/v), for 68 h at 40 °C. Sample was cocrystallized with CHCA matrix and measured using a Shimadzu MALDI-8020 spectrometer. Numerical labels are defined in Table A.24.

Table A.24. MALDI-TOF MS of crude αCT11-1NH$_2$(I9)-OMe, esterified at a 10000:1 MeOH:αCT11 ratio, with a solvent of 47.5:47.5:5 MeOH/DMF/HCl (v/v), for 68 h at 40 °C. Labels correspond to Figure A.69.

label	Mass (Da)	Intensity (%)	Species
1	1123.437	40	[αCT11-1NH2-1OMe + H]+
2	1124.449	20	
3	1125.656	3	
4	1137.488	54	[αCT11-1NH2-2OMe + H]+
5	1138.428	35	
6	1139.446	12	
7	1140.7	3	
8	1151.547	13	[αCT11-1NH2-3OMe + H]+
9	1152.492	6	
10	1153.596	3	
11	1229.478	100	[αCT11-1NH2-1OMe + H + 106 Da]+
12	1230.455	67	
13	1231.514	18	
14	1232.329	4	
15	1243.438	93	[αCT11-1NH2-2OMe + H + 106 Da]+
16	1244.503	84	
17	1245.567	19	
18	1257.435	13	[αCT11-1NH2-3OMe + H + 106 Da]+
19	1258.382	8	
20	1259.536	3	
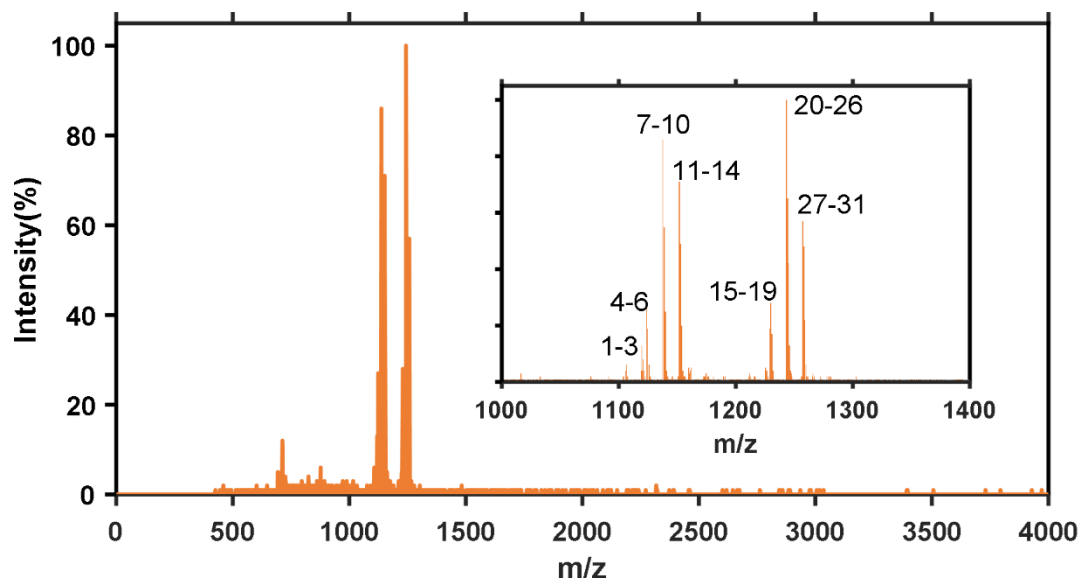
Figure A.70. MALDI-TOF MS of crude esterified αCT11-1NH$_2$(I9) (αCT11-1NH$_2$(I9)-OMe), as shown in Figure 5.2. Crude αCT11-1NH$_2$(I9) (Figure 2.7, A.67, Table D.22) was esterified at a 10000:1 MeOH:αCT11 ratio, with a solvent of 45:45:10 MeOH:DMF:HCl (v/v), for 68 h at 40 °C. Sample was cocrystallized with CHCA matrix and measured using a Shimadzu MALDI-8020 spectrometer. Numerical labels are defined in Table A.25.

Table A.25. MALDI-TOF MS of crude αCT11-1NH$_2$(I9)-OMe, esterified at a 10000:1 MeOH:αCT11 ratio, with a solvent of 45:45:10 MeOH:DMF:HCl (v/v), for 68 h at 40 °C. Labels correspond to Figure A.70.

label	Mass (Da)	Intensity (%)	Species
1	1119.783	13	[αCT11-1NH2/2OMe -H2O + H]+
2	1120.793	8	
3	1121.804	4	
4	1123.749	27	[αCT11-1NH2-1OMe + H]+
5	1124.761	19	
6	1125.851	6	
7	1137.723	86	[αCT11-1NH2-2OMe + H]+
8	1138.819	55	
9	1139.838	25	
10	1140.857	4	
11	1151.783	71	[αCT11-1NH2-3OMe + H]+
12	1152.808	49	
13	1153.912	20	
14	1154.937	4	
15	1229.234	19	[αCT11-1NH2-1OMe + H + 106 Da]+
16	1229.804	28	
17	1230.293	14	
18	1230.781	17	
19	1231.84	4	
20	1243.274	100	[αCT11-1NH2-2OMe + H + 106 Da]+
21	1243.766	64	
22	1244.257	65	
23	1244.83	42	
24	1245.895	13	
25	1246.797	4	
26	1247.289	3	
27	1257.312	57	[αCT11-1NH2/3OMe + H + 106 Da]
28	1257.806	32	
29	1258.3	48	
30	1258.876	22	
31	1259.865	6	
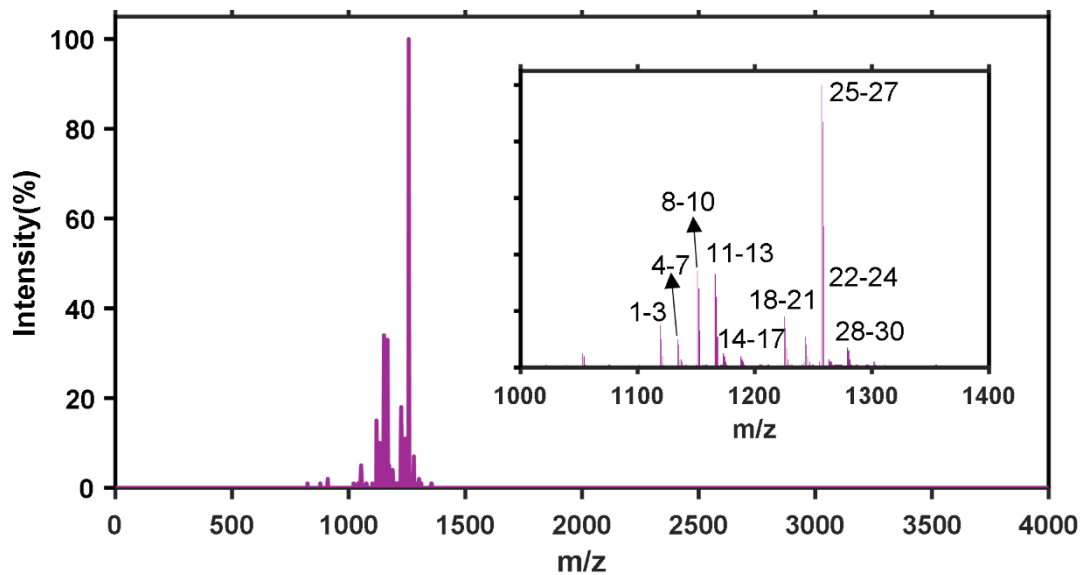
Figure A.71. MALDI-TOF MS of crude esterified αCT11-1NH$_2$(I9) (αCT11-1NH$_2$(I9)-OMe), as shown in Figure 5.2. Crude αCT11-1NH$_2$(I9) (Figure 2.7, A.67, Table D.22) was esterified at a 10000:1 MeOH:αCT11 ratio, with a solvent of 95:5 MeOH:HCl (v/v), for 68 h at 40 °C. Sample was cocrystallized with CHCA matrix and measured using a Shimadzu MALDI-8020 spectrometer. Numerical labels are defined in Table A.26.

Table A.26. MALDI-TOF MS of crude αCT11-1NH$_2$(I9)-OMe, esterified at a 10000:1 MeOH:αCT11 ratio, with a solvent of 95:5 MeOH:HCl (v/v), for 68 h at 40 °C. Labels correspond to Figure A.71.

label	Mass (Da)	Intensity (%)	Species
1	1119.239	15	[αCT11-1NH2/2OMe -H2O + H]+
2	1120.249	10	
3	1121.26	4	
4	1134.202	10	[αCT11-3OMe - H2O + H]+
5	1135.218	8	
6	1136.235	3	
7	1137.253	3	[αCT11-1NH2/2OMe + H]+
8	1151.232	34	[αCT11-1NH2/3OMe + H]+
9	1152.256	28	
10	1153.202	13	
11	1166.247	33	[αCT11-4OMe + H]+
12	1167.278	25	
13	1168.23	11	
14	1173.235	5	[αCT11-1NH2/3OMe + Na]+
15	1174.269	4	
16	1188.232	4	[αCT11-4OMe + Na]+
17	1189.193	3	
18	1225.168	18	[αCT11-1NH2/2OMe -H2O + H + 106 Da]+
19	1226.224	14	
20	1227.2	7	
21	1228.176	3	
22	1243.192	11	[αCT11-1NH2-2OMe + H + 106 Da]+
23	1244.175	8	
24	1245.158	4	
25	1257.147	100	[αCT11-1NH2/3OMe + H + 106 Da]+
26	1258.218	87	
27	1259.206	50	
29	1279.305	7	[αCT11-1NH2/3OMe + Na + 106 Da]+
30	1280.301	6	
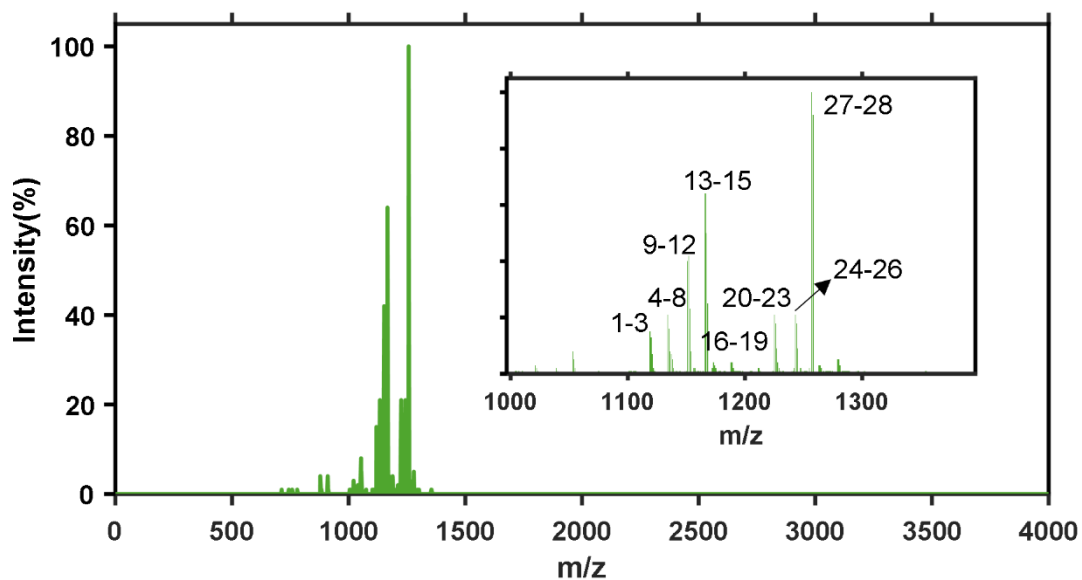
Figure A.72. MALDI-TOF MS of crude esterified αCT11-1NH$_2$(I9) (αCT11-1NH$_2$(I9)-OMe), as shown in Figure 5.2. Crude αCT11-1NH$_2$(I9) (Figure 2.7, A.67, Table D.22)was esterified at a 10000:1 MeOH:αCT11 ratio, with a solvent of 90:10 MeOH:HCl (v/v), for 68 h at 40 °C. Sample was cocrystallized with CHCA matrix and measured using a Shimadzu MALDI-8020 spectrometer. Numerical labels are defined in Table A.27.

Table A.27. MALDI-TOF MS of crude αCT11-1NH$_2$(I9)-OMe, esterified at a 10000:1 MeOH:αCT11 ratio, with a solvent of 90:10 MeOH:HCl (v/v), for 68 h at 40 °C. Labels correspond to Figure A.72.

label	Mass (Da)	Intensity (%)	Species
1	1119.006	15	[αCT11-1NH2/2OMe -H2O + H]+
2	1120.016	13	
3	1121.026	7	
4	1134.045	21	[αCT11-3OMe - H2O + H]+
5	1134.984	16	
6	1136.001	8	
7	1137.096	7	[αCT11-1NH2/2OMe + H]+
8	1138.036	5	
9	1151.074	40	[αCT11-1NH2/3OMe + H]+
10	1152.02	42	[αCT11-1NH2/3OMe + H]+ or [αCT11-3OMe + H]+
11	1153.044	23	
12	1153.99	8	
13	1166.089	64	[αCT11-4OMe + H]+
14	1167.04	50	
15	1168.071	25	
16	1173.155	4	[αCT11-1NH2/3OMe + Na]+
17	1174.109	3	
18	1188.072	4	[αCT11-4OMe + Na]+
19	1189.113	4	
20	1225.005	21	[αCT11-1NH2/2OMe -H2O + H + 106 Da]+
21	1225.98	18	
22	1226.956	9	
23	1227.932	4	
24	1243.029	21	[αCT11-1NH2-2OMe + H + 106 Da]+
25	1244.011	18	
26	1244.994	9	
27	1256.983	100	[αCT11-1NH2/3OMe + H + 106 Da]+
28	1258.053	92	
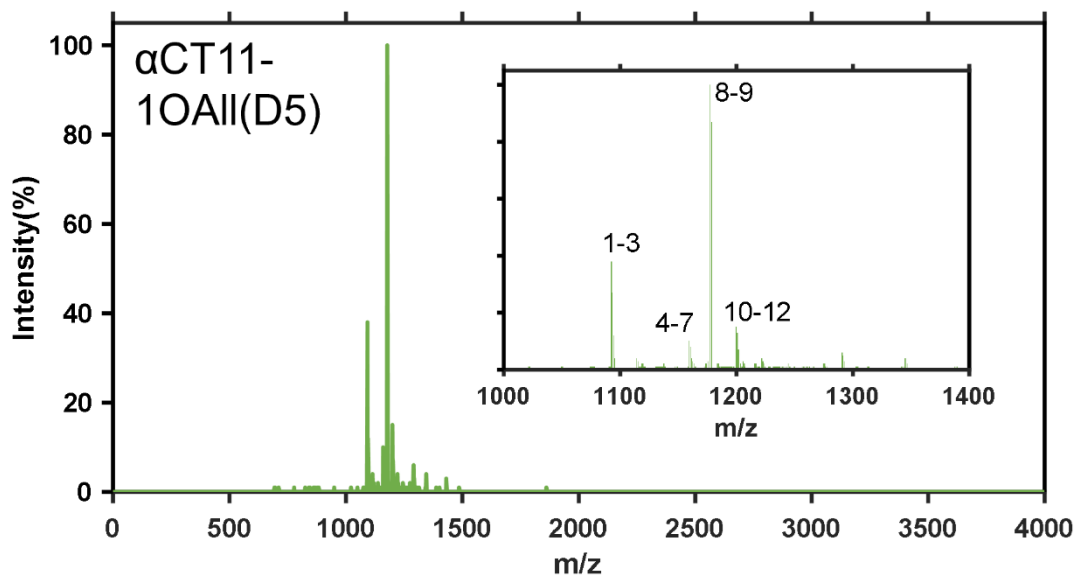
Figure A.73. MALDI-TOF MS of crude synthesized αCT11 with 1 allyl ester in the D5 position (αCT11-1OAll(D5)), as shown in Figure 2.8. Spectra show the presence of aspartimides, either through intramolecular cyclization with the peptide backbone amides or the addition of piperidine during synthesis. Sample was cocrystallized with CHCA matrix and measured using a Shimadzu MALDI-8020 spectrometer. Numerical labels are defined in Table A.28.

Table A.28. MALDI-TOF MS of crude synthesized αCT11-1OAll(D5). Labels correspond to Figure A.73.

label	Mass (Da)	Intensity (%)	Species
1	1092.45	38	[αCT11 - H2O + H]+
2	1093.448	27	
3	1094.446	12	
4	1159.439	10	[αCT11 - H2O + Piperidine + H]+
5	1160.467	8	
6	1161.416	4	
7	1162.445	3	
8	1177.453	100	[αCT11 + Piperidine + H]+
9	1178.569	87	
10	1199.623	15	
11	1200.588	13	
12	1201.554	7	
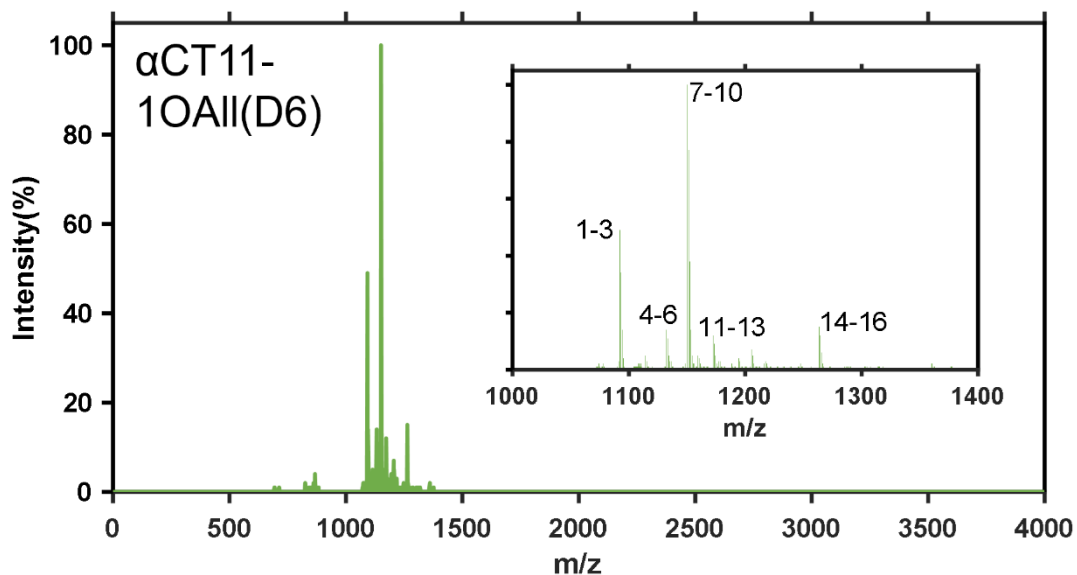
Figure A.74. MALDI-TOF MS of crude synthesized αCT11 with 1 allyl ester in the D6 position (αCT11-1OAll(D6)), as shown in Figure 2.8. Spectra show the presence of intramolecular aspartimides. Sample was cocrystallized with CHCA matrix and measured using a Shimadzu MALDI-8020 spectrometer. Numerical labels are defined in Table A.29.

Table A.29. MALDI-TOF MS of crude synthesized αCT11-1OAll(D6). Labels correspond to Figure A.74.

label	Mass (Da)	Intensity (%)	Species
1	1092.373	49	
2	1093.371	34	[αCT11 - H2O + H]+
3	1094.369	14	
4	1132.404	14	
5	1133.42	11	[αCT11-1OAll -H2O + H]+
6	1134.358	5	
7	1150.365	100	
8	1151.389	77	
9	1152.414	38	[αCT11-1OAll + H]+
10	1153.36	14	
11	1172.439	12	
12	1173.473	9	[αCT11-1OAll + Na]+
13	1174.428	5	
14	1263.494	15	
15	1264.484	12	[αCT11-1OAll + Leu/Ile + H]+
16	1265.475	6	
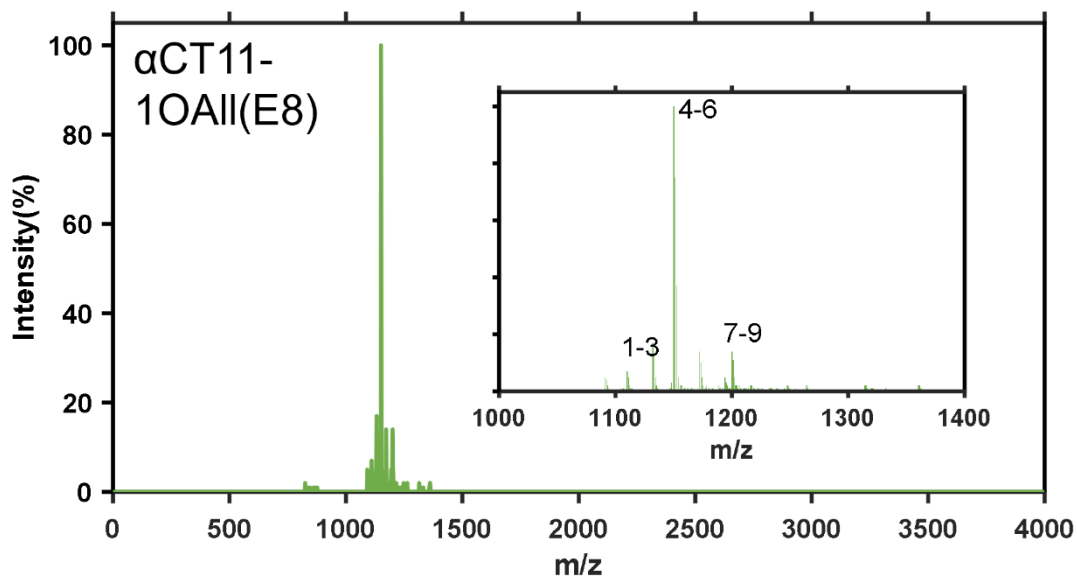
Figure A.75. MALDI-TOF MS of crude synthesized αCT11 with 1 allyl ester in the E8 position (αCT11-1OAll(E8)), as shown in Figure 2.8. Spectra show a very small presence of intramolecular aspartimides. Sample was cocrystallized with CHCA matrix and measured using a Shimadzu MALDI-8020 spectrometer. Numerical labels are defined in Table A.30.

Table A.30. MALDI-TOF MS of crude synthesized αCT11-1OAll(E8). Labels correspond to Figure A.75.

label	Mass (Da)	Intensity (%)	Species
1	1132.248	17	[αCT11-1OAll -H2O + H]+
2	1133.264	13	
3	1134.28	5	
4	1150.208	100	[αCT11-1OAll + H]+
5	1151.311	75	
6	1152.335	37	
7	1172.28	14	[αCT11-1OAll + Na]+
8	1173.314	10	
9	1174.269	5	
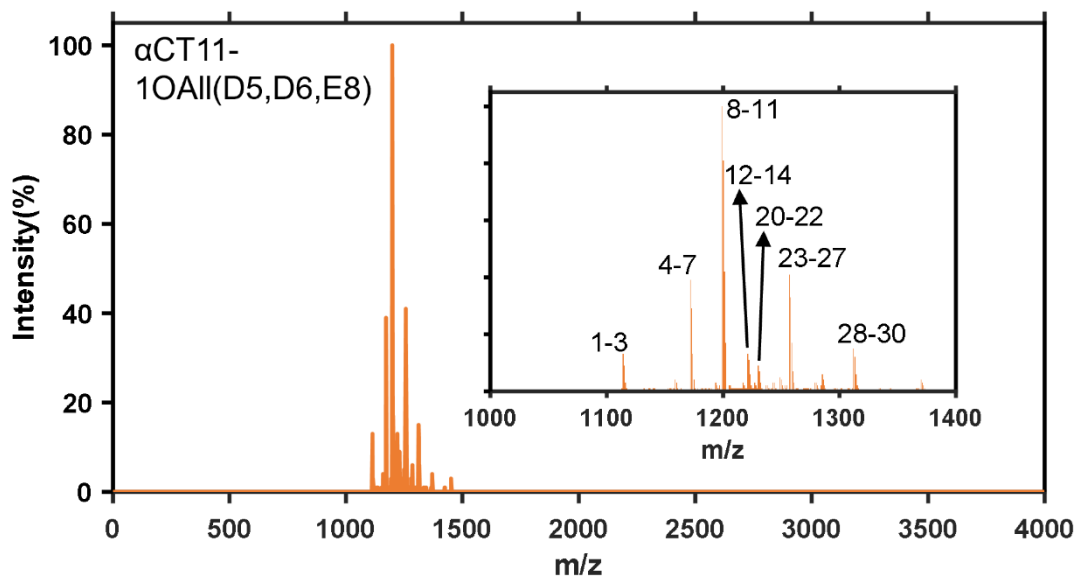
Figure A.76. MALDI-TOF MS of crude synthesized αCT11 with 3 allyl ester in the D5, D6, and E8 positions (αCT11-3OAll(D5,D6,E8)), as shown in Figure 2.8. Spectra shows the presence of imides, either through intramolecular binding with peptide backbone amides, the addition of piperidine, or both, with very little signal representing the true molecular weight of the sample (20-22). Sample was cocrystallized with CHCA matrix and measured using a Shimadzu MALDI-8020 spectrometer. Numerical labels are defined in Table A.31.

Table A.31. MALDI-TOF MS of crude synthesized αCT11-3OAll(D5,D6,E8). Labels correspond to Figure A.76.

label	Mass (Da)	Intensity (%)	Species
1	1114.041	13	
2	1115.049	9	[αCT11-1OAll - 2H2O - H]+
3	1116.057	3	
4	1171.963	39	
5	1172.996	29	
6	1174.03	13	[αCT11-2OAll - H2O + H]+
7	1175.064	4	
8	1198.98	100	
9	1200.106	81	
10	1201.152	42	[αCT11-1OAll + Piperidine - H2O + H]+
11	1202.117	17	
12	1221.108	13	
13	1222.163	11	[αCT11-1OAll + Piperidine - H2O + Na]+
14	1223.137	6	
20	1230.13	9	
21	1231.107	7	[αCT11-3OAll + H]+
22	1232.085	3	
23	1257.147	41	
24	1258.135	33	
25	1259.124	17	[αCT11-2OAll + Piperidine + H]+
26	1260.112	7	
27	1261.102	3	
28	1312.147	15	
29	1313.156	12	[αCT11-1OAll + Piperidine - H2O + Leu/Ile + H]+
30	1314.166	6	

CHAPTER B::
SUPPLEMENTARY INFORMATION FOR CHAPTER 3: ESTERIFICATION TO ENABLE REVERSIBLE ENCAPSULATION OF THERAPEUTIC PETPIDES INTO POLYELECTROLYTE COMPLEXES (PECS)

LIST OF FIGURES

LIST OF TABLES

Figure B.1. [1]H Nuclear magnetic resonance (NMR) spectroscopy-based end group analysis of poly(methacrylic acid) to estimate the degree of polymerization (DP) of the polymer. ^{1}H NMR spectroscopy was performed on a Bruker 400 MHz spectrometer. Spectrum is referenced to deuterated dimethylsulfoxide (DMSO-d6).
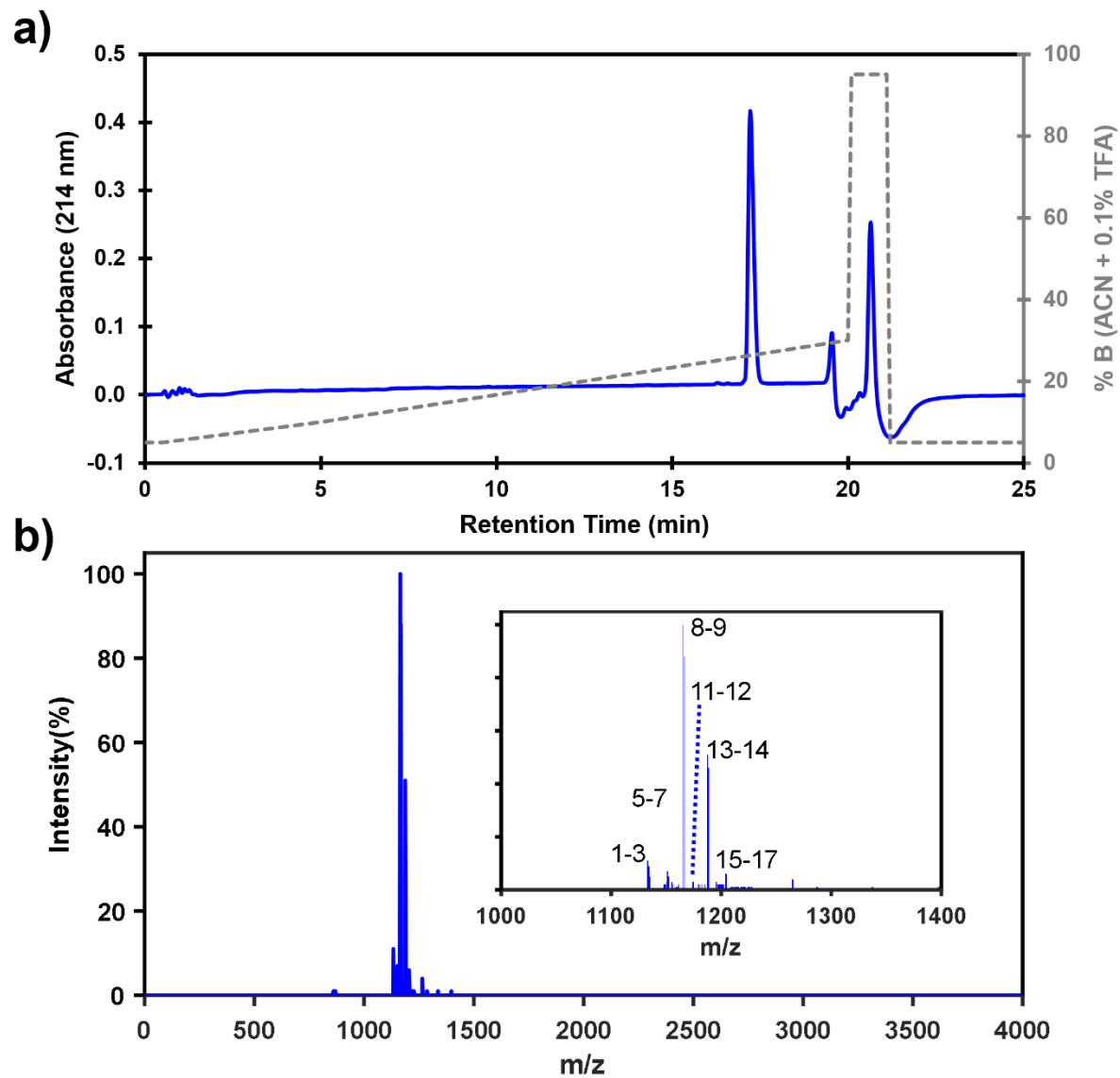
Figure B.2. Characterization of αCT11-4OMe. **a)** RP-HPLC of purified αCT11-4OMe, which had over 95% purity. **b)** MALDI-TOF MS spectra of αCT11-4OMe, with a spectrum zoomed in between 1000 and 1400 m/z inset. Labels in the inset spectrum correspond to **Table B.1**.

Table B.1. Molecular weight of αCT11-4OMe from MALDI-TOF MS, with labels corresponding to those listed in Figure B.2.

label	Mass (Da)	Intensity (%)	Species
1	1133.3	11	
2	1134.2	9	[αCT11-3OMe -H2O + H]+
3	1135.2	5	
4	1150.3	3	?*
5	1151.2	7	
6	1152.1	5	[αCT11-3OMe + H]+
7	1155.1	3	[αCT11-3OMe - H2O + Na]+
8	1165.3	100	
9	1166.4	88	[αCT11-4OMe + H]+
10	1174.1	3	?*
11	1174.5	3	
12	1174.9	3	[αCT11-3OMe + Na]+
13	1187.5	51	
14	1188.5	46	[αCT11-4OMe + Na]+
15	1195.5	3	[αCT11-3OMe + 2Na - H]+
16	1203.7	6	
17	1204.5	6	[αCT11-4OMe + K]+
18	1264.7	4	?*
19	1265.6	4	?*

*? corresponds to a molecular weight that could not be attributed to either αCT11-4OMe or the CHCA matrix. As MALDI-TOF MS is not representative of the quantity of different molecules in the peptide, we still used the peptide as it had a > 95% purity by RP-HPLC
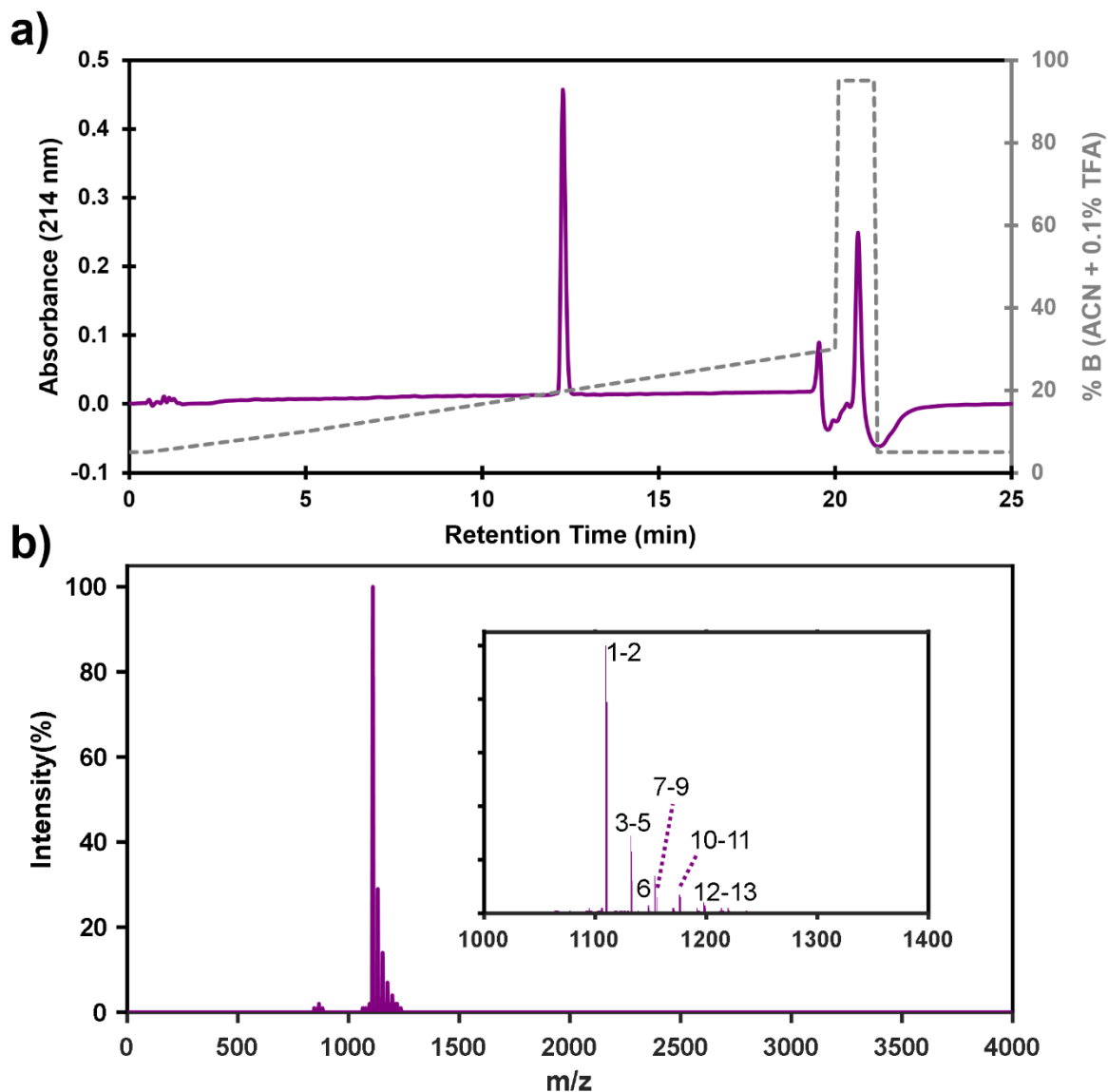
Figure B.3. Characterization of αCT11. **a)** RP-HPLC of purified αCT11, which had over 95% purity. **b)** MALDI-TOF MS spectra of αCT11, with a spectrum zoomed in between 1000 and 1400 m/z inset. Labels in the inset spectrum correspond to **Table B.2**.

Table B.2. Molecular weight of αCT11-4OMe from MALDI-TOF MS, with labels corresponding to those listed in Figure B.3.

label	Mass (Da)	Intensity (%)	Species
1	1109.6	100	[αCT11 + H]+
2	1110.7	79	
3	1131.8	29	[αCT11 + Na]+

4	1132.8	23	
5	1133.8	12	
6	1147.9	3	[αCT11 + K]+
7	1153.8	14	
8	1154.8	11	[αCT11 + 2Na - H]+
9	1155.7	6	
10	1175.8	7	[αCT11 + 3Na - 2H]+
11	1176.8	6	
12	1197.8	4	[αCT11 + 4Na - 3H]+
13	1198.8	3	
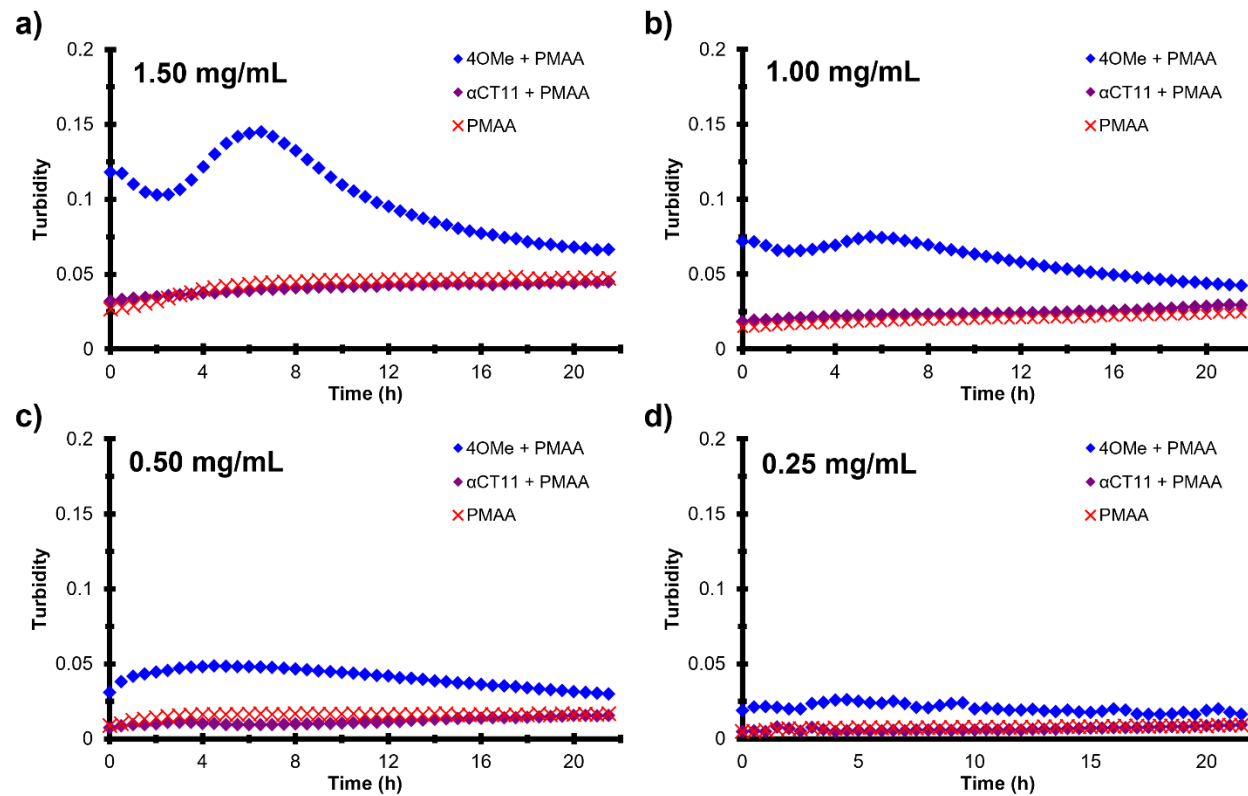
Figure B.4. Turbidity of αCT11-4OMe and PMAA mixtures (blue diamonds), αCT11 and PMAA mixtures (purple, diamonds), and PMAA solutions (red) at **a)** 1.50, **b)** 1.00, **c)** 0.50, and **d)** 0.25 mg PMAA/mL solution. All solutions were made in 26 mM phosphate buffer (pH 7.4).
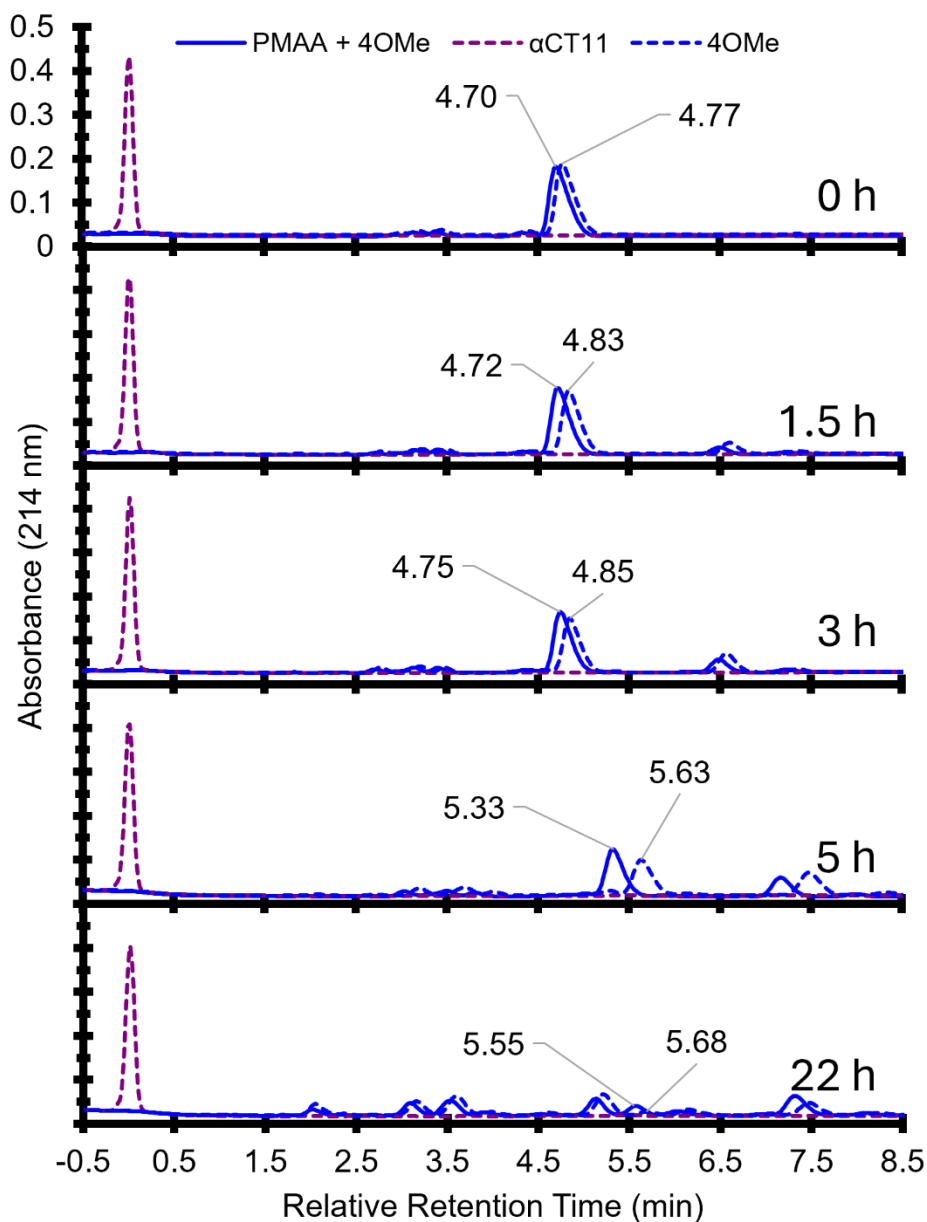
Figure B.5. Unedited RP-HPLC traces of PMAA/4OMe (blue, solid line), αCT11-4OMe (blue, dashed line), or αCT11 alone (purple, dashed line). Retention times of αCT11-4OMe peak in each plot is listed.

      Figure B.5 shows unedited chromatograms of the various timepoints measured over 22 h. As RP-HPLC chromatograms are highly dependent upon mobile phase preparation, even minute changes in mobile phase composition could affect the retention time of peaks. To that end observed some variation in the retention times of αCT11-4OMe-related peaks in each of the chromatograms over time. We first aligned the αCT11-

4OMe peak in both the PMAA/4OMe and αCT11-4OMe samples to more directly compare the effect of hydrolysis on αCT11-4OMe, and then set the relative retention time of each αCT11-4OMe peak that of the -4OMe peak at the initial timepoint (4.70 min). To identify the αCT11-4OMe peaks, especially in later timepoints, we selected peaks until we noticed all peaks (especially the peak at ~6.5 min) aligned over the 22 h.

CHAPTER C::
SUPPLEMENTARY INFORMATION FOR CHAPTER 4: EXPANDING THE DESIGN SPACE OF POLYMER-METAL ORGANIC FRAMEWORK (MOF) GELS BY UNDERSTANDING POLYMER-MOF INTERACTIONS

LIST OF FIGURES

synthesized samples incubated with Ang 1-7 for 7 d. Error bars represent the standard deviation of the average. C-32

LIST OF TABLES

C.1 Characterization of UiO-66 composite gels and controls

C.1.1 Characterization of UiO-66

Figure C.1. Formation of UiO-66 particles in DMSO. **a)** Zr-oxo cluster solution in DMSO, which is transparent. **b)** Formation of UiO-66 particles in DMSO as evidenced by the solution turning white upon the addition of H$_2$BDC and the GIXD pattern closely resembling the simulated pattern for UiO-66 (Figure 4.1 in manuscript).
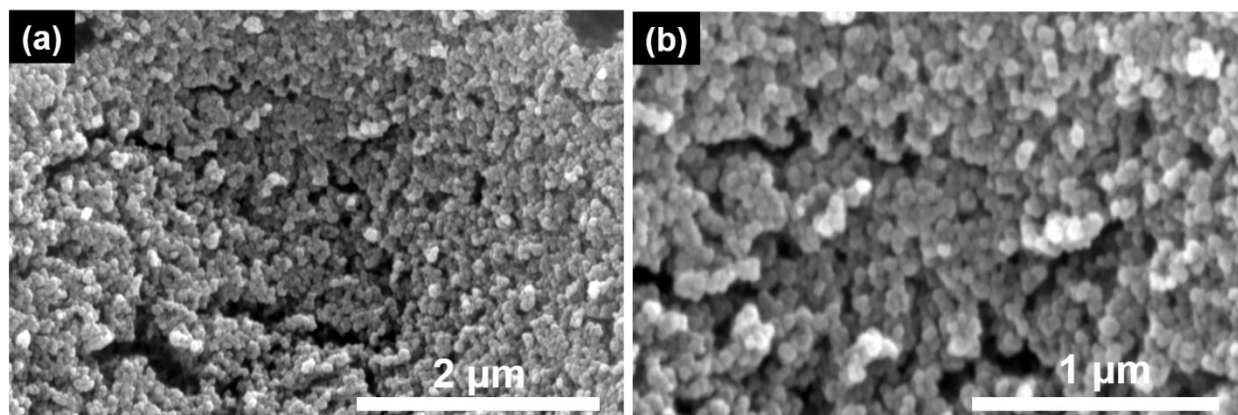
Figure C.2. High-magnification scanning electron microscopy (SEM) images of UiO-66 synthesized in DMSO show the formation of spherical particles. Bars in bottom right corner represent **a)** 2 μm and **b)** 1 μm.

C.1.2 Polymer-UiO-66 composite gel formation with different linker: metal ratios

Since UiO-66 particles were synthesized at linker: metal ratio of 1:1, we attempted to form

the polymer-UiO-66 composites at the same ratio. For this, we chose PVA as a polymer.

To make the composite gels at a 1:1 linker: metal ratio, we added a solution of Zr-oxo

clusters (70 mM in 5 mL of DMSO) to the PVA-H$_2$BDC solution (72 mM H$_2$BDC in 5 mL of DMSO) at room temperature for 24 h. No gelation occurred after 24 h, as suggested by the inversion test (**Figure C.3a**). On the contrary, doubling the H$_2$BDC concentration in the PVA-H$_2$BDC solution (144 mM H$_2$BDC in 5 mL of DMSO) and adding the Zr-oxo cluster solution at room temperature resulted in gelation after 24 h (**Figure C.3b**). Therefore, we synthesized all the polymer-UiO-66 composite gels (PAA-UiO-66, PAAA-UiO-66, PVA-UiO-66, and PEG-UiO-66) at a linker: metal ratio of 2:1.

We avoided lowering the linker:metal ratio (i.e., 1:2 or 1:4) to form composite gels. We suspect that lowering the linker concentration slows down the UiO-66 crystal formation, which might result in crystals with less defects/open metal sites.[14] Since we suspect that defects are required for gel formation, lowering linker concentration might not produce gel network. Another way to lower the linker:metal ratio is to increase the Zr-oxo cluster concentration. However, we are already using a very high concentration of Zr-oxo clusters in DMSO. Further increasing the Zr-oxo concentration might not be possible due to the solubility limitations of Zr propoxide in DMSO. Additionally, adding more Zr propoxide might change the equilibrium of Zr$_6$ species and may produce other unfavorable Zr species not suitable for UiO-66 formation.[15] Zr-oxo cluster formation is a complex process and it requires further study.
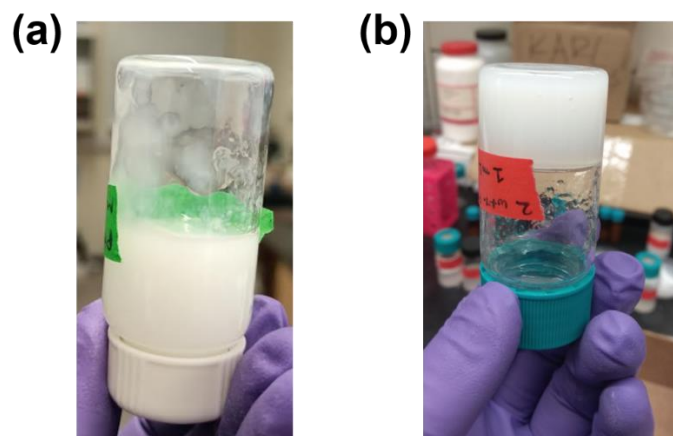
Figure C.3. Inversion test of PVA-UiO-66 composites synthesized at a linker: metal ratio of **a)** 1:1 and **b)** 2:1. The gelation occurs at linker: metal ratio of 2:1. The PVA wt% is 2 for both cases. The images were taken one min after inverting the vials.

Section S1c: Characterization of PAA-based composite gels
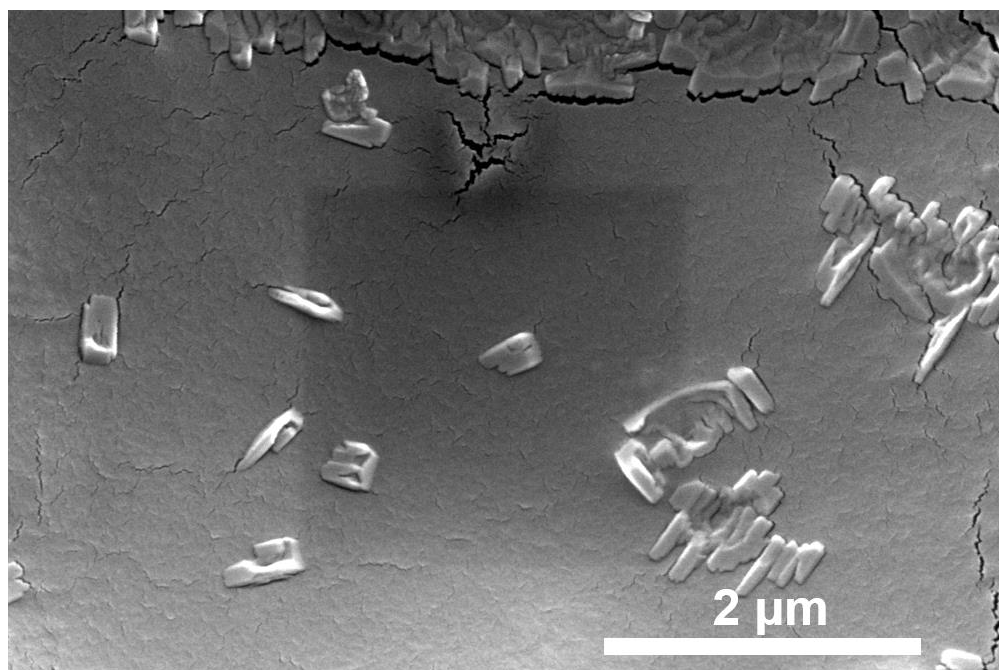
Figure C.4. High-magnification SEM image of PAA-UiO-66 gel shows no spherical particles such as those observed in Figure C.2 for UiO-66 particles synthesized in DMSO in the absence of PAA. The absence of spherical particles in the PAA-UiO-66 gels suggests no UiO-66 formation in the presence of PAA.

Figure S4.

C.1.3 Inversion test of polymer-UiO-66 physical mixtures
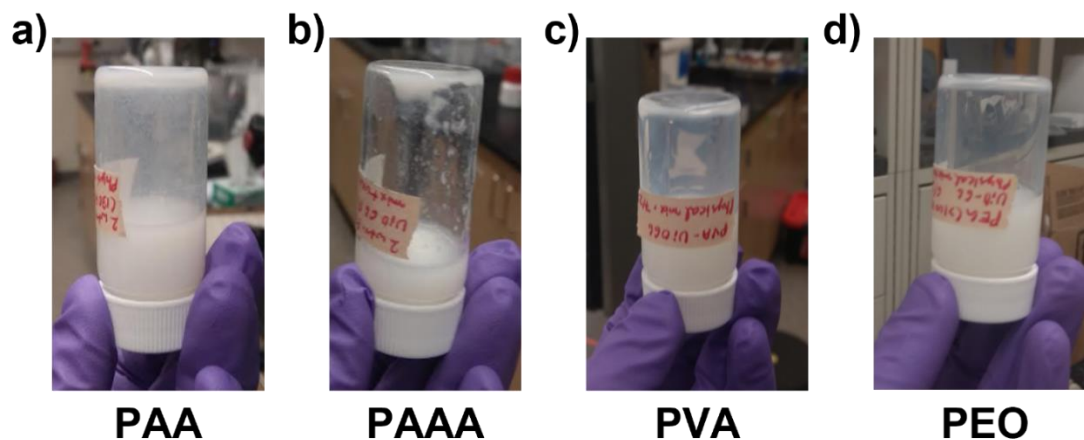
Figure C.5. Inversion tests of physical mixtures of **a)** PAA and UiO-66, **b)** PAAA and UiO-66, **c)** PVA and UiO-66, and **d)** PEG and UiO-66 showing the absence of gelation when pre-formed MOFs are mixed with polymers. Photographs were taken one minute after inverting the vials.

C.1.4 Characterization of PAAA-based composite gels
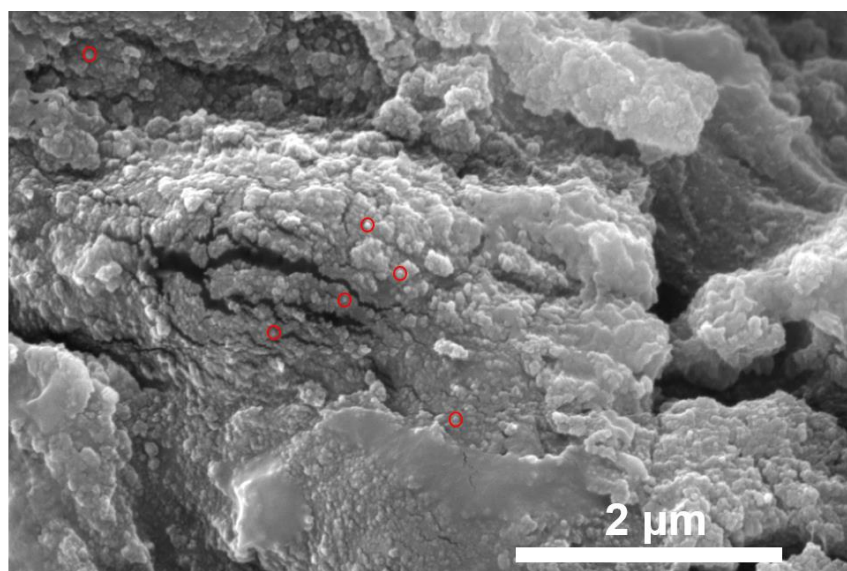
Figure C.6. High-magnification SEM image of PAAA-UiO-66 composite gel showing the presence of spherical particles, suggesting the formation of UiO-66 in the presence of PAAA. Red circles show the UiO-66 particles within the composite gel.

C.1.5 Characterization of PVA-based composite gels
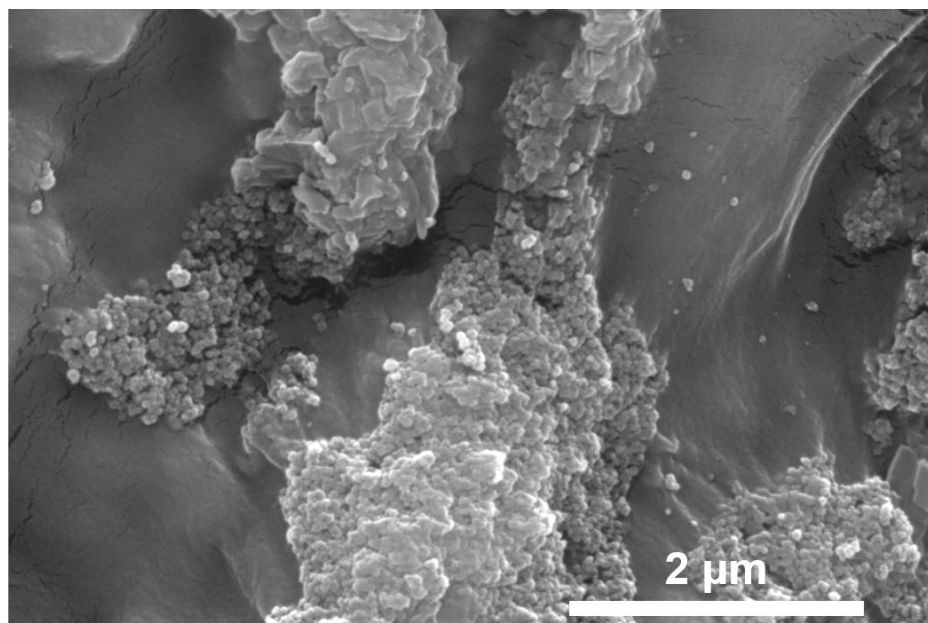
Figure C.7. High-magnification SEM image of PVA-UiO-66 composite gel showing the presence of spherical particles, suggesting the formation of UiO-66 in the presence of PVA.
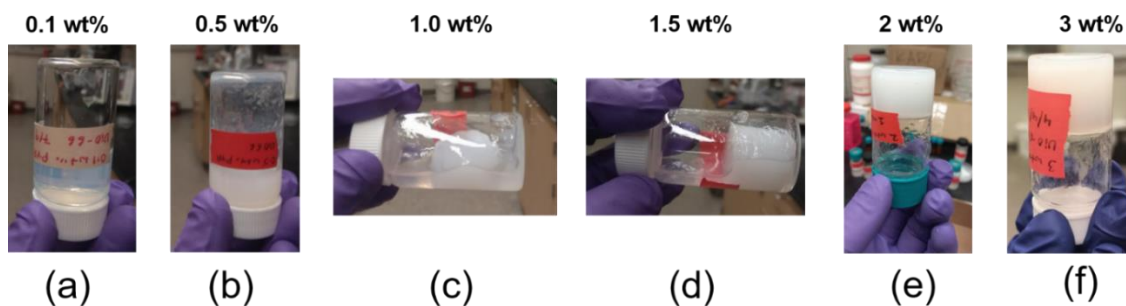
Figure C.8 Inversion tests of PVA (146000-186000 g/mol) - UiO-66 formulations as a function of polymer concentration: **a)** 0.1; **b)** 0.5; **c)** 1.0; **d)** 1.5; **e)** 2; and **f)** 3 wt% PVA. The study shows that a critical PVA concentration (1.5-2 wt%) is required to induce gelation. Images were taken one min after inverting the vial.
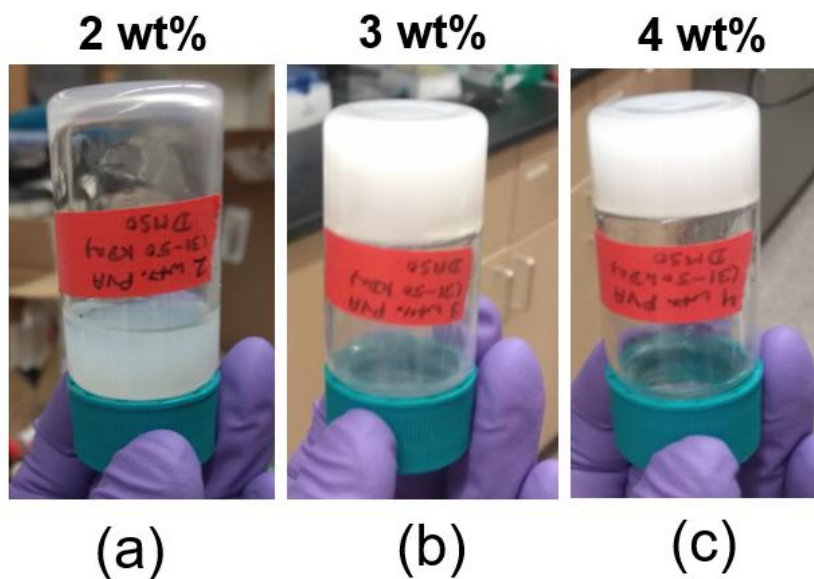
Figure C.9. Inversion tests of PVA (31000-50000 g/mol) – UiO-66 formulations at **a)** 2, **b)** 3, and **c)** 4 wt% PVA. For this lower molecular weight PVA, gelation requires at least 3 wt% PVA, slightly higher than the concentration needed for gelation using the higher molecular weight PVA (146000-186000 g/mol). Images were taken one min after inverting the vial.
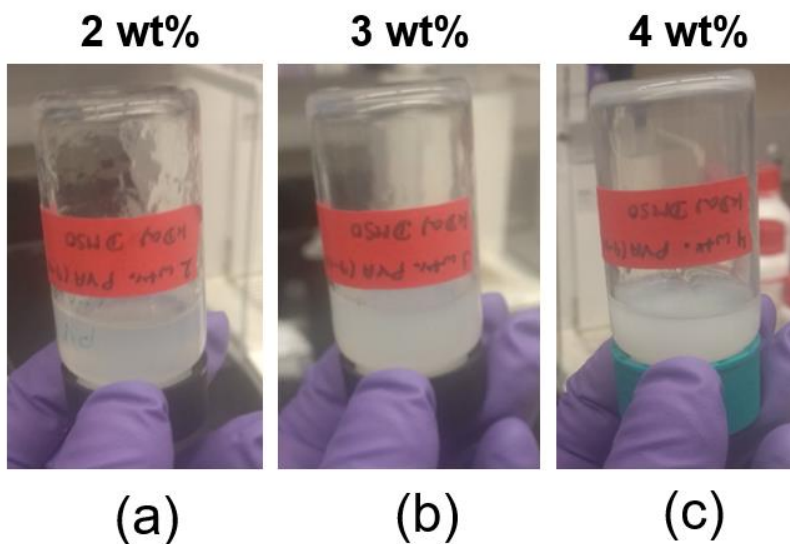
Figure C.10. Inversion test of PVA (9000-10000 g/mol) - UiO-66 formulations at **a)** 2, **b)** 3, and **c)** 4 wt% PVA. No gelation was observed, even at 4 wt% PVA using this low molecular weight polymer. Images were taken one min after inverting the vial.
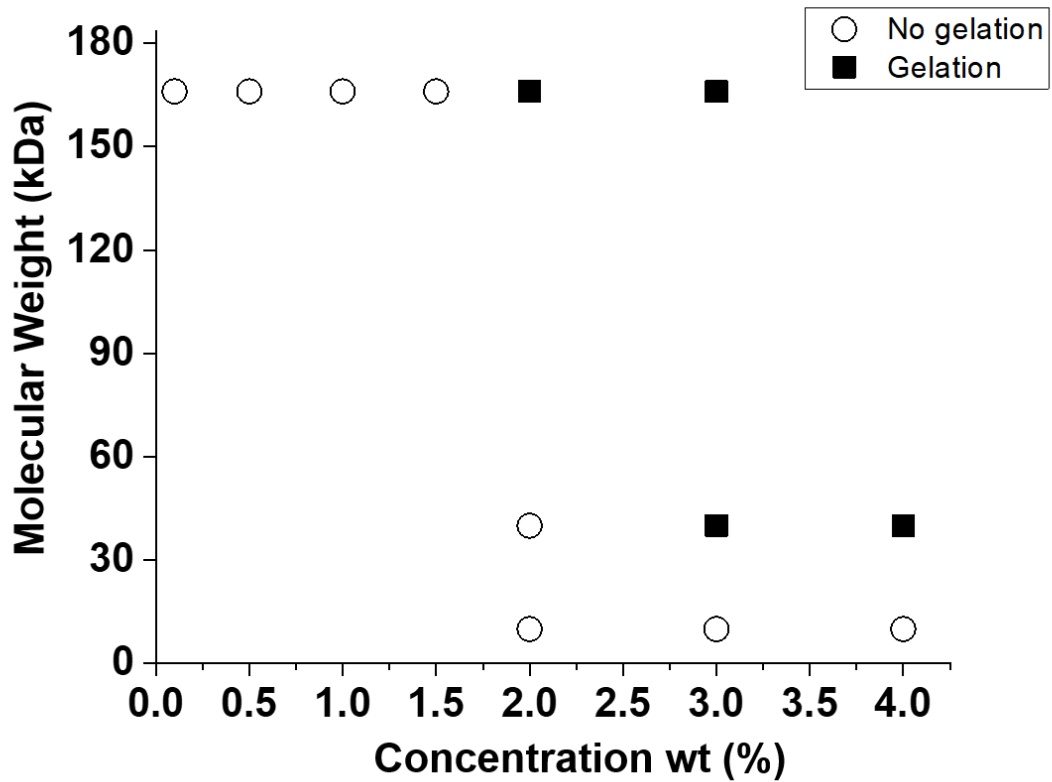
Figure C.11. Phase diagram of PVA-UiO-66 formulations with different concentrations (wt%) and molecular weight of PVA demonstrating the conditions where no gelation and gelation occurred.

Section S1g: Characterization of PEG-based composite gels
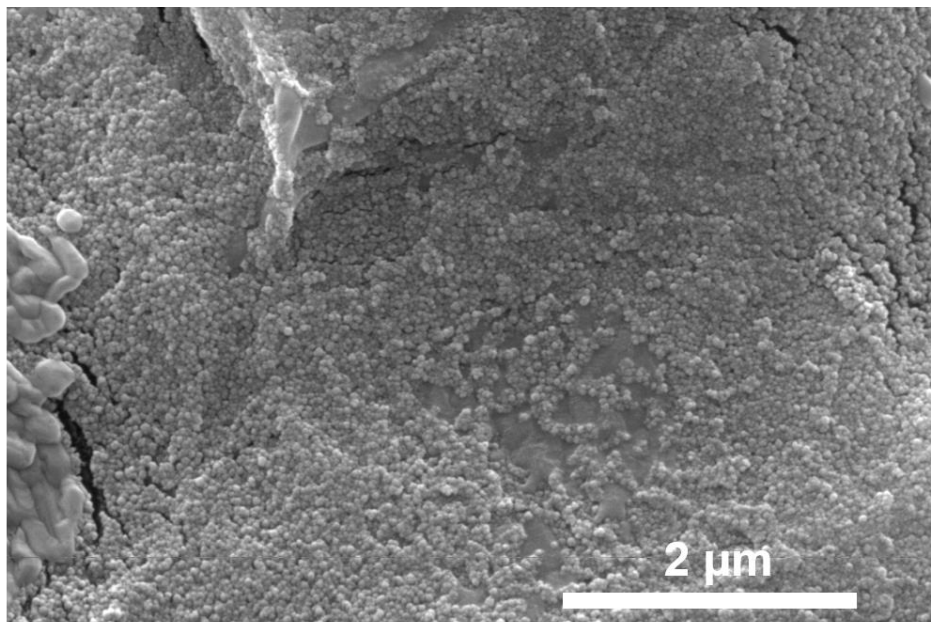
Figure C.12. High-magnification SEM image of PEG-UiO-66 composite gel shows the presence of spherical particles, suggesting the formation of UiO-66 in the presence of PEG.
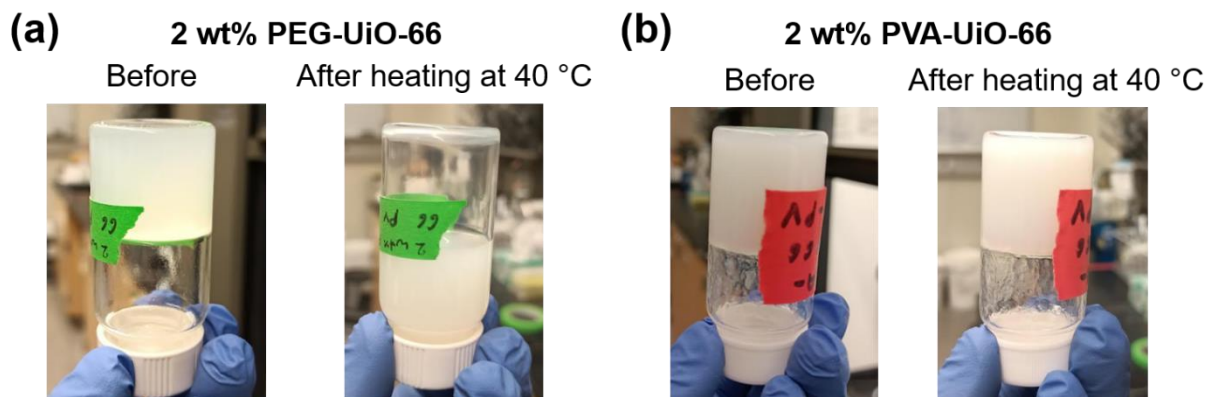
Figure C.13. Composite gel stability at room temperature and after heating to 40 °C. **a)** PEG-UiO-66 composite gel collapses after heating at 40 °C for 24 h, while **b)** PVA-UiO-66 composite gel remains intact. This experiment suggests that heating promotes the reptation of PEG chains out of UiO-66 pores and the PEG-UiO-66 composite collapses. Therefore, entrapment of PEG chains inside UiO-66 is responsible for gelation.

C.2 Characterization of PVA-based composite gels prepared with a variety of Zr-based MOFs
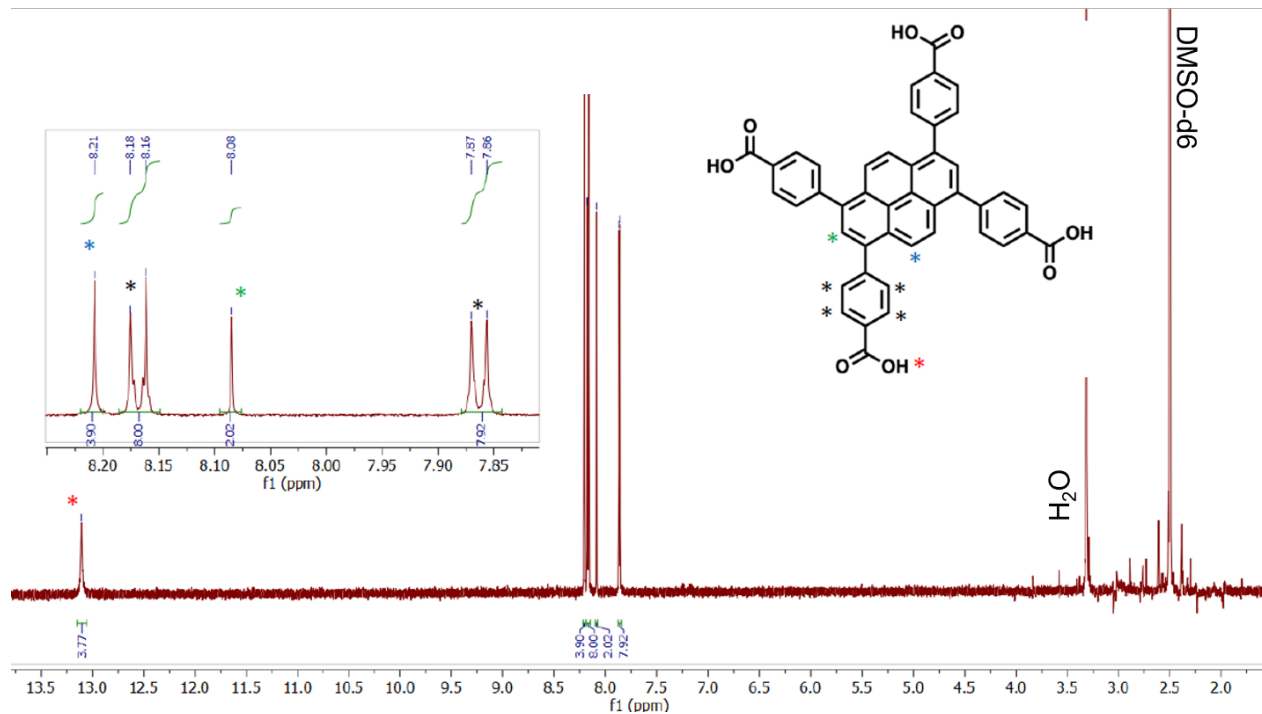
Figure C.14. ¹H NMR (600 MHz, DMSO-d6) of 4,4',4'',4'''-(pyrene-1,3,6,8-tetrayl)tetrabenzoic acid (H₄TBAPy), the organic linker for NU-901.
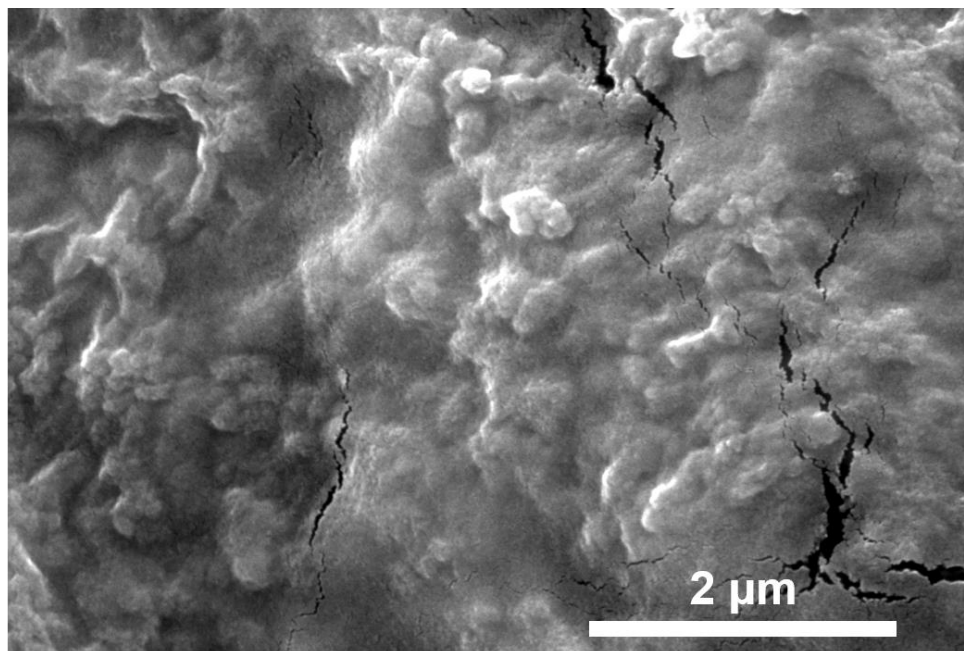
Figure C.15. High-magnification SEM image of PVA-NU-901 composite gel showing the presence of spherical particles, suggesting the formation of NU-901 in the presence of PVA.
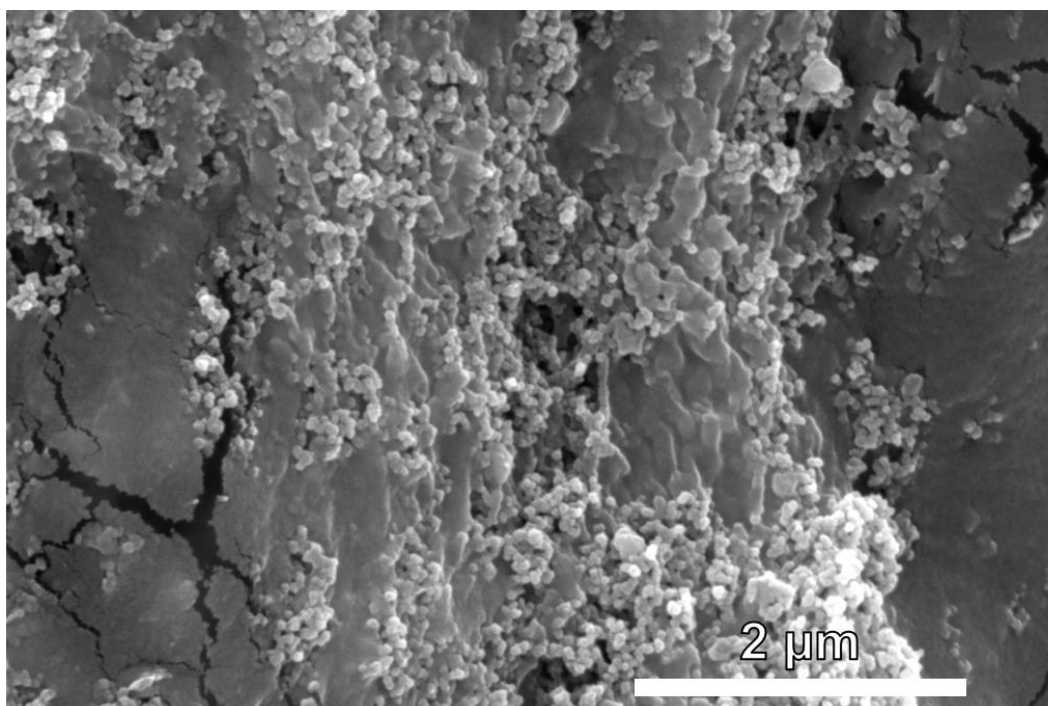
Figure C.16. High-magnification SEM image of PVA-UiO-67 composite gel shows the presence of spherical particles, suggesting the formation of UiO-67 in the presence of PVA.
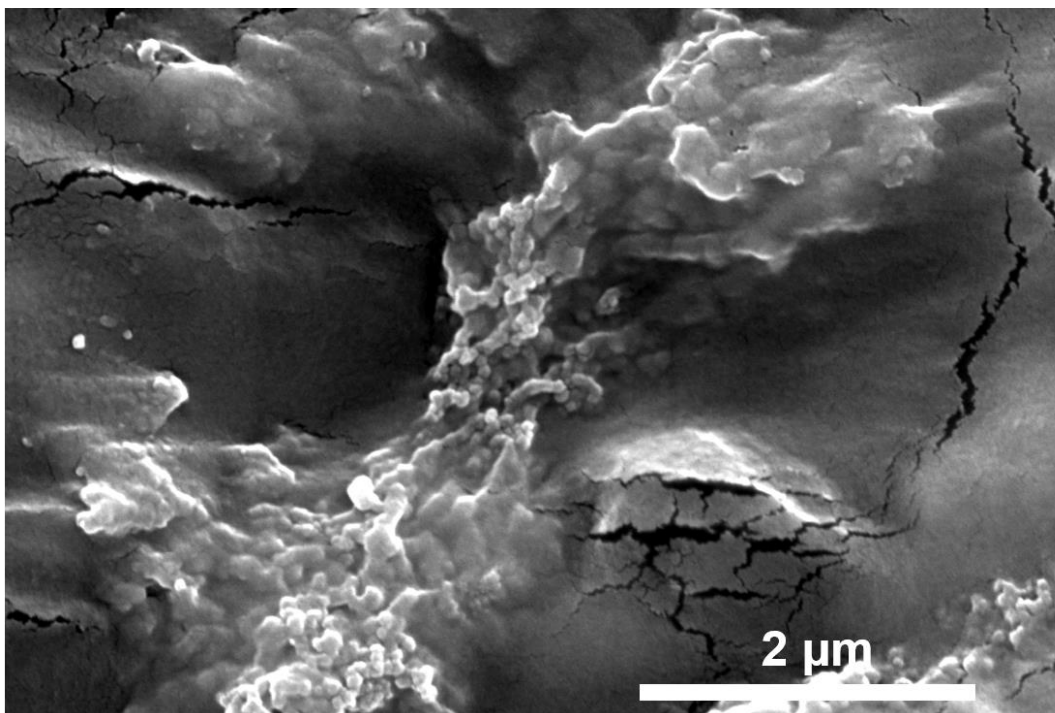
Figure C.17. High-magnification SEM image of PVA-MOF-525 composite gel shows the presence of spherical particles, suggesting the formation of MOF-525 in the presence of PVA.
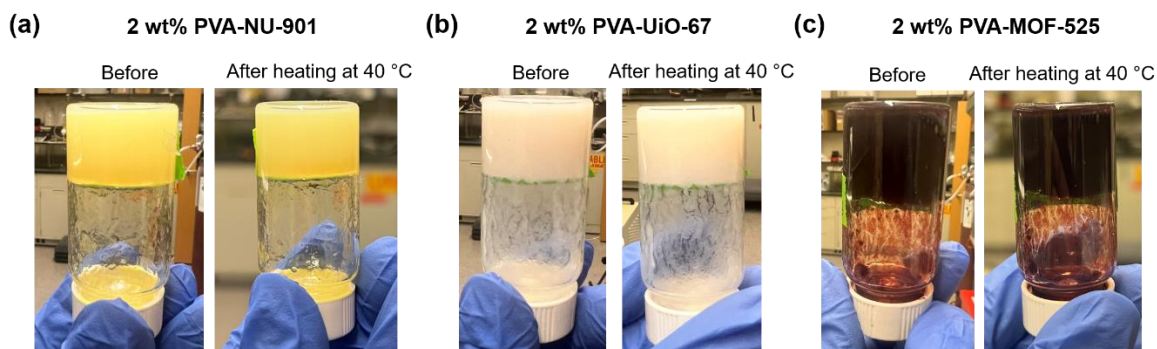
Figure C.18. a) PVA-NU-901, **b)** PVA-UiO-67, and **c)** PVA-MOF-525 composite gels stability at room temperature and after heating to 40 °C for 24 h.

C.3 Composite gel solvent exchange
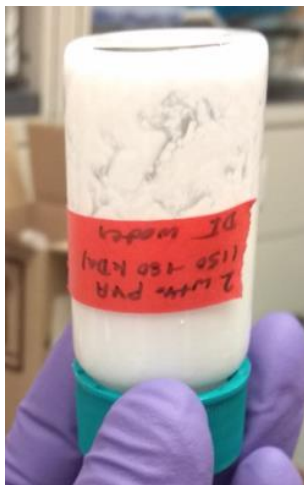
Figure C.19. Gelation behavior of reagents used for the 2 wt% PVA-UiO-66 composite, when synthesized in RO water instead of DMSO. The inversion test indicates no gelation in water.
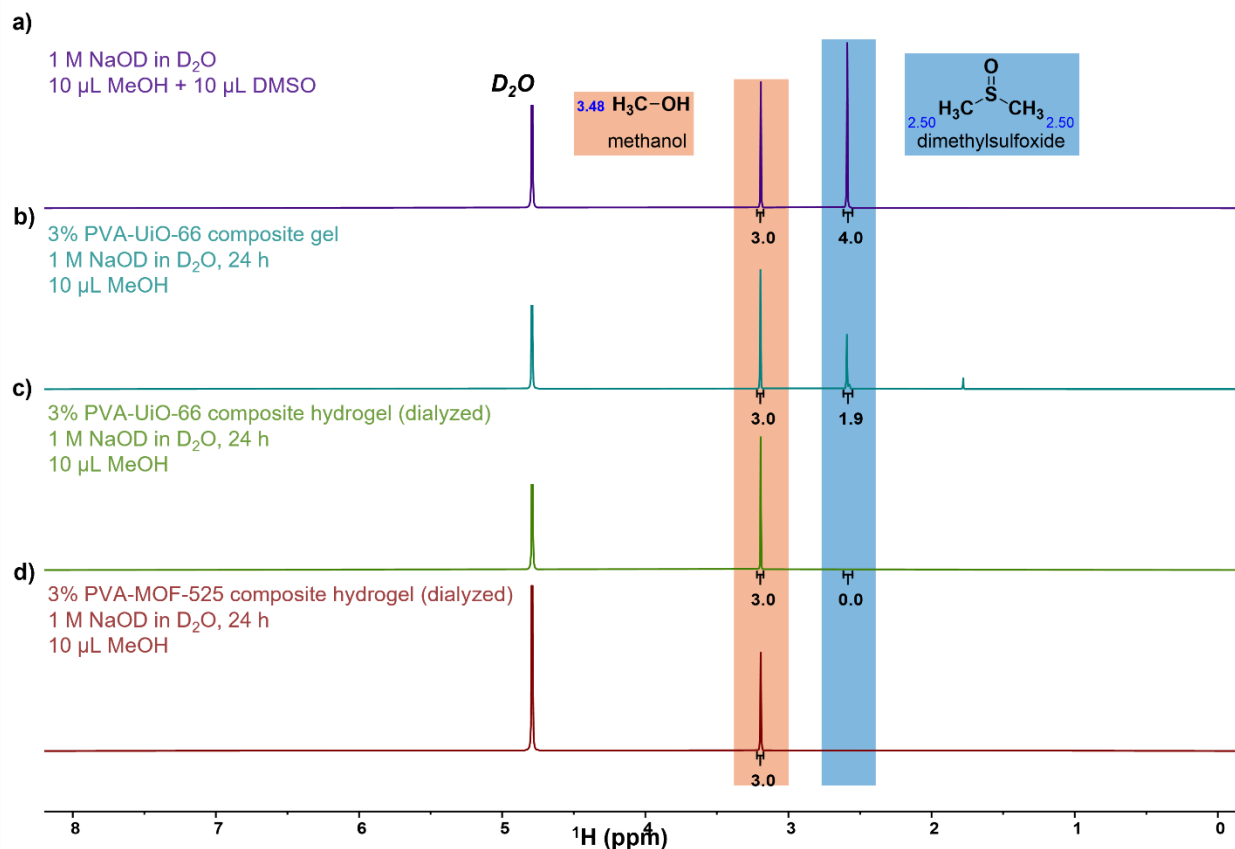
Figure C.20. Quantification of dimethylsulfoxide (DMSO) removal during composite gel solvent switch. ^{1}H NMR (400 MHz) of a) 1M sodium deuteroxide (NaOD) in deuterium oxide (D$_2$O), spiked with 10 µL of methanol (MeOH) and 10 µL of DMSO, b) 3% PVA-UiO-66 composite gel, c) 3% PVA-UiO-66 composite hydrogel (after dialysis), and d) 3% PVA-MOF-525 composite hydrogel (after dialysis). All gel samples were stirred in 1 M NaOD (10 mg gel/mL solvent) for 24 h to solubilize them and were then spiked with 10 µL of MeOH as a reference to determine the concentration of DMSO in each gel. Spectra were referenced to D$_2$O (4.79 ppm).

Table C.1. Quantification of DMSO in polymer-MOF composite hydrogels

Sample:		3% PVA-UiO-66 Composite Gel	3% PVA-UiO-66 composite hydrogel (dialyzed)	3% PVA-MOF-525 composite hydrogel (dialyzed)
MOF Gel Weight	mg	26	18	30
MeOH amount	mmol	0.25		
MeOH Peak Integration		3.00	3.00	3.00
DMSO Peak Integration		1.90	0.00	0.00
DMSO:MeOH Ratio		0.63	N/A	N/A
DMSO amount	mg	5.07	0	0
	wt%	20%	0%	0%
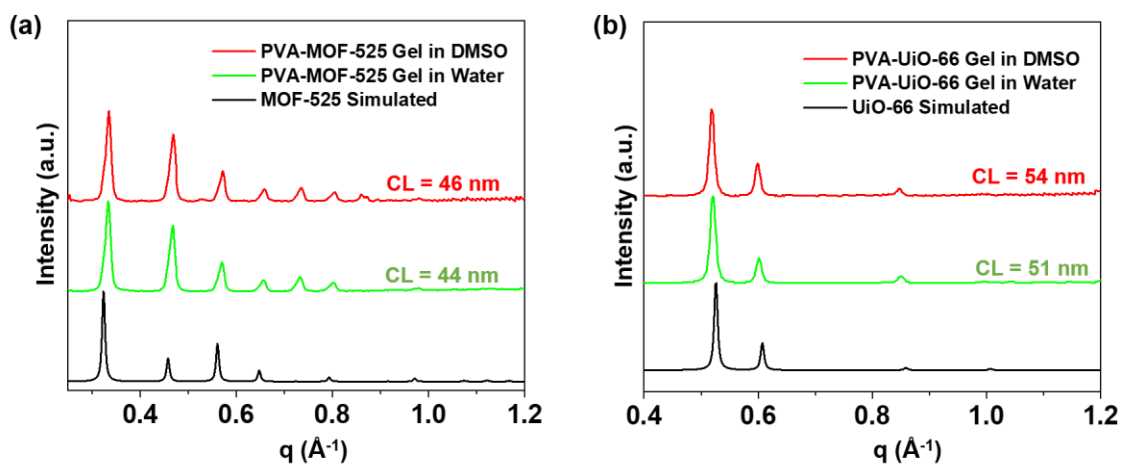
Figure C.21. GIXD patterns of 3 wt% **a)** PVA-MOF-525 and **b)** PVA-UiO-66 composite gels in DMSO (red) and hydrogels in water (green), showing the MOFs to exhibit similar coherence lengths (CLs) before and after the 48 h solvent exchange (dialysis) process.
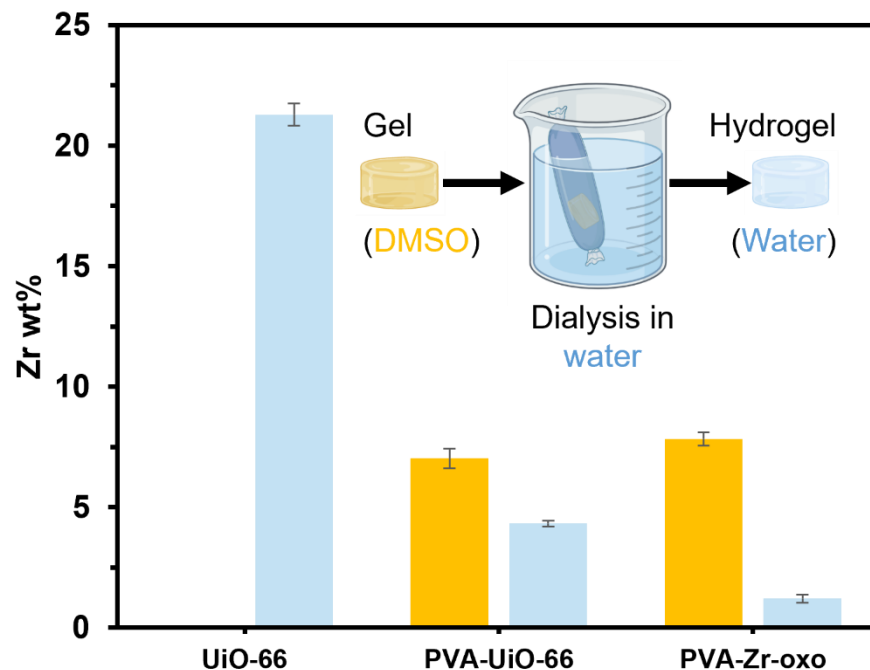
Figure C.22. Zr content before and after solvent exchange of PVA-UiO-66 and PVA-Zr-oxo gels from DMSO (yellow) into water (blue) by dialysis, as determined by TGA in air after drying samples at room temperature for 24 h. Zr content decreased significantly in the PVA-Zr-oxo gels during dialysis, but not in the PVA-UiO-66 composite hydrogels. UiO-66 prepared in the absence of polymer contained 21.3 wt% Zr following dialysis. Zr content is reported as an average of 3 samples, with error bars representing the standard deviation across sample sets.

Table C.2. ZrO_2 and Zr wt% of PVA-UiO-66 composite gels, PVA-Zr-oxo gels, and UiO-66 powder before and after solvent exchange

		Before Dialysis		After Dialysis	
		% ZrO_2	% Zr	% ZrO_2	%Zr
PVA-UiO-66 composite gel	1	9.1	6.7	5.8	4.3
	2	10.4	7.7	5.7	4.2
	3	9.9	7.3	6.0	4.4
	Average	**9.8**	**7.3**	**5.8**	**4.3**
	St. Dev.	**0.7**	**0.5**	**0.2**	**0.1**
PVA-Zr-oxo gel	1	10.5	7.8	1.7	1.2
	2	11.0	8.2	1.9	1.4
	3	10.3	7.6	1.4	1.0
	Average	**10.6**	**7.8**	**1.6**	**1.2**
	St. Dev.	**0.4**	**0.3**	**0.2**	**0.2**
UiO-66	1	-	-	28.3	20.9
	2	-	-	29.5	21.8
	3	-	-	28.6	21.1
	Average	**-**	**-**	**28.8**	**21.3**
	St. Dev.	**-**	**-**	**0.6**	**0.5**
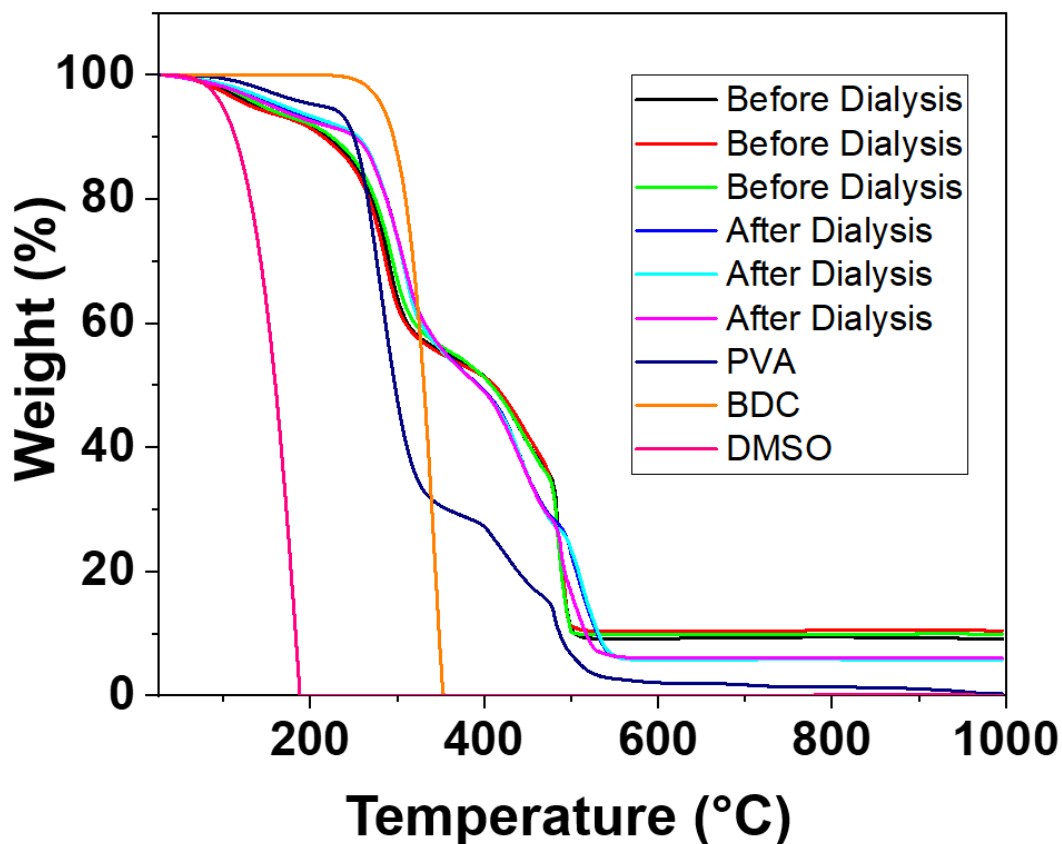
Figure C.23. TGA profiles of 3 wt% PVA-UiO-66 composite gels before (black, red, green) and after dialysis (blue, cyan, magenta), BDC (orange), PVA (navy blue), BDC linker (orange) and DMSO (pink). PVA, BDC, and DMSO completely decompose at 1000 °C, suggesting that all the organic components in the PVA-UiO-66 composite gels have been completely removed at 1000 °C and the remaining wt% can be attributed to the formation of ZrO_2. After dialyzing the 3 wt% PVA-UiO-66 composite gels, the ZrO_2 wt% slightly decreases from 9.8 wt% to 5.8 wt%. All the samples were run under air.
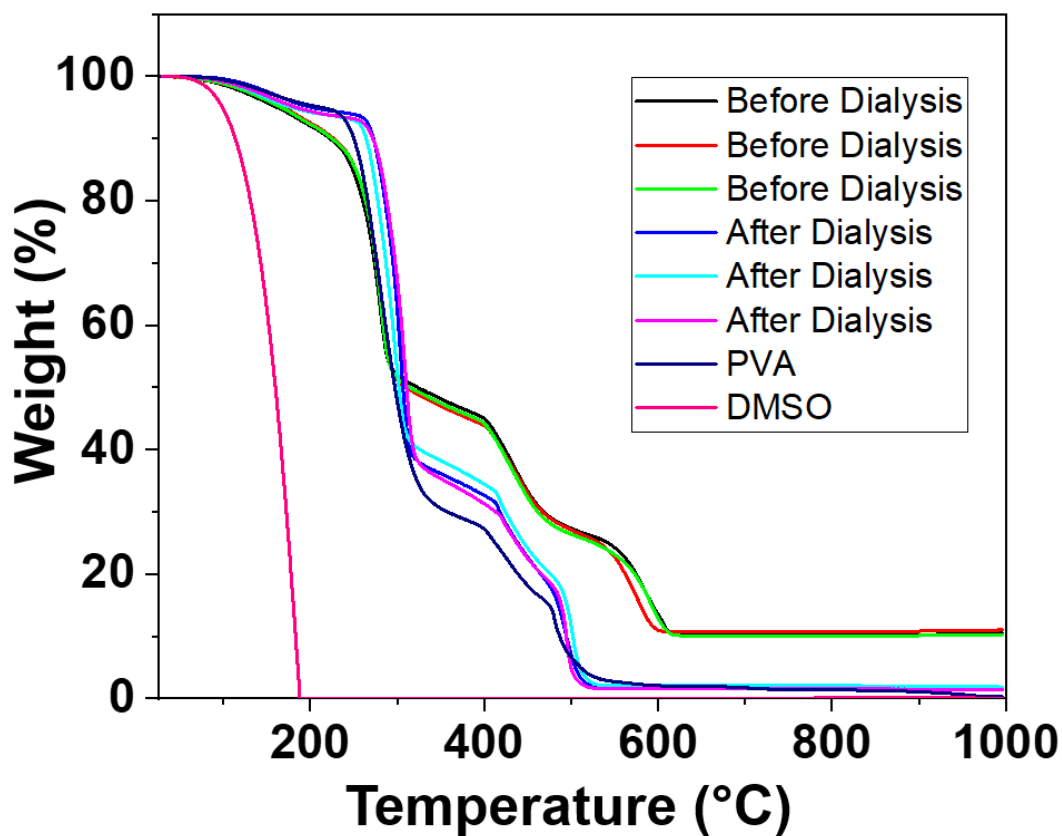
Figure C.24. TGA profiles of 3 wt% PVA-Zr-oxo gels before (black, red, green) and after dialysis (blue, cyan, magenta), PVA (navy blue), and DMSO (pink). PVA and DMSO completely decompose at 1000 °C, suggesting that all the organic components in the PVA-UiO-66 composite gels have been completely removed at 1000 °C and the remaining wt% can be attributed to the formation of ZrO_2. After dialyzing the 3 wt% PVA-Zr-oxo gels, the ZrO_2 wt% significantly decreases from 10.6 wt% to 1.6 wt%. All the samples were run under air.
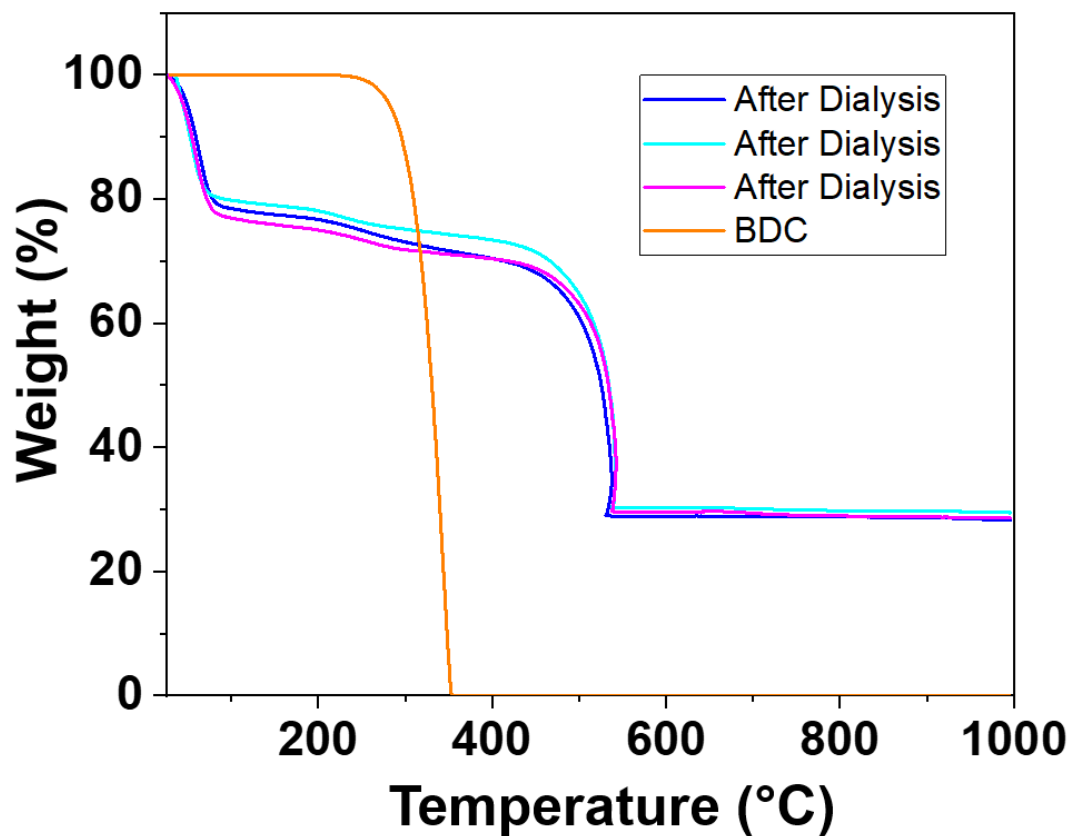
Figure C.25. TGA profiles of UiO-66 powder synthesized in DMSO (blue, cyan, magenta) and BDC linker (orange). BDC completely decomposes at 1000 °C, suggesting that the remaining wt% 1000 °C can be attributed to the formation of ZrO_2. All the samples were run under air.

C.4 MB sorption into and release from PVA-MOF composite gels
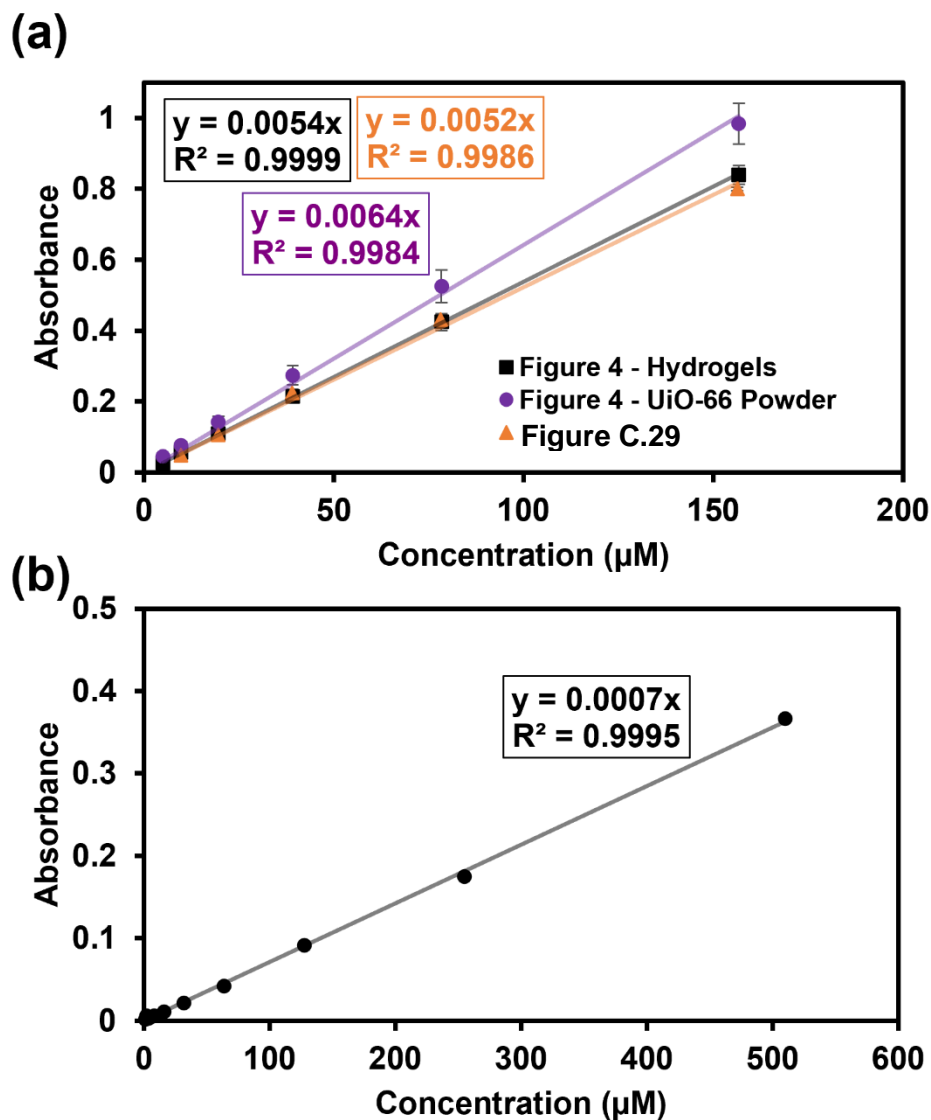
Figure C.26. Calibration curves for **a)** MB and **b)** Ang 1-7 encapsulation and release experiments into the composite gel carriers and their respective controls (Zr-cross-linked gels and MOF alone). **a)** MB calibration curves for MB sorption into 3 wt% PVA-UiO-66 composite hydrogels and 3 wt% PVA-Zr-oxo hydrogels (Figure 4.3, Figures C27-29, and Table S3), developed from serial dilution of the respective stock solutions used in the encapsulation experiments. A separate calibration curve was developed for every MB stock solution (all prepared at 0.05 mg/mL) prepared for the experiments: one for the hydrogels (black, squares) one for UiO-66 powder (purple, circles), and one for Figure S29, (orange, triangles). Absorbance values were measured at 660 nm, the absorbance maximum for MB. **b)** Calibration curve for Ang 1-7, developed from serial dilution of the stock solution used in the encapsulation experiments. Absorbance values were measured at 277 nm, the measured absorbance maximum of Ang 1-7. All stock solutions were prepared in RO water. The absorbance conversion constant ($\varepsilon_s b$) is shown as the slope of the linear interpolations for each dataset, and is listed in the boxes with corresponding colors to each dataset.
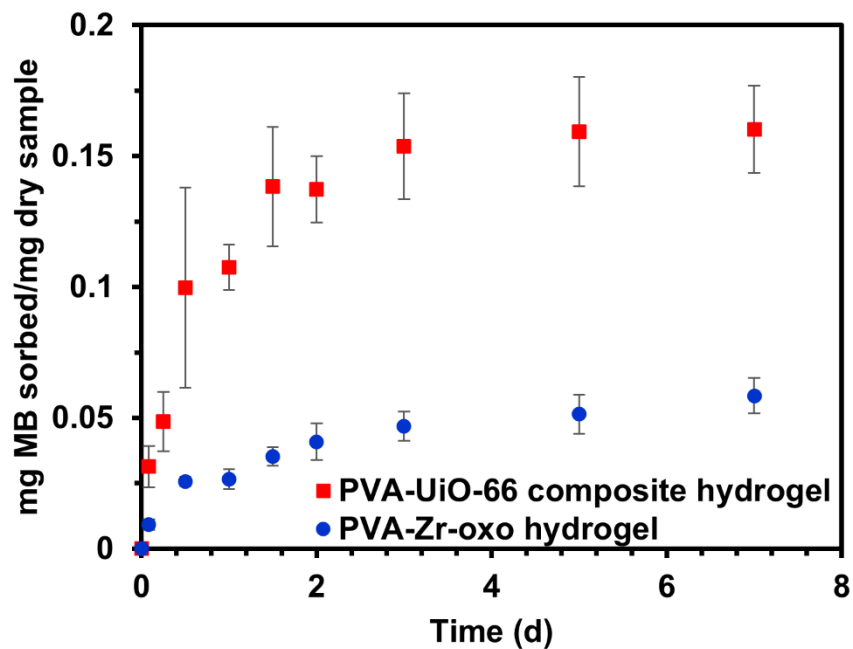
Figure C.27. MB sorption profiles of PVA-UiO-66 composite hydrogels (red, squares) and PVA-Zr-oxo hydrogels (blue, circles) over 7 d, normalized by the dry weight of the carrier, showing MB sorption to plateau after 7 d. Points represent the means of three independently synthesized samples, and error bars represent the standard deviation of that mean.
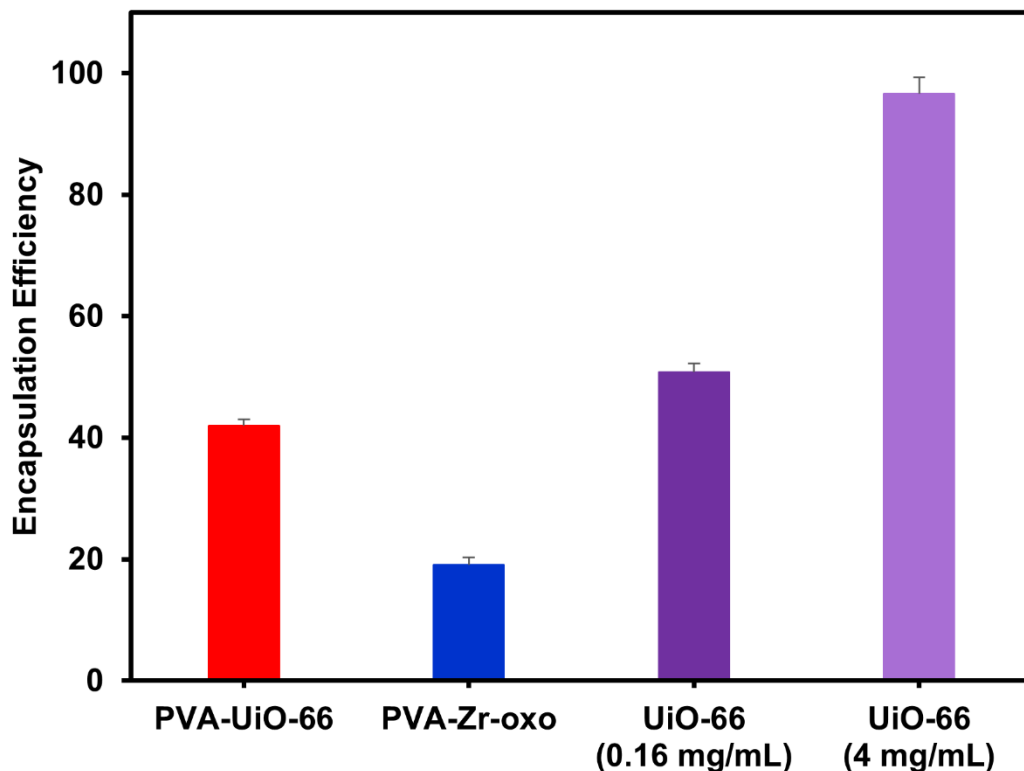
Figure C.28. Encapsulation efficiency, or % of MB in solution sorbed, of tested carriers after 7 d. Plot depicts PVA-UiO-66 composite hydrogels (red), PVA-Zr-oxo hydrogels (blue), and UiO-66 (purple). Two separate experiments with UiO-66 are depicted, where the concentration of UiO-66 added into the solution was normalized by total weight (4 mg sample/mL) and by Zr weight (0.16 mg sample/mL), relative to the PVA-UiO-66 composite hydrogels. While the PVA-UiO-66 composite hydrogel, PVA-Zr-oxo hydrogel, and UiO-66 normalized by Zr weight (0.16 mg sample/mL) all reached sorptive capacity after 7 d, as they all sorbed less than 100% of the MB in solution, the UiO-66 samples normalized by total weight (4 mg sample/mL) sorbed ~100% of the MB in the solution, suggesting that it was not at sorptive capacity. Therefore, to ensure all analyzed samples were at sorptive capacity, the Zr-weight normalized UiO-66 samples (0.16 mg sample/mL) were used to compare to the gel samples. Plotted bars represent the average of three independently synthesized samples incubated with MB for 7 d. Error bars represent the standard deviation of the average.
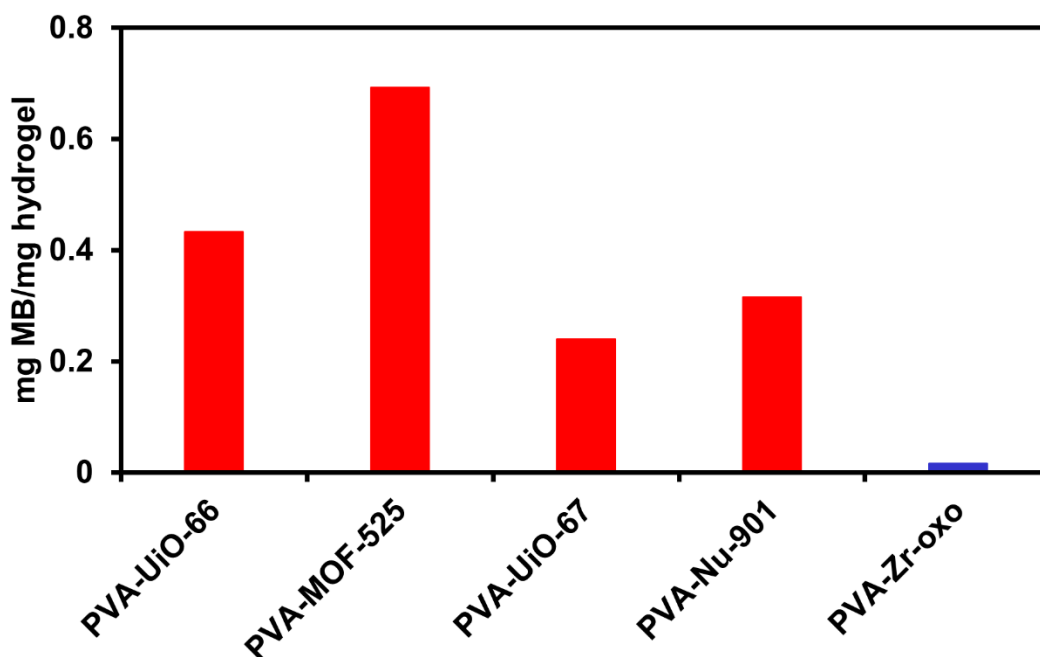
Figure C.29. MB sorptive capacity of various PVA-MOF composite hydrogels. Amount of MB sorbed into each PVA-MOF hydrogel shown in Figure 4.2 (PVA-UiO-66, PVA-MOF-525, PVA-UiO-67, and PVA-NU-901) (red) and PVA-Zr-oxo (blue) hydrogels after 7 d, normalized by the weight of each hydrated gels added to the MB solution. All synthesized PVA-MOF composite hydrogels exhibited higher MB sorptive capacity than the PVA-Zr-oxo control hydrogels. Each gel was synthesized with 2 wt% PVA, and lightly agitated in solution of MB over 7 d.

Table C.3. MB sorption into PVA-UiO-66 composite hydrogels, PVA-Zr-oxo hydrogels, and UiO-66 powder.

	mg MB 1-7/mg carrier			mg MB 1-7/mg dry carrier			mg MB/mg Zr		
		Avg	StDev		Avg	StDev		Avg	StDev
PVA-UiO-66 composite gel	0.005			0.141			3.267		
	0.007	0.006	0.001	0.172	0.160	0.017	3.981	3.708	0.385
	0.006			0.167			3.875		
PVA-Zr-oxo gel	0.002			0.052			4.324		
	0.003	0.003	0.000	0.057	0.058	0.007	4.752	4.838	0.561
	0.003			0.066			5.436		
UiO-66	0.157			0.157			0.731		
	0.156	0.160	0.006	0.156	0.160	0.006	0.727	0.744	0.027
	0.167			0.167			0.776		

Table C.4. Reported values and conditions for UiO-66 MB sorptive capacities in literature.

Sorptive Capacity (mg MB/g sorbent)	pH	Starting MB concentration (mg/L)	Sorbent	Reported by:
64.5	-	50	UiO-66	ref. 1
~544	10	130	UiO-66	ref. 2
160 +/- 17	-	50	3% PVA-UiO-66 composite hydrogels	this study
160 +/- 6	-	50	UiO-66	this study

C.5 Ang 1-7 sorption into and release from PVA-MOF-525 composite gels

a)

b)
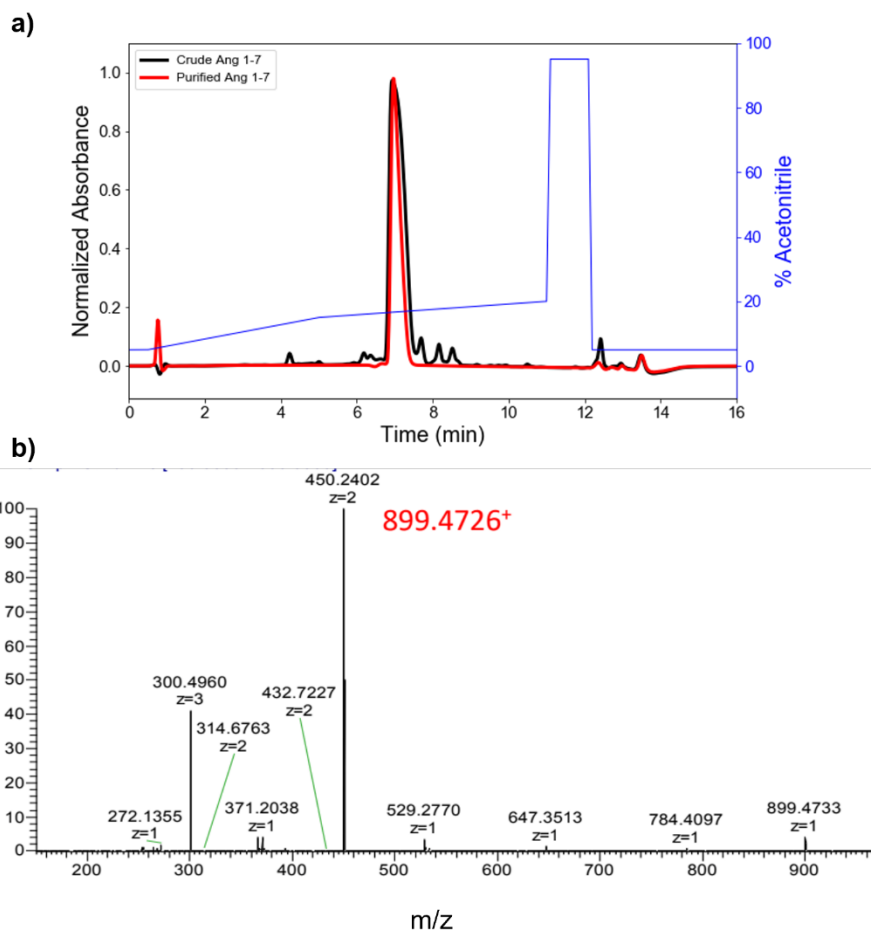
Figure C.30. Characterization of Ang 1-7 peptide. **a)** Analytical reverse phase high performance liquid chromatography (RP-HPLC) of Ang 1-7 before (black) and after purification (red) using preparative scale RP-HPLC. Analytical RP-HPLC was performed on a Waters E2695 Alliance Separations Module, using a 4.5 mm x 50 mm XBridge C18 3.5 μm chromatographic separation column, where the acetonitrile gradient is plotted in blue. Preparative scale RP-HPLC was performed on a Waters Empower system, using a 30 mm x 150 mm XBridge Prep C18 5 μm optimum bed density chromatographic separation columns. UV absorbance was measured at 214 nm. **b)** Electrospray ionization (ESI) spectrometry of Ang 1-7 after purification. ESI was measured a Thermo Orbitrap Exploris 480 mass spectrometer by the UVA Biomolecular Analysis Core.
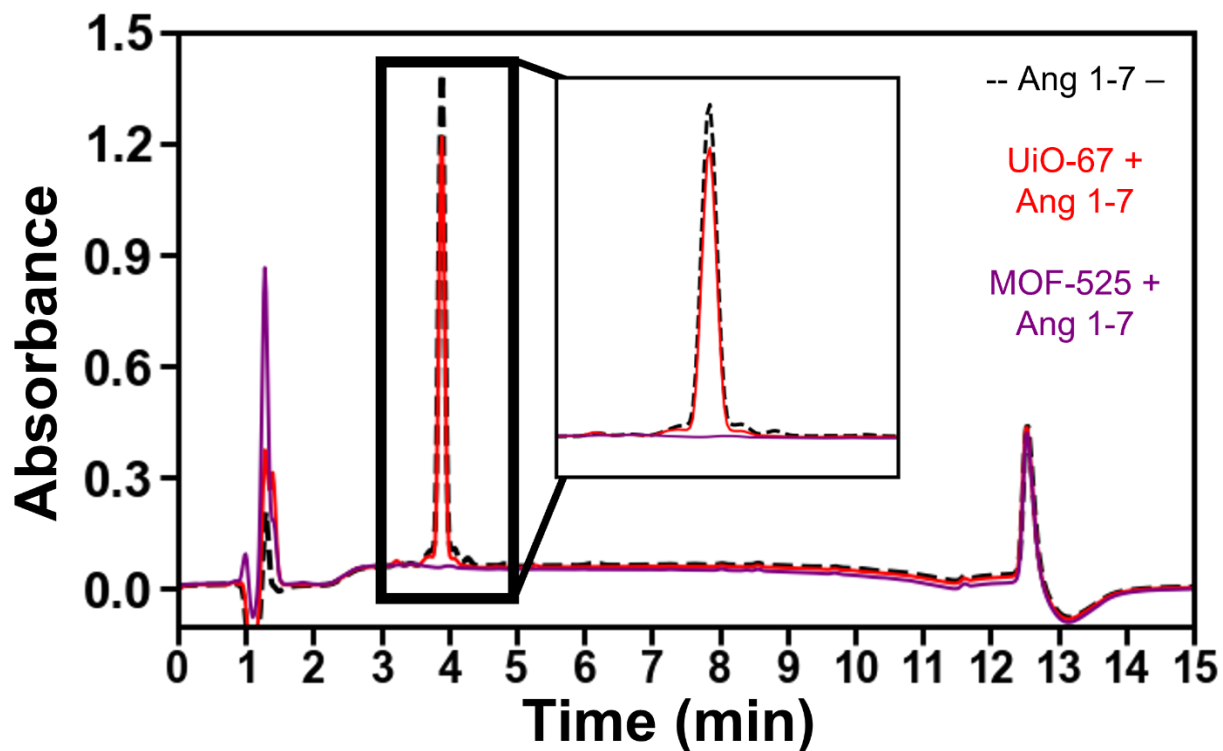
Figure C.31. RP-HPLC depicting Ang 1-7 (black) encapsulation into UiO-67 (red) and MOF-525 (purple). Little-to-no decrease in the Ang 1-7 peak (~3.75 m) was detected after incubation with UiO-67, suggesting little-to-no encapsulation of Ang 1-7 in UiO-67. In contrast, the complete disappearance of the Ang 1-7 peak in the sample incubated with MOF-525 suggests encapsulation of Ang 1-7. Therefore, we used MOF-525 based carriers for the Ang 1-7 encapsulation and release studies. Analytical RP-HPLC was performed on a Waters E2695 Alliance Separations Module, using a 4.5 mm x 50 mm XBridge C18 3.5 μm chromatographic separation column. Mobile phase composed of ultrapure water and acetonitrile + 0.1% trifluoroacetic acid, run at a gradient of 15 to 20% ACN from 2 to 12 min. UV absorbance was measured at 214 nm.
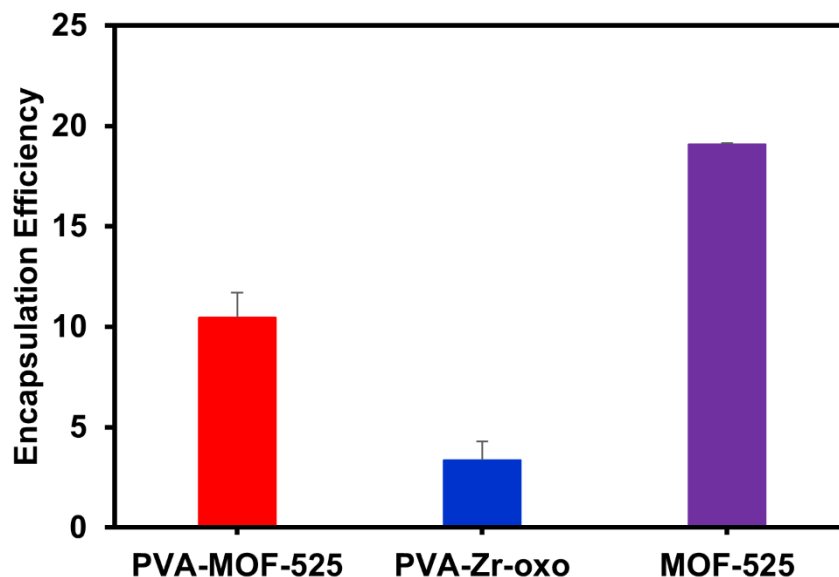
Figure C.32. Encapsulation efficiency, or % of Ang 1-7 in solution sorbed, of PVA-MOF 525 composite hydrogels (red), PVA-Zr-oxo hydrogels (blue) and MOF-525 powder (purple). All samples were determined to be at sorptive capacity, as their encapsulation efficiencies were lower than 100%. Plotted bars represent the average of 3 independently synthesized samples incubated with Ang 1-7 for 7 d. Error bars represent the standard deviation of the average.
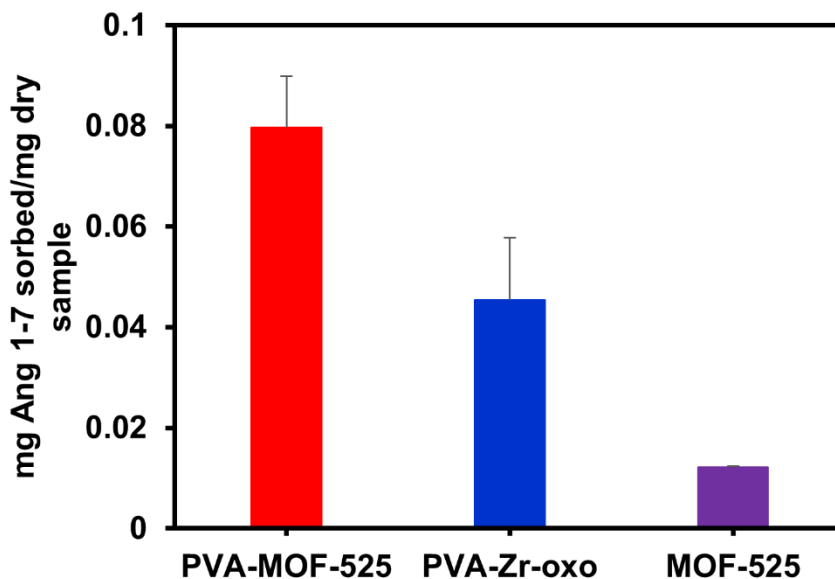
Figure C.33. Sorptive capacity of PVA-MOF-525 composite hydrogels (red), PVA-Zr-oxo hydrogels (blue), and MOF-525 powder (purple) for the therapeutic peptide Ang 1-7. Amount of Ang 1-7 sorbed into each sample after 7 d, normalized relative to the dry mass of each sample, showing more Ang 1-7 to sorb into the PVA-MOF-525 composite hydrogels than into the PVA-Zr-oxo hydrogels and MOF-525 on a per dry mass basis. Despite normalizing to dry weight, the hydrogels were added to Ang 1-7 solution in a swollen state, and the MOF-525 powder was added in a dry state.

Table C.5. Ang 1-7 sorption into PVA-MOF-525 composite hydrogels, PVA-Zr-oxo hydrogels, and MOF-525 powder

	µg Ang 1-7/mg carrier			µg Ang 1-7/mg dry carrier		
		Avg	StDev		Avg	StDev
PVA-MOF-525 composite gel	5.7			68.2		
	7.0	6.7	0.9	83.3	79.7	10.2
	7.3			87.6		
		Avg	StDev		Avg	StDev
PVA-Zr-oxo	1.7			36.2		
	1.9	2.2	0.6	40.3	45.3	12.5
	2.8			59.5		
		Avg	StDev		Avg	StDev
MOF-525	12.0			12.0		
	12.3	12.2	0.2	12.3	12.2	0.2
	12.2			12.2		

Figure C.34. % of Ang 1-7 sorbed into PVA-MOF-525 composite hydrogels (red, square), PVA-Zr-oxo hydrogels (blue, circle), and MOF-525 powder (purple, triangle) that was released into ultrapure water.

Table C.6. % of Ang 1-7 sorbed into PVA-MOF-525 composite hydrogels, PVA-Zr-oxo hydrogels, and MOF-525 powder released into ultrapure water.

Time (d)	PVA-MOF-525		PVA-Zr-oxo		MOF-525	
	Average	StDev	Average	StDev	Average	StDev
0.0	7.4	0.7	17.1	8.9	8.7	1.4
0.2	19.3	1.5	56.0	26.7		
0.3	16.3	0.8	58.9	15.3	21.5	4.1
0.7	26.8	8.0	51.9	12.1	22.9	2.0
1.0	26.1	1.5	51.8	18.2	25.0	1.6
1.7	27.0	2.1	55.8	12.8	24.9	1.1
2.7	28.8	3.3	57.7	14.9	26.1	2.0

C.6 References

(1) Mohammadi, A. A.; Alinejad, A.; Kamarehie, B.; Javan, S.; Ghaderpoury, A.; Ahmadpour, M.; Ghaderpoori, M. Metal-Organic Framework Uio-66 for Adsorption of Methylene Blue Dye from Aqueous Solutions. *Int. J. Environ. Sci. Technol.* **2017**, *14* (9), 1959–1968. https://doi.org/10.1007/s13762-017-1289-z.

(2) Song, X.; Yang, P.; Wu, D.; Zhao, P.; Zhao, X.; Yang, L.; Zhou, Y. Facile Synthesis of Metal-Organic Framework UiO-66 for Adsorptive Removal of Methylene Blue from Water. *Chem. Phys.* **2020**, *531*, 110655. https://doi.org/10.1016/j.chemphys.2019.110655.